

University of Nottingham
UK | CHINA | MALAYSIA

Thermal Modelling of a Totally Enclosed Fan - Cooled Electrical Machine

by

Salvatore La Rocca, MEng (Hons)

Fluids and Thermal Engineering Research Group

Faculty of Engineering

University of Nottingham

Thesis submitted to the University of Nottingham for the Degree of Doctor of Philosophy

September 2018

Abstract

A Totally Enclosed Fan-Cooled (TEFC) low voltage induction motor has been extensively investigated by means of Computational Fluid Dynamics (CFD) in order to look at detailed airflow and heat transfer modelling of such machines.

The typical structure of this machine design, where the heat removal is dependent on both the internal and external features, provides a significant modelling challenge as the internal and external flows and heat transfer must be analysed jointly, creating a complex scenario with multiple dependencies. Local fluid flow and thermal investigations of the most critical regions of the internal and external domains respectively allowed the identification of the best modelling approach and optimal mesh settings in terms of solution accuracy and computational cost.

A new modelling approach for more realistic end windings representation, which potentially can be applied to different kinds of machines, was developed in order to achieve more accurate predictions of complex fluid flow and heat transfer phenomena compared to a simplified representation commonly used. The developed methodology allowed different levels of end windings porosity to be investigated with results showing a significant impact on overall fluid flow and thermal predictions.

A full thermal CFD 3D model of the selected TEFC motor which includes all internal/external fluid and solid domains, in conjunction with electrical/thermal losses distributed across the whole machine, was then developed. The thermal and airflow analysis performed with the CFD conjugate model allowed an accurate understanding and prediction of the overall machine temperature distribution.

Experimental tests were carried out to validate the CFD model developed: temperatures, heat fluxes and torque were measured throughout the tests and data collected were compared to quantities predicted analytically and numerically showing a good agreement with predictions.

The validation of the developed CFD model allowed also to identify opportunities to improve the machine performance; enhanced cooling can lead to significant improvements in terms of reduction of temperature dependent losses and materials lifetime. Alternative design improvements were therefore proposed to enhance the overall TEFC machine performance and they were investigated with the numerical model developed.

Geometrical modifications of the internal original cooling design, consisting of shaft mounted stirrers in the machine's end region, were considered. The more realistic and detailed end windings representation developed in this work allowed to investigate the impact of higher level of porosity/cavities of the end windings on the overall machine thermal perfomance; results showed how a more accurate and detailed control of the porosity of the end windings can lead to sensible cooling improvements.

An alternative external cooling design consisting of a new fan and fan cover was also considered and the impact on the overall machine efficiency was numerically investigated; a 3D printed version of the proposed cooling fan was also manufactured and used for further experimental investigation.

The methodology presented in this thesis highlights the capability of CFD to model and simulate very complex geometries and fluid flows, with a high degree of detail and flexibility, allowing accurate predictions of temperature distribution within the electrical machine to be achieved.

Acknowledgements

I would like to thank my supervisors Prof. Stephen J. Pickering, Dr. Carol N. Eastwick and Prof. Christopher Gerada for their valuable support and encouragement throughout the duration of the PhD at the University of Nottingham.

I am very grateful to the Machine and Drives Group and IT Support at ABB Corporate Research Centre in Västerås (Sweden) for their support and interest in the work carried out during this PhD. Special thanks to Mr. Kristian Rönnberg, Dr. Dmitry Svechkarenko, Dr. Robert Chin and Mrs. Wenliang Chen for the support provided during my three-month visit to ABB CRC and for letting me feel like home while I was there.

Sponsorship of this PhD from ABB Group is gratefully recognised.

Thanks to Mr. Alessandro Marfoli for his support and collaboration during the whole project. I am grateful to John Hinchliffe, Colin Blackburn, Christopher Varley and the whole Power Electronics, Machines and Control (PEMC) team of technicians for their help and support with the experimental apparatus.

I would like to thank all my colleagues at the Fluids and Thermal Engineering Research Group: Dr. Antonino La Rocca, Dr. Peter H. Connor, Dr. Zeyuan Xu and Mr. Kevin Bersch. Thanks for all your support and the great time spent together.

Last, but no least, I give my special thanks to my family. My work and my studies are dedicated to my parents, Enzo and Lina, to my sister and brother, Anna and Antonio, and to my little niece Stefania. Thank you for your support and unconditional love.

Table of Contents

1 Introduction....1

1.1 Aim and objectives....3

1.2 Totally Enclosed, Fan–Cooled (TEFC) induction motor....4

1.3 Thesis structure....6

1.4 Publications....7

2 Literature review....8

2.1 Introduction....8

2.2 Heat transfer in electrical machines....8

2.2.1 Conduction....10

2.2.2 Convection....12

2.2.3 Radiation....16

2.3 Losses in electrical machines....18

2.3.1 Winding-Copper losses (Electrical loss)....18

2.3.2 Iron losses (Electro-magnetic loss)....19

2.3.3 Windage losses (Mechanical loss)....20

2.3.4 Bearing losses (Mechanical loss)....21

2.4 Thermal analysis techniques....22

2.4.1 Lumped parameter thermal network (LPTN)....23

2.4.2 Finite element analysis (FEA)....25

2.4.3 Computational fluid dynamics (CFD)....25

2.5 Summary....29

3 Experimental Test Facility....31

3.1 Introduction....31

3.2 Thermal Measurements....35

3.2.1 Temperature Measurements....38

3.2.2 Heat Flux Measurements....45

3.3 Torque and Speed Measurement....47

3.4 Uncertainty Analysis....48

3.5 Summary....48

4 Machine thermal modelling: internal domain methodology....49

4.1 Introduction....49

4.2 Overview of CFD Theory....50

4.3 Domains analysed 51
4.3.1 End Windings 55
4.3.2 End Region 63
4.3.2.1 Simplified and real housing geometry 67
4.3.2.2 Simplified and improved EWs geometry 76
4.3.3 Airgap 88
4.4 Optimisation and improvements 96
4.4.1 Stirrers model 1 101
4.4.2 Stirrers model 2 105
4.5 Summary 108
5 Machine thermal modelling: external domain methodology 110
5.1 Introduction 110
5.2 Complexity of the model and geometrical simplifications 111
5.3 Domain analysed 116
5.3.1 180° and 360° external model - CFD results 124
5.4 Optimisation and improvements 135
5.4.1 CFD results 138
5.5 Summary 147
6 Validation of CFD conjugate model 148
6.1 Introduction 148
6.2 Domain analysed 150
6.2.1 Discretization process 154
6.2.2 Boundary conditions and material properties 161
6.3 Experimental testing and validation 166
6.3.1 Validation and results of thermal performance 167
6.3.2 Validation and results of mechanical performance 183
6.4 Summary 185
7 Machine optimisation and improvements 187
7.1 Introduction 187
7.2 End Windings porosity: EWs model 1 and 2 189
7.3 Improved internal cooling design 194
7.4 Improved external cooling design 197
7.5 Summary 209
8 Conclusions and Recommendations 210

8.1 CFD thermal modelling conclusions 211
8.2 Novelty in this Thesis 213
8.3 Future works 214
References 215
Appendices 220
A. Dimensionless numbers 220
B. Theory behind CFD 222
B.1 Turbulence Modelling 223
B.2 Wall Treatment 225
C. CFD General Algorithm 227
C.1 Domain Identification 228
C.2 Geometry of Domain 228
C.3 Domain Discretisation 229
C.4 Solver Settings 230
C.5 Convergence 232
C.6 Post-Processing 233

List of Figures

Figure 1.1: Cutaway view of a generic TEFC induction motor [8] 5
Figure 2.1: Thermal flow paths – typical TEFC induction motor [9] 9
Figure 2.2: Schematic representation of Taylor vortices in an annulus with rotation [21] 15
Figure 2.3: Typical induction motor thermal network generated with Motor-CAD [9] 23
Figure 3.1: Schematic of Test Rig 31
Figure 3.2: TEFC motor platforms support 32
Figure 3.3: Schematic of test rig and coupling 33
Figure 3.4: Micro-foil heat flux sensor 36
Figure 3.5: Stator – DE and NDE side 38
Figure 3.6: Thermocouples location - Stator teeth and back iron 39
Figure 3.7: Thermocouples location: End Region 40
Figure 3.8: Thermocouples location: external housing, angular locations 41
Figure 3.9: Thermocouples location: external housing, axial locations 42
Figure 3.10: Heat flux sensors location – end caps 45
Figure 3.11: Heat flux sensors location - fins channels 46
Figure 3.12: Torque transducer Datum Electronics M425 47
Figure 3.13: M425 Torque transducer dimensions 47
Figure 4.1: TEFC machine structure 51
Figure 4.2: 3D CFD modelling approach of TEFC machine 52
Figure 4.3: Simplified (left) and real (right) end windings geometry 55
Figure 4.4: Cavities around the end windings geometry 56
Figure 4.5: Phase 1 extrusion from stator slot and change of cross section to elliptical 57
Figure 4.6: Phase 1 curvature and closure 58
Figure 4.7: Motor's three phases 59
Figure 4.8: Generic end winding configuration – radial thickness view 59
Figure 4.9: EWs geometry – 0% porosity model (no cavities) 60
Figure 4.10: EWs geometry – model 1 61
Figure 4.11: EWs geometry – model 2 61
Figure 4.12: Fluid end region, EWs model 2, 90° sector (solid included only for clarity) 63
Figure 4.13: Fluid end region, EWs model 2, 90° sector, reference frames 64
Figure 4.14: End Region – thermal and fluid flow investigation 66
Figure 4.15: Case A - Fluid end region, simplified housing and EWs 68
Figure 4.16: Case B - Fluid end region, simplified EWs and real housing 68
Figure 4.17: Case A and B – axial and radial plane 70
Figure 4.18 Case A - End region primary swirling flow – $v^*_{int} = v/v_{rotor\ tip}$ 71
Figure 4.19 Case B - End region primary swirling flow – $v^*_{int} = v/v_{rotor\ tip}$ 71

Figure 4.20: Case A - End region secondary flow – $v^*_{int} = v/v_{rotor\ tip}$ 72
Figure 4.21: Case B - End region secondary flow – $v^*_{int} = v/v_{rotor\ tip}$ 72
Figure 4.22: EWs sub-surfaces division – Case A and B 73
Figure 4.23: Fluid end region mesh, simplified EWs model 76
Figure 4.24: Fluid end region mesh, EWs model 1 77
Figure 4.25: Fluid end region mesh, EWs model 2 77
Figure 4.26: Simplified and improved EWs – axial and radial plane 79
Figure 4.27: End region primary swirling flow, simplified EWs – $v^*_{int} = v/v_{rotor\ tip}$ 80
Figure 4.28: End region primary swirling flow, EWs model 1 – $v^*_{int} = v/v_{rotor\ tip}$ 80
Figure 4.29: End region primary swirling flow, EWs model 2 – $v^*_{int} = v/v_{rotor\ tip}$ 81
Figure 4.30: End region secondary flow, simplified EWs – $v^*_{int} = v/v_{rotor\ tip}$ 82
Figure 4.31: End region secondary flow, EWs model 1 – $v^*_{int} = v/v_{rotor\ tip}$ 82
Figure 4.32: End region secondary flow, EWs model 2 – $v^*_{int} = v/v_{rotor\ tip}$ 83
Figure 4.33: Housing wall heat flux (negative as it is leaving the domain), simplified EWs model 84
Figure 4.34: Housing wall heat flux (negative as it is leaving the domain), EWs model 1 85
Figure 4.35: Housing wall heat flux (negative as it is leaving the domain), EWs model 2 85
Figure 4.36: Airgap fluid domain 20° sector 88
Figure 4.37: Airgap mesh 90
Figure 4.38: Normalised velocity profile across the slotted airgap at 1500 rpm 91
Figure 4.39: Open (left) and closed (right) stator slots 92
Figure 4.40: Non-dimensional windage power loss comparison: analytical and CFD (slotted and smooth airgap) 92
Figure 4.41: Normalised velocity profile across the slotted airgap at 1500 rpm and 400 rpm 93
Figure 4.42: Heat transfer coefficient 95
Figure 4.43: Stirrers model 1 97
Figure 4.44: Stirrers model 2 97
Figure 4.45: Stirrers geometrical details 98
Figure 4.46: Stirrers model 1 - axial and radial plane 100
Figure 4.47: Stirrers model 2 - axial and radial plane 100
Figure 4.48: End region primary swirling flow,EWs 2, original cooling design – $v^*_{int} = v/v_{rotor\ tip}$ 102
Figure 4.49: End region primary swirling flow,EWs 2, Stirrers Model 1 – $v^*_{int} = v/v_{rotor\ tip}$ 102

Figure 4.50: End region secondary flow, original cooling design – $v^*_{int} = v/v_{rotor\ tip}$ 103
Figure 4.51: End region secondary flow, Stirrers Model 1 – $v^*_{int} = v/v_{rotor\ tip}$ 103
Figure 4.52: End region primary swirling flow,EWs 2, Stirrers Model 2 – $v^*_{int} = v/v_{rotor\ tip}$ 106
Figure 4.53: End region secondary flow, Stirrers Model 2 – $v^*_{int} = v/v_{rotor\ tip}$ 106
Figure 5.1: Geometrical simplifications, external housing 111
Figure 5.2: TEFC motor external air cooling (fan cover removed) 112
Figure 5.3: External radial cooling fan 113
Figure 5.4: External radial fan, backplate simplification 114
Figure 5.5: External solid domain, housing and platforms 115
Figure 5.6: External hemispherical fluid domain 116
Figure 5.7: External hemispherical fluid domain dimensions 117
Figure 5.8: External fluid domain sub-regions – Ext Fan set as rotating frame 119
Figure 5.9: External fluid domain, MRF approach 120
Figure 5.10: Fan symmetry 121
Figure 5.11: External fluid domain mesh 122
Figure 5.12: Radial planes along axial direction 125
Figure 5.13: Fan outlet radial plane, non-dimensional velocity, 180° model – $v^*_{ext} = v/v_{original\ fan\ tip}$ 126
Figure 5.14: Fan outlet radial plane, non-dimensional velocity, 360° model – $v^*_{ext} = v/v_{original\ fan\ tip}$ 126
Figure 5.15: Housing radial plane, non-dimensional velocity, 180° model – $v^*_{ext} = v/v_{original\ fan\ tip}$ 128
Figure 5.16: Housing radial plane, non-dimensional velocity, 360° model – $v^*_{ext} = v/v_{original\ fan\ tip}$ 128
Figure 5.17: External airflow non-dimensional velocity streamlines – $v^*_{ext} = v/v_{original\ fan\ tip}$ 129
Figure 5.18: Fan angular position – MRF approach 131
Figure 5.19: Fan outlet radial plane, non-dimensional velocity, Fan position "1" – $v^*_{ext} = v/v_{original\ fan\ tip}$ 132
Figure 5.20: Fan outlet radial plane, non-dimensional velocity, Fan position "2" – $v^*_{ext} = v/v_{original\ fan\ tip}$ 132
Figure 5.21: Housing radial plane, non-dimensional velocity, Fan position "1" – $v^*_{ext} = v/v_{original\ fan\ tip}$ 133
Figure 5.22: Housing radial plane, non-dimensional velocity, Fan position "2" – $v^*_{ext} = v/v_{original\ fan\ tip}$ 133
Figure 5.23: Mass flow rate comparison – Fan angular position 134
Figure 5.24: Proposed new Fan cover geometry 136
Figure 5.25: Fan – original (left) and proposed new design (right) 137
Figure 5.26: Proposed cooling design investigation 138

Figure 5.27: Fin channel, L_1 and L_2 x-radial location 139
Figure 5.28: Fin channel, Airflow z-direction 139
Figure 5.29: Fin channel, non-dimensional airflow velocity plot - L_1 – v^*_{ext} = $v/v_{original\ fan\ tip}$ 140
Figure 5.30: Fin channel, non-dimensional airflow velocity plot - L_2 – v^*_{ext} = $v/v_{original\ fan\ tip}$ 140
Figure 5.31: Housing radial plane, non-dimensional velocity, Case 1– v^*_{ext} = $v/v_{original\ fan\ tip}$ 142
Figure 5.32: Housing radial plane, non-dimensional velocity, Case 4– v^*_{ext} = $v/v_{original\ fan\ tip}$ 142
Figure 5.33: Non-dimensional mass flow rate comparison, Fan inlet plane, Case 1-2-3-4 143
Figure 5.34: External heat transfer coefficient wall zones 144
Figure 5.35: Non-dimensional CFD heat transfer coefficients–Case 1-2-3-4 145
Figure 6.1: TEFC full thermal model, modelling approach 149
Figure 6.2: TEFC machine solid components – EWs model 1 implemented. 150
Figure 6.3: Fluid and solid domains, symmetry plane view 151
Figure 6.4: Rotating fluid zones – Airgap and End Region 152
Figure 6.5: Rotor and Stator domain sub-division 153
Figure 6.6: Stator and rotor mesh, axial view (airgap domain excluded) 155
Figure 6.7: EWs model 1 mesh 156
Figure 6.8: EWs model 1, solid-fluid interface refinement 157
Figure 6.9: 360° CFD model, EWs model 1, symmetry plane view showing internal and external domain 159
Figure 6.10: EWs sub-division for anisotropic thermal conductivity 163
Figure 6.11: Axial mid-plane location (x = 0 and y=0) 168
Figure 6.12: Non-dimensional TEFC machine temperature rise, axial mid-plane – $\Delta T^* = \Delta T / \Delta T_{exp,EWs\ DE}$ 168
Figure 6.13: Non-dimensional rotor and shaft temperature rise, axial mid-plane – $\Delta T^* = \Delta T / \Delta T_{exp,EWs\ DE}$ 169
Figure 6.14: Non-dimensional velocity and stator temperature rise, NDE stator plane side 170
Figure 6.15: Non-dimensional stator temperature rise, axial gradient and DE-NDE side radial view – $\Delta T^* = \Delta T / \Delta T_{exp,EWs\ DE}$ 170
Figure 6.16: Stator teeth and back iron non-dimensional temperature rise, DE side 172
Figure 6.17: Stator teeth and back iron non-dimensional temperature rise, NDE side 172
Figure 6.18: EWs non-dimensional temperature rise, DE and NDE side 174
Figure 6.19: End region non-dimensional temperature rise, DE and NDE side 175
Figure 6.20: External housing planes, DE and NDE 176

Figure 6.21: Stator-housing interface – Interface Resistance Stator (I.R. - left) and Ideal Contact Stator (I.C. - right) 177
Figure 6.22: Housing non-dimensional temperature rises, DE plane 178
Figure 6.23: Fan geometry comparison, real sized fan on the right 180
Figure 6.24: Housing radial plane, non-dimensional velocity, small fan – $v^*_{ext} = v/v_{original\ fan\ tip}$ 181
Figure 6.25: Housing radial plane, non-dimensional velocity, real sized fan– $v^*_{ext} = v/v_{original\ fan\ tip}$ 181
Figure 6.26: Mechanical power losses CFD (bearings + windage) and experimental trend 184
Figure 7.1: CFD modelling approach of alternative cooling configurations 187
Figure 7.2: Non-dimensional EWs temperature rise, DE 190
Figure 7.3: Non-dimensional windings temperature rise, DE 190
Figure 7.4: Machine components maximum non-dimensional temperature rise –EWs model 1 and 2 191
Figure 7.5: Machine components average non-dimensional temperature rise – EWs model 1 and 2 192
Figure 7.6: Non-dimensional end region airflow velocity magnitude 195
Figure 7.7: Non-dimensional EWs temperature rise, DE 196
Figure 7.8: non-dimensional EWs temperature rise, DE 198
Figure 7.9: non-dimensional stator temperature rise, DE 198
Figure 7.10: Machine components maximum non-dimensional temperature rise – original and proposed external cooling design 199
Figure 7.11: Machine components average non-dimensional temperature rise – original and proposed external cooling design 200
Figure 7.12: Non-dimensional mechanical power losses – original and new design 201
Figure 7.13: Original (left) and proposed new fan (right) design 202
Figure 7.14: 3D printed new fan mounted on the TEFC machine, tests included the original fan cover design 203
Figure 7.15: Stator teeth and back iron non-dimensional temperature rise, DE side 204
Figure 7.16: Stator teeth and back iron non-dimensional temperature rise, NDE side 204
Figure 7.17: EWs experimental non-dimensional temperature rise, original and new cooling design 205
Figure 7.18: End region experimental non-dimensional temperature rise, original and new cooling design 206
Figure 7.19: Non-dimensional mechanical power losses CFD (bearings + windage) and experimental trends 208
Figure 0.1: Near-Wall Regions [66] 225
Figure 0.2: Wall Modelling Approaches [66] 226

Figure 0.3: CFD process 228
Figure 0.4: Typical mesh elements 229
Figure 0.5: Control volume 231

List of Tables

Table 2.1: Typical thermal conductivity of electrical machine materials 11
Table 2.2: Flow regime thresholds and Nusselt correlations [27, 31].....16
Table 2.3: Typical Emissivity of electrical machines materials [3] 17
Table 2.4: A, α and β coefficients for different flow regimes [38].....21
Table 3.1: Experimental thermal instrumentation 35
Table 3.2: Thermocouple labels – external housing.....43
Table 3.3: Thermocouple labels – external housing overview.....44
Table 4.1: EWs models porosity.....62
Table 4.2: Air properties from Ansys Fluent at 120°C [66].....65
Table 4.3: Mesh details and computational cost – Case A and B.....69
Table 4.4: Heat flow comparison: EWs sub-surfaces, Case A and Case B.....74
Table 4.5: Heat flow comparison – Housing, Case A and B.....75
Table 4.6: Mesh details and computational cost – Simplified and improved EWs.....78
Table 4.7: Rate of heat flow comparison, simplified and new EWs models....86
Table 4.8: Airgap flow regimes (laminar shear flow) 90
Table 4.9: Heat transfer coefficient, End region comparison, Stirrers Model 1 104
Table 4.10: Heat transfer coefficient, End region comparison, Stirrers Model 2 107
Table 5.1: External fluid domain cell count, refer to Figure 5.8 for naming of zones 123
Table 5.2: New external cooling fan details 137
Table 5.3: Non-dimensional CFD heat transfer coefficients – Case 1-2-3-4, percentage differences 145
Table 6.1: Rotor and Stator domain sub-division.....153
Table 6.2: EWs model 1 and 2 – mesh cell count of EWs solid domain.....156
Table 6.3: Mesh details of 360° CFD conjugate model – EWs model 1.....160
Table 6.4: TEFC machine losses distribution at 1,500 rpm 162
Table 6.5: Employed materials.....165
Table 6.6: Stator teeth and back iron non-dimensional temperature rise, % difference with experimental data 173
Table 6.7: EWs and ER non-dimensional temperature rise, % difference with experimental data.....175
Table 6.8: Housing DE plane non-dimensional temperature rise, % difference with experimental data.....178
Table 6.9: non-dimensional CFD heat transfer coefficients – small and real sized fan percentage differences.....182
Table 7.1: Machine components maximum non-dimensional temperature rise – EWs model 1 and 2, % difference 192

Table 7.2: Machine components maximum non-dimensional temperature rise – original and proposed external cooling design 199
Table 7.3: Stator non-dimensional experimental temperature rise, original and new cooling design % difference..... 205
Table 7.4: EWs and ER experimental non-dimensional temperature rise, original and new cooling design % difference 206

Nomenclature

Symbols

Symbol	Description	Units
L	Length	m
x	Distance	m
y	Distance	m
z	Distance	m
A	Surface area	m^2
V	Volume	m^3
y^+	Near wall distance	
D	Diameter	m
r	Radius	m
g	Airgap width	m
F_g	Geometry correction factor	
I	Electric current	Ampere
f	Frequency	Hz
R_{phase}	Electrical winding resistance	Ω
T_q	Torque	Nm
C_M	Torque coefficient	
n	Rotational speed	rpm
Re	Reynolds number	
Re_r	Taylor-Couette Reynolds number	
Nu	Nusselt number	
Ta	Taylor number	
v	velocity	m/s
u'_i	Fluctuating velocity	m/s
$\bar{u}_i$	Average velocity	m/s
$\dot{m}$	Mass flow rate	kg/s
P	Power	W
q	Heat flow	W

Q”	Heat flux	W/m^2
T	Temperature	K
c_p	Heat Capacity	J/kgK
R_{th}	Thermal resistance	K/W
k	Thermal conductivity	W/mK
h	Heat transfer coefficient	W/m^2K

Greek symbols

Symbol	**Description**	**Units**
α	Linear temperature coefficient	
ρ	Density	kg/m^3
ε	Emissivity	
μ	Dynamic viscosity	kg/ms
σ	Stefan-Boltzmann constant	W/m^2K^4
φ	Electrical resistivity	Ωm
τ	Shear strees	Pa
ν	Kinematic viscosity	m^2/s
ω	Rotational speed	rad/s
π	Pi	
ϕ	Porosity	

Abbreviations

Abbreviation	Description
CFD	Computational Fluid Dynamics
LPTN	Lumped Parameter Thermal Network
FEA	Finite Element Analysis
MRF	Moving Reference Frame
SM	Sliding Mesh
2D	2 Dimensional
3D	3 Dimensional
TEFC	Totally Enclosed Fan-Cooled
DE	Drive End
NDE	Non Drive End
EWs	End Windings
ER	End Region
rpm	Revolutions Per Minute

Non-Dimensional Numbers

Velocity – internal domain $$v_{int}^{*} = \frac{v}{v_{rotor\ tip}}$$

Velocity – external domain $$v_{ext}^{*} = \frac{v}{v_{original\ fan\ tip}}$$

Temperature $$\Delta T^{*} = \frac{\Delta T}{\Delta T_{exp,EWs\ DE}}$$

Mechanical power loss $$P_{m}^{*} = \frac{P_{m}}{P_{m,exp,1500rpm}}$$

1 Introduction

The world industry is facing a significant energy challenge: industrial processes are highly energy intensive and currently account for one-third of global energy use and the demand for energy is still rising steadily. The increase in energy consumption is associated with increase in CO_2 industry emissions which nowadays make up to 40% of the total CO_2 emissions worldwide [1]. It has been estimated that electrical motors account for about 65% of the electricity consumed in industrial applications and therefore the energy saving potential in this sector is huge; high-efficiency motors can play a significant part in reducing CO_2 emissions [2].

For electrical machines along with the electromagnetic design, in the last decade thermal design has begun to attract serious attention of design engineers. This can be explained by the fact that high temperature gradients can significantly limit the overall machine efficiency; high copper temperatures reduce the efficiency by increasing winding-copper losses. In addition temperature impacts the lifetime of the materials, in particular of the insulating materials; for instance, above the maximum temperature allowed for the given insulation class, a rise of 10 K can reduce the lifetime of the insulation by as much as 50% [3].

In the past, motor designers have dealt with the thermal design aspect mostly based on prior knowledge of parameters related to the operating conditions such as winding to ambient thermal resistance or housing heat transfer coefficient [4]. In reality very complex thermal phenomena involving conduction, convection and radiation take place in electrical machines and detailed thermal modelling is required to investigate the machine's thermal behaviour. Effective thermal management leads to a reduction in winding temperature dependent losses and improved airflow can additionally reduce windage losses and thus increases the performance of the machine; with consequential, economic advantages.

Totally Enclosed, Fan-Cooled (TEFC) induction motors are the most commonly used in ordinary industrial enviroments due to their robustness and capability to work in dirty, moist or mildly corrosive operating conditions [2]. The design of this type of machine has been unchanged for decades, being a low cost high volume design where the benefits around improvement have been regarded as marginal. However, with the increasing emphasis on efficiency and sustainability there is now a growing awareness within industry of the need to address the thermal management of this machine type.

1.1 Aim and objectives

The aim of the work presented in this thesis is to develop a full thermal CFD 3D model of a TEFC induction machine and look at detailed airflow and heat transfer modelling of such machines. The model developed is used to investigate optimising the balance between reduction of machine temperature and reduction of losses associated with driving ventilation through the machine.

The main objectives of the present work are stated as follows:

- Establish the best modelling approach for the most critical areas of the selected TEFC machine by developing CFD techniques.

- Creation of a CFD methodology for conjugate heat transfer analysis of full 3D TEFC machine including internal/external fluid and solid domains for accurate understanding and prediction of machine thermal and fluid flow behaviour.

- Experimental validation of the numerical models by carrying out experimental investigations under full and no load conditions.

- Identification of most promising areas of improvement and optimisation of the cooling machine performance.

1.2 Totally Enclosed, Fan–Cooled (TEFC) induction motor

The TEFC machine topology investigated in this work was identified as a low voltage induction motor with an output power (P) of 11kW at a rated rotational speed of 1500 rpm. The manufacturer provided information necessary for defining simulation models as well as a machine for experimental testing.

These motors are probably the most commonly used motors in industrial environments. A TEFC induction motor is a type of industrial motor with an enclosure that does not permit outside air to freely circulate through the interior of the motor: the internal parts are totally isolated from the surrounding air.

The TEFC motor is cooled by blowing air over the motor frame with an external fan mounted on the rear shaft of the motor; a fan cover or shroud covers the fan to direct the airflow over the external fins. In the TEFC motor, radial fins running in the axial direction are usually included on the frame surface in order to increase its surface area and therefore reduce the convective thermal resistance between frame and surrounding environment [5, 6]. Furthermore, internal features for enhancing the removal of the heat generated may include rotor bar extensions and wafters fixed to the rotor end ring which provide an internal mixing effect and improve the convective heat transfer in the end region area [7]. Figure 1.1 below shows a typical structure of a TEFC motor and its main elements.

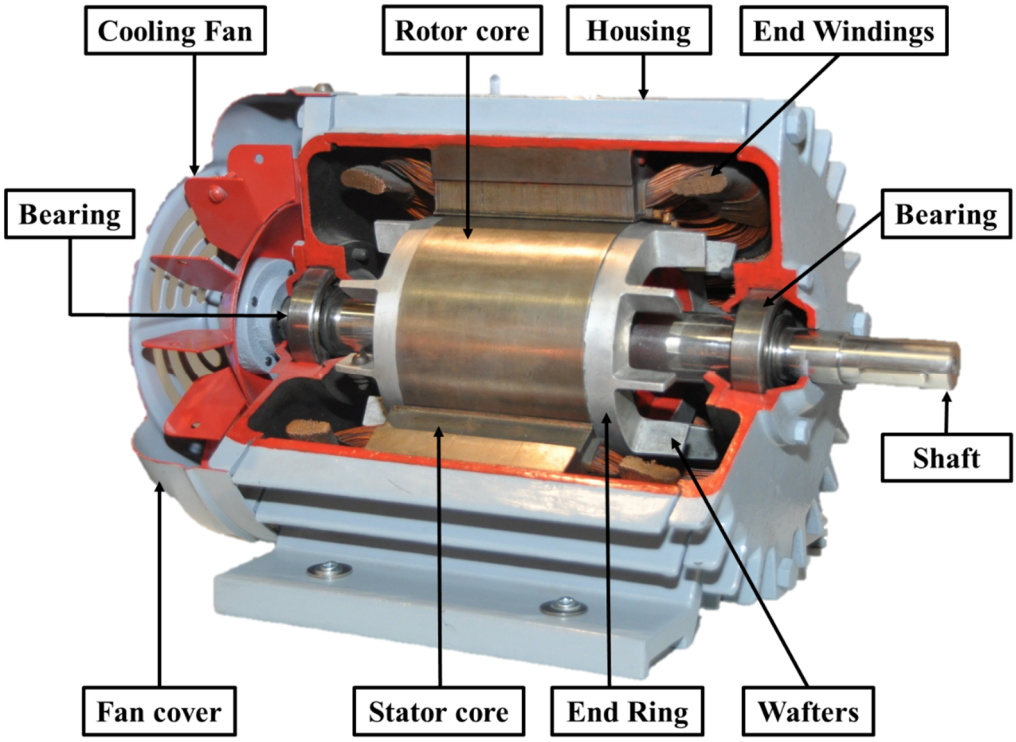


Figure 1.1: Cutaway view of a generic TEFC induction motor [8]

1.3 Thesis structure

- Chapter 2 provides a literature review of the heat transfer problem in electrical machines and the modelling techniques used for thermal analysis.
- Chapter 3 provides a description of the rig used for experimental testing and collection of data.
- Chapter 4 describes the CFD thermal modelling approach of the internal domain of the machine and its most critical areas: end region and airgap.
- Chapter 5 describes the CFD modelling of the machine external fluid domain.
- Chapter 6 reports a comparison between CFD predictions and experimental results and provides experimental validation of the numerical models developed.
- Chapter 7 describes alternative cooling arrangements considered and numerically investigated to improve the overall TEFC machine performance.
- Chapter 8 summarises the main achievements of this work and provides final conclusions and future recommendations.

1.4 Publications

1. La Rocca, S., Pickering, S.J., Eastwick, C.N., Gerada, C., Connor, P.H., Rönnberg, K., *Challenges in modelling totally enclosed fan-cooled electrical machines*, in *International Heat Transfer Symposium and Heat Powered Cycles Conference*, 26-29 June 2016, Nottingham (U.K.).
2. La Rocca, S., Pickering, S. J., Eastwick, C.N., Gerada, C., Rönnberg, K., *Fluid flow and heat transfer analysis of TEFC machine end regions using more realistic end-winding geometry*, in *9th IET International Conference on Power Electronics, Machines and Drives (PEMD 2018),* 17-19 April 2018, Liverpool (U.K.).
3. La Rocca, S., Pickering, S. J., Eastwick, C.N., Gerada, C., Rönnberg, K., *Numerical study on the impact of end windings porosity on the fluid flow and heat transfer in a Totally Enclosed Fan – Cooled electrical machine,* in *11th IEEE International Electric Machines and Drives Conference (IEMDC),* 12-15 May 2019, San Diego, California (U.S.A.).
4. Connor, P.H., La Rocca, A., La Rocca, S., Bersch, K., Eastwick, C.N., Pickering, S. J., *Key challenges for the Thermal management of Electrical Machines,* in *Vehicle Thermal Management System Conference and Exhibition (VTMS 14),* 05 - 06 June 2019, London (U.K.).

2 Literature review

2.1 Introduction

This chapter provides a review of power losses and heat transfer methods and how these are related to electrical machines. Several modelling techniques can be used to perform thermal analysis of electrical machines and these are discussed and presented.

2.2 Heat transfer in electrical machines

Heat transfer always occurs when there is a temperature gradient in a system. In the case of electrical machines thermal management is a fundamental area of analysis; the specific power density in electrical machines has continuously risen over recent years and, due to industry demands and material costs, machines are becoming always more compact. This has resulted in higher temperature gradients which can significantly reduce the overall efficiency and determine the capacity for increased power density; high temperatures could particularly lead to a rapid deterioration of windings insulation, giving rise to serious failure or reduced lifetime.

Regarding the study of thermal performances of electrical machines, the three existing heat transfer modalities are considered: conduction, convection and radiation. Due to complex geometries typical of electrical machines, thermal analysis is not an easy task as several complex variables need to be considered such as anisotropic material properties and turbulent fluid flow phenomena.

Figure 2.1 [9] below provides a schematic view of the major heat transfer paths occurring in a typical induction motor due to electrical losses occurring in rotor, stator and windings. Typically the main sources of losses are the copper windings and rotor bars with about 45% and 30% of total losses occurring respectively; the remaining 25% are roughly the iron losses generated in the stator (10%) and rotor core (10%) and the mechanical losses (bearings – 5%).

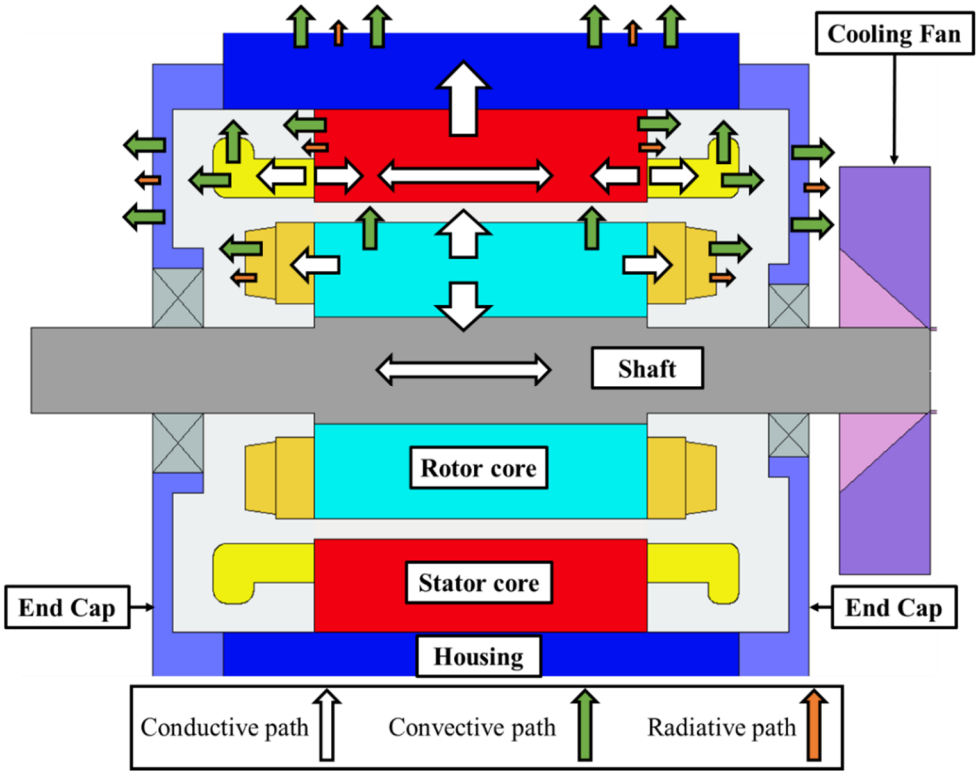


Figure 2.1: Thermal flow paths – typical TEFC induction motor [9]

As shown in Figure 2.1 part of the heat generated in the rotor core and rotor bars flows by conduction through the motor shaft; the rest is dissipated by convection to the air surrounding the rotor core in the end regions and in the stator-rotor airgap. The heat generated in the stator core and windings is mainly dissipated by conduction through the external housing and the end windings; in the end regions convection is the predominant heat transfer method as the heat generated in the end windings is dissipated to the surrounding air and then passes to the housing and end caps. The heat passed to the external frame is then dissipated to the surrounding ambient environment by forced convection provided by the external cooling fan. The dissipation rate though the different paths shown in Figure 2.1 is strongly dependent by the cooling system; in the machine under investigation, most of the losses are dissipated radially through the housing in proximity of the external fan.

2.2.1 Conduction

Thermal conduction is the transfer of internal energy by microscopic diffusion and collisions of particles within a body: it is the main heat transfer modality between solids when a temperature difference exists. Fourier's law gives the heat flow rate transferred by conduction: for many simple applications it is used in its one-dimensional form as reported in Equation 2.1 for the x-direction [10].

$$q_x = -k(T)A\frac{\delta T}{\delta x} \quad \textbf{2.1}$$

Where q_x [W] is the heat flow rate, $k(T)$ [W/mK] is the thermal conductivity of the material, A [m^2] is the heat transfer area normal to the direction of heat transfer, δT [K] is the temperature gradient between the surfaces considered and δx [m] is the material thickness. Thermal conductivity is the property of the material to conduct heat and depends on the temperature: materials which are good electrical conductors are, usually, also good thermal conductors, while insulators used in the electrical machines are poor thermal conductors. Typical values of thermal conductivity of the materials used in an electrical machine are listed below in Table 2.1 [3].

Material	**k** [W/mK]
Aluminium	209 - 231
Copper	394
Slot insulation	0.2 - 1.2
Cast Iron	27 – 52
Steel	22 - 45
Resin	0.08 - 0.21

Table 2.1: Typical thermal conductivity of electrical machine materials

The stator and rotor are usually of a laminated construction (a stack of electrical steel laminations) therefore thermal conductivity is not an isotropic property, leading to different values along axial and radial directions of the electrical machine [3]: typical ratios of radial-to-axial thermal conductivity are 20 to 40 [4]. In the case of laminated materials, a thermal conductivity analysis strongly depends also on other variables, such as lamination thickness, clamping pressure, lamination surface finish, interlamination insulation material [11]; moreover, other variables to consider are the winding insulation and impregnation and the interface gaps between components (e.g., stator lamination to housing, slot-liner to stator lamination) which eventually introduce additional thermal contact resistances [11]. Further thermal resistances can be also found at the interface between stator lamination and external frame where small airgaps, due to imperfections in the touching surfaces, are located; this is a complex function of material hardness, interface pressure and surface roughness. In the case of a TEFC machine, where most of the heat dissipation takes place through the external frame, the existence of these interface gaps lead to an overall increase of thermal resistance [11].

2.2.2 Convection

Convective heat transfer occurs between a solid surface and a fluid in motion when there is a temperature difference between them. According to the nature of the fluid motion, convection can be classified as:

- Natural convection: fluid motion is not driven by any external source (pump, fan), but only by density differences in the fluid due to temperature gradients.
- Forced convection: fluid motion is generated by external mechanisms (pump, fan).

Newton's law (Equation 2.2) gives the heat flow rate transferred by convection [10].

$$q_x = hA(T_s - T_f) \qquad \textbf{2.2}$$

h [W/m^{2}K] is the convective heat transfer coefficient, A [m^2] is the contact surface between the solid surface and the fluid flow, T_s and T_f [K] are the solid surface and fluid temperature respectively. The determination of h is a challenging task since it is a function of many factors: geometry and roughness of the surface, flow velocity and regime of the medium and its properties such as viscosity, thermal conductivity, specific heat capacity etc [10]. Typical values of the heat transfer coefficient for natural convection are in the range between 5 and 25 W/m^{2}K, whilst for forced convection the range is between 10 and 300 W/m^{2}K and between 50-20k W/m^{2}K if the coolant is liquid [12].

In order to calculate the heat transfer coefficient, empirical correlations based on dimensionless numbers (Reynolds *Re*, Grashof *Gr*, Nusselt *Nu* and Prandtl *Pr* – Appendices A) are usually used:

- *Reynolds number* (Re): it is defined as the ratio of inertial forces to viscous forces. The magnitude of Re provides information about the flow regime which could be laminar or turbulent.
- *Grashof number* (Gr): it is the ratio of the buoyancy to viscous force acting on a fluid.
- *Nusselt number* (Nu): it is the ratio of convective to conductive heat transfer across (normal to) the boundary and it provides indications about the relevance of convection with respect to conduction processes.
- *Prandtl number* (Pr): it is the ratio of momentum diffusivity (kinematic viscosity) to thermal diffusivity. In heat transfer problems, the Prandtl number controls the relative thickness of the momentum and thermal boundary layers.

The application of empirical correlations based on dimensionless number analysis allows the same formulation to be used for similar shaped geometries with different size and/or different fluid from the original experiments [13].

In electrical machines, due to complex geometries and fluid flow regimes, the prediction and calculation of the convective heat transfer coefficient is very challenging. Many studies have been conducted and published in order to investigate the convective phenomena in the most critical areas of a TEFC machine: end space region [4, 14-16], housing [6, 17-19], airgap between rotor and stator [4, 20-22].

For instance, analytical studies on the end region lead to the following correlation for the calculation of the heat transfer coefficient h [4] as reported in Equation 2.3: k_1, k_2, k_3 are curve fit coefficients and v is the velocity of the fluid.

$$h = k_1[1 + k_2 v^{k_3}] \qquad \textbf{2.3}$$

Regarding the airgap between the rotor and stator in electrical machines, many studies demonstrated the importance of convective heat transfer within the cylindrical gap [16, 21]; moreover, it is particularly important to have accurate estimations of windage losses since they strongly affect the machine efficiency [23]. The determination of the flow field is therefore essential because without the knowledge of the predominant flow regime, a thermal analysis in this region is a very difficult task [24, 25].

Flow and heat transfer between two smooth concentric rotating cylinders, known as Taylor – Couette flow, has been extensively investigated over recent years; these studies show the existence of different flow regimes dependent on rotational speed and on the Taylor number (Ta) [26] as reported in Equation 2.4.

$$Ta = \frac{\omega^2 r_r g^3}{\upsilon^2} \qquad \textbf{2.4}$$

The Taylor number is a dimensionless quantity that characterizes the importance of centrifugal or inertial forces due to rotation of a fluid about an axis, relative to viscous forces; ω [rad/s] is the rotor speed, r_r [m] the rotor radius, g [m] the airgap width and υ [m^2/s] the kinematic viscosity.

Assuming the annular gap length is small compared to the mean radius (known as small gap approximation [26]) and that there is no axial flow (as typically occurs in a TEFC machine), three main flow regimes can be identified:

- Laminar shear flow.
- Laminar flow plus vortices.
- Turbulent flow plus vortices.

For low Taylor number the flow is considered steady and laminar and the heat transfer in the airgap region is mostly dominated by conduction [27]. Above a critical value of speed and Taylor number (Ta_{crit} = 1700 for this geometric configuration [26, 28]) the laminar flow becomes unstable and results in a secondary flow structure of regularly spaced vortices, known as Taylor vortices [26], which occurs along the axial length of the annulus. These vortices occur in pairs and are counter rotating with the plane of rotation normal to the axis of the cylinders as schematically shown in Figure 2.2 [21]; Taylor vortices cause a rapid transport of fluid and this leads to a rise of the heat transfer [27, 29, 30]. With increasing rotational speed, the flow becomes more and more complex and finally turns into turbulent flow.

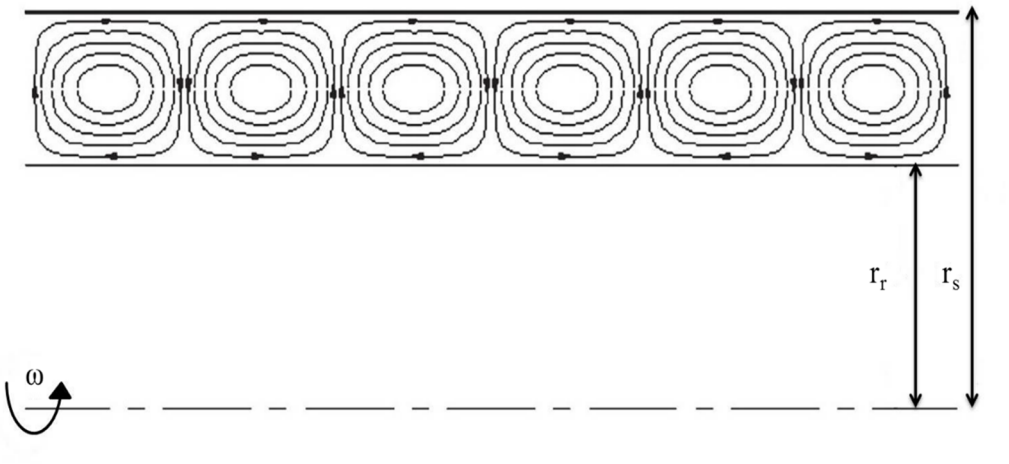


Figure 2.2: Schematic representation of Taylor vortices in an annulus with rotation [21]

Table 2.2 below reports the threshold values of Taylor number and the correlations for the Nusselt number proposed by Becker and Kaye [27, 31] for each flow regime; F_g is a geometry correction factor [31] which takes into account the aspect ratio of the smooth annular gap and it is close to 1 for a narrow airgap.

Laminar shear flow	$Ta/F_g < 1700$	$Nu = \frac{2 \cdot \frac{g}{r_r}}{\ln(1 + \frac{g}{r_r})}$
Laminar flow with vortices	$1700 < Ta/F_g < 10^4$	$Nu = 0.128 \cdot (\frac{Ta}{F_g})^{0.367}$
Turbulent flow	$10^4 < Ta/F_g < 10^7$	$Nu = 0.409 \cdot (\frac{Ta}{F_g})^{0.241}$

Table 2.2: Flow regime thresholds and Nusselt correlations [27, 31]

2.2.3 Radiation

Heat transfer through radiation takes place in the form of electromagnetic waves, mainly in the infrared region, from all material that has a temperature greater than absolute zero. Thermal radiation can propagate without the presence of matter through the vacuum of space; it depends on the type of material and surface of the body and its temperature. The Stefan-Boltzmann equation provides radiative heat flux between two objects [10] as reported in equation 2.5 below.

$$q'' = \varepsilon\sigma(T_1^4 - T_2^4) \qquad \textbf{2.5}$$

σ [W/m^{2}K^4] is the Stefan-Boltzmann constant ($5.6703 \cdot 10^{-8}$ W/m^{2}K^4), ε is the relative emissivity between the two surfaces, T_1 and T_2 [K] are their temperatures respectively.

In most applications of electrical machines, heat transfer by radiation does not have a significant role in comparison with the total heat transfer of the machine and thus it often can be neglected. Nevertheless, thermal radiation must be taken into account in the total heat transfer calculations of an electrical machine if, besides radiation, there is only natural convection without any fan in the system or if the machine operates at very low speeds [4, 11].

The rate of heat transfer by radiation depends on the emissivity ε, which is a property of the material; Table 2.3 below reports the emissivity of some materials in typical electrical machines [3].

Material	Emissivity
Polished aluminium	0.04
Polished copper	0.025
Mild steel	0.2-0.3
Cast iron	0.3
Stainless steel	0.5-0.6
Black paint	0.9-0.95
Aluminium paint	0.5

Table 2.3: Typical Emissivity of electrical machines materials [3]

2.3 Losses in electrical machines

The difference between the mechanical output power and the electrical input power are the losses which reduce the machine efficiency. Typically, 10% of the electrical energy input is converted into heat [3]: these power losses lead to a decrease of the overall efficiency of the machine.

According to their nature, the main losses in an electrical machine can be classified as listed below:

- Electrical: resistive losses generated in the copper windings.
- Electro - Magnetic: generated in the stator and rotor due to variation of magnetic fields.
- Mechanical: generated due to friction between rotating parts. These are mostly located in the bearings, in the airgap between stator and rotor and in the external cooling fan.

2.3.1 Winding-Copper losses (Electrical loss)

The winding or copper losses in an electrical machine are losses created by the current flow in the windings of the machine. These losses can be calculated by Equation 2.6.

$$P_{Cu} = \mathrm{m} I^2 R_{phase} \quad \textbf{2.6}$$

Where R_{phase} [Ω] is the resistance of one phase winding, I [A] the value of the current flowing into the winding, m the number of phases of the machine. R_{phase} depends on the geometry of the winding, the material and the number of turns N as in Equation 2.7:

$$R_{phase} = \frac{N\varphi(T)L_c}{A_c} \quad \textbf{2.7}$$

Where L_c [m] and A_c [m^2] are the length and cross sectional area of the conductor, $\varphi(T)$ [Ω·m] is the electrical resistivity which is a function of the conductor's temperature.

The resistivity of copper as a function of the temperature can be calculated using Equation 2.8.

$$\varphi(T) = \varphi_0[1 + \alpha_0(T - T_0)] \quad \textbf{2.8}$$

Where T_0 is a fixed reference temperature, α_0 is the linear temperature coefficient of resistivity of the material in use and φ_0 is the resistivity. Both α_0 and φ_0 are calculated at the temperature T_0: typical values of copper at 273K are $4.2 \cdot 10^{-3}$ $°C^{-1}$ for α_0 and $1.68 \cdot 10^{-8}$ Ω·m for φ_0.A temperature rise of 50K above ambient (323 K) increases the resistance by 20% and a temperature rise of 135K by 53% [3]. Therefore it can be seen that copper losses are strongly affected by the temperature; thermal cooling of the windings is therefore essential in order to keep this type of loss as low as possible.

2.3.2 Iron losses (Electro-magnetic loss)

The losses in the magnetic parts of the machine are also referred to as core losses or magnetic losses. They are created by the changing magnetic field in the stator and rotor machine cores respectively. For conducting ferromagnetic materials, the iron losses are often separated into hysteresis losses and eddy current losses as in Equation 2.9 below.

$$P_I = P_h + P_{eddy} \quad \textbf{2.9}$$

The hysteresis loss is caused by variations of the magnetic field; they are related to the energy required in moving domain walls from a naturally occurring state of orientation of the applied external field. The eddy current

loss is associated to the variation of the magnetic field applied. As ideally the rotor does not see a changing magnetic field, this loss can be considered mainly occurring in the stator iron [32-34] and it can also be affected by the lamination cutting process [35].

The impact of these losses can be reduced by using alternative materials and by an accurate design of slots (removal of sharp corners, teeth sizing) [36, 37].

2.3.3 Windage losses (Mechanical loss)

Windage losses are a consequence of the viscous friction between rotating surfaces and the surrounding fluid; in the case of electrical machines, they are mostly generated in the airgap between the rotor surface and the air. According to Saari [23, 38], these losses can be calculated as reported in Equation 2.10 below. This power loss is strongly dependent on the geometry considered, the shaft rotating speed and the nature of the fluid flow.

$$P_{w,analytical} = \frac{1}{32} \mathrm{k} C_M \pi \rho \omega^3 D_r^4 L_r \qquad \textbf{2.10}$$

k is a roughness coefficient of the rotating surface (k = 1 for a smooth surface), ρ [kg/m^3] is the density of the fluid, ω [rad/s] the rotational speed, D_r [m] the rotor diameter and L_r [m] the rotor length, C_M [39] is the torque coefficient which is determined by measurements and depends on the Taylor-Couette Reynolds number (Equation 2.11).

$$Re_r = \frac{\rho \omega D_r g}{2\mu} \qquad \textbf{2.11}$$

g [m] and μ [kg/ms] are the airgap width and the fluid dynamic viscosity respectively.

The torque coefficient is calculated as in Equation 2.12 below: A, α and β depend on the flow regime as shown in Table 2.4.

$$C_M = A\left(\frac{2\,g}{D_r}\right)^{\alpha} Re_r^{\beta} \qquad \textbf{2.12}$$

Flow Regime	***A***	**α**	**β**
Laminar: $Re_r < 64$	10	0.3	-1
Transition: $64 < Re_r < 500$	2	0.3	-0.6
Turbulent I: $500 < Re_r < 10^4$	1.03	0.3	-0.5
Turbulent I: $Re_r > 10^4$	0.065	0.3	-0.2

Table 2.4: *A*, α and β coefficients for different flow regimes [38]

2.3.4 Bearing losses (Mechanical loss)

Bearing losses are mechanical losses due to the friction between bearing balls and inner and outer races; they are a function of shaft speed, bearing type, properties of the lubricant and the load applied. These kinds of losses are usually calculated by using empirical correlations or by following the bearing manufacturer guidelines: according to SKF [40], a general correlation which can be used to estimate bearing losses is reported in Equation 2.13 below:

$$P_B = 0.5\omega\mu F D_b \qquad \textbf{2.13}$$

Where ω [rad/s] is shaft rotating speed, μ the friction coefficient which depends from the type of bearing (deep groove ball bearings, roller bearings etc), F [N] is the bearing load and D_b [m] the inner diameter of the bearing.

2.4 Thermal analysis techniques

Several modelling techniques can be used for thermal analysis of electrical machines. Depending on the approach, these techniques can be classified into two categories:

- Analytical: lumped parameters thermal network (LPTN).
- Numerical: finite element analysis (FEA) and computational fluid dynamics (CFD).

Each modelling approach has its own benefits and drawbacks; for this reason an optimal strategy could consist of the utilization of both modelling techniques [21, 41, 42]. Boglietti et al. [41] suggest the combination of analytical models with CFD simulations for future thermal analysis in order to reduce the computational cost: specifically, it is recommended to use CFD simulations to predict fluid flow and estimate the heat transfer coefficients h [W/m^2K], then implement the numerical results in the thermal network in order to calibrate the model and examine in detail the thermal behaviour of the machine. However this approach may change in the future due to the higher computational resources now available which significantly reduce the CFD simulation cost and time and also allow fluid flow and thermal problems to be investigated with a high degree of detail.

The following sections (2.4.1, 2.4.2, 2.4.3) briefly describe and discuss both thermal analysis techniques used for electrical machines.

2.4.1 Lumped parameter thermal network (LPTN)

The lumped parameter thermal network (LPTN) method has been successfully used for thermal analysis of electrical machines [4, 30, 43-45]. The heat transfer network is analogous to an electrical network, and the analysis consists of the calculation of conductive, convective and radiative resistances for all machine components. One of the most common commercially available lumped circuit analysis packages is Motor-CAD [9]; Figure 2.3 below shows a typical thermal resistance network of an induction motor calculated by the software.

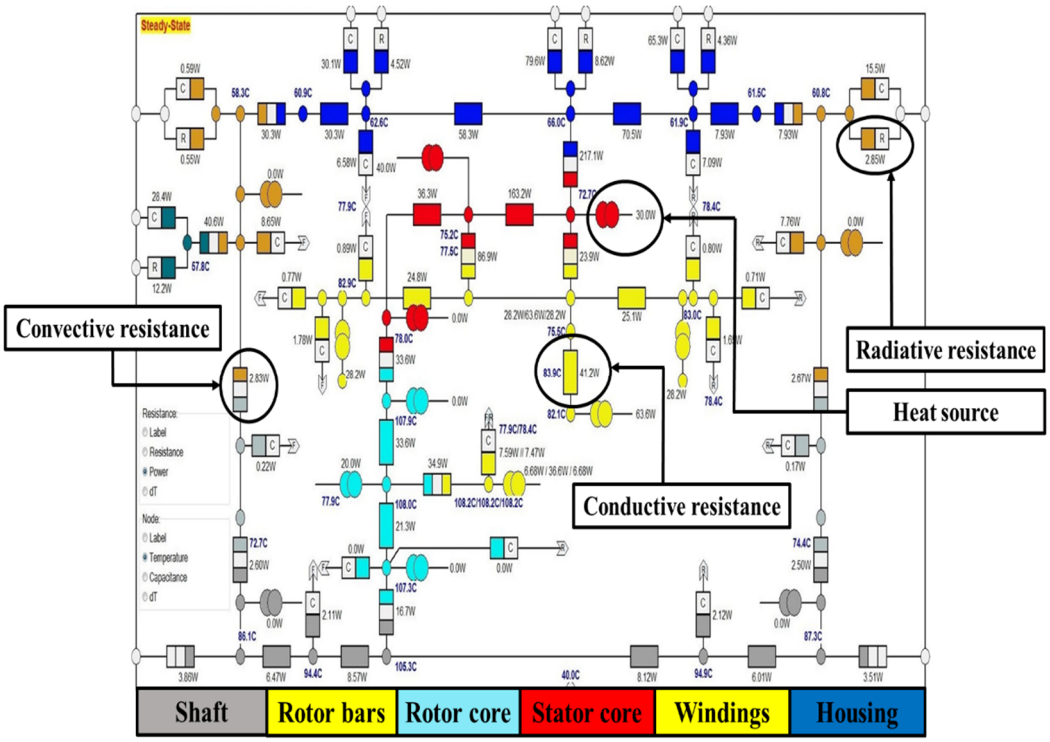


Figure 2.3: Typical induction motor thermal network generated with Motor-CAD [9]

The circuit consists of a network of heat sources nodes representing each individual motor component connected by thermal resistances and thermal capacitors (for transient analysis, not shown in Figure 2.3). Thermal resistances model the heat transfer paths in the machine and they can be

quickly derived from dimensions and material data; the heat sources represent the mechanical and electromagnetic power losses which are usually defined as input data by the user.

The main benefits of Motor-CAD are the quick set up and fast calculations speed due to the limited number of nodes; the network is automatically generated based on the machine design. The near instantaneous calculation capabilities of the analysis technique make it possible to run "what-if" scenarios in real time and provide a quick prediction of heat flow and temperature distribution of the electrical machine under investigation. On the other hand, this software is not capable of computing fluid flow simulations over complex geometries and this leads to uncertainties in the prediction of convective heat transfer coefficients of the electrical machines [12]; complex fluid flow and thermal phenomena occurring in the end regions, airgap and external frame cannot be accurately modelled.

For instance, in the case of a finned housing typical of a TEFC machine, the external cooling air speed is not constant along the axial direction due to air leakages in the open fin channels [6, 11]; in addition some of them could also be blocked by bolt lugs and this causes an uneven air speed distribution over the frame depending on the location. The prediction of these phenomena is a complex function of many factors, such as fan type, fin design, airflow regime and rotational speed [44]. This means that the heat transfer coefficient used by LPTN will not capture the correct behaviour and it will not allow local temperatures to be computed; a single frame/casing temperature is predicted instead.

In conclusion, whilst LPTN provides a very quick answer it is reliant on accurate estimates of heat transfer coefficients, meaning that its accuracy is limited to known designs [41]. The analytical approach is a useful tool for having a rough and quick estimation of thermal behaviours of electrical machines.

2.4.2 Finite element analysis (FEA)

The Finite element analysis (FEA) method has been successfully used for combined electromagnetic-thermal analyses of electrical machines [46-48]. This modelling technique is based on the sub-division of the domain under investigation into small elements; the conduction heat flow equation are then solved for each individual element.

FEA provides a potential route for an accurate calculation of conduction heat transfer in complex geometric shapes; however this also usually leads to a high discretisation and computational cost. Another important limitation of FEA is the use of analytical/empirical based algorithms for convection boundaries since most FEA software packages do not model fluid flow. Therefore the estimation of the convective heat transfer is based on assumptions made by the user; the accuracy of this method is strongly dependent on accurate estimates of heat transfer coefficients like the LPTN approach [41]. For this reason, the best use of the FEA method can be achieved in combination with other analysis methods.

2.4.3 Computational fluid dynamics (CFD)

Computational Fluid Dynamics is a finite volume technique allowing governing equations of fluid flow and heat transfer to be solved; it is one of the most accurate and versatile techniques used to investigate in detail coolant flow rate, velocities, turbulent flows, pressure distributions and surface heat transfer coefficients in electrical machines and it allows modelling and simulation of very complex geometries and fluid flows with a high degree of detail and flexibility [41]. Nonetheless, CFD has a high computational cost and requires highly-skilled users familiar with fluid mechanics since a full understanding of fluid flow and thermal phenomena is required.

The main steps of CFD software implementation are listed below:

- Pre-processor: creation of the geometry representative of the regions under examination, fluid, solid or both; this will be the domain of the CFD study. The domain is then discretized using a suitable mesh (or grid).
- Solver: set up of thermal properties of the domain and specification of boundary conditions, then run the simulation and the solution is computed.
- Post-processor: numerical results obtained from the solver are reviewed and analysed.

CFD is a very promising technique for thermal analysis of electrical machines, thanks to its capability to provide a very detailed view of complex thermal and flow aspects of the machine and trend predictions; experimental validation of numerical results is usually required for good accuracy [15]. However, a lot of attention must be paid to the mesh generation process (elements type, elements size) and to the boundary conditions setup of the domain under investigation which could strongly affect numerical results [41].

In the past analysis concentrated on sub-systems or components as modelling capabilities were limited by computational considerations; several investigations of the end region of electrical machines were carried out as it is well recognised to be one of the most difficult to thermally investigate due to the complex airflow patterns. [49-51].

A numerical and experimental investigation was conducted in [52] aimed to describe the nature of the flow field and the influence of the end winding's porosity within the end region of a high voltage TEFC induction machine. The end windings were replaced by a series of rectangular columns of various widths in order to vary the porosity: although a simplified end winding geometry was used, results showed how the flow field in the end region can

largely be affected by the openness of the end windings. This could have an impact on the thermal performance which was not investigated. The porosity was varied from 0% (impermeable geometry) to 100% (geometry fully open). With low percentage of porosity, most of the flow was confined in the inner area of the end region above the wafters/end rings; as the porosity was increased up to 65%, the recirculating flow above the end ring was also going through the end windings and combining with the recirculating flow behind them.

A similar CFD investigation for local heat transfer coefficients by changing the wafter design in the end region of permanent magnet synchronous motor (PMSM) was carried out in [53]. A simplified end windings geometry was implemented, but an initial attempt to consider a more realistic representation was performed in order to investigate the impact on the end region flow distribution. Channels/duct underneath the end windings (space between the stator teeth) were considered and results showed improvements in terms of end windings cooling and heat transfer rate through the external housing.

A fluid flow and heat transfer analysis on the complex stator end winding regions of a TEFC motor was performed in [7]. This work was used as a starting point for the investigations considered in [50, 54], where both experimental and numerical fluid flow and thermal analyses of the end region were carried out. Only a sector of the fluid end region domain was periodically modelled to reduce the computational cost; CFD results were successfully validated and then alternative cooling arrangements options were proposed to improve the thermal performance. In comparison with a conventional wafter configuration, a shaft mounted stirrer design [54] was considered which, at a rotational speed of 1500 rpm, led to a significant rise of the heat transfer coefficient at the tip of the end windings (+60%) and at the end shield (+265%). However the proposed design would also affect and increase the windage loss which is a function of the wafter/stirrer diameter and this aspect

was not fully investigated; this can affect the overall efficiency and therefore it should not be neglected when designing an electrical machine.

Due to the complexity of the end winding geometries, often consisting of several insulated copper strands bound together, approximated and simplified geometries were employed to model the end windings in order to reduce the complexity of the model and the computational cost [55-59]; however the impact that these simplifications can have on fluid flow and thermal predictions, and therefore on the fidelity of the answer, was not investigated.

Since in a TEFC machine the losses are dissipated through the finned external housing, several CFD local investigations of the fluid flow and heat transfer over the frame were performed. CFD was used to conduct a parameter sensitivity analysis of the cooling fin design and significant differences between their performance were found [60]; the number of cases considered were limited by high computational costs and therefore a simplified model was used. A similar investigation was carried out in [61] where a design optimisation of a single fin was conducted to reduce the computational cost; the impact of different fin height and thickness were considered. Valenzuela et al. [6] carried out an investigation where measurements of the heat transfer coefficient between finned housing and air was measured for different numbers and dimensions of the fins were taken; differences of the results were up to 20% which highlights the importance of a good housing design.

The published literature of CFD works on electrical machines shows that the numerical approach is capable of providing very detailed predictions of complex thermal and flow aspects throughout the machine making it a very useful tool for the designing process of electrical machines. However most of the fluid flow and thermal investigations of electrical machines found in literature considered only limited sectors and specific critical areas of the machine. Particularly for TEFC machines, where heat removal is dependent on both the internal and external features, it is the opinion of the author that

internal and external flows and heat transfer must be analysed jointly in order to gain a fuller understanding of thermal performance. This would lead to a complex scenario with multiple dependencies but would also provide a very detailed view of the fluid flow and thermal behaviour of a TEFC machine.

From this point of view, there is now the potential to create a full system model as in [62, 63], where a combined airflow and conjugate heat transfer CFD investigations were carried out to provide a full thermal model of electrical machines.

2.5 Summary

Due to the increasing emphasis on efficiency and sustainability there is now a growing awareness within industry of the need to address the thermal management of electrical machines; this is a crucial step since the rise of temperature can significantly reduce the overal machine efficiency.

Several modelling techniques, both numerical and analytical, can be used to perform thermal investigation of electrical machines. The LPTN approach provides a very quick answer but it is not capable of computing fluid flow simulations over complex geometries and this leads to uncertainties in the prediction of convective heat transfer coefficients of electrical machines. FEA techniques allow accurate calculation of conduction heat transfer in complex geometric shapes; however, like the LPTN approach, it is reliant on accurate estimates of heat transfer coefficients.

Numerous CFD investigations on simplified or sub-models were carried out showing how CFD is a very flexible and accurate technique thanks to its capability to provide a very detailed view of complex thermal and flow aspects of electrical machines and trend predictions. In the numerical investigations of the end regions, simplified geometries were usually used to model end

windings in order to reduce the complexity of the model and the computational cost. The impact that simplifications can have on the fidelity of the answer needs to be further investigated. With the improvements and increase of computational resources available, it is now possible to verify those simplifications by considering far more detailed geometries and performing full conjugate heat transfer analysis of entire electrical machines.

This is particularly relevant for TEFC machines where, due to their structure, the heat removal is dependent on both the internal and external features; a full conjugate heat transfer investigation is therefore required which consists of a simultaneous internal and external flows and heat transfer analysis of the entire TEFC machine.

3 Experimental Test Facility

3.1 Introduction

Experimental tests were carried out to provide validation of the CFD models described in Chapters 6 and 7; the comparisons between CFD and experimental results are presented and discussed in Chapter 6. A test rig was commissioned to validate thermal aspects of the machine; the rig consisted of a 160kW drive machine connected to the TEFC motor under investigation (output power of 11kW) through a torque meter (Datum Electronics M425, Section 3.3) using coupling connection with key hubs. The layout of the test rig is described below (Figure 3.1).

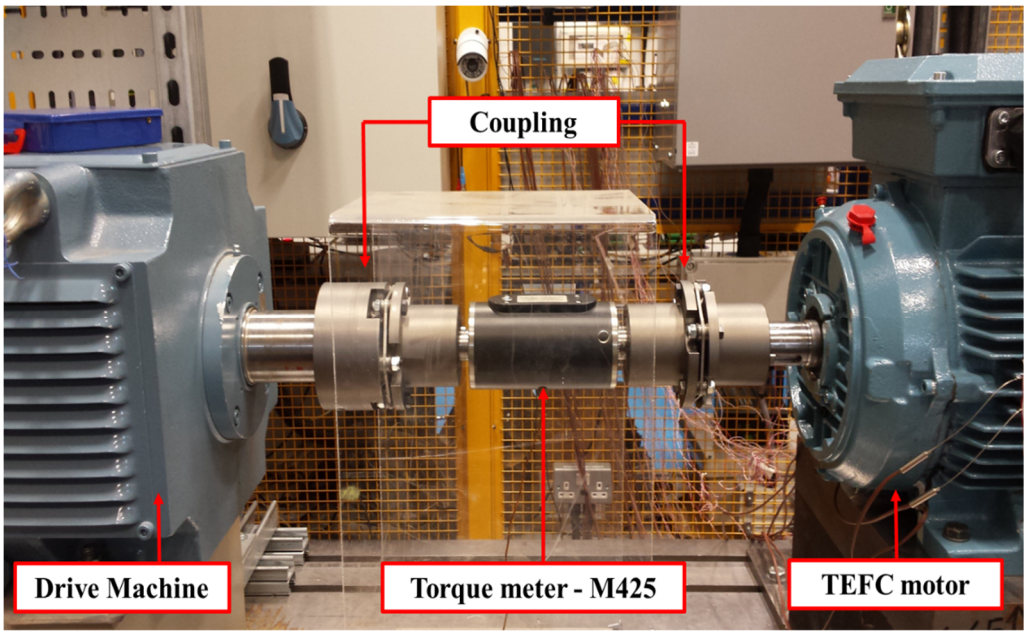


Figure 3.1: Schematic of Test Rig

The TEFC motor was placed on two 280 mm high steel platforms (Figure 3.2) which were designed to achieve a perfect shaft alignment with the drive machine and torque meter in order to avoid any misalignment which could lead to excessive vibrations and hence inaccuracies on torque measurements.

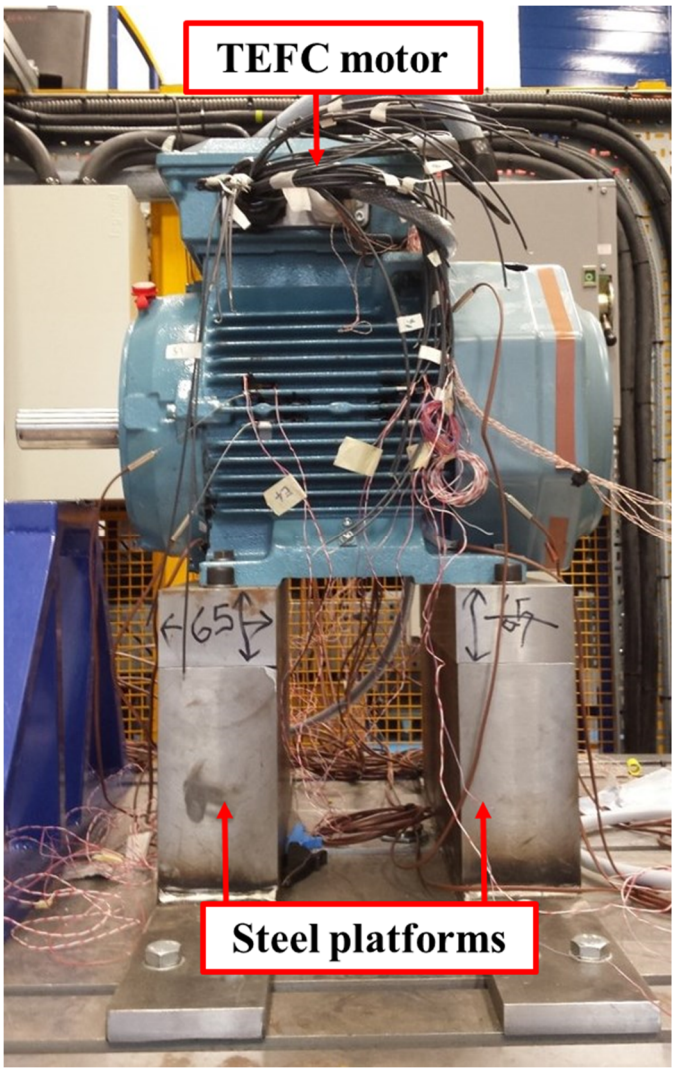


Figure 3.2: TEFC motor platforms support

The selected TEFC motor and the drive machine were coupled through the torque meter using two single-jointed coupling connections with key hubs as schematically shown in Figure 3.3.

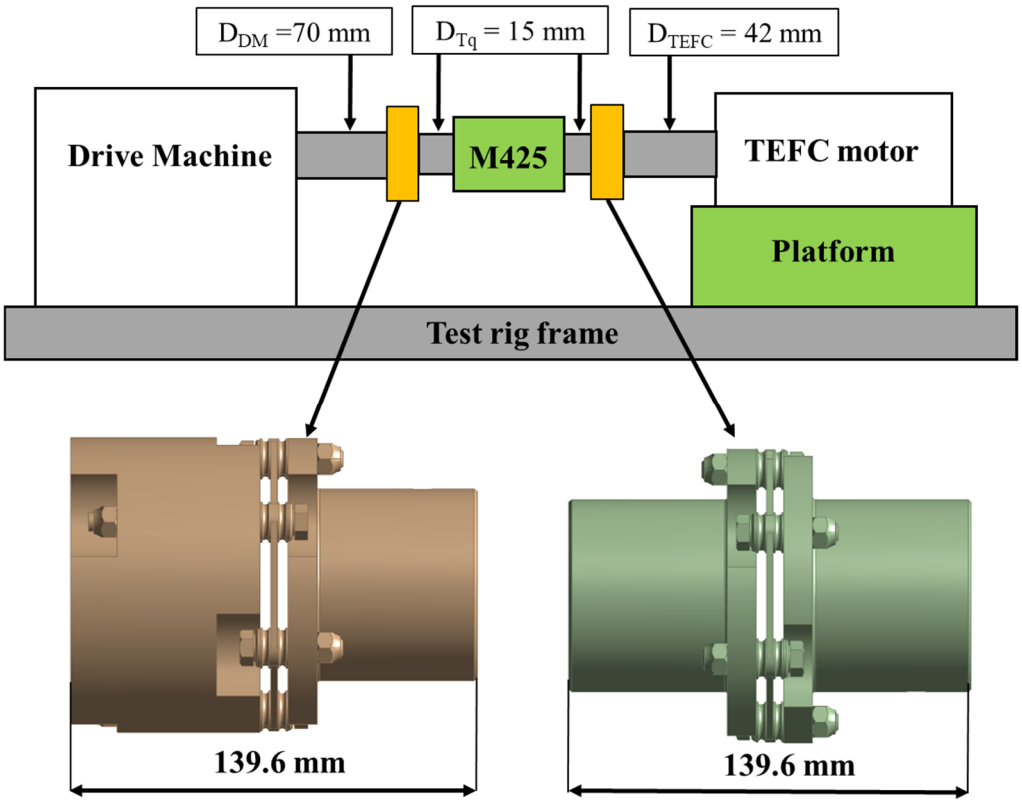


Figure 3.3: Schematic of test rig and coupling

The hubs of the selected coupling (except the one for the 70 mm drive machine shaft) were provided with tapered bores in order to use taper lock bushes; in this way the same coupling set could be easily adapted to different shaft diameters.

Temperatures and torque were the quantities acquired throughout the tests and used for validating the CFD models. Two different testing programmes were planned and performed: no-load and full load test.

A No-Load (electrical) Test was carried out for a speed range from 400 to 1500 rpm in order to validate the analytical and numerical predictions of the mechanical losses: bearing frictions and windage. During this test, the electromagnetic torque was absent since the induction motor terminals were left in an open circuit condition; the motor was then driven at different

operating speeds by using the drive machine and the measured torque provided an estimation of the total mechanical power loss.

The second planned test was a Load Test: the induction motor drove the drive machine at rated full load condition (n = 1466 rpm, T = 71.6 Nm). Thermal steady-state tests were carried out and the motor was found to reach steady state condition over a period of approximately 4 hours; the measured temperatures and torque at steady-state were then used to validate the CFD models of the whole machine.

A more detailed description of the instrumentations employed will be provided in sections 3.2 and 3.3.

3.2 Thermal Measurements

Temperature measurements were required to ensure that the heat distribution throughout the solid regions of the machine was being modelled correctly by the CFD thermal models.

Thermocouples and heat flux sensors were placed in different areas of the motor in order to provide experimental thermal data to validate the CFD models; Table 3.1 below lists the thermal equipment used for experimental measurements and their location.

Measurement	Instrumentation	Location	Quantity
Temperature [K]	Welded tip T- type thermocouples	Stator teeth	8
		Stator back iron	4
		End Windings	6
	Mineral insulated T-type thermocouples	End Regions	4
		Back iron/Housing	12
Temperature [K] - Heat Flux [W/m^2]	Heat flux sensors	End Caps	6
		External Fins	6

Table 3.1: Experimental thermal instrumentation

Since the machine provided had no in-built thermal sensors, they were all added post manufacture.

As reported in Table 3.1, a total of 34 T-type thermocouples (1 mm diameter), class 1 (temperature range of -75°C ≤ T ≤250°C) with an accuracy of ±0.5 °C (according to IEC-584-2 standard) were used in this project. The mineral insulated thermocouples had the sensing junction covered with a stainless steel

sheath 150 mm long. This sheath is malleable so it can be easily bent and formed into a variety of shapes; this feature made these thermocouples suitable for temperature measurements of end region and external housing as discussed in section 3.2.1.

RdF Corporation Micro-Foil Heat Flux Sensors (P/N 27036-2) were used to measure the heat flux (Q") and wall surface temperature at various locations on the end caps and on the external frame. As reported in Figure 3.4, these sensors consist of a thermopile and a T-type thermocouple mounted on either side of a thin polymer film to measure the temperature across the film due to the heat flux.

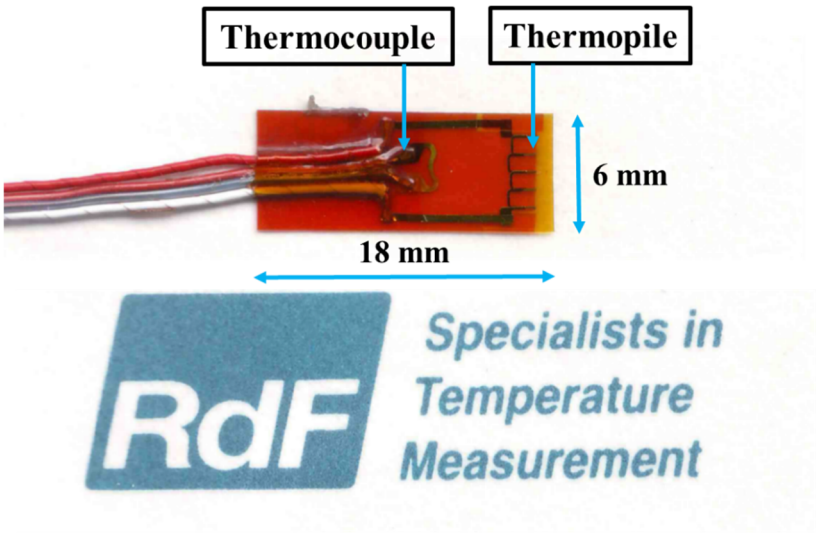


Figure 3.4: Micro-foil heat flux sensor

Thermocouples and heat flux sensors were connected to a “dataTaker DT80” data logger and to two “CEM20” 20-channel multiplexers to increase the number of connections to the data logger. A serial port was used to interface the data logger to a PC where thermal measurements could be monitored and stored; the DT80 provides an embedded web interface “dEX”. Thermal measurements were sampled and saved every 10 seconds and taken over a period of 4 hours, when the machine was found to reach the thermal steady state condition; measurements were then averaged over a time period of 5 minutes.

A more detailed description of the location and placement of the thermal sensors is provided in the following sections 3.2.1 and 3.2.2.

3.2.1 Temperature Measurements

A total of 12 welded tip thermocouples, both on Drive End (DE) and Non Drive End (NDE) side of the motor, were employed to provide temperature measurements of the stator. Figure 3.5 below shows an axial view of the stator where the DE and NDE sides are highlighted.

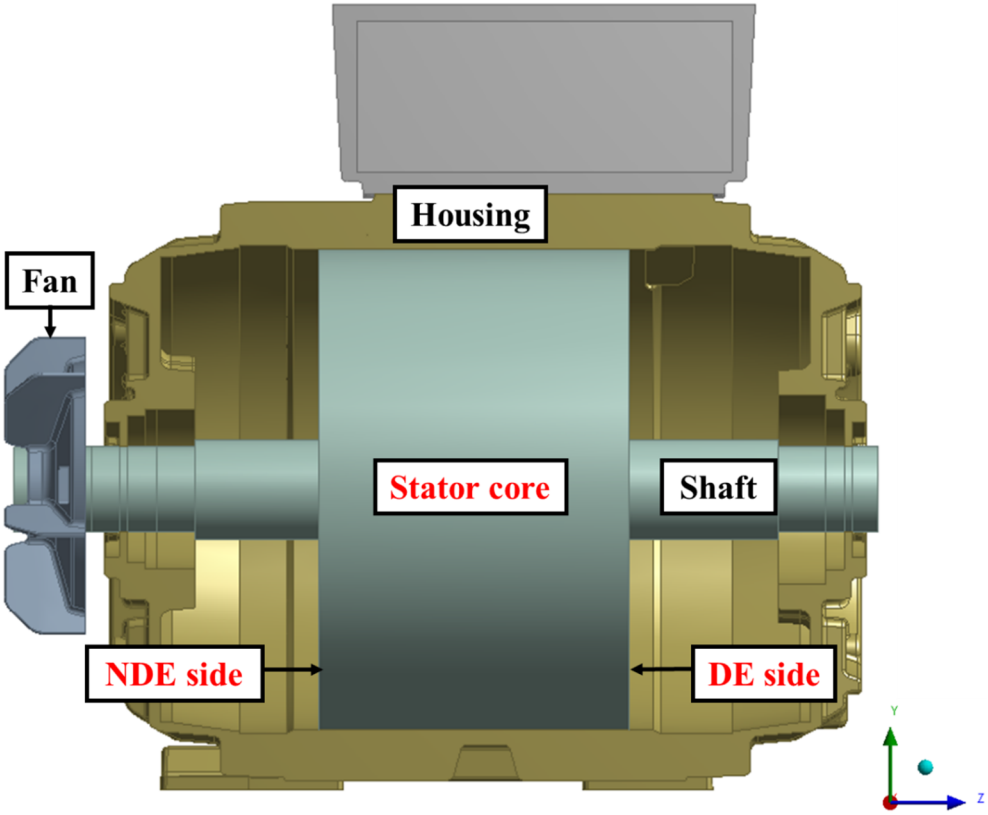


Figure 3.5: Stator – DE and NDE side

Figure 3.6 below, reports a schematic view of the thermocouples location on the DE side of the stator; the same layout was used on the NDE side.

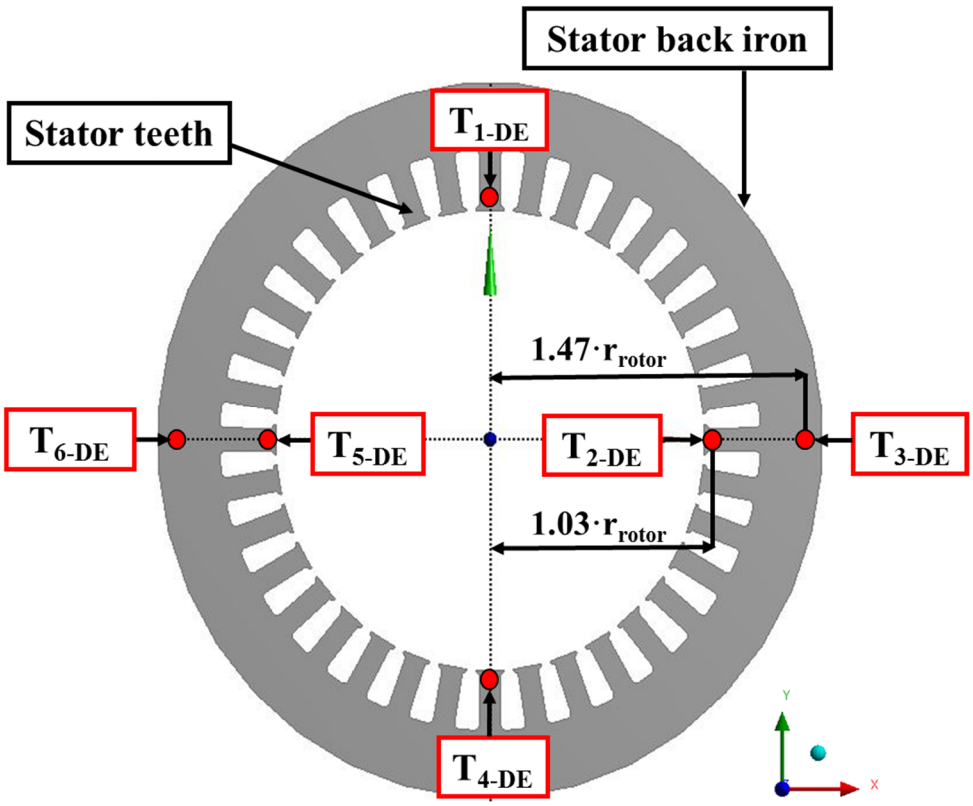


Figure 3.6: Thermocouples location - Stator teeth and back iron

$T_{1\text{-}DE}$, $T_{2\text{-}DE}$, $T_{4\text{-}DE}$ and $T_{5\text{-}DE}$ were located on the stator teeth laminations at 90° circumferential intervals; these four thermocouples provided a measure of the stator laminations teeth temperature where major losses were expected. $T_{3\text{-}DE}$ and $T_{6\text{-}DE}$ were radially aligned with $T_{2\text{-}DE}$ and $T_{5\text{-}DE}$ in outer stator region in order to provide a measurement of the stator back iron temperature.

To guarantee a good contact with the surfaces and avoid any damage a suitable thermal paste (epoxy resin with an operating temperature range of -60°C to 200°C) was used to hold the thermocouples in place.

A total of 10 thermocouples were located in both end regions of the machine aimed to measure the end windings surface temperature and the air temperature in this region for use on the calculation of the heat transfer coefficients in this area. Figure 3.7 below reports a schematic view (end winding and end ring

geometries from the CFD model) of the thermocouples location in one of the end regions.

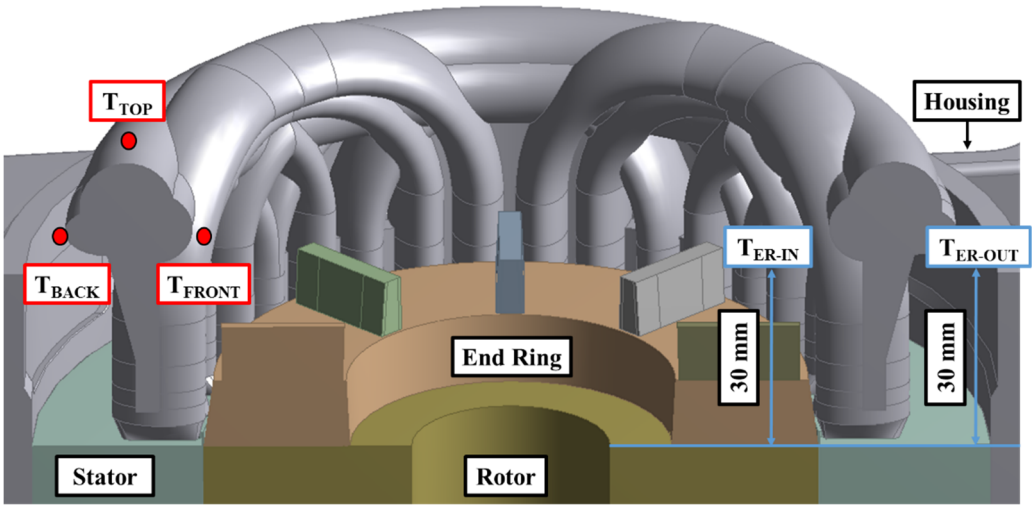


Figure 3.7: Thermocouples location: End Region

Three welded tip thermocouples were located in three different locations over the end windings surface (T_{FRONT}, T_{TOP} and T_{BACK}); the PFA insulated wires were mounted over the end windings surface while the epoxy resin was used to guarantee a good thermal contact between the thermocouples tips and the planned location for temperature measurements.

Two mineral insulated thermocouples were used to measure the air temperature in the areas between the end windings and the end ring (T_{ER-IN}) and between end windings and the external housing (T_{ER-OUT}). The thermocouples PFA wires were made to pass through the end windings cavities and were attached to the cavity surface with an insulating tape leaving 5 mm of the steel sheath tip exposed; the rest of the sheath was bent accordingly in order to minimise, as much as possible, the interference to the internal swirling airflow.

Another twelve mineral insulated T-type thermocouples were placed in holes drilled over the external housing placed at 90° circumferential intervals and in two different planes in the axial direction; the steel sheath of these type of thermocouples made them particularly suitable to be placed in drilled holes. Figure 3.8 and Figure 3.9 below show the angular and axial locations respectively.

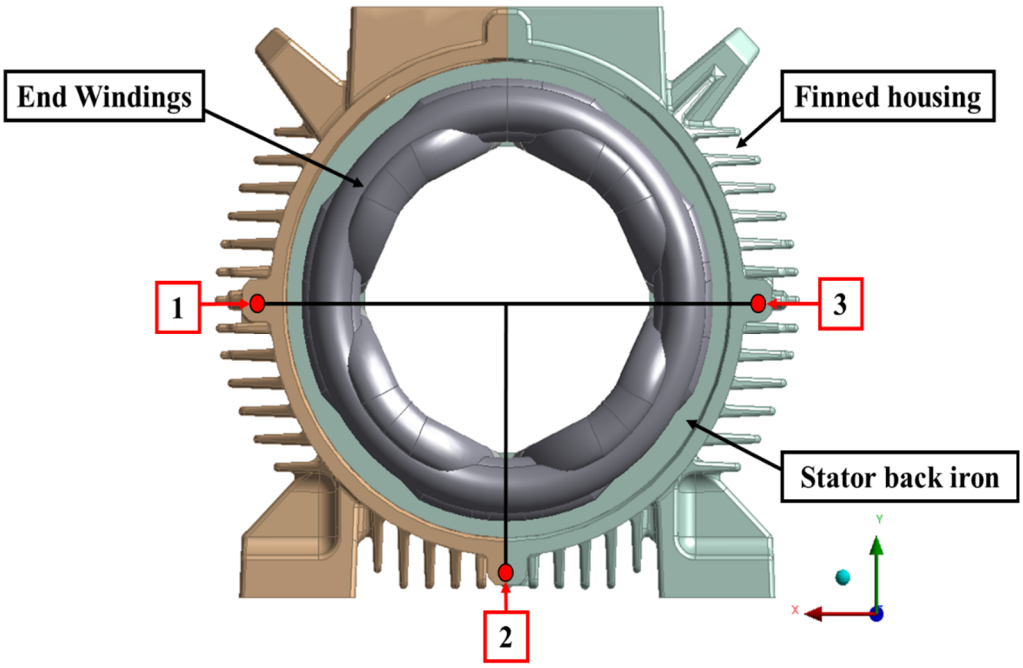


Figure 3.8: Thermocouples location: external housing, angular locations

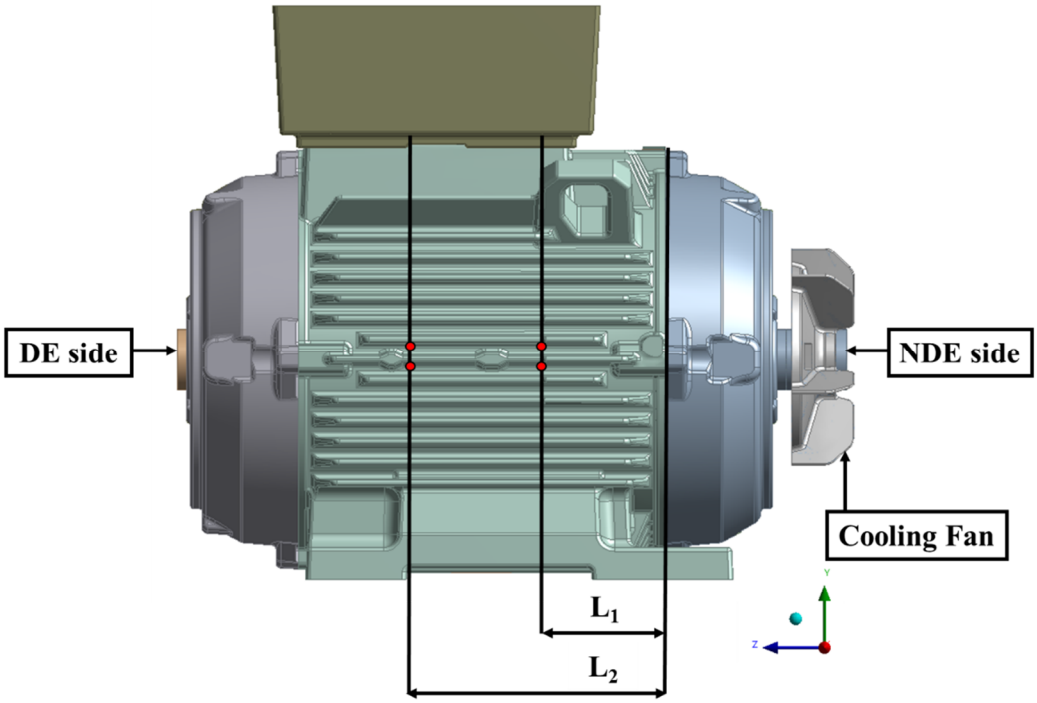


Figure 3.9: Thermocouples location: external housing, axial locations

L_1 and L_2 (Figure 3.9) were chosen in order to get temperature measurements of both frame and back iron at 25% and 75% of the stator axial length respectively.

Considering that the housing had a 8 mm radial thickness (fins excluded), twelve holes were externally drilled on the angular and axial locations as shown in Figure 3.8 and Figure 3.9. Six thermocouples were used to measure the frame temperature by placing them halfway through the frame thickness (4 mm depth); the remaining six were placed in 8 mm deep holes with the housing pierced through in order to reach the back iron outer surface and measure its temperature. All these temperature measurements provided a measure of the thermal resistance between frame and back iron and therefore the heat transfer coefficient in this region.

Table 3.2 and Table 3.3 below explain how the twelve mineral insulated thermocouples were labelled as a function of the hole depth, the angular and axial location.

Thermocouple label: T xy-z			
x = angular location	**1**	**2**	**3**
y = depth	**1** = back iron (8 mm)	**2** = housing (4 mm)	
z = axial location	L_1 = **NDE**	L_2 = **DE**	

Table 3.2: Thermocouple labels – external housing

	Thermocouple label	Angular location	Hole depth	Axial location
1	**$T_{11\text{-NDE}}$**	1	8 mm	L_1 – NDE
2	**$T_{12\text{-NDE}}$**	1	4 mm	L_1 – NDE
3	**$T_{21\text{-NDE}}$**	2	8 mm	L_1 – NDE
4	**$T_{22\text{-NDE}}$**	2	4 mm	L_1 – NDE
5	**$T_{31\text{-NDE}}$**	3	8 mm	L_1 – NDE
6	**$T_{32\text{-NDE}}$**	3	4 mm	L_1 – NDE
7	**$T_{11\text{-DE}}$**	1	8 mm	L_2 – DE
8	**$T_{12\text{-DE}}$**	1	4 mm	L_2 – DE
9	**$T_{21\ \text{DE}}$**	2	8 mm	L_2 – DE
10	**$T_{22\text{-DE}}$**	2	4 mm	L_2 – DE
11	**$T_{31\text{-DE}}$**	3	8 mm	L_2 – DE
12	**$T_{32\text{-DE}}$**	3	4 mm	L_2 – DE

Table 3.3: Thermocouple labels – external housing overview

3.2.2 Heat Flux Measurements

In this project a total of 12 sensors (both on DE and NDE side of the motor) were applied on the inside of the end caps and on the external housing fins channels, as shown in Figure 3.10 and Figure 3.11, where the surfaces were flat enough to achieve the best possible thermal contact using the epoxy resin.

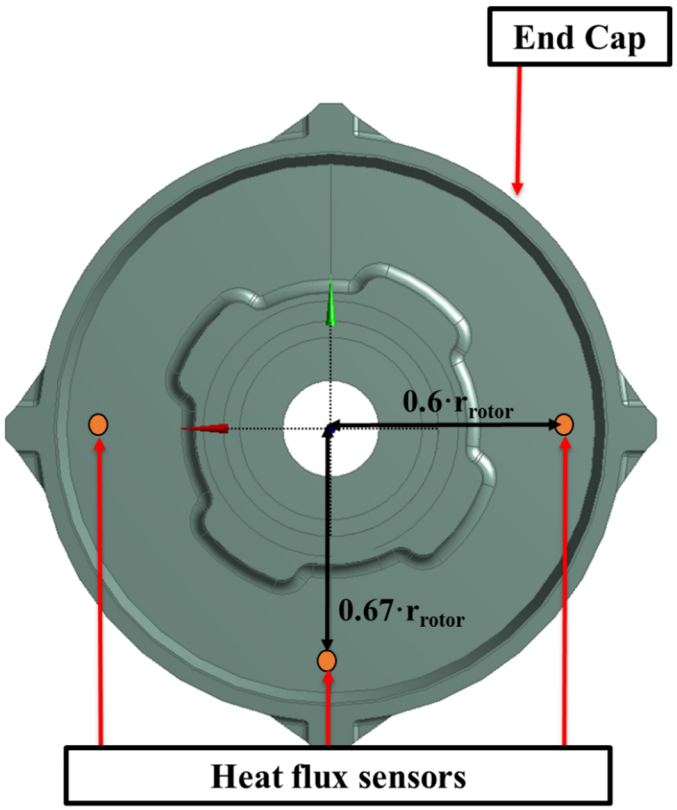


Figure 3.10: Heat flux sensors location – end caps

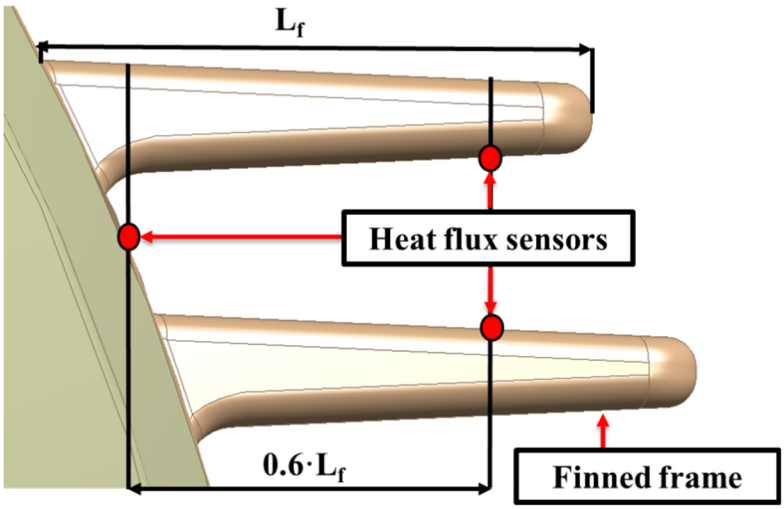


Figure 3.11: Heat flux sensors location - fins channels

These sensors placed in the end caps and on the external fins channels provided measurements of temperature and heat flux on these surfaces to be used as further thermal points of the housing for validation of the CFD thermal models.

The manufacturer, RdF, supplies calibration factors per each sensor which were used to calculate the heat flux; the voltage output from the sensors were converted into a heat flux at a constant temperature at 70°F (21.1°C). A calibration curve, provided by the manufacturer, was then used to adjust the output in accordance to the temperature measured by the in-built T-type thermocouple.

3.3 Torque and Speed Measurement

A torque transducer, Datum Electronics M425 (Figure 3.12 and Figure 3.13), was used for torque measurements in order to identify the mechanical losses at different operating speeds (from 400 to 1500 rpm): these data can then be compared to the windage and bearing losses estimated numerically and analytically. The torque meter has a range of 0-100 Nm with an accuracy of 0.1% of FSD (0.1 Nm); it was axially connected between the motor and the drive machine using a single-jointed coupling with key hubs as previously discussed in section 3.1.



Figure 3.12: Torque transducer Datum Electronics M425

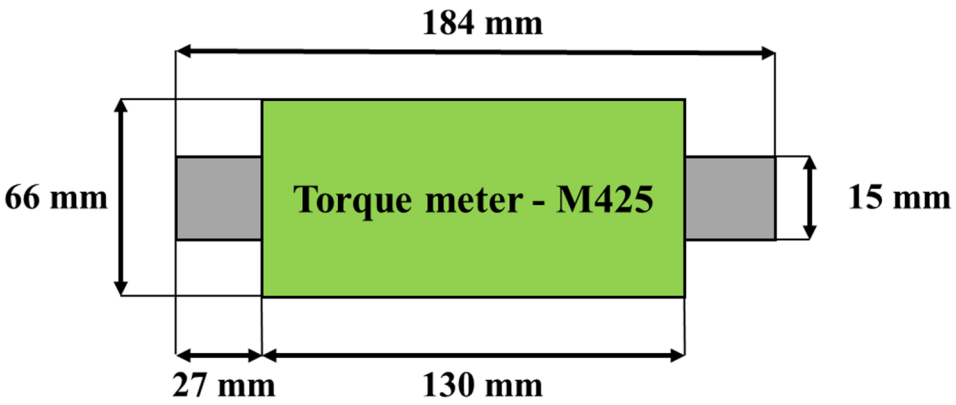


Figure 3.13: M425 Torque transducer dimensions

Throughout testing torque measurements were taken when mechanical and thermal steady state conditions were achieved. The transducer was connected to a PC using a direct USB interface; the supplied software "TorqueLog" was used for simple on-screen reading of shaft torque, speed and power values which were exported to Microsoft Excel for further analysis.

3.4 Uncertainty Analysis

Every equipment and instrumentation used for the experimental measurements has their own level of accuracy which is usually stated by the manufacturers as an uncertainty range; therefore, the experimental data are affected by errors introduced by the equipment used and this must be taken into account.

Moreover, if some quantities are obtained as function of several variables all or partially experimentally determined an uncertainty analysis must be carried out as well; this is performed in Chapter 6 where a comparison between CFD predictions and experimental results is presented in order to validate the numerical models developed in this work.

3.5 Summary

An experimental test facility was developed to investigate the thermal behaviour of the motor; several tests were carried out in order to provide enough experimental data in order to validate the analytical and CFD models of the selected machine.

An analysis and comparison of numerical and experimental results are presented in the Chapters 6 and 7.

4 Machine thermal modelling: internal domain methodology

4.1 Introduction

The aim of the work presented in this chapter is to identify the best modelling approach for the internal domain and to gain a fuller understanding of the internal fluid flow and thermal behaviour of the selected TEFC machine.

The numerical modelling of an entire electrical machine can be very demanding from a computational point of view. In order to reduce the cost of the simulations the approach adopted in this work is based on initially separate modelling and performance of local investigations of limited sectors of the most critical areas. This approach is aimed to identify the best modelling approach both in terms of numerical accuracy and computational cost.

This chapter explains the modelling approaches adopted in this work, the assumptions utilised and their impact on the fidelity of the results. A detailed description of the numerical thermal modelling of the most critical internal fluid domain regions, such as airgap, end regions and end windings is presented; this includes the description of the domain analysed, meshing approach and solver set-up.

A new modelling approach for the end windings, to allow a more realistic representation which potentially can be applied to different kinds of electrical machines, has been developed and is presented.

Furthermore, in order to improve the performance of the internal cooling system of the machine, two alternative internal cooling arrangements were considered and discussed.

4.2 Overview of CFD Theory

CFD is a finite volume technique allowing the study of fluid dynamics by numerically solving the governing equations of fluid flow and heat transfer when the complexity of the problems analysed no longer allows an analytical approach.

The governing equations of fluid flow are commonly known as the Navier-Stokes equations and they consist of coupled non-linear second order partial differential equations [64] (Appendices B).

With the Finite Volume Method (FVM) the domains under investigation are discretised into sub-domains (knows as elements or cells) and all the governing equations of fluid flow and heat transfer are solved simultaneously for each of them. CFD is one of the most accurate and versatile technique used to investigate in detail coolant flow rate, velocities, turbulent flows, pressure distributions and surface heat transfer coefficients in electrical machines and it allows the modelling and simulation of very complex geometries and fluid flows with an high degree of detail and flexibility [50]. Nonetheless, CFD has a high computational cost and requires highly-skilled users familiar with fluid mechanics since a full understanding of fluid flow and thermal phenomena is required; moreover, the processes of simulations set up and run time can require more time than is typically acceptable in an industrial environment [50]. However, CFD has become more widely used recently as high power computing became more affordable.

4.3 Domains analysed

A TEFC induction motor is a type of industrial motor with an enclosure that does not permit outside air to freely circulate through the interior of the motor: the internal parts are totally isolated from the surrounding air. Internal features (end ring wafters) for enhancing the removal of the heat generated due to electrical losses are included in the end region design in order to provide an internal mixing effect and improve the convective heat transfer in this area [7]. Figure 4.1 below shows the structure of the TEFC machine under investigation.

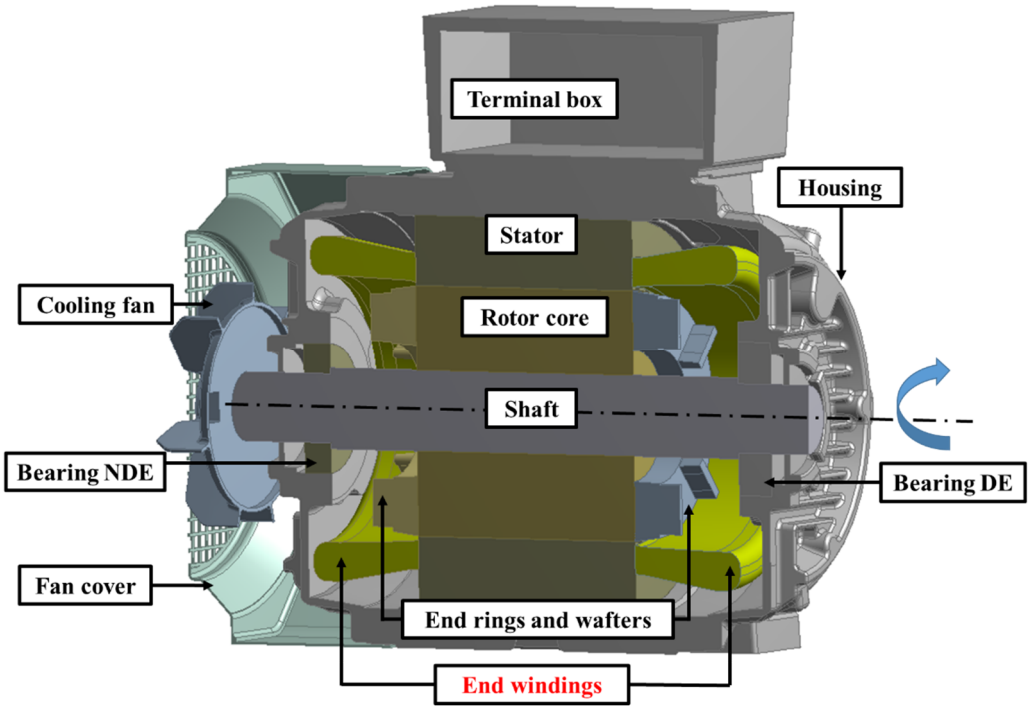


Figure 4.1: TEFC machine structure

The development of a full 3D thermal model of the TEFC machine, where the heat removal is dependent on both the internal and external features, provides a significant challenge as the internal and external flows and heat transfer must be analysed jointly, creating a complex scenario with multiple dependencies.

The flowchart below (Figure 4.2) schematically summarises and shows the modelling approach adopted in this work: this was based on the separate modelling of internal (Chapter 4) and external domain (Chapter 5) in order to identify the best modelling approach for the most critical areas of the machine. These modelling methodologies were then combined and used to develop a full 3D thermal model of the selected TEFC machine which was experimentally validated (Chapter 6). The developed CFD conjugate model was then used to investigate and identify opportunities aimed to improve the machine performance: this is presented and discussed on Chapter 7.

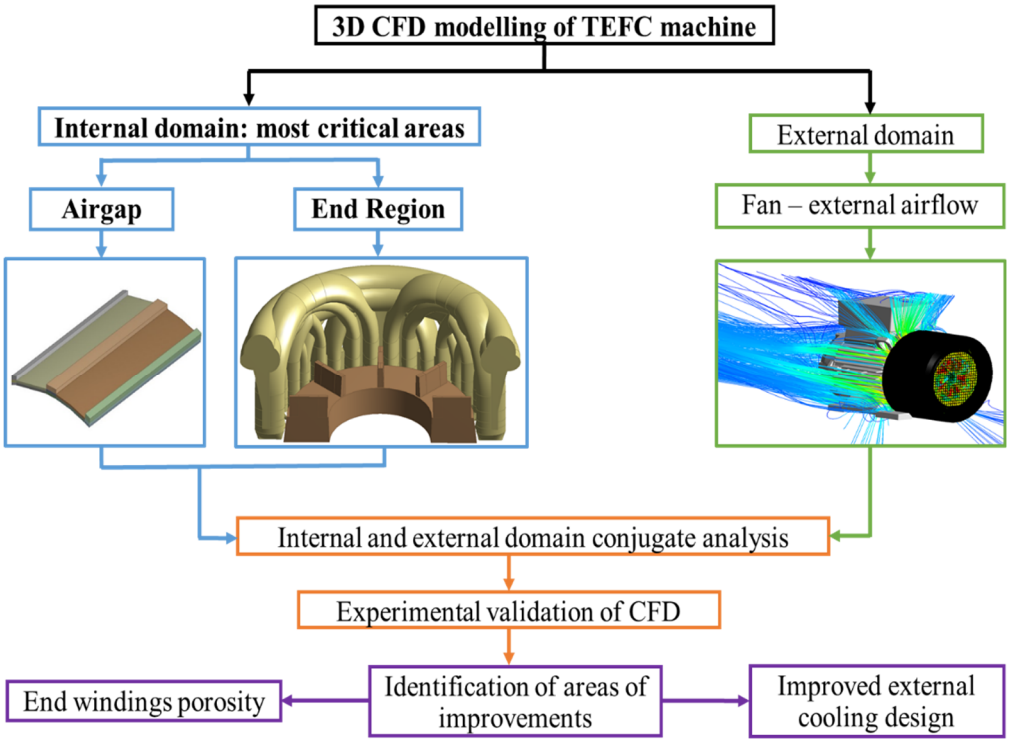


Figure 4.2: 3D CFD modelling approach of TEFC machine

Because of the losses generated within the core rotor and stator windings, it was necessary to carry out a fluid flow and thermal analysis of the internal domain and its most relevant and critical areas:

- End regions, defined as the area within the end caps that contains the end winding and the rotor's end ring.
- Airgap region between rotor and stator lamination.

All domains considered were generated using Ansys Design Modeller and more details will be provided in the following sections; the developed methodology and mesh configurations for the internal domain were used in the full 3D conjugate thermal model presented in Chapter 6 and 7.

The complexity of the end winding geometries, consisting of several individual insulated copper strands bound together into coils, provides a challenge in the modelling and analysis of heat transfer and fluid flow phenomena occurring in the end region. This complexity results in approximated and simplified geometries usually being employed to model the end windings in order to reduce the complexity of the model and the computational cost [55-59].

Moreover, since in TEFC machines the internal parts are totally isolated from the surrounding external air, all the heat generated due to rotor core and stator windings losses is dissipated through the machine's outer housing. Therefore it is very important to have, as much as possible, an accurate end winding geometry which would allow a better and accurate prediction of the complex fluid flow and thermal phenomena occurring in the end regions.

For these reasons in the present work a new modelling approach for a more realistic end windings representation has been developed and is presented in the following sections.

When modelling electrical machines two different approaches are available to take rotation into account:

- Multiple Reference Frame (MRF): this approach is usually used for steady-state analysis. The fluid domain is required to be split into stationary and rotating domains; the flow is steady relative to the rotating frame and consequently a steady state analysis is performed. This technique is less expensive from a computational point of view and is equivalent to fixing the rotating fluid in a particular position to evaluate the flow field developing only for that position.
- Sliding Mesh (SM): this approach is suitable for transient analysis and takes into account the large scale transient effects which might develop inside the domain. The flow time is discretised into time steps and the governing equations describing the air flow and heat transfer are solved as a function of time: the SM model moves the rotor mesh incrementally before starting each new time step and this leads to a much higher computational cost.

Despite the MRF technique being an approximation, it provides reasonably accurate results particularly when the interaction between stationary and rotating domains is not significant. In the work presented in this thesis a steady-state fluid flow and thermal analysis was required and the MRF approach was therefore preferred over the SM model as in previous works [7, 55, 65].

The PC running the simulations was a 3.70 GHz Intel Xeon Quad core CPU with 64GB RAM running Windows 7 64-bit operating system.

4.3.1 End Windings

The motor under investigation had a distributed end winding configuration with variable pitch factor; initially a simplified geometry, similar to those typically used in previous works, was considered. Figure 4.3 below shows a simplified winding geometry and the real geometry of the machine under investigation.

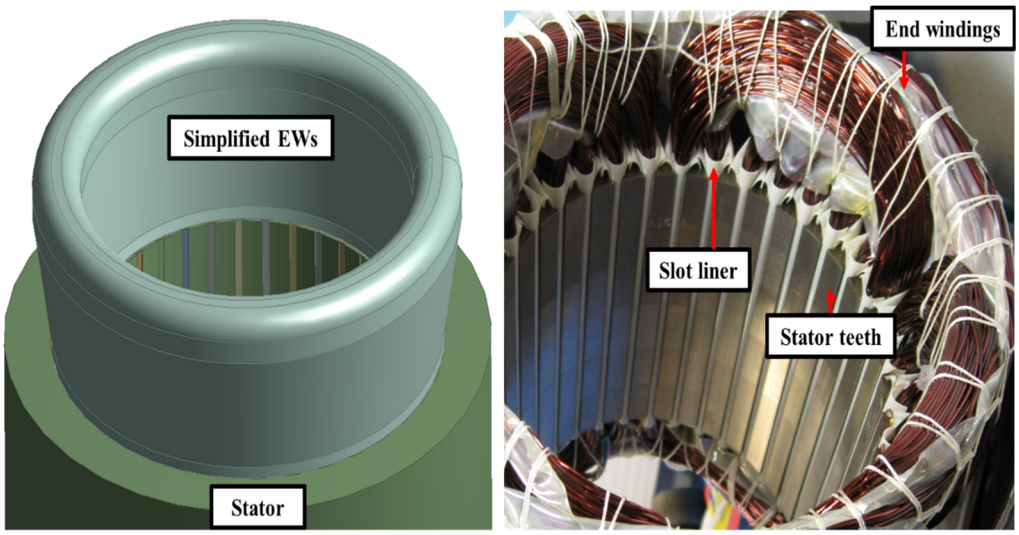


Figure 4.3: Simplified (left) and real (right) end windings geometry

As can be seen from the comparison in Figure 4.3, some specific features from the real end windings geometry were not considered on the simplified model:

- Cavities between windings leaving the stator slots were neglected.
- Cavities in-between the conductors were neglected.
- Conductors were not individually modelled.
- Surface roughness given by the insulated copper strands bound together was neglected: the simplified model had a totally smooth surface.

Figure 4.4 below provides a better view of the mentioned cavities around the end windings geometry of the induction motor.

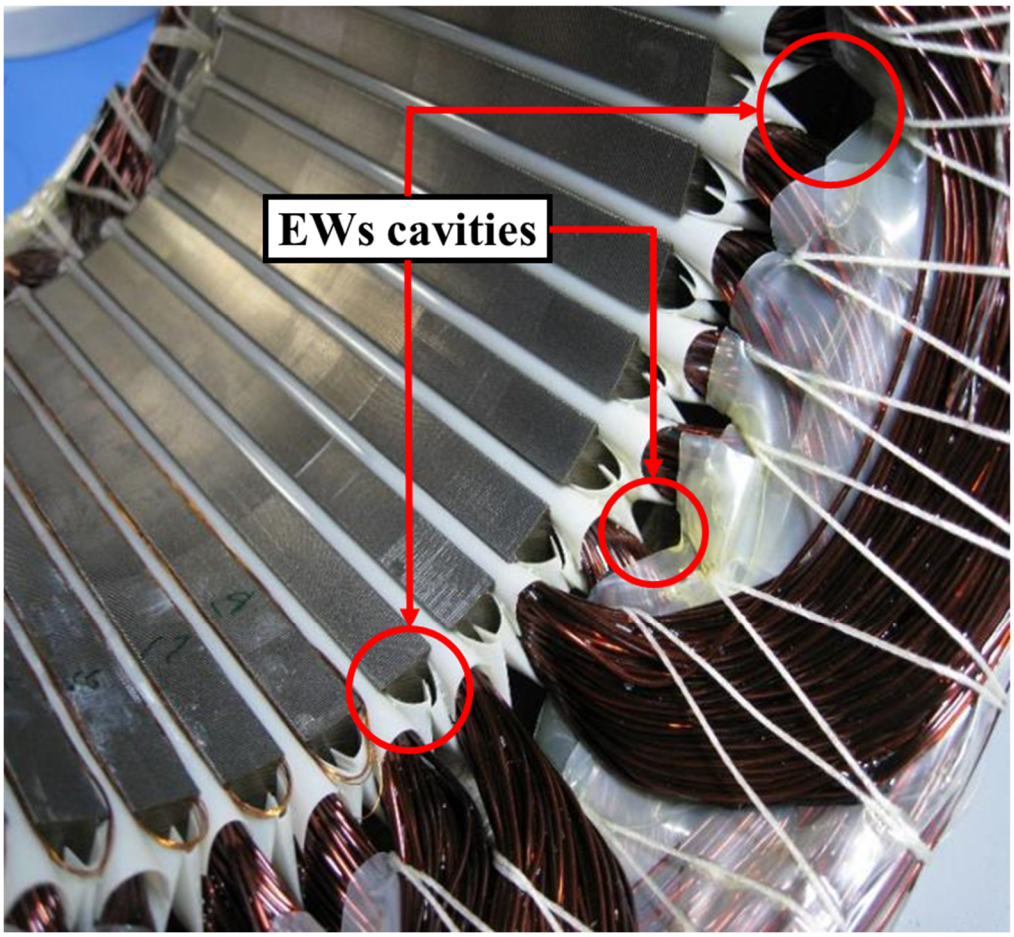


Figure 4.4: Cavities around the end windings geometry

The cavities around the end winding geometry would introduce additional fluid flow paths which would affect the predictions of fluid flow and heat transfer coefficient in this region.

Taking into account these features of the end windings would lead to a more complex geometry and to an additional modelling effort; however, this would also provide a far more accurate representation of the whole end region of the machine.

In the case under investigation, a new methodology was developed to create a more realistic 3D end winding representation using Ansys Design Modeler, based on the individual modelling of each coil with thickness and height comparable to the real geometry. Each machine's phase was extruded from the stator slots and its cross section was turned to elliptical in order to model the roundish shape of the conductors as shown in Figure 4.5.

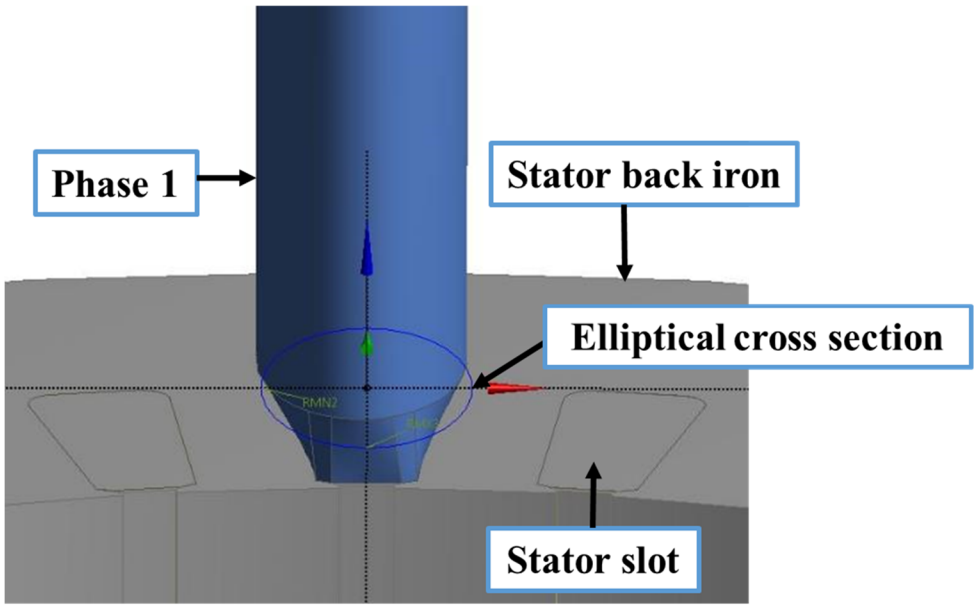


Figure 4.5: Phase 1 extrusion from stator slot and change of cross section to elliptical

In accordance to the pitch factor and topology of the real end windings geometry, a 2D sketch was created in order to provide a sweep path for the conductor's curvature as shown in Figure 4.6.

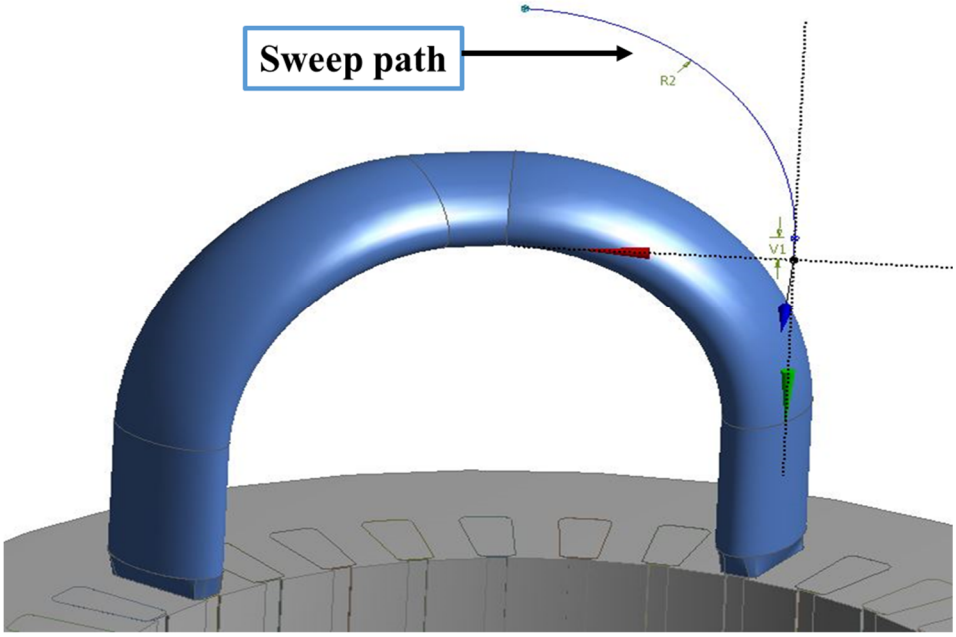


Figure 4.6: Phase 1 curvature and closure

The same approach was used to create the remaining two phases with two main differences:

- Phase 2 and 3 extrusion from the stator slot were slightly bent backwards in the radial direction in order to obtain a more roundish surface in the back of the end winding geometry.
- Phase 2 and 3 were shorter in the axial direction than phase 1 in order to model the several cavities between the conductors.

Figure 4.7 below depicts the generated three phases; the partial collision between the phases was considered in order to better represent the shape of the bundles of conductors typical of this end windings geometry. A repeating pattern was then performed for all the other stator slots in accordance to the topology of the real end winding geometry.

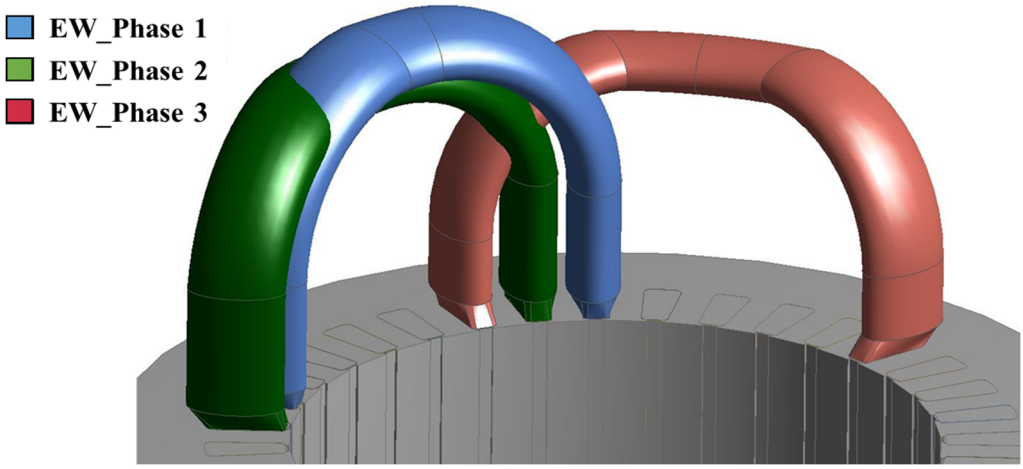


Figure 4.7: Motor's three phases

As a final step a cylindrical and conical filler were introduced around the new geometry in order to model the different conductor layers in the radial direction. The radial thickness of the conductors can be noted in Figure 4.8 where a generic end winding configuration, similar to the one under investigation, is shown.

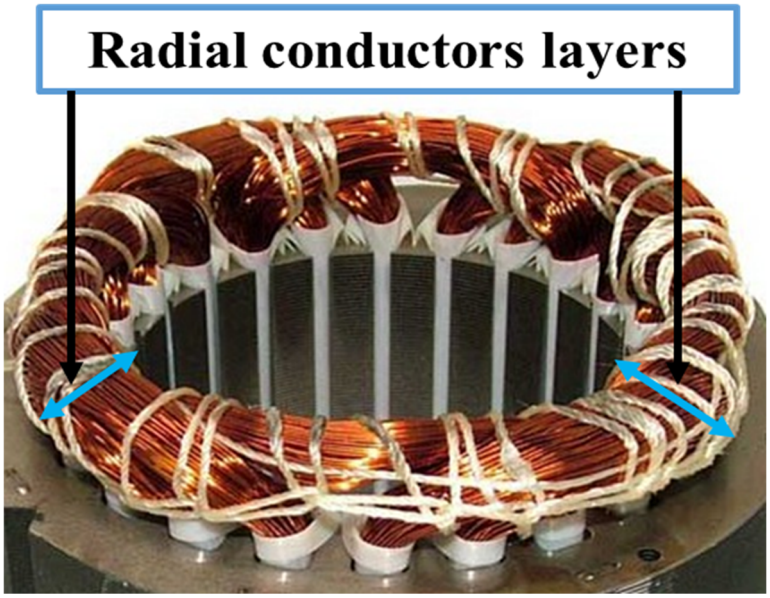


Figure 4.8: Generic end winding configuration – radial thickness view

In order to create, as much as possible, a more realistic representation of the end windings and to investigate how different levels of porosity can affect the predictions of heat dissipation rate in the end region, different thicknesses of the cylindrical/conical filler were used.

Porosity or void fraction (ϕ) is a measure of the void spaces in a material: as shown in Equation 4.1, it is a fraction of the volume of voids over the total volume and its range is between 0 and 1 (or, as percentage, between 0% and 100%).

$$\Phi = \frac{V_v}{V_t} \cdot 100 \qquad \textbf{4.1}$$

Where V_v (m^3) is the void's volume and V_t (m^3) is the total volume which in this case was equal to the volume of the new end windings geometry but without any cavities as shown in Figure 4.9.

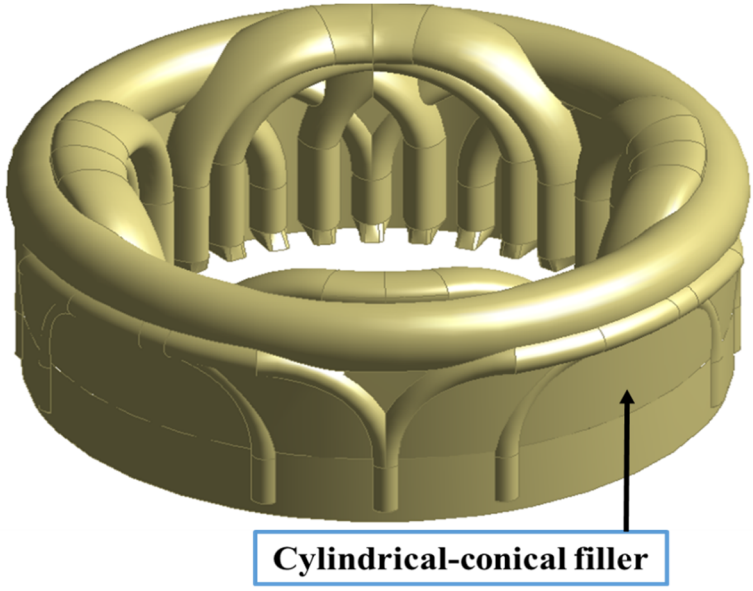


Figure 4.9: EWs geometry – 0% porosity model (no cavities)

Two new end winding models with higher porosity level were then generated as shown in Figure 4.10 (EWs model 1) and Figure 4.11 (EWs model 2) below.

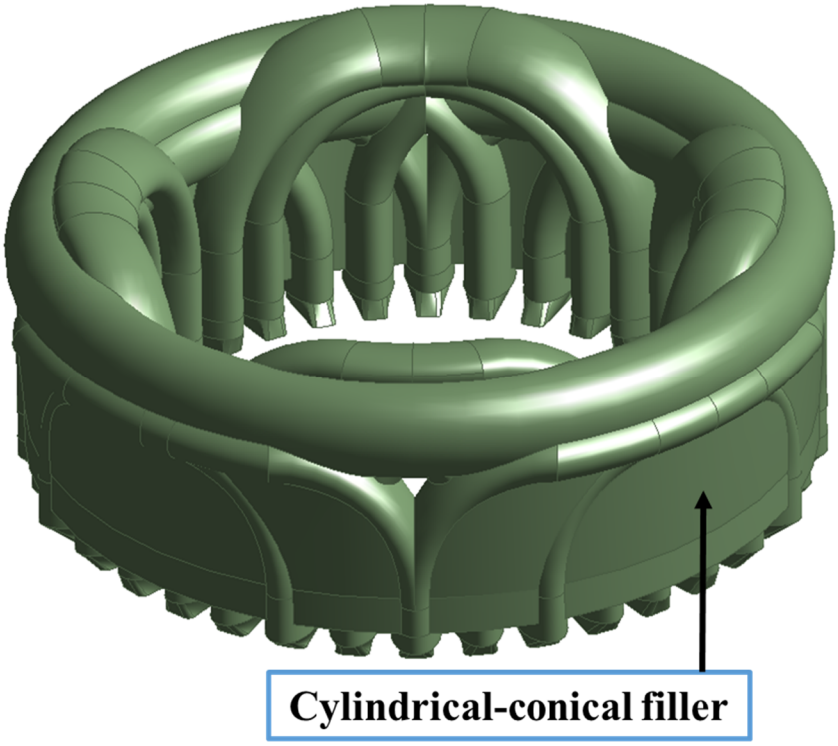


Figure 4.10: EWs geometry – model 1

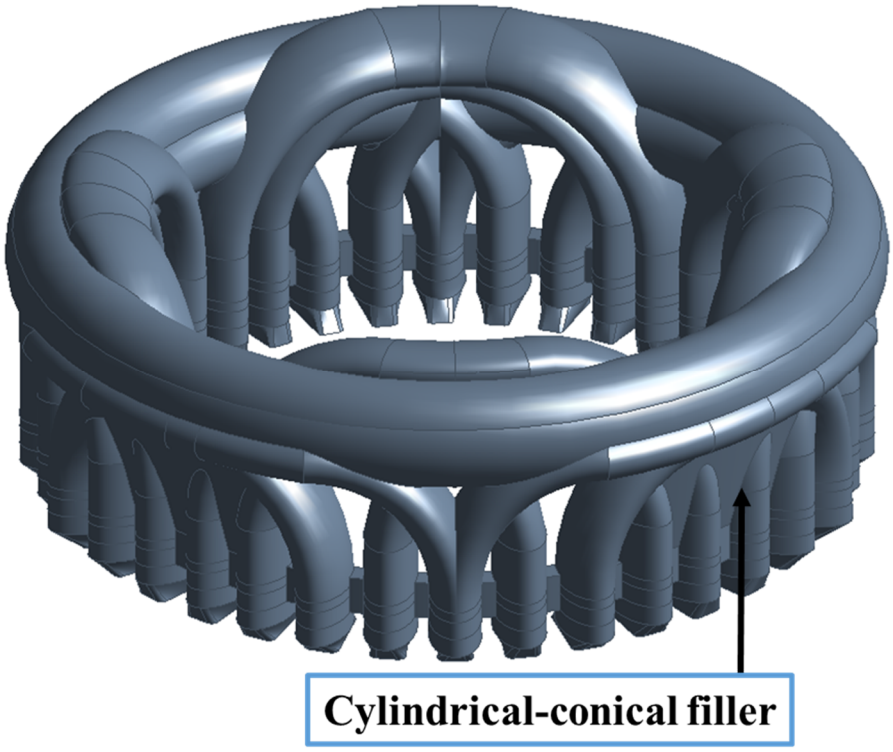


Figure 4.11: EWs geometry – model 2

Table 4.1 below reports the level of porosity Φ for the two developed geometries:

	Porosity Φ percentage [%]
EWs model 1	3.7 %
EWs model 2	15.2 %

Table 4.1: EWs models porosity

The proposed methodology for a more realistic end windings representation led to a 90° repeating pattern model with the following characteristics:

- End windings height and width comparable with the real geometry.
- Cavities created between windings leaving the stator slots and conductors.
- Conductors modelled as a bundle of wires in order to better represent the irregular surface as a result of the winding process.

The geometry of EWs model 1was judged to be the most physically realistic representation of the end windings of the machine under investigation; EWs model 2 was considered in order to assess the impact of different level of end windings porosity on the thermal performance of the TEFC machine. The computational cost associated with the two more realistic end windings models was investigated, as well as their impact on the fluid flow and thermal behaviour of the end regions of the machine as presented and discussed in section 4.3.2.2.

4.3.2 End Region

A 3D model of the fluid end region was created using Ansys Design Modeler in order to carry out a thermal and fluid flow investigation of this region. Considering the symmetry of the machine, a 90° sector was periodically modelled using the simplified EWs form (Figure 4.3) and the more realistic geometries EWs model 1 (Figure 4.10) and 2 (Figure 4.11). Figure 4.12 and Figure 4.13 below report the fluid end region created using the EWs model 2: Figure 4.13 shows the negative of the end region where only fluid zones were considered and used for numerical analysis.

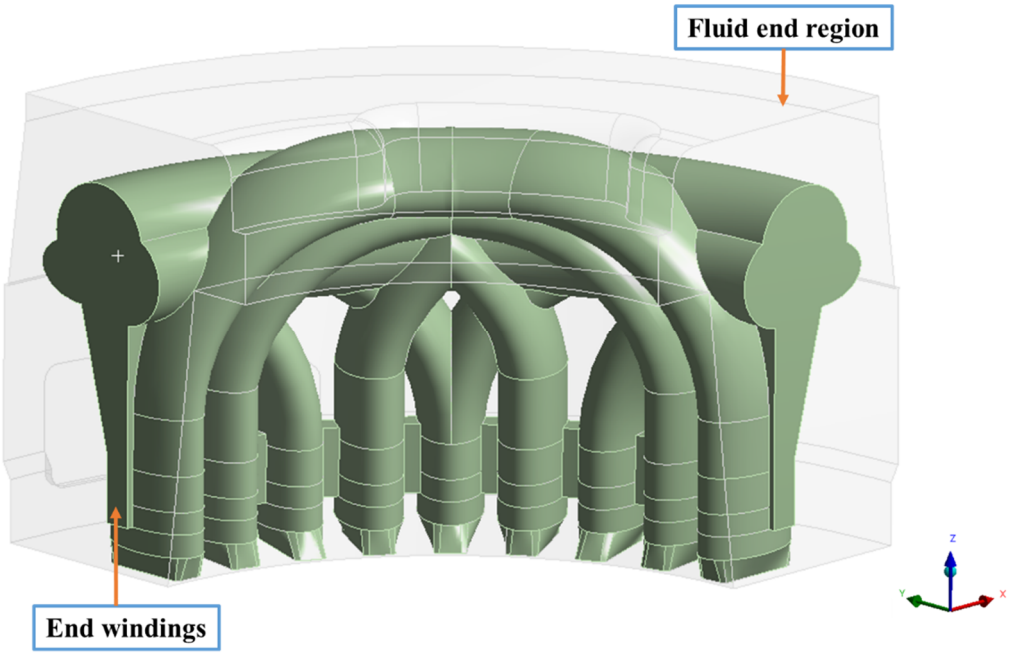


Figure 4.12: Fluid end region, EWs model 2, 90° sector (solid included only for clarity)

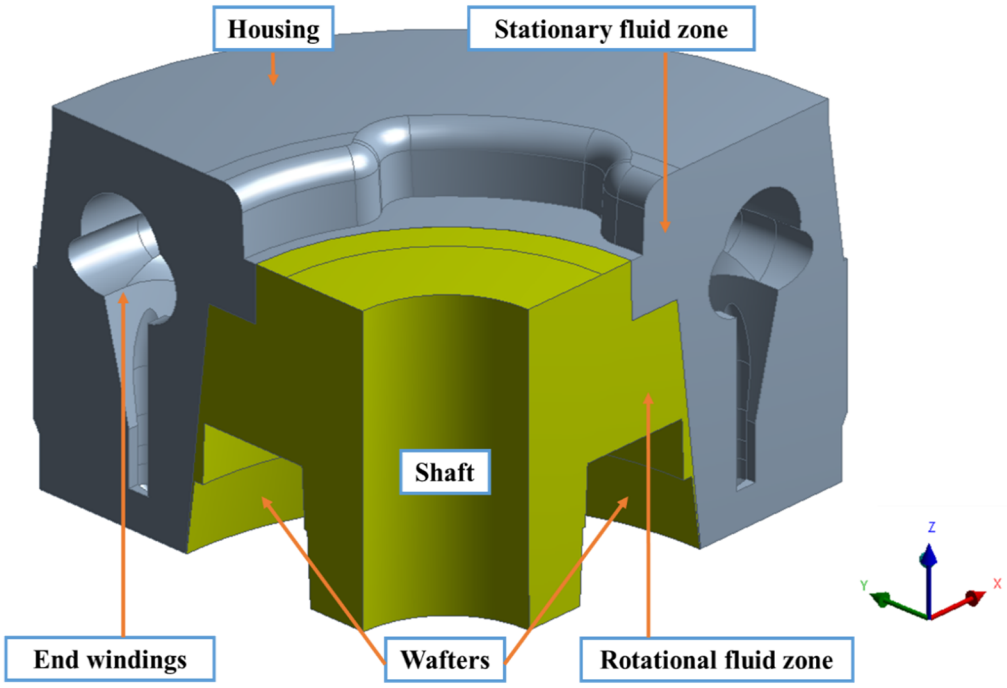


Figure 4.13: Fluid end region, EWs model 2, 90° sector, reference frames

Computational Fluid Dynamics (CFD) was then utilised to investigate the flow fields present in the end region area for the cases under investigation. The CFD code used in this project was Ansys Fluent, version 17.2 [66]; this solves the governing conservation equations of mass, momentum and energy using the finite volume method.

The Multiple Reference Frame (MRF) or frozen rotor approach was used in order to simulate the rotation of the rotor around the z-axis [66]. As shown in Figure 4.13, the fluid region was split into two reference frames: one containing all rotating parts, such as the shaft, end ring and wafters, and another stationary reference frame which contains the motor housing and the end windings; in the case under investigation, the rotational speed was set at 1500 rpm.

The realizable k-ε turbulence model was implemented since it is more suitable for rotation and high shear stresses problems and it can generally provide better performance than the standard k – ε model [56].

A thermal sensitivity analysis, focused on convection was performed; radiation was assumed to be negligible for this application. As part of the methodology development process, an investigation of the convective heat transfer and heat flux dissipated through the external frame was carried out. In order to investigate the impact of different levels of geometrical simplification of the end region, same thermal boundary conditions for the end windings and the housing were used for all the cases under investigation: the end windings and end ring walls were set at a constant temperature of 150°C while the housing temperature was set at 100°C. The enclosed fluid was air which was assumed to be incompressible with thermal properties, such as thermal conductivity k (W/mK) and specific heat c_p (J/kgK), set from the internal database within Ansys Fluent as reported in Table 4.2.

Density ρ [kg/m^3]	Specific heat c_p [J/kgK]	Thermal conductivity k [W/mK]	Viscosity μ [kg/ms]
0.9	1010.4	0.0303	2.25e-05

Table 4.2: Air properties from Ansys Fluent at 120°C [66]

In order to investigate the geometrical simplifications of the end region and their impact on the fidelity of the airflow and thermal predictions and on the computational cost, two areas were investigated as schematically depicted from Figure 4.14 below; these were the end cap/casing (section 4.3.2.1) and the end windings (section 4.3.2.2). The simplifications were assessed to understand the relative computational cost bearing in mind the final aim of creating a model to link the internal and external domains for design analysis.

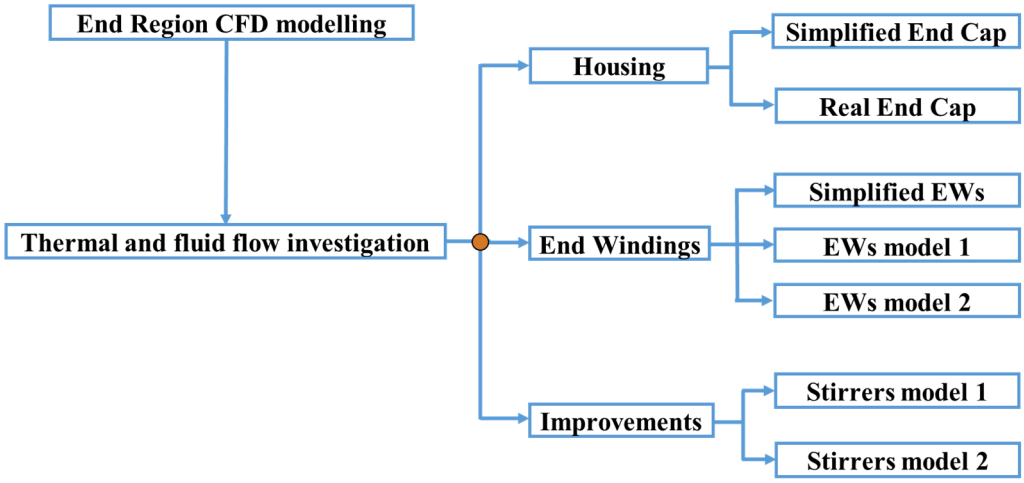


Figure 4.14: End Region – thermal and fluid flow investigation

For the housing/end cap analysis case the simplified form of end windings (Figure 4.3) was utilised. An alternative internal cooling design consisting of a shaft mounted stirrers was also considered and investigated as discussed in section 4.4.

For all the cases under investigation, the rotor tangential velocity ($v_{rotor\ tip}$) was used to normalise the numerical results of the internal airflow velocity v^*_{int} (Equation 4.2) presented in the following sections.

$$v^*_{int} = \frac{v}{v_{rotor\ tip}} \qquad \textbf{4.2}$$

4.3.2.1 Simplified and real housing geometry

The aim of the investigation was to verify the validity of the proposed simplification for the housing wall in the end region: an investigation of the fluid flow distribution and the heat transfer rate from the end windings to the external housing was performed.

The simplified model had a flat and smooth internal surface where the cavities from the real geometry are not considered; the modelling of these features leads to a higher number of cells for the discretization process of the end region and hence, a higher computational cost and time.

As stated in section 4.3.1, a 90° sector of the fluid end region was periodically modelled for the case with the simplified and real housing wall shape; for both cases, the approximated end windings geometry (Figure 4.3) was initially used in order to reduce the computational cost and time.

For the discretization process unstructured meshes, with an average cell size of 2 mm, were generated within Ansys Mesher for the cases under investigation. According to the published literature [67, 68], a strong recirculating toroidal vortex flow, superimposed on the main swirling flow, was expected over the wafters and end windings area; therefore in order to correctly model and capture these phenomena, local mesh refinements of 1 mm were performed in proximity of wafters and end windings surfaces. Figure 4.15 and Figure 4.16 show the discretized 3D geometry for the fluid end region with the simplified (Case A) and real housing (Case B) wall shape respectively.

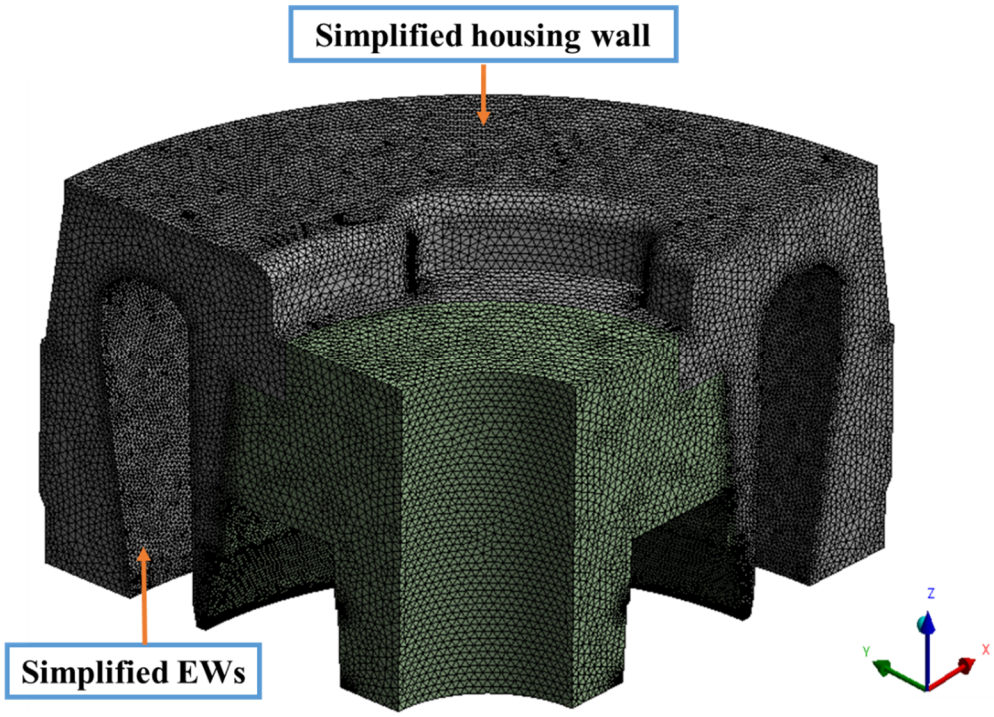


Figure 4.15: Case A - Fluid end region, simplified housing and EWs

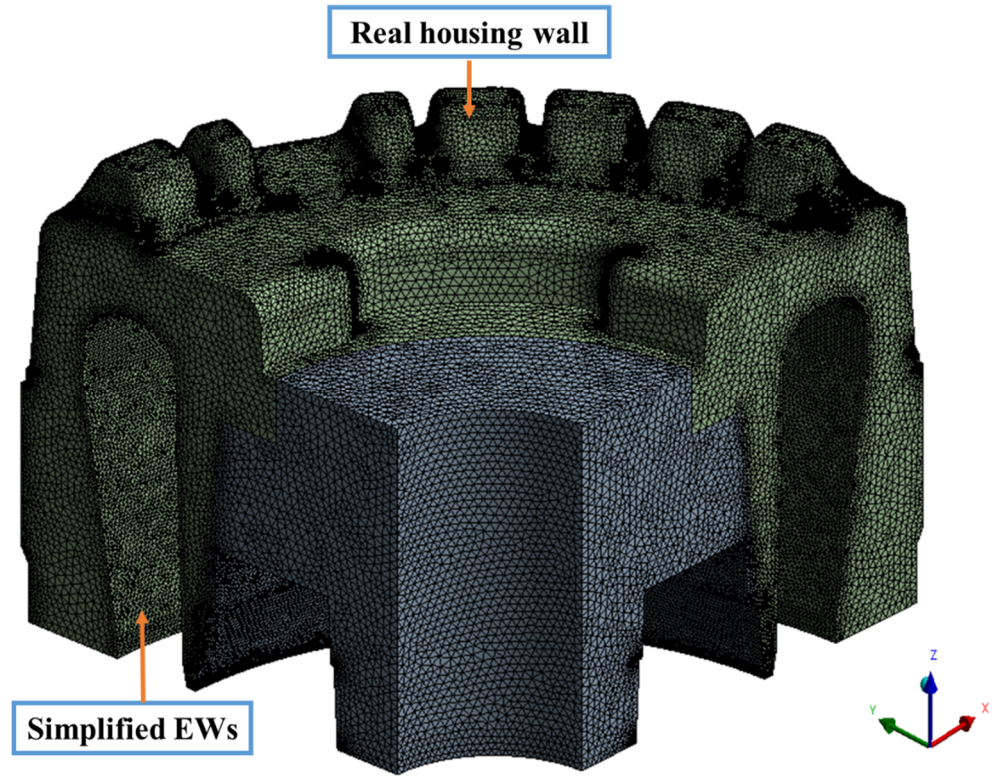


Figure 4.16: Case B - Fluid end region, simplified EWs and real housing

Table 4.3 below reports the mesh details and the computational cost of the two cases under investigation. The generated meshes have a maximum skewness of 0.95 which is considered acceptable [66]; this parameter provides an indication about the quality of the mesh generated. Another parameter which is usually considered to evaluate the quality of the mesh is the aspect ratio: this is defined as the ratio between the long and the short edges of the single cell and generally this value should not exceed 100.

	Case A – simplified housing	**Case B – real housing**
Cell count	2,075,000	3,200,000
Skewness	0.94	0.95
Aspect Ratio	14.2	24
Simulation time	6 hours	9 hours

Table 4.3: Mesh details and computational cost – Case A and B

The majority of the post-processing was carried out using Ansys CFD-Post which allows detailed 3D contour and vector plots of velocity, temperature and heat flux to be generated. Figure 4.17 below shows the location of the axial and radial planes used to investigate both the secondary and primary swirling flow respectively: the axial plane was created at an angular location of 45° over the wafters while the radial plane was located 25 mm above the end ring.

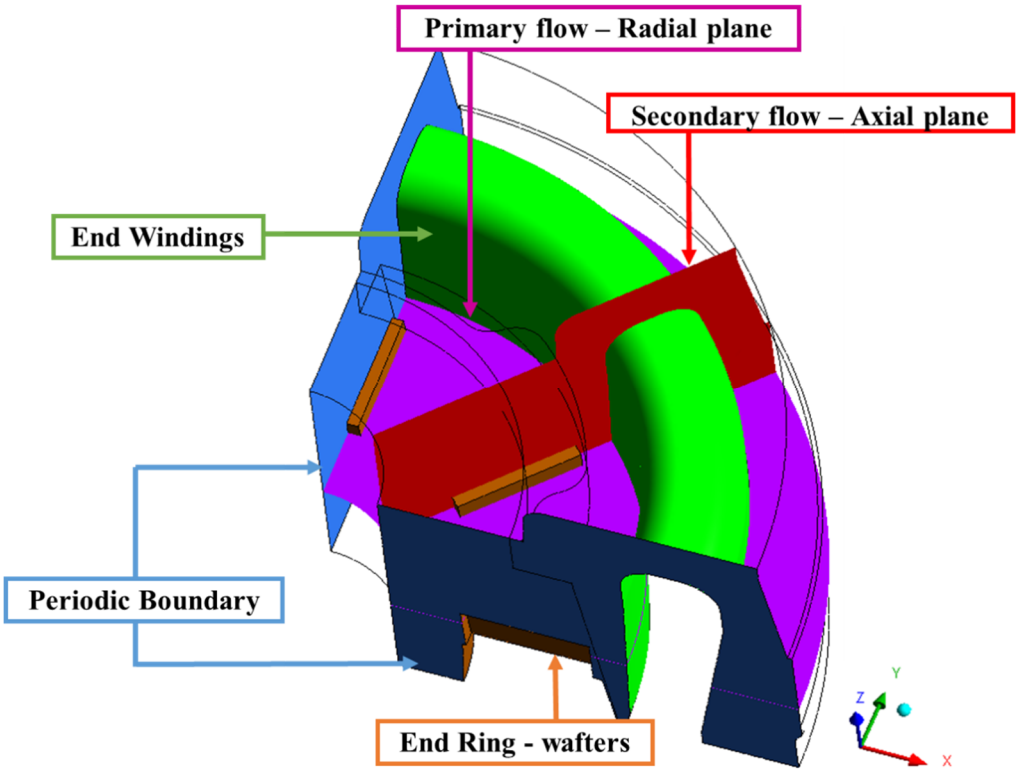


Figure 4.17: Case A and B – axial and radial plane

Results of airflow and heat transfer were computed and compared in both Case A and B. Figure 4.18 and Figure 4.19 below show the non-dimensional vector velocity plot of the primary swirling flow for both the cases under investigation; as can be noticed from the comparison, the cavities of the real housing wall do not affect or change the distribution and magnitude of the primary swirling flow.

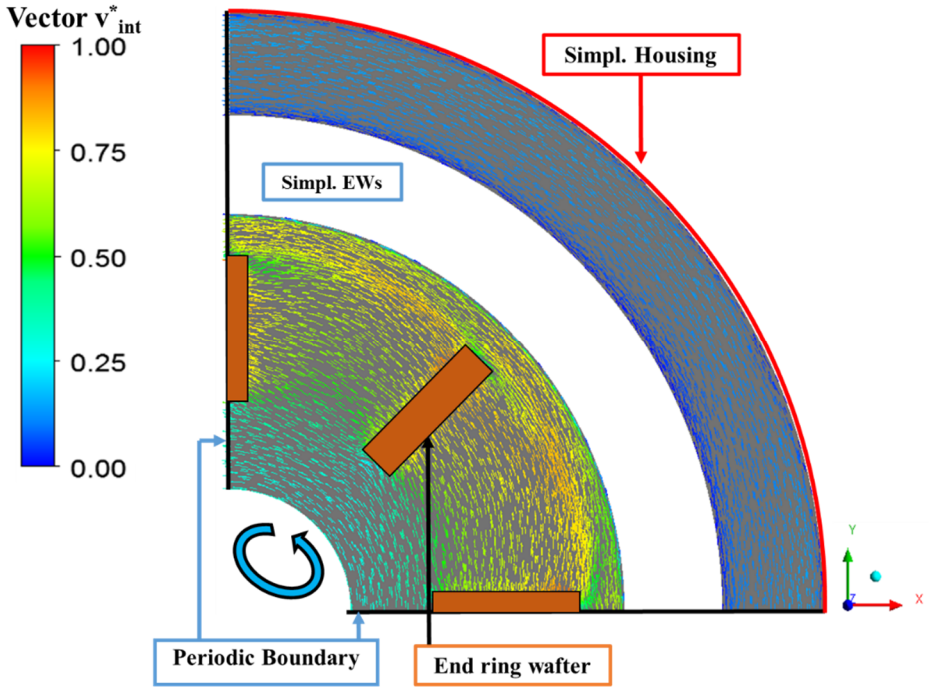


Figure 4.18 Case A - End region primary swirling flow – $v^*_{int} = v/v_{rotor\ tip}$

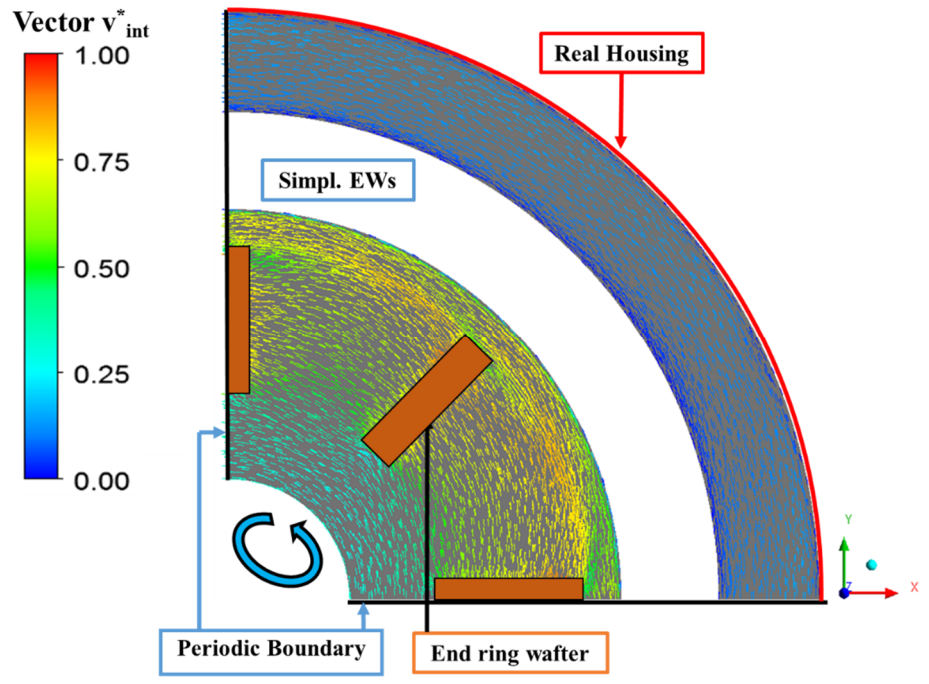


Figure 4.19 Case B - End region primary swirling flow – $v^*_{int} = v/v_{rotor\ tip}$

A slight change of the airflow distribution due to the features of the real housing wall can be seen from the investigation of the secondary flow as reported in Figure 4.20 and Figure 4.21 below.

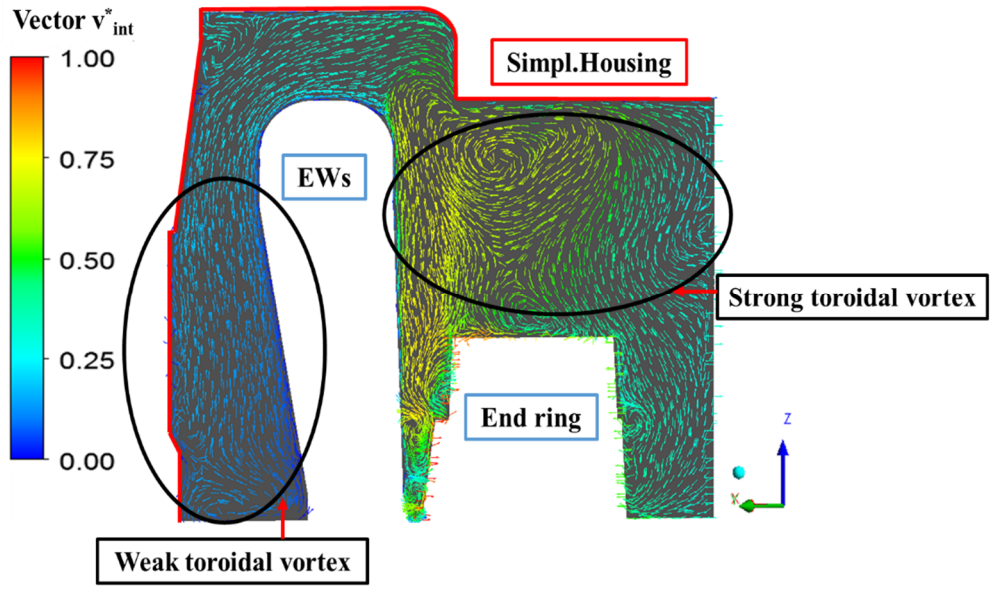


Figure 4.20: Case A - End region secondary flow – $v^*_{int} = v/v_{rotor\ tip}$

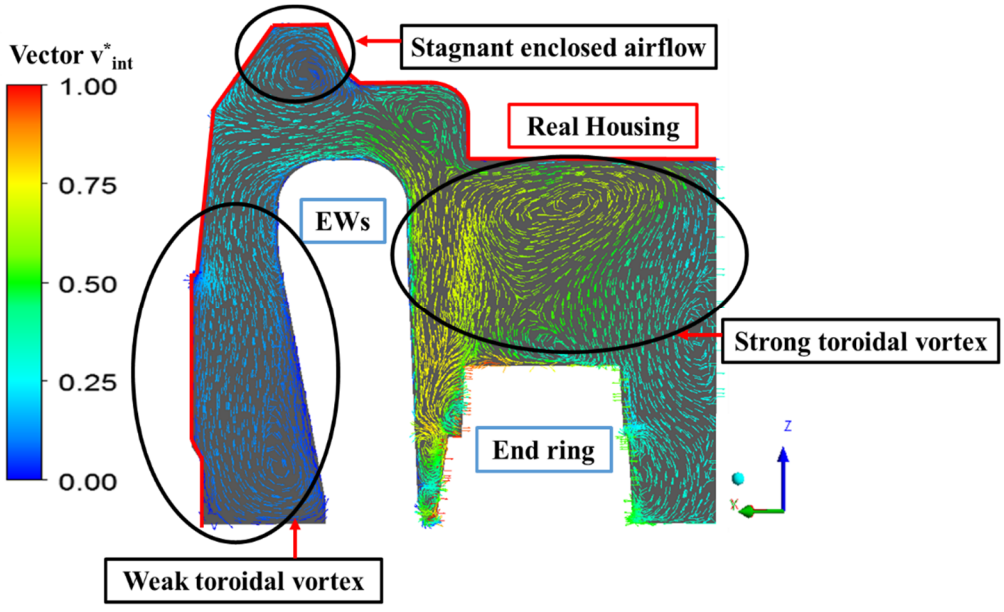


Figure 4.21: Case B - End region secondary flow – $v^*_{int} = v/v_{rotor\ tip}$

In both cases in accordance to the literature, there is a strong recirculating toroidal vortex flow located in the area between the end winding and the end ring; another recirculating flow, which is much weaker in magnitude, is located in the area behind the end windings.

This airflow distribution has a strong impact on the thermal behaviour of this region: stronger convective phenomena over the end winding surface are expected where the secondary flow is stronger in magnitude. In order to proceed to a local thermal investigation of the end winding surface, a subdivision of 15 sub-surfaces was created (Figure 4.22) and for each of them the heat flow (W) was computed for both Case A and B.

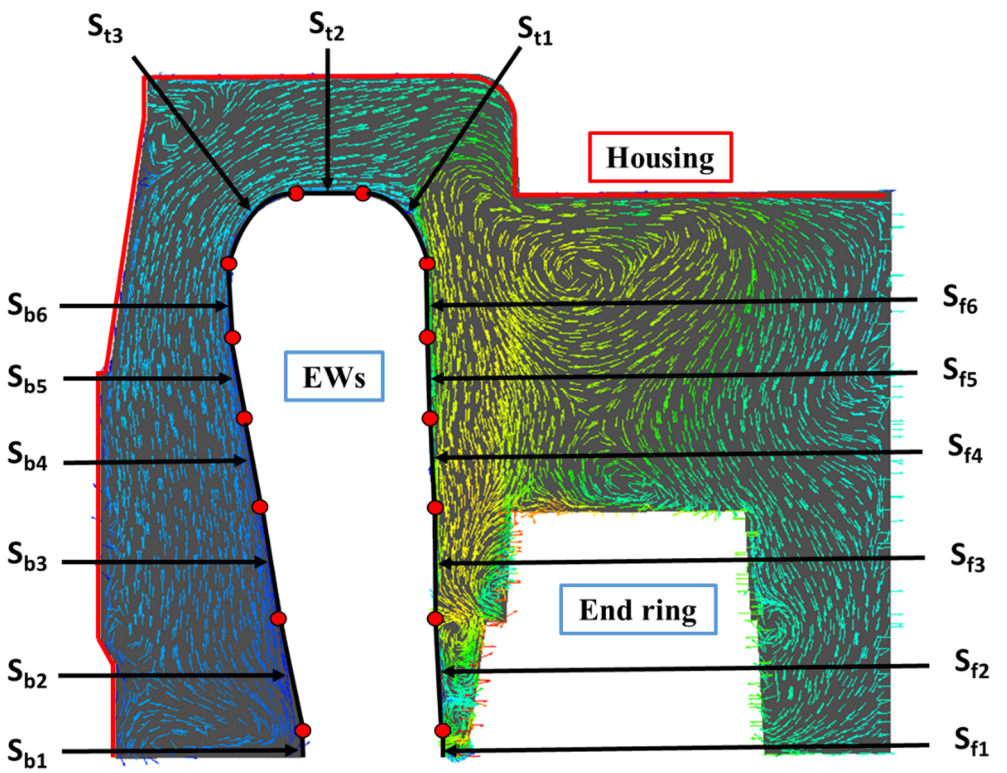


Figure 4.22: EWs sub-surfaces division – Case A and B

Table 4.4 reports results and the percentage difference of heat flow for each sub-surface for the simplified and real housing shape cases calculated as shown in Equation 4.4. The heat flow dissipated through the external housing wall (red boundary in Figure 4.22) was computed as well; Table 4.5 reports the comparison between the CFD results of heat flow for the cases under investigation. The housing value of heat flow computed from Case B ($q_{Housing,Case\ B}$) was used to normalise the results presented below as in Equation 4.3.

		Case A - Simplified housing	**Case B - Real housing**	**% difference**
EWs - back	S_{b1}	$3.41 \cdot 10^{-3}$	$3.11 \cdot 10^{-3}$	-8.8
	S_{b2}	0.017	0.018	+6.6
	S_{b3}	0.023	0.022	-4.9
	S_{b4}	0.032	0.029	-7.1
	S_{b5}	0.026	0.024	-7.1
	S_{b6}	0.031	0.029	-6.2
Total Heat flow		**0.132**	**0.127**	**-4.7**
EWs - front	S_{f1}	$1.55 \cdot 10^{-3}$	$1.66 \cdot 10^{-3}$	+7.3
	S_{f2}	0.028	0.027	-2.6
	S_{f3}	0.095	0.102	+7.1
	S_{f4}	0.078	0.083	+5.8
	S_{f5}	0.045	0.048	+7.5
	S_{f6}	0.043	0.046	+6.9
Total Heat flow		**0.292**	**0.309**	**+5.7**
EWs - top	S_{t1}	0.083	0.08	-3.6
	S_{t2}	0.027	0.026	-5.4
	S_{t3}	0.063	0.065	+3.5
Total Heat flow		**0.175**	**0.172**	**-1.3**

Table 4.4: Heat flow comparison: EWs sub-surfaces, Case A and Case B

	Case A - Simplified housing	Case B- Real housing	% difference
Total Heat flow	0.96	1	+4.4

Table 4.5: Heat flow comparison – Housing, Case A and B

$$q_1^* = \frac{q}{q_{Housing,Case\ B}} \qquad \textbf{4.3}$$

$$\%\ difference = \frac{|q_{(Case\ A)} - q_{(Case\ B)}|}{\frac{1}{2} \cdot (q_{(Case\ A)} + q_{(Case\ B)})} \cdot 100 \qquad \textbf{4.4}$$

The two models show comparable nature and magnitude of the secondary flow with differences within 8% of the computed heat flow from the end windings sub-surfaces and housing walls. Results also show that the heat transfer rate in the end region is not significantly affected by the cavities from the real housing shape. The flow is completely stagnant with a recirculation enclosed within it and this has only a marginal impact on the heat transfer rate of the end region. Therefore the simplified model was used for fluid and thermal characterisation of full 3D model of the TEFC machine as the percentage difference of the computed heat transfer rate was 3-8% whilst a computational cost reduction of 40% was achieved.

A fluid flow and thermal transient investigation of the end region of the machine was also performed to compare the performances of the SM and MRF models. The high computational cost associated with the SM approach made it not suitable for the modelling of the whole TEFC machine; in addition, the simulation time needed for the whole machine model to reach a thermal steady state condition was prohibitive with the computational resources available. The MRF approach was then preferred for rotation modelling; future studies using SM simulations and higher computational resources for comparison with MRF would be recommended.

4.3.2.2 Simplified and improved EWs geometry

The aim of this analysis was to investigate the impact of a more accurate representation of the end windings geometry on the airflow distribution and on the rate of heat transfer from the end windings to the external housing.

As discussed in section 4.3.1, a 3D model of the fluid end region using both the simplified (Figure 4.3) and more realistic end winding geometry (EWs model 1 and 2, Figure 4.10 and Figure 4.11) were created using Ansys Design Modeller.

The same considerations stated in section 4.3.1 and 4.3.2.1 for the meshing process and solver setup were used for this investigation; Figure 4.23, Figure 4.24 and Figure 4.25 show the generated meshes for the 90° sectors of the fluid end regions using both the simplified and more realistic (EWs model 1 and 2) end winding geometries.

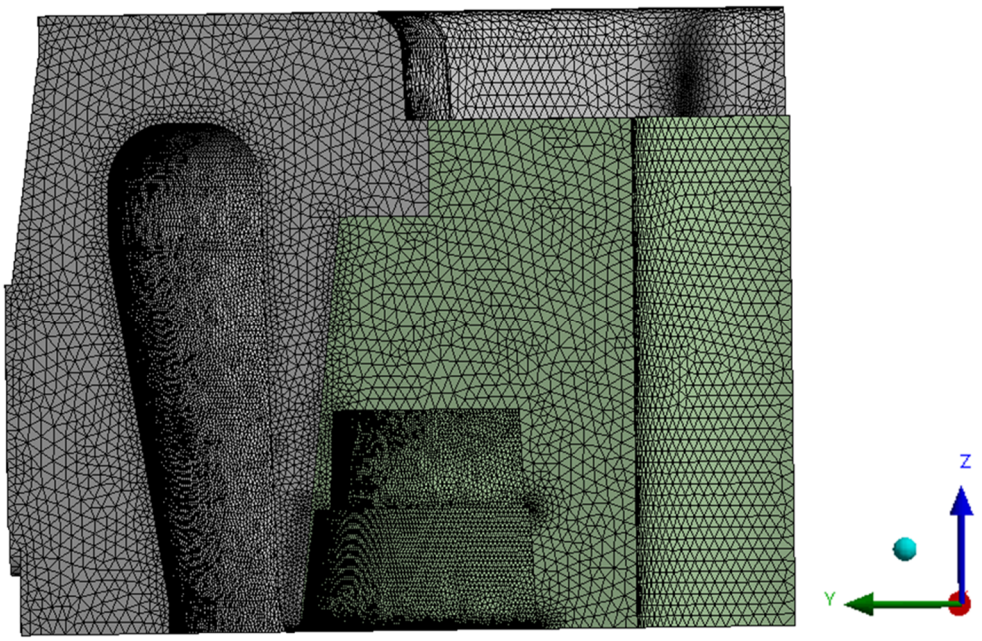


Figure 4.23: Fluid end region mesh, simplified EWs model

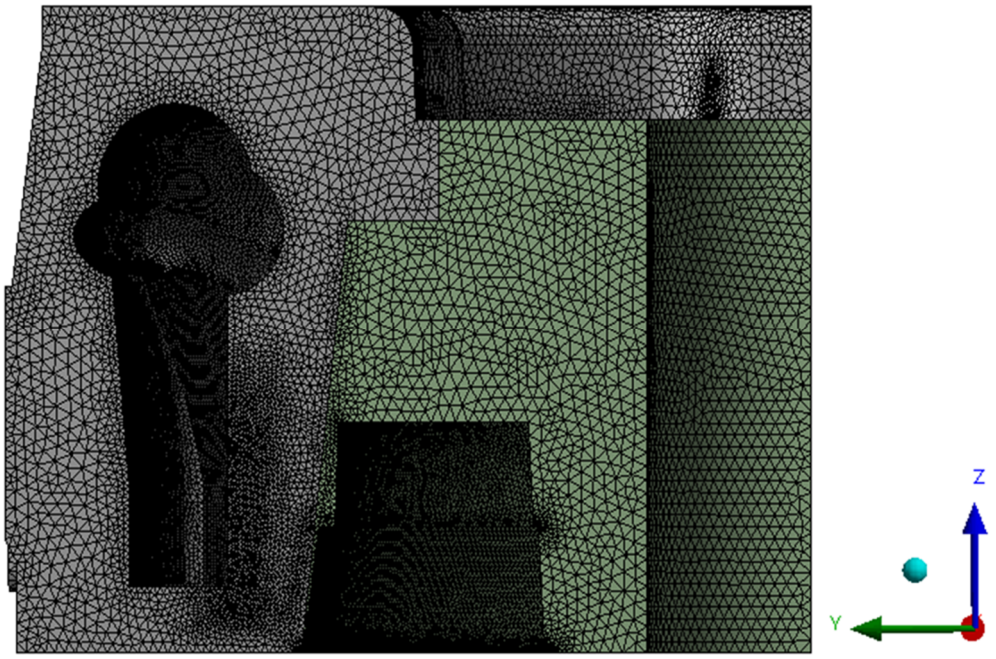


Figure 4.24: Fluid end region mesh, EWs model 1

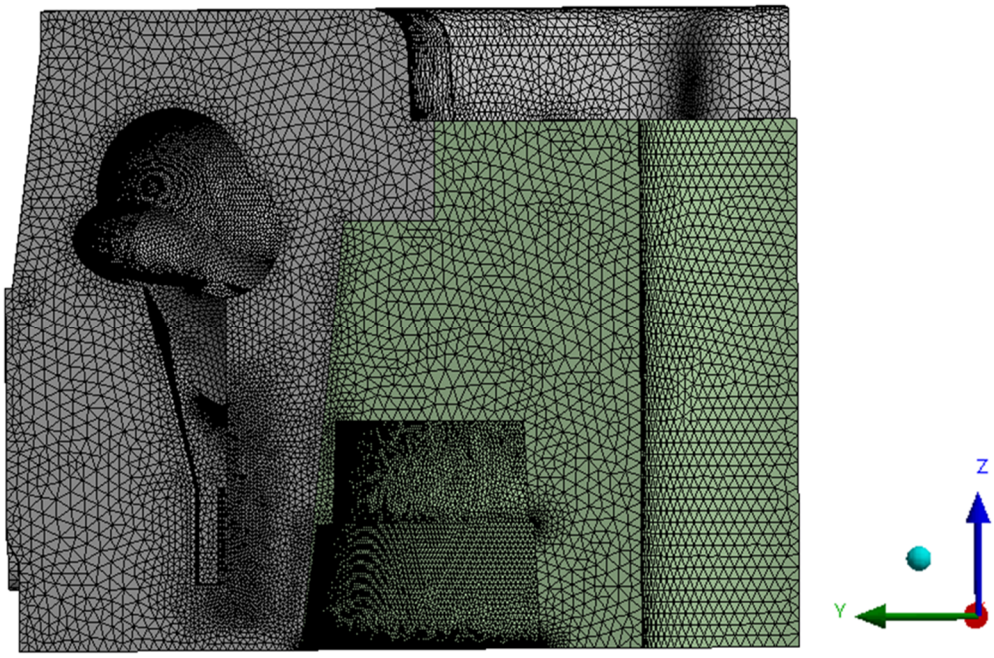


Figure 4.25: Fluid end region mesh, EWs model 2

Table 4.6 below reports the cell count for the 90° sector of the fluid end region for the case with the simplified and more realistic end winding geometries respectively; due to the higher porosity of the new geometries, the cell count of the fluid end region increased by up to 12% and 20% for the EWs model 1 and 2 respectively compared to the case with the simplified geometry. A converged steady-state solution is run in around 6 hours for the simplified geometry case and around 9 hours for the cases with the new geometry.

	Simplified EWs	**EWs model 1**	**EWs model 2**
Cell count	2,075,000	2,330,550	2,490,670
Skewness	0.95	0.93	0.942
Aspect Ratio	14.2	15.8	14.4
Simulation time	6 hours	9 hours	9 hours

Table 4.6: Mesh details and computational cost – Simplified and improved EWs

Results compare the airflow and heat transfer in both the simplified and new end winding geometries; the impact of the developed new models on both the primary swirling flow and on the secondary flow was considered. Figure 4.26 below shows the location of the axial and radial planes used to investigate the velocity airflow distribution and magnitude in the end region for the cases under investigation. The axial plane was created at an angular location of 30° in order to better show the impact of the new end winding model cavities on the secondary airflow of the end region; the radial plane was located 25 mm above the end ring.

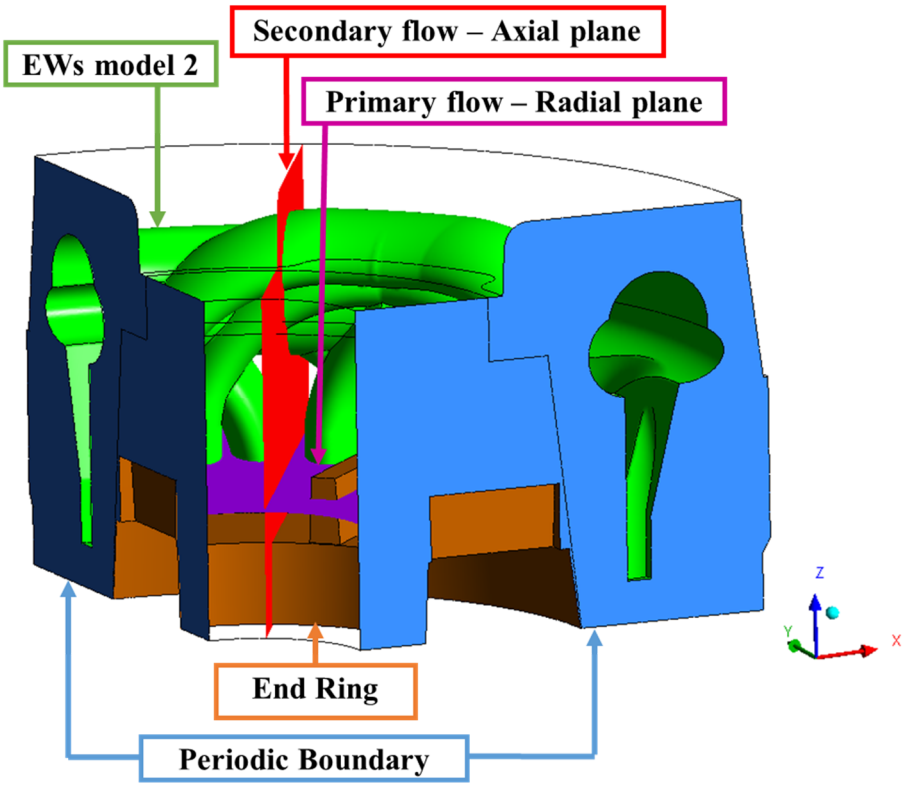


Figure 4.26: Simplified and improved EWs – axial and radial plane

Figure 4.27, Figure 4.28 and Figure 4.29 show the non-dimensional vector velocity plot of the primary swirling flow on the radial plane of the end region for the case with the simplified end windings model, EWs model 1 and 2 respectively.

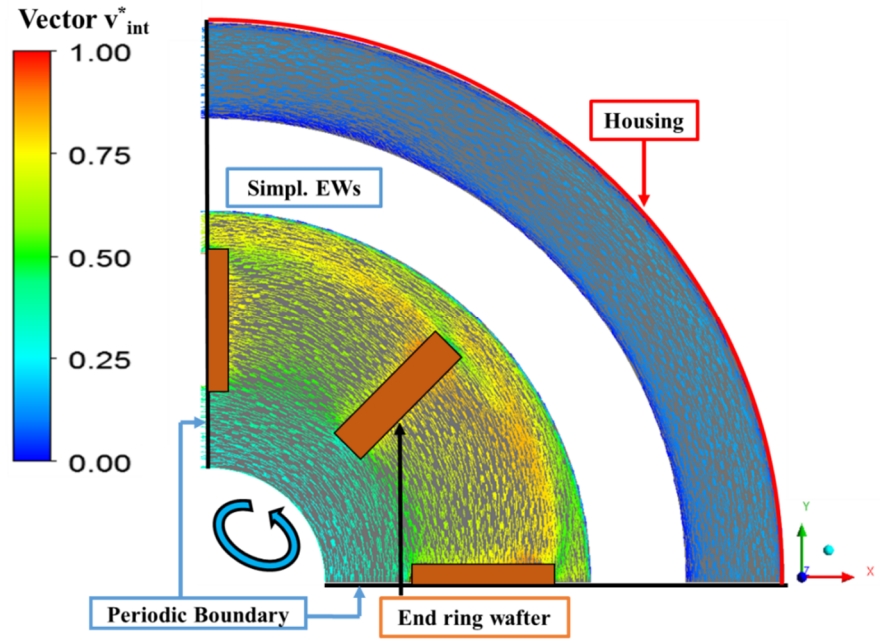


Figure 4.27: End region primary swirling flow, simplified EWs – $v^*_{int} = v/v_{rotor\ tip}$

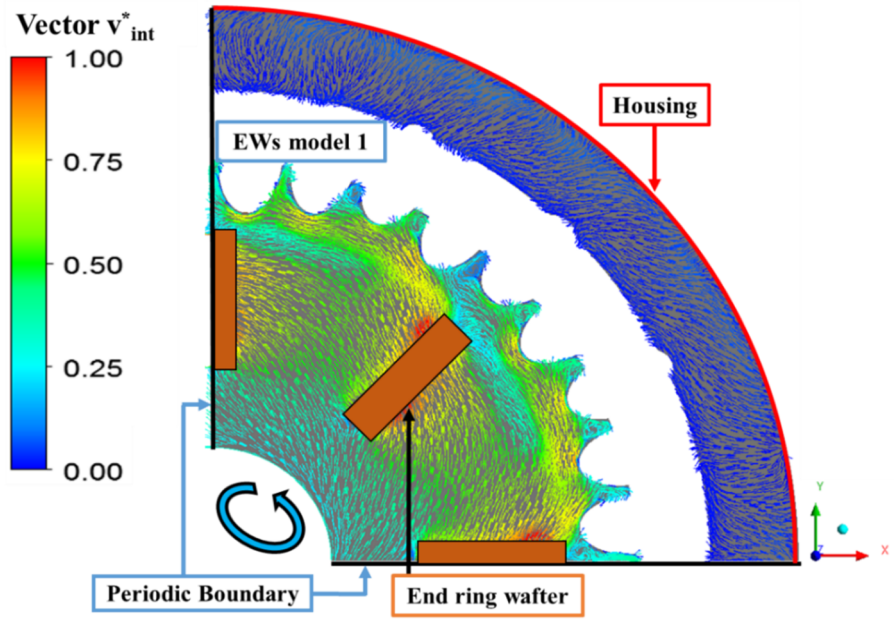


Figure 4.28: End region primary swirling flow, EWs model 1 – $v^*_{int} = v/v_{rotor\ tip}$

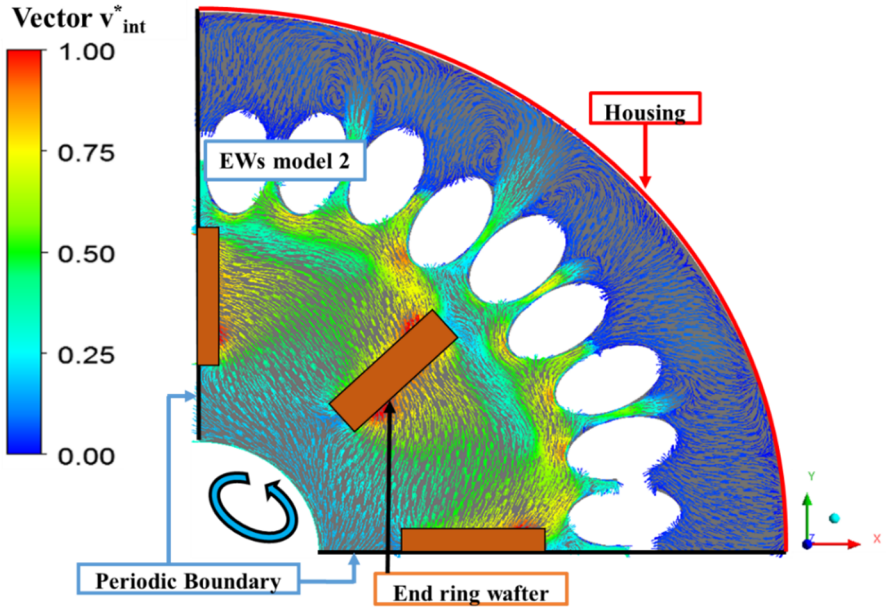


Figure 4.29: End region primary swirling flow, EWs model 2 – $v^*_{int} = v/v_{rotor\ tip}$

As can be seen from results, the more irregular surface of both EWs model 1 (Figure 4.28) and 2 (Figure 4.29) gives a more turbulent airflow and higher velocities in proximity of the end ring and wafters. While the simplified end windings geometry almost entirely blocks the airflow to flow along the radial direction (Figure 4.27), the introduction of a more porous end windings model significantly affects the airflow distribution. The cavities created between the stator slots and the conductors provides multiple flow patterns which overall lead to a more uniform airflow distribution in the end region; this can be better seen from the analysis of the secondary flow as reported in Figure 4.30 , Figure 4.31 and Figure 4.32 below.

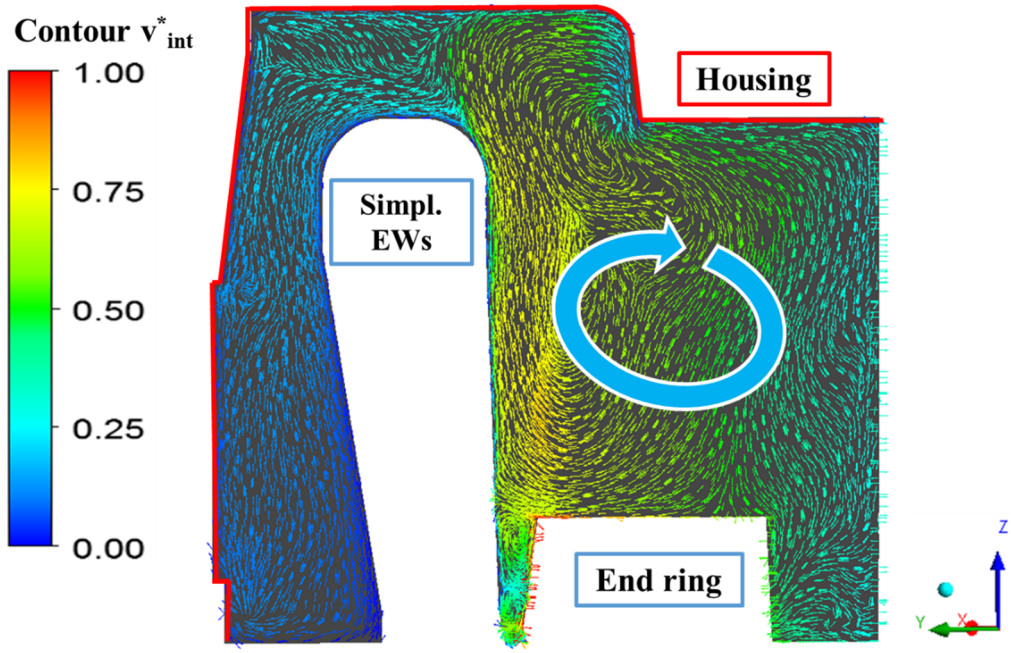


Figure 4.30: End region secondary flow, simplified EWs – $v^*_{int} = v/v_{rotor\ tip}$

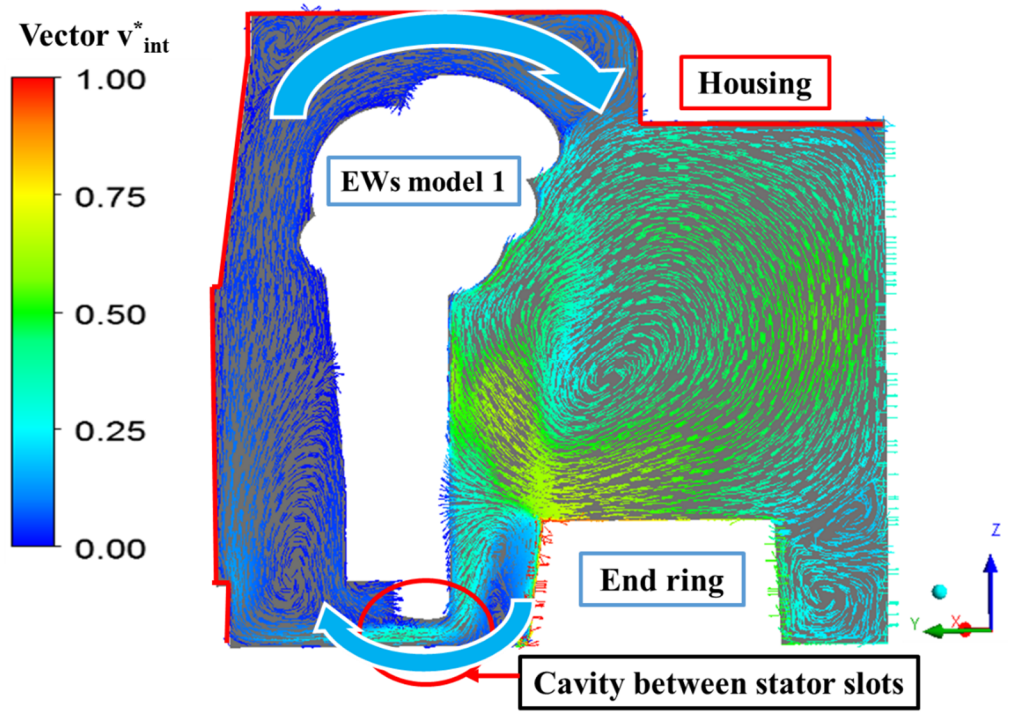


Figure 4.31: End region secondary flow, EWs model 1 – $v^*_{int} = v/v_{rotor\ tip}$

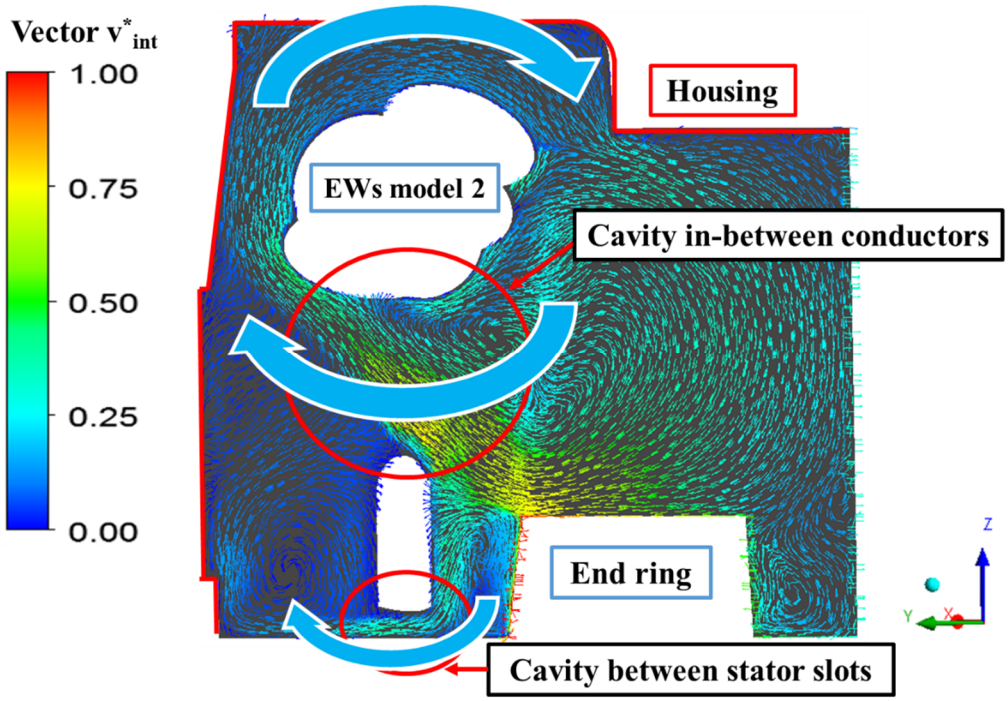


Figure 4.32: End region secondary flow, EWs model 2 – $v^*_{int} = v/v_{rotor\ tip}$

Similarly to the results from section 4.3.2.1, there is a strong toroidal vortex flow located in the region between the end windings and the end ring while a recirculating flow, weaker in magnitude, is located in the area between the end windings and the outer housing. However, as reported in Figure 4.31 and Figure 4.32, both EWs model 1 and 2 provide a more realistic representation of the fluid flow distribution in the end region due to the higher porosity of the new geometries. In addition to the strong recirculating toroidal vortex over the end ring, the weaker recirculating flow penetrates through the cavities between the stator slots near the end windings base (Figure 4.31 and Figure 4.32) and through the conductors layers (Figure 4.32); the airflow then flows upwards behind the end windings and passes over the tip to combine with the other main recirculating flow.

The thermal behaviour of the end region is affected by the new fluid flow distribution reported in Figure 4.31 and Figure 4.32: a stronger convective phenomena over the end windings surface is expected where the secondary

flow is stronger in magnitude and the more uniform flow distribution through the conductors cavities would also strongly affect the heat dissipation through the external housing. In order to investigate the thermal impact of the new end winding geometry in the end region, the heat flux dissipated through the external housing was computed as reported in Figure 4.33, Figure 4.34 and Figure 4.35; the highest value of heat flux computed with the EWs model 2 ($Q"_{max,\ EWs\ 2}$) was used to normalise the numerical results of $Q"^{*}$ (Equation 4.5) presented below.

$$Q"^{*} = \frac{Q"}{Q"_{max,EWs\ 2}} \qquad \textbf{4.5}$$

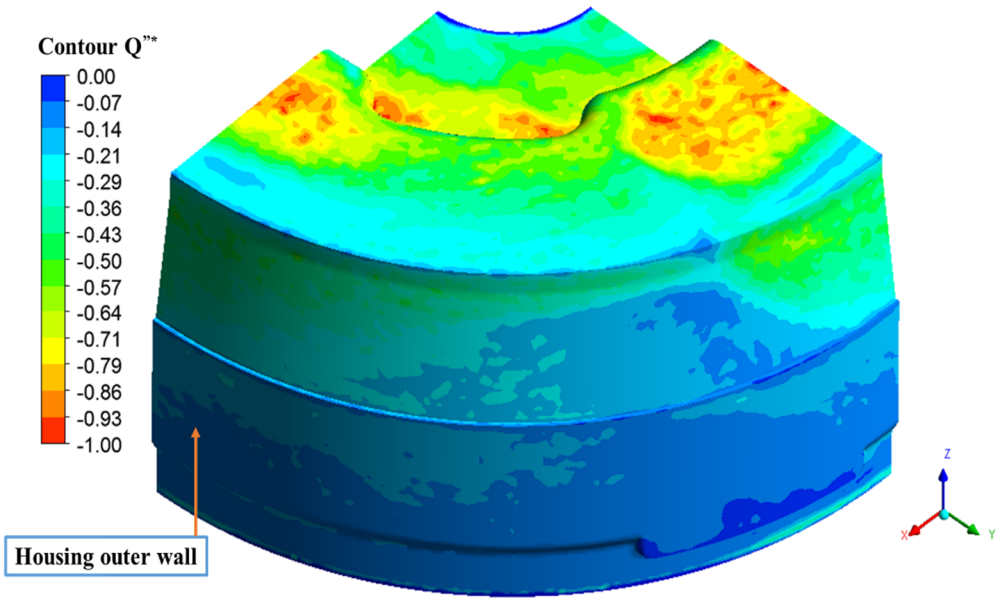


Figure 4.33: Housing wall heat flux (negative as it is leaving the domain), simplified EWs model

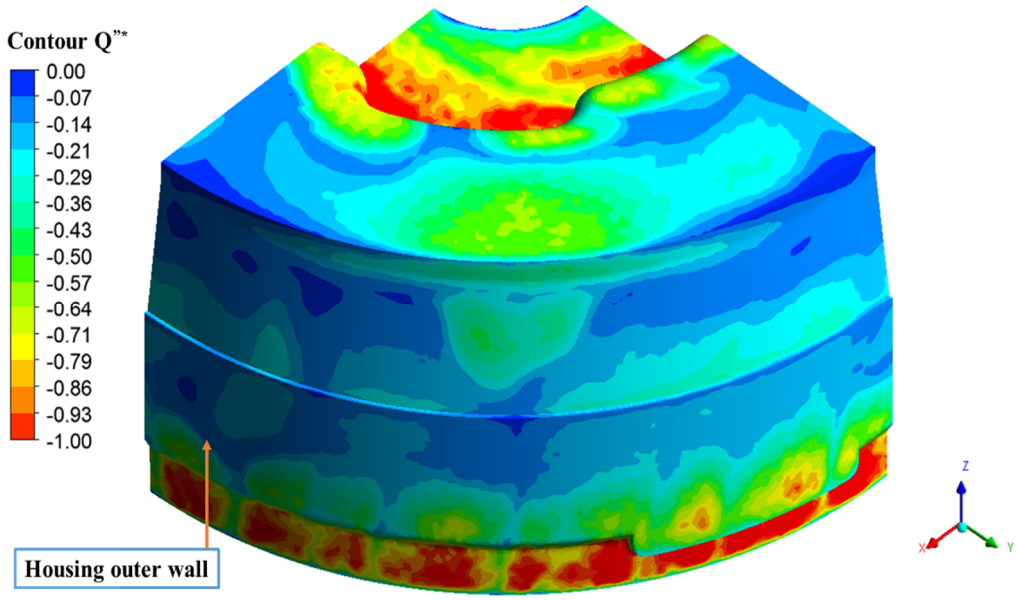


Figure 4.34: Housing wall heat flux (negative as it is leaving the domain), EWs model 1

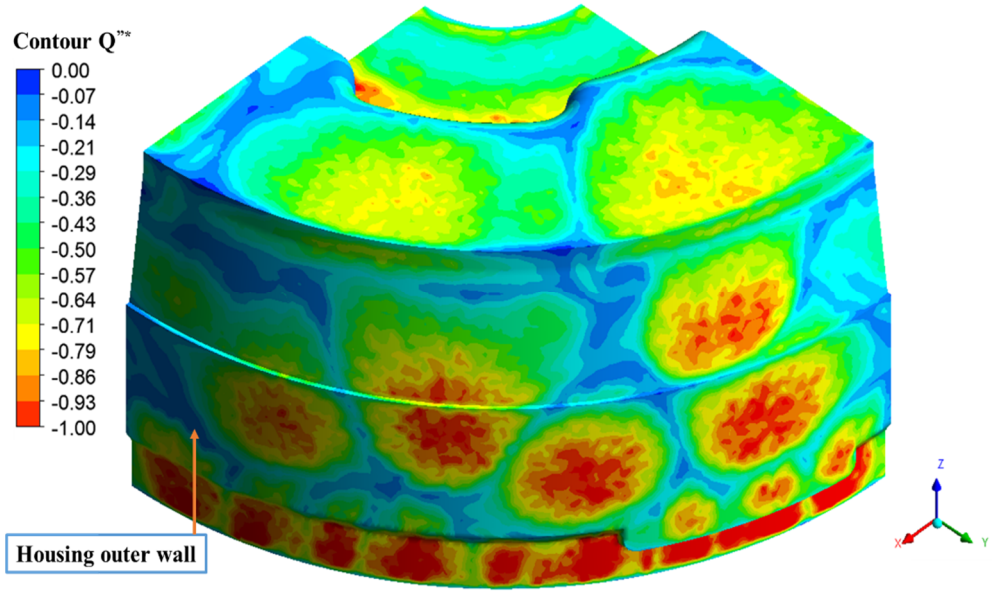


Figure 4.35: Housing wall heat flux (negative as it is leaving the domain), EWs model 2

From the comparison with the model with the simplified end winding geometry (Figure 4.33), results show how a more realistic and detailed end windings geometry can significantly affect the predictions of the complex thermal phenomena occurring in the end region (Figure 4.34 and Figure 4.35); the heat dissipation rate through the outer housing increases by up to 45%.

Table 4.7 below reports the comparison between the CFD results of rate of heat flow (expressed in W) dissipated from outer housing and end windings surfaces for the cases under investigation; the percentage difference was calculated as shown in Equation 4.7. The housing value of heat flow computed with the simplified EWs model ($q_{Housing,simpl.EWs}$) was used to normalise the results presented below as in Equation 4.6.

	Simpl. EWs model	EWs model 1	EWs model 2
Housing	1	1.18 (**+16.6 %**)	1.59 (**+45.6 %**)
EWs	0.57	0.73 (**+24.4 %**)	1.08 (**+62.2 %**)

Table 4.7: Rate of heat flow comparison, simplified and new EWs models

$$q_2^* = \frac{q}{q_{Housing,simpl.EWs}} \qquad \textbf{4.6}$$

$$\%\, difference = \frac{|q_{(EWs\ model\ x)} - q_{(simpl.EWs\ model)}|}{\frac{1}{2} \cdot (q_{(EWs\ model\ x)} + q_{(simpl.EWs\ model)})} \cdot 100 \qquad \textbf{4.7}$$

CFD results show how a more realistic representation of the end windings can help to capture those complex fluid flow and heat transfer phenomena which would be neglected if a simplified representation would be used instead. This aspect results to be very important as it enhance the accuracy and reliability of the numerical model developed; indeed the experimental validation carried out has shown a good agreement between measurements and numerical prediction, this is broadly presented and described in Chapter 6. It can be also seen that by modelling end windings geometries with different level of porosity the heat dissipation rates through the external housing changes; for instance a higher level of porosity leads to a higher heat dissipation rate, this is caused by the more uniform distribution of the airflow. A more controlled winding process can therefore lead to an improved cooling effect of the end regions without altering the geometry and design of the whole machine.

The impact of different levels of porosity of the developed end windings geometries (section 4.3.1) on the overall thermal predictions of the whole TEFC machine is discussed in Chapter 7, where a CFD conjugate analysis of the full TEFC machine (modelling both external, internal flows and solid parts) is presented and discussed.

4.3.3 Airgap

In the electrical machines, the airgap between stator and rotor lamination is a key region within the model for its important impact on the heat transfer and it requires an adequate fine mesh in order to correctly model and capture the local fluid flow and thermal phenomena; appropriate modelling of this region is crucial for the quality of CFD airflow predictions and any associated conjugate heat transfer modelling.

For the TEFC motor under investigation, the geometry of the annular gap is challenging to model due to its very narrow structure and the presence of stator slot openings: this can be seen in Figure 4.36 below where a sector of the fluid domain of the airgap is shown.

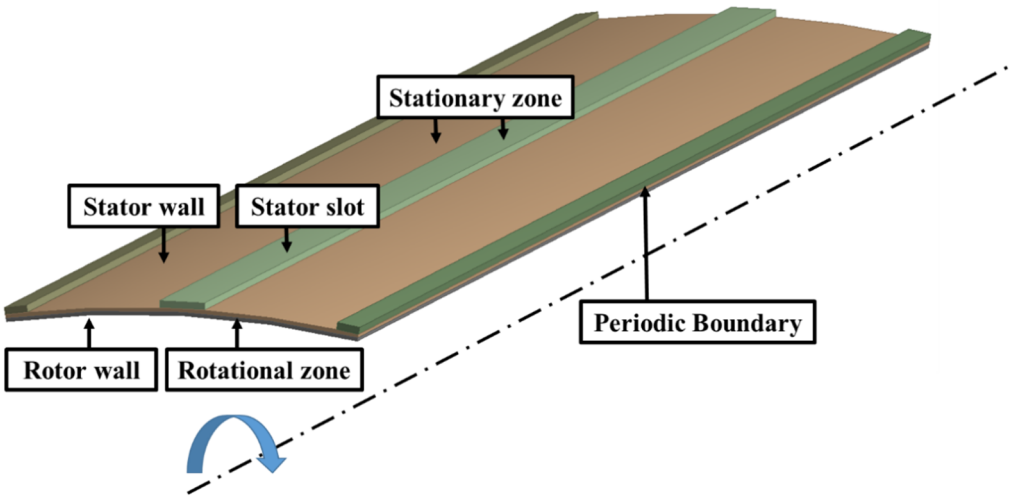


Figure 4.36: Airgap fluid domain 20° sector

As shown in Figure 4.36, given the geometry periodicity, a 20° sector was considered by using periodic boundary conditions on the lateral surfaces of the domain in order to reduce the computational cost required and consequently the calculation time. The rotation was modelled using the MRF approach, this required the domain division in a rotational and stationary zone. Since in TEFC machines external air cannot circulate in the internal parts, there is no axial imposed airflow in the airgap and therefore, in this case, the front and rear sides of the domain were considered as symmetry planes.

The discretisation process was conducted using Ansys Mesher; since the airgap domain has a regular cross-section geometry, the sweep meshing method and hexahedral cells were adopted for the mesh generation process in order to achieve a high numerical accuracy and to reduce the number of elements.

The sweep method begins by meshing a particular "source" surface using either the automatic global settings, or any local sizing controls/inflation layers that have been applied by the user; the source mesh is then swept through the body, spacing it by a certain incremental dimension or by splitting the swept side faces into a desired number of divisions. This method allows to have a regular and uniform mesh for the entire domain. In order to get an accurate prediction of windage losses and heat transfer coefficient, it is recommended for this kind of geometries to set 10 divisions at least in the radial direction [55].

Because of the narrow airgap in the case under investigation, in order to correctly model the critical near wall phenomena a total of 30 divisions were assigned in the radial direction with 15 further divisions for the stator slot opening and 150 divisions along the axial direction; Figure 4.37 shows the mesh generated which counted 1,237,500 elements for the 20° sector.

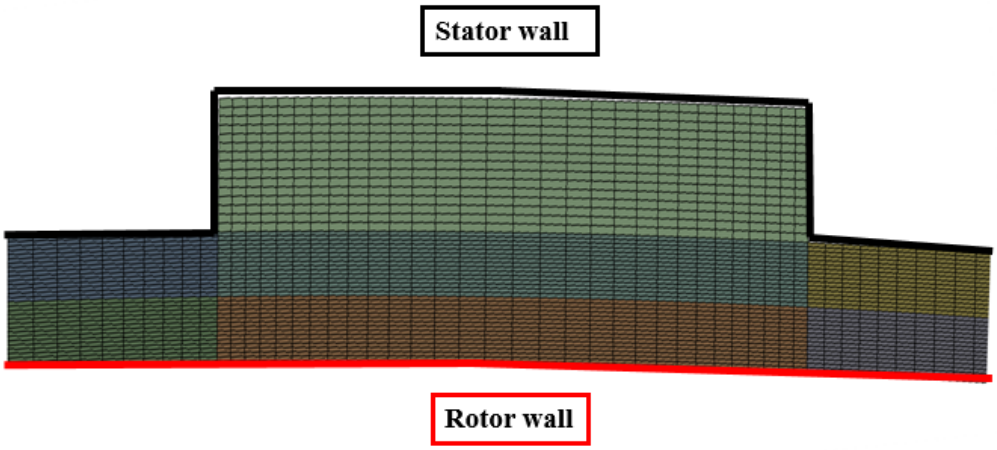


Figure 4.37: Airgap mesh

In this work several cases with different rotational speed (from 400 rpm to 1500 rpm) were considered in order to investigate the accuracy of the CFD model. The determination of the flow regime was based on the definition of the Taylor number (Equation 2.4, section 2.2.2) and to the thresholds values reported in Table 2.2 in section 2.2.2; the expected flow regimes for the case under investigation (laminar shear flow) are shown in Table 4.8 below.

Rotational speed [rpm]	Rotational Reynolds number	Taylor number	Ta/Fg
400	129.25	112.12	111.74
600	193.87	252.26	251.42
800	258.50	448.47	446.96
1000	323.12	700.73	698.38
1100	355.44	847.88	845.04
1200	387.75	1009.05	1005.67
1300	420.06	1184.24	1180.26
1400	452.37	1373.43	1368.83
1500	484.69	1576.65	1571.36

Table 4.8: Airgap flow regimes (laminar shear flow)

In order to validate the CFD model for the domain under investigation, the tangential velocity profile obtained from the different operating speeds was plotted along a line created in the middle of the airgap. As reported in Figure 4.38, the trend of the obtained normalised velocity v_{int}^* (Equation 4.2 – section 4.3.2) at rotational speed of 1500 rpm is in good agreement with a typical case of laminar tangential flow.

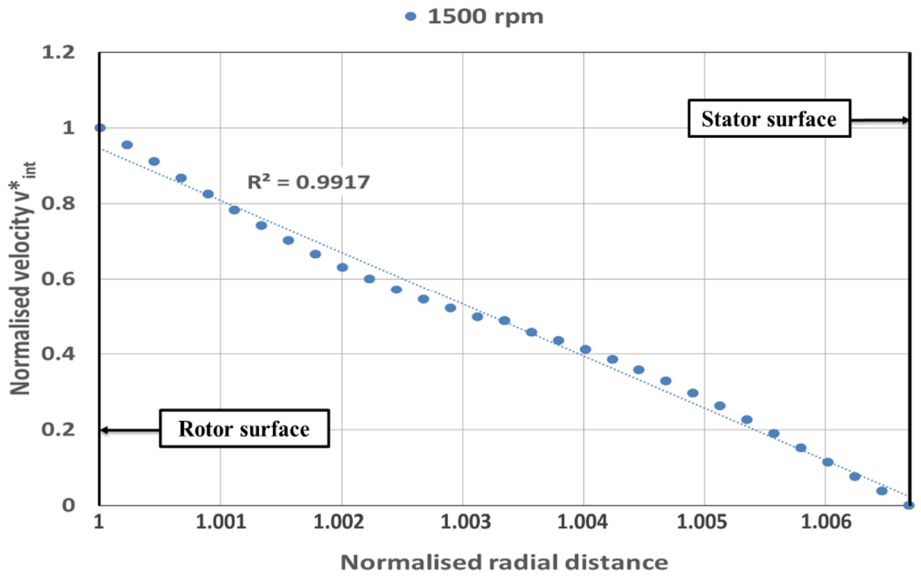


Figure 4.38: Normalised velocity profile across the slotted airgap at 1500 rpm

Also the windage loss, due to the relative motion between rotor and stator, was investigated and compared with analytical results calculated as discussed in section 2.3.3 (Equation 2.10). The aim of the investigation was to determine whether the surface roughness caused by the stator slot openings (Figure 4.39) affects the friction losses predictions in the airgap.

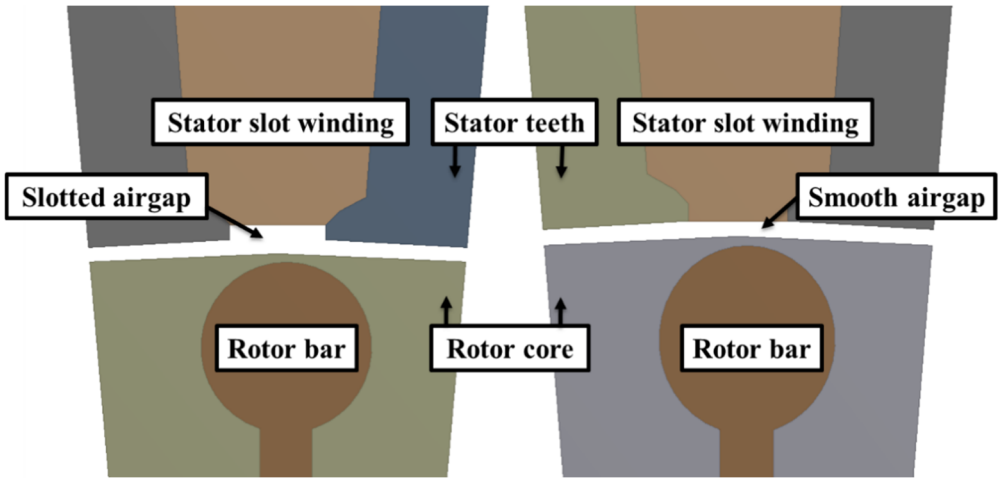


Figure 4.39: Open (left) and closed (right) stator slots

For this reason, CFD simulations of smooth and slotted airgaps were performed and the results of friction losses were computed and compared with analytical results ($P_{w,analytical}$) which were used to normalise the data P^*_w (Equation 4.8) presented below. The generated mesh in conjuction with the Enhanced Wall Treatment function adopted (y^+ value of about 1 – see Appendices, section B.2) allowed to achieve a good agreement between the two CFD models with analytical predicitons as shown in Figure 4.40.

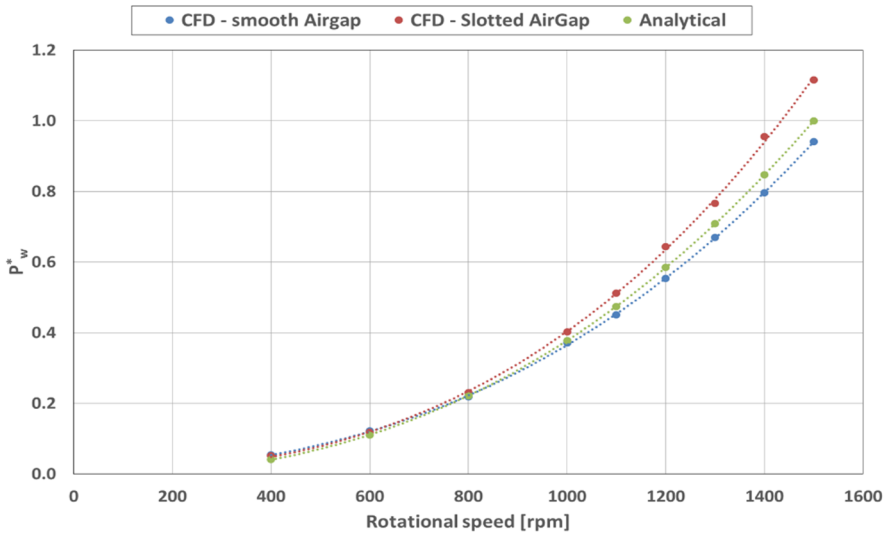


Figure 4.40: Non-dimensional windage power loss comparison: analytical and CFD (slotted and smooth airgap)

$$P_w^* = \frac{P_w}{P_{w,analytical}} \qquad 4.8$$

As expected the stator slot opening seems to slightly increase the friction losses in the airgap with increasing speed; the difference, however, is only marginal and, for the range of speeds under investigation, is below 10% compared with analytical results.

Figure 4.41 below reports the normalised velocity across the slotted airgap for the maximum and minimum speeds investigated; it can be seen how the stator slot openings have a marginal impact on the flow regime predictions in this region.

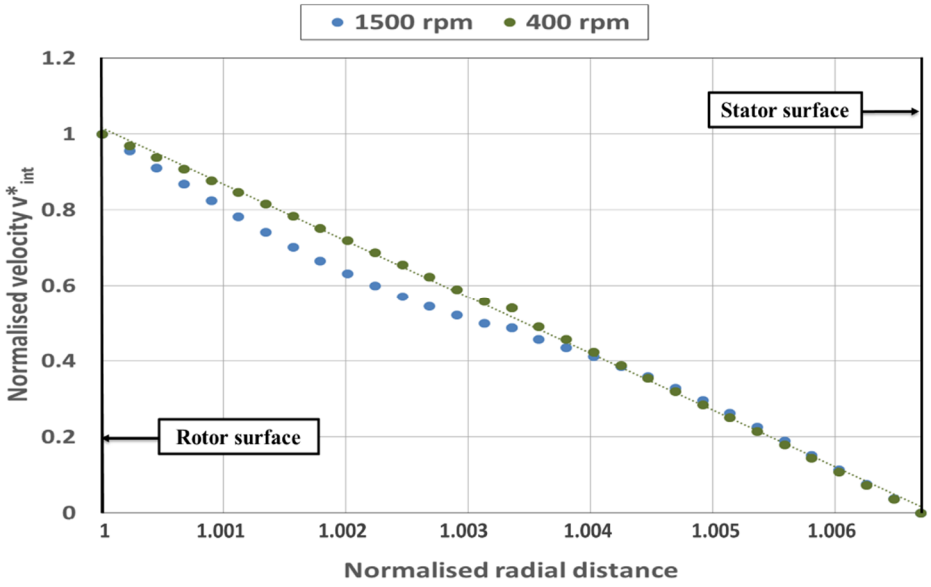


Figure 4.41: Normalised velocity profile across the slotted airgap at 1500 rpm and 400 rpm

The obtained results show that the model developed leads to a good level of accuracy, being capable of accurately resolving the fluid flow. The mesh developed for the airgap model was later used for the full 3D machine model which is described in Chapter 6.

Another important parameter to take into account and evaluate for the airgap domain is the heat transfer coefficient on the rotor surface. Constant temperatures were set at the rotor and stator side as boundary conditions: T_{rotor} and T_{stator} were set at 150°C and 100°C respectively, giving a reasonable gradient of 50°C between the two surfaces.

The heat transfer coefficient is calculated in Fluent by using Equation 4.9. $Q^{"}$ and T_w are the heat flux and the wall temperature respectively and they are computed or assigned as boundary condition; the reference temperature T_{ref} instead is set manually by the user.

$$h = \frac{Q^{"}}{T_w - T_{ref}} \qquad \textbf{4.9}$$

The selection of the reference temperature is a critical step, in [62] the airgap midstream temperature is taken whilst in [27] the stator bore temperature is used. Figure 4.42 shows the comparison between the heat transfer coefficients computed numerically and analytically. Analytical results were calculated with the correlation previously presented in Table 2.2 and reported below in Equation 4.10 and Equation 4.11 (Nusselt number definition).

$$Nu = \frac{2 \cdot \frac{g}{r_r}}{\ln(1 + \frac{g}{r_r})} \qquad \textbf{4.10}$$

$$h_{analytical} = \frac{kNu}{2g} \qquad \textbf{4.11}$$

The calculated analytical results ($h_{analytical}$) were then used to normalise the heat transfer coefficient results h_{rotor}^{*} presented below (Equation 4.12); as can be seen, a very good agreement is achieved when the stator bore temperature [27] is used as reference for the heat transfer coefficient.

$$h_{rotor}^{*} = \frac{h_{rotor}}{h_{analytical}} \qquad \textbf{4.12}$$

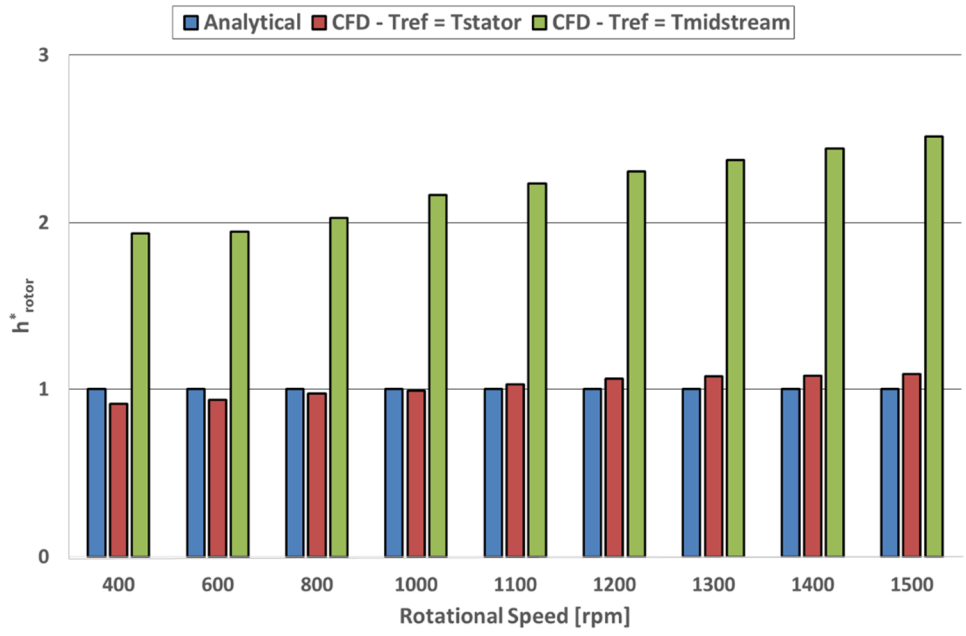


Figure 4.42: Heat transfer coefficient

4.4 Optimisation and improvements

One of the main targets of the present work was the identification of areas of improvement of the selected machine in terms of maximising the overall efficiency and minimising costs.

Temperature is a key factor which dictates the machine's efficiency: thermal management is crucial since the rise of temperature can significantly reduce the overall machine efficiency. Moreover, the temperature impacts the lifetime of the materials and in particular the insulation materials.

The main target in designing the end region of TEFC induction motors is to limit the end winding temperature and this is achieved by maximising heat transfer. The end region basically consists of two thermal resistances in series from the end windings to the external frame: these are the convective thermal resistance from the end windings to the enclosed air and the convective thermal resistance from the enclosed air to the external frame surface. In order to maximise the heat transfer it is therefore important to minimise, as much as possible, the thermal resistance offered by both the end windings and external frame.

After the fluid flow and thermal investigation of the end region carried out and discussed in section 4.3.1, two alternative cooling arrangements were considered and investigated.

The proposed internal cooling design consists of a shaft mounted fan at two different axial positions in the end region as shown in Figure 4.43 and Figure 4.44; considering that the TEFC machine under investigation can rotate in clockwise and anti-clockwise direction, the stirrers were designed in order to work the same in both directions.

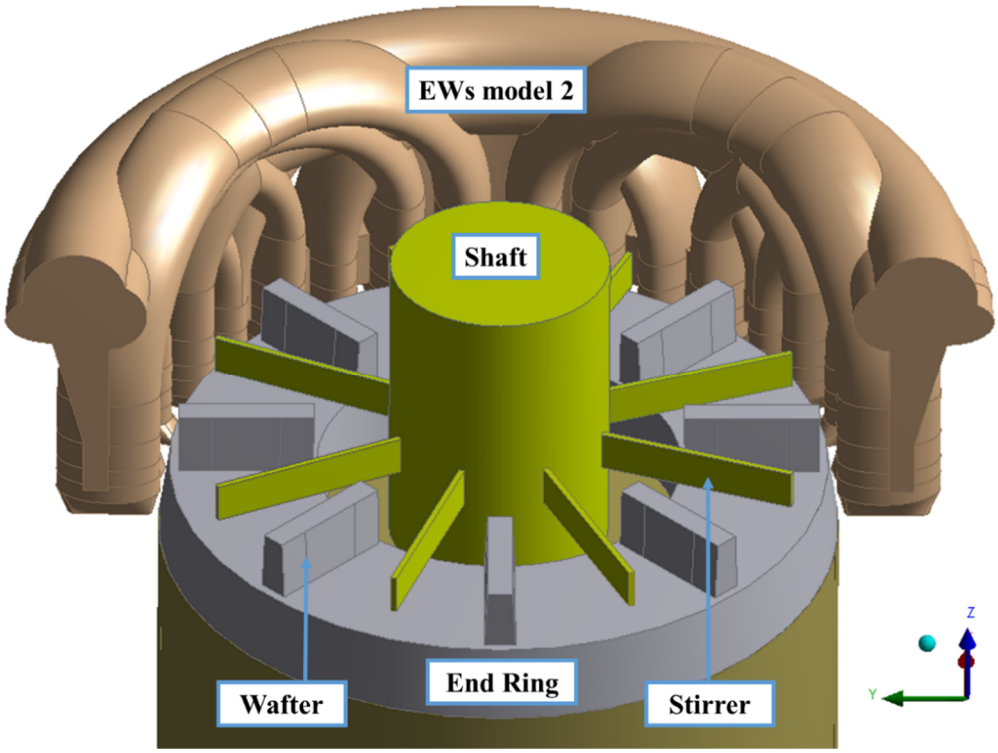


Figure 4.43: Stirrers model 1

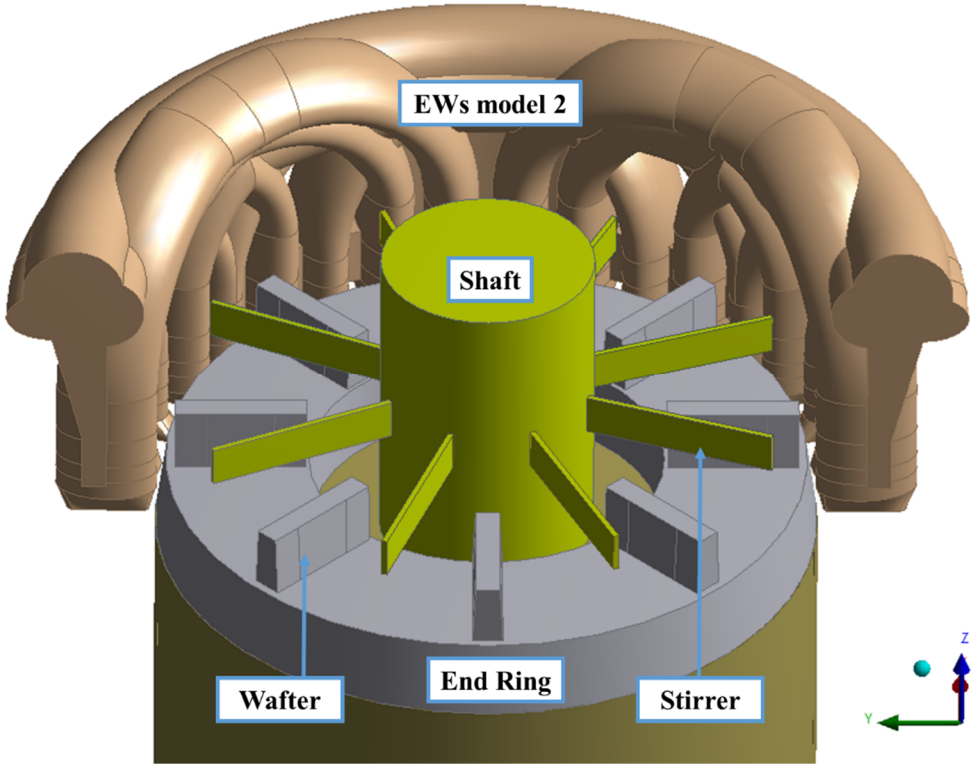


Figure 4.44: Stirrers model 2

The stirrers shown in Figure 4.43 were axially aligned with the end ring's wafters while in the second cooling arrangement in Figure 4.44 they were located 10 mm above the wafters; both cooling arrangements were created using Ansys Design Modeller and Figure 4.45 below reports the geometrical dimensions of the shaft mounted stirrers.

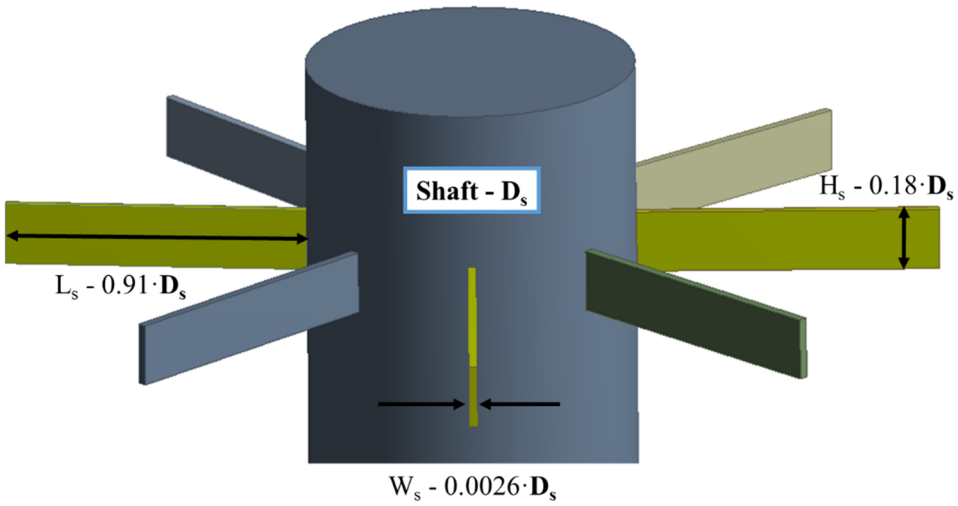


Figure 4.45: Stirrers geometrical details

The proposed internal cooling design was based on previous works carried out by Micallef and Saliba [15, 50, 54] where similar cooling arrangements were employed in the end region of TEFC induction machines and CFD was successfully used to locally investigate whether improvements in end windings cooling could be achieved. Their results show how the overall heat transfer coefficient in the end region was increased compared with the conventional wafter configuration as well as the windage losses which is function of the wafter/stirrers diameter. Windage losses can affect the overall efficiency and therefore they should not be neglected when designing an electrical machine.

However, the impact of locally improved thermal performance and increased windage losses on the machine as a whole was not considered in those previous works.

A local CFD investigation, similar to the one described in section 4.3.1, was then carried out in order to investigate the impact of the proposed internal cooling designs on the fluid flow and thermal behaviour of the end region of the machine under investigation.

The simplified housing geometry and the EWs model 2 presented in the previous sections were used to generate the 3D model of the fluid end region; results of airflow velocity and heat transfer were computed and compared with the case with conventional wafters. Similarly to section 4.3.2.1 and 4.3.2.2, the primary swirling flow and the secondary flow were investigated; Figure 4.46 and Figure 4.47 below show the location of the axial and radial planes used to plot the velocity airflow distribution and magnitude in the end region for the cases under investigation. The axial plane was created at an angular location of 25° in order to better show the impact of the stirrers on the secondary airflow of the end region; the radial plane was located 25 mm above the end ring.

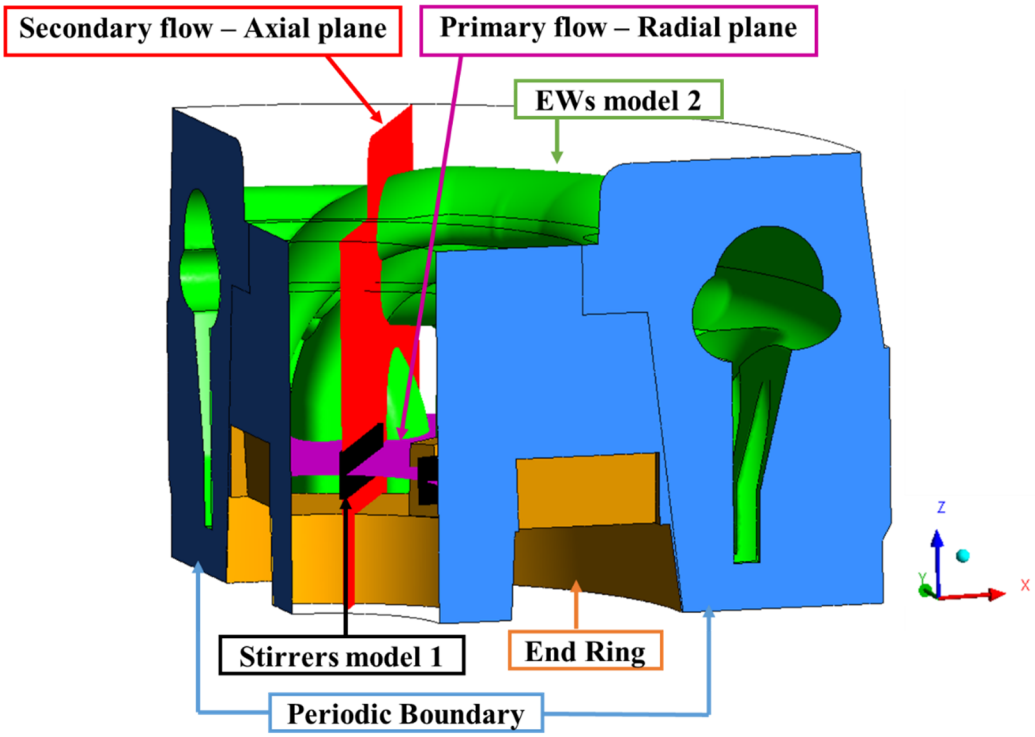


Figure 4.46: Stirrers model 1 - axial and radial plane

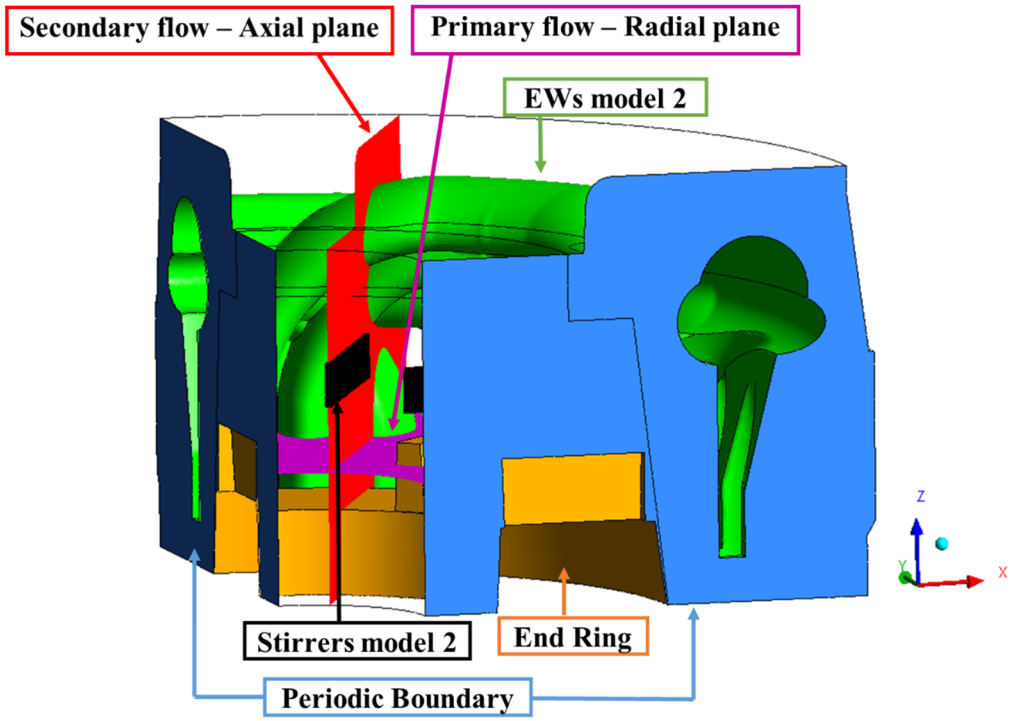


Figure 4.47: Stirrers model 2 - axial and radial plane

4.4.1 Stirrers model 1

CFD results of airflow velocity and heat transfer allowed the impact of the proposed cooling design on the end region thermal performance to be assessed.

Figure 4.48 and Figure 4.49 show the non-dimensional vector velocity plot of the primary swirling flow on the radial plane of the end region for the case with the original and proposed cooling design respectively As can be seen from results, the mounted shaft stirrers have a sensible impact on the airflow velocity magnitude in the end region; in particular, higher velocities in proximity of the wafters and end windings surfaces are achieved.

The impact of the Stirrers model 1 can also be seen from the comparison between Figure 4.50 and Figure 4.51; a non-dimensional vector velocity plot of the secondary airflow for the original and proposed cooling design models is reported respectively. The presence of shaft mounted stirrers aligned with the conventional wafters causes an overall stronger fluid flow recirculation in the end region. This factor has a beneficial impact on the thermal behaviour of the end region; a rise of the heat transfer coefficient on the end windings and external frame surfaces is achieved.

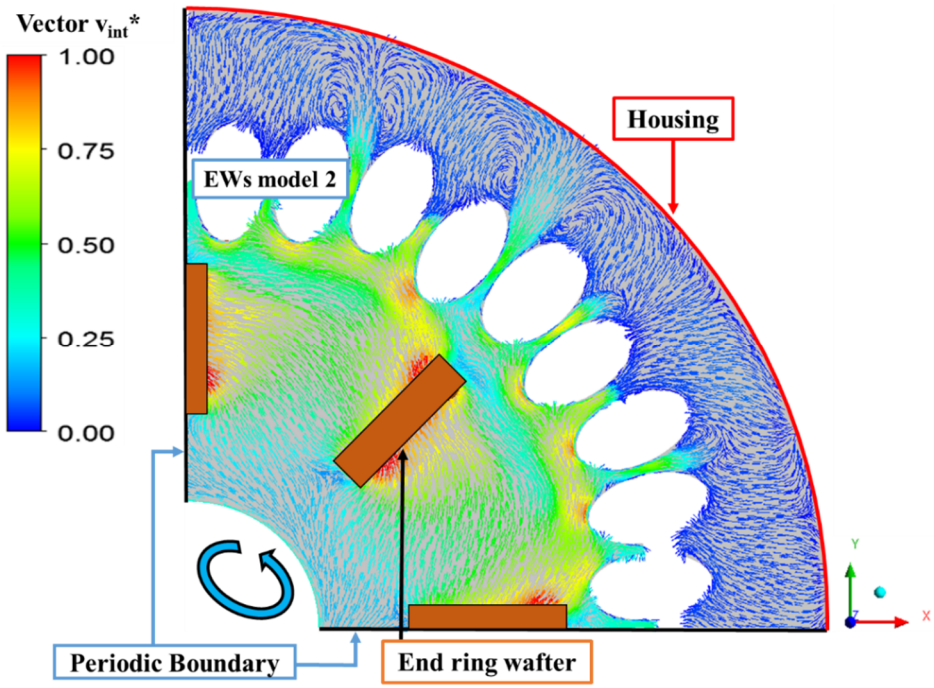


Figure 4.48: End region primary swirling flow,EWs 2, original cooling design – $v^*_{int} = v/v_{rotor\ tip}$

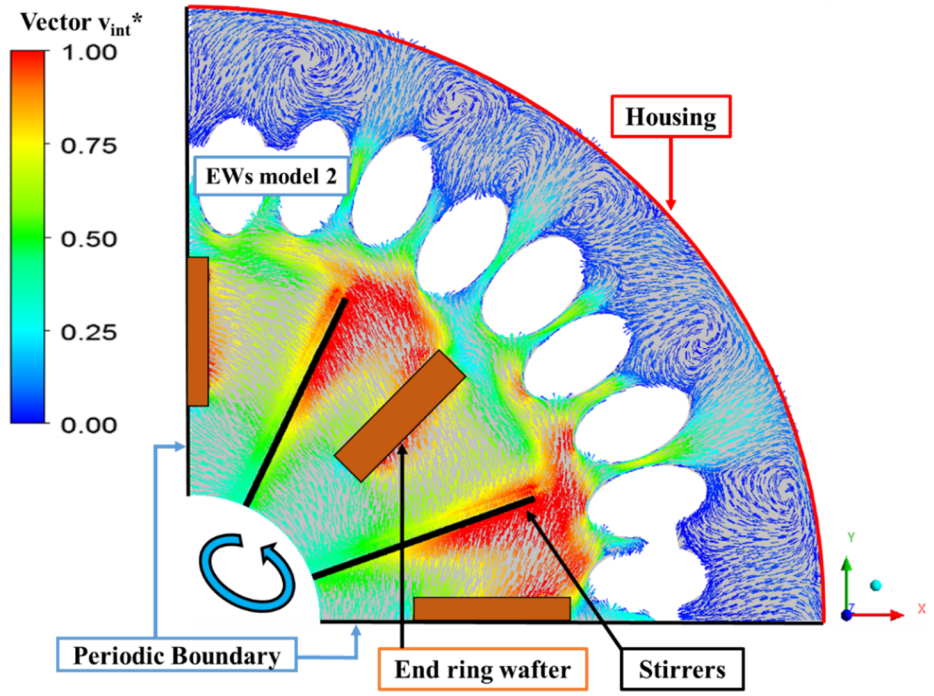


Figure 4.49: End region primary swirling flow,EWs 2, Stirrers Model 1 – $v^*_{int} = v/v_{rotor\ tip}$

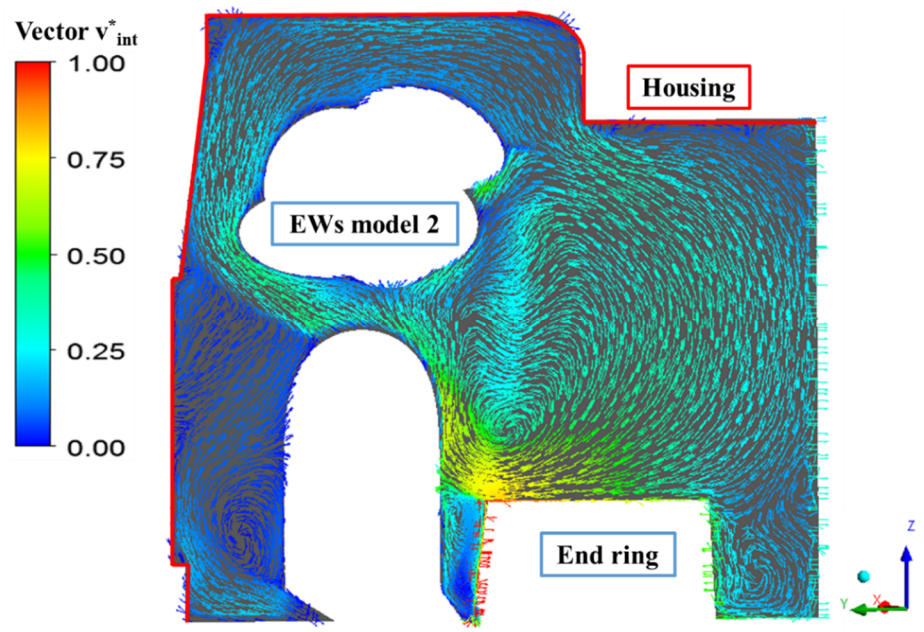


Figure 4.50: End region secondary flow, original cooling design – $v^*_{int} = v/v_{rotor\ tip}$

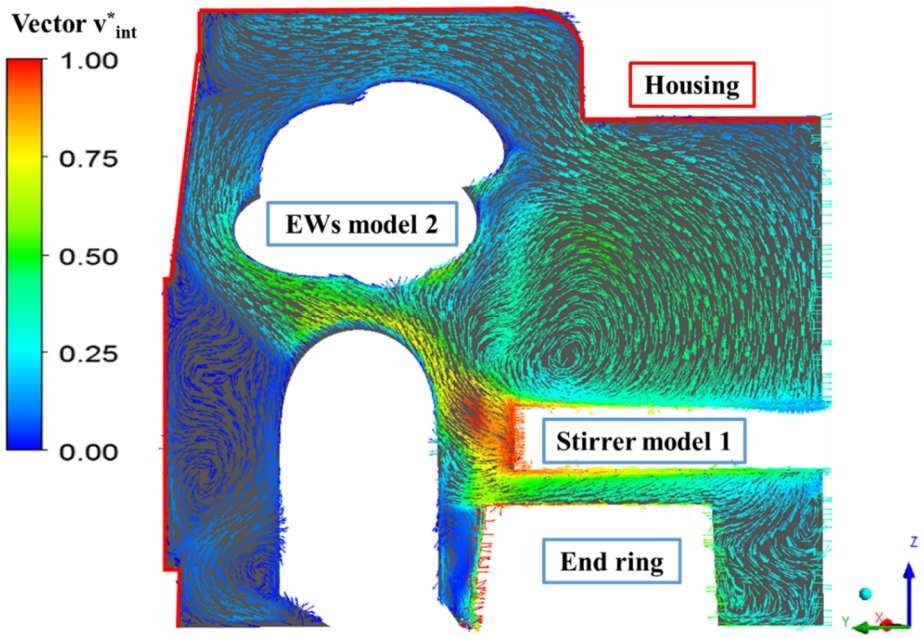


Figure 4.51: End region secondary flow, Stirrers Model 1 – $v^*_{int} = v/v_{rotor\ tip}$

Table 4.9 below shows the average heat transfer coefficient computed on the end windings and external frame surfaces for the two cases considered; in both models the reference temperature used was the average air temperature inside the end region. The value of heat transfer coefficient computed on the end windings surface with the original cooling design ($h_{EWs,original\ design}$)was used to normalise the results (Equation 4.13) presented below and the percentage differences are calculated as in Equation 4.14.

	Original design	**Stirrers Model 1**	**% difference**
h^*_{ews}	1	1.06	+ 6.1
h^*_{frame}	0.76	0.87	+ 13.3

Table 4.9: Heat transfer coefficient, End region comparison, Stirrers Model 1

$$h^* = \frac{h}{h_{EWs,original\ design}} \qquad \textbf{4.13}$$

$$\%\ difference = \frac{|h_{(Stirrers\ 1)} - h_{(original\ design)}|}{\frac{1}{2}\cdot(h_{(Stirrers\ 1)} + h_{(original\ design)})} \cdot 100 \qquad \textbf{4.14}$$

Results show how the introduction of the stirrers as depicted in Figure 4.43 affects positively the thermal performance of the end region: in accordance with Micallef and Saliba investigation, an increase of the heat transfer coefficient of end windings and frame surfaces is achieved. This latter result leads to a reduction of the convective internal thermal resistance between end windings and external frame of about 12%.

As expected though, the proposed cooling design introduced also a rise of windage losses by up to 20% compared to the case with conventional wafters.

4.4.2 Stirrers model 2

The second proposed cooling design (Stirrers Model 2, Figure 4.44), consisting of shaft mounted stirrers located 10 mm above the end ring's wafters was numerically investigated as described in section 4.4.1 with Stirrers Model 1.

Figure 4.52 reports the non-dimensional vector velocity plot of the primary swirling flow on the radial plane (depicted in Figure 4.47) for the proposed cooling design case. In comparison with Figure 4.48 (original cooling design) the primary flow is only marginally affected by the shaft mounted stirrers placed above the considered plane. Slightly lower velocities in proximity of wafters and end windings surfaces can be seen with the proposed cooling design.

The negative impact of Stirrers Model 2 arrangement can be better seen in Figure 4.53 where the non-dimensional vector velocity plot of the secondary flow in the end region is reported. In comparison with the original cooling design (Figure 4.50) and the Stirrers Model 1 (Figure 4.51), it can be seen how the stirrers in this case are interfering with the recirculating toroidal vortex flow located in the area between the end winding and the end ring. The overall velocity magnitude of the toroidal vortex is reduced and this affects the airflow velocity distribution around the end windings and external frame walls.

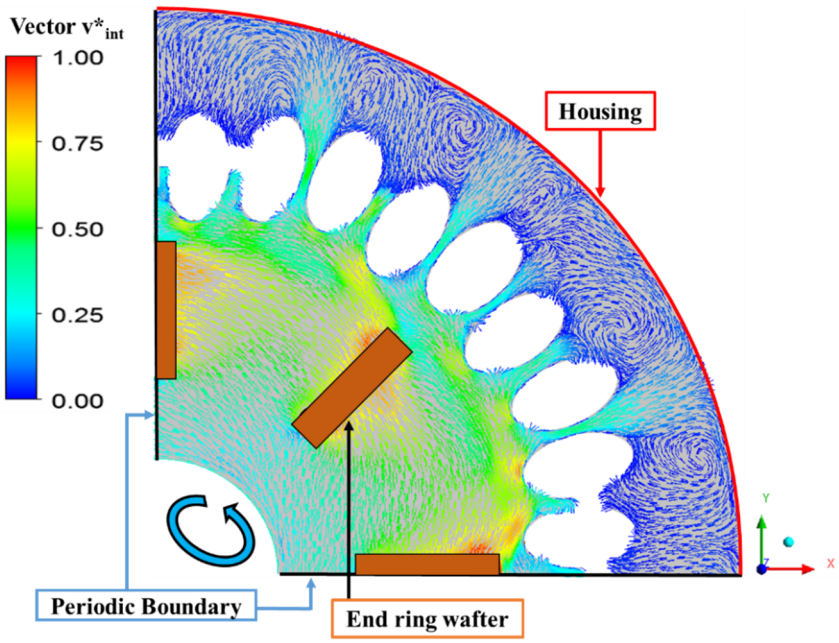


Figure 4.52: End region primary swirling flow,EWs 2, Stirrers Model 2 – $v^*_{int} = v/v_{rotor\ tip}$

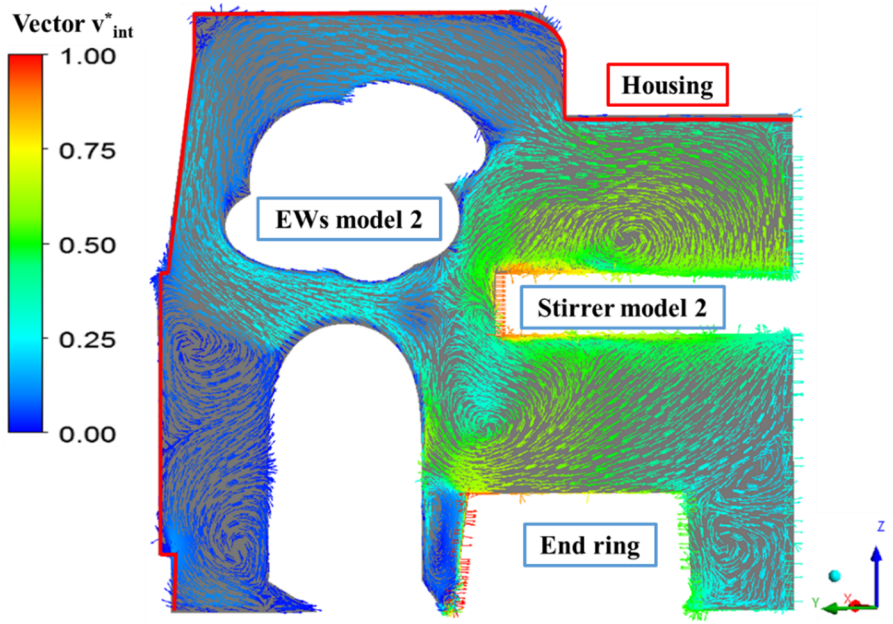


Figure 4.53: End region secondary flow, Stirrers Model 2 – $v^*_{int} = v/v_{rotor\ tip}$

The impact on the thermal behaviour of the end region can be seen on Table 4.10 below, where a comparison of the computed average heat transfer coefficients for end windings and external frame surfaces is reported; the reference temperature used was again the average air temperature inside the end region. The value of heat transfer coefficient computed on the end windings surface with the original cooling design was used to normalise the results (Equation 4.13) presented below and the percentage differences are calculated as in Equation 4.14.

	Original design	**Stirrers model 2**	**% difference**
h^*_{ews}	1	0.84	- 17.2
h^*_{frame}	0.76	0.72	- 5.1

Table 4.10: Heat transfer coefficient, End region comparison, Stirrers Model 2

In comparison with the results from section 4.4.1, the same designed stirrers shifted 10 mm in the axial direction do not lead to thermal improvements of the end region; due to the weaker airflow recirculation, there is a decrease of the overall heat transfer coefficient in the end region which lead to an overall rise of the convective thermal resistance from the end windings to the enclosed air and the convective thermal resistance from the enclosed air to the external frame surface of about 10%.

Similarly to the Stirrers Model 1 case, the windage losses increase by up to 20% compared to the case with conventional wafters. To conclude, results presented in this section shows how the Stirrers Model 2 arrangement leads to several drawbacks both from the fluid flow and thermal point of views; therefore this model was not considered for further investigation using the full 3D conjugate model of the TEFC machine presented in Chapter 6.

4.5 Summary

Computational Fluid Dynamics is one of the most versatile technique used to investigate fluid flow and thermal problems on very complex geometries with a high degree of details and flexibility. However, the processes of domain creation, simulation set up and running time can be very expensive from the computational point of view.

In order to reduce the computational cost of the numerical modelling of the electrical machine under investigation, the approach adopted in this work was based on the separate modelling, and local fluid flow and thermal investigations, of limited sectors of the most critical regions of the internal domain: end region and airgap.

A new modelling approach for a more realistic end windings representation, which potentially can be applied also to different type of machines, was developed and presented; the new geometry has comparable topology and dimensions with the real end winding geometry of the motor under investigation.

Results from the comparison with a simplified end winding geometry show how a more geometrically accurate and detailed representation can significantly affect the prediction of the local complex thermal phenomena occurring in the end region; in particular, the heat dissipation rate from the end windings and through the outer housing increase up to 62.26% and 45.6% respectively with EWs model 2.

In addition, in order to reduce the end winding temperature and maximise heat transfer in the end region, a cooling design based on previous works on TEFC machines was proposed and investigated. CFD results are in agreement with literature and they show how the introduction of shaft mounted stirrers axially aligned to the end ring wafters (Stirrers Model 1) can lead to a rise of the heat transfer coefficients of end windings and frame surfaces and therefore to an

overall 12% reduction of the thermal resistance between the two surfaces, on the other hand a 20% rise of the windage losses was also computed.

The modelling approach and mesh configurations for the internal domain were used in the full 3D conjugate model of the TEFC machine as described and discussed in Chapter 6; the simplified housing wall was used to reduce the computational cost and EWs Model 1 was implemented within the full CFD conjugate model instead of the simplified geometry provided by the manufacturer.

The impact of the different end windings porosity (EWs model 1 and 2) on the overall thermal predictions of the machine is investigated and presented in Chapter 7.

The full 3D conjugate model was used also to evaluate the impact on the overall thermal performance of the selected TEFC machine due to the proposed Stirrers Model 1 arrangement of the end region: this is presented and discussed in Chapter 7.

5 Machine thermal modelling: external domain methodology

5.1 Introduction

The aim of this chapter was to identify the best modelling approach for the external domain, identifying critical areas and optimising the computational cost. The lessons learnt from the internal domain (Chapter 4) were built upon in this chapter.

This chapter provides a detailed description of the numerical modelling of the machine external fluid domain; this was mainly focused on an accurate modelling of the external cooling fan and the airflow distribution around the external housing. A description of the domain analysed, meshing approach and solver set-up is provided in the following sections.

In addition, alternative geometries for the external fan and fan cover were considered to improve the thermal performance of the external cooling.

The modelling approaches and the developed methodology presented in Chapter 4 and 5 were then combined to generate a full 3D conjugate thermal model of the selected TEFC machine to accurately predict the thermal performance as shown in Chapter 6.

5.2 Complexity of the model and geometrical simplifications

Several geometrical simplifications of the external housing were made in order to obtain a suitable geometry for the CFD model by reducing the complexity of the geometry features; those simplifications allowed the reduction of the cell count and the associated computational cost.

Simplifications were made where a geometry feature does not affect the airflow or thermal behaviour of the machine significantly to justify an increased cell count. Figure 5.1 below shows a comparison between the original and simplified geometry of the external housing.

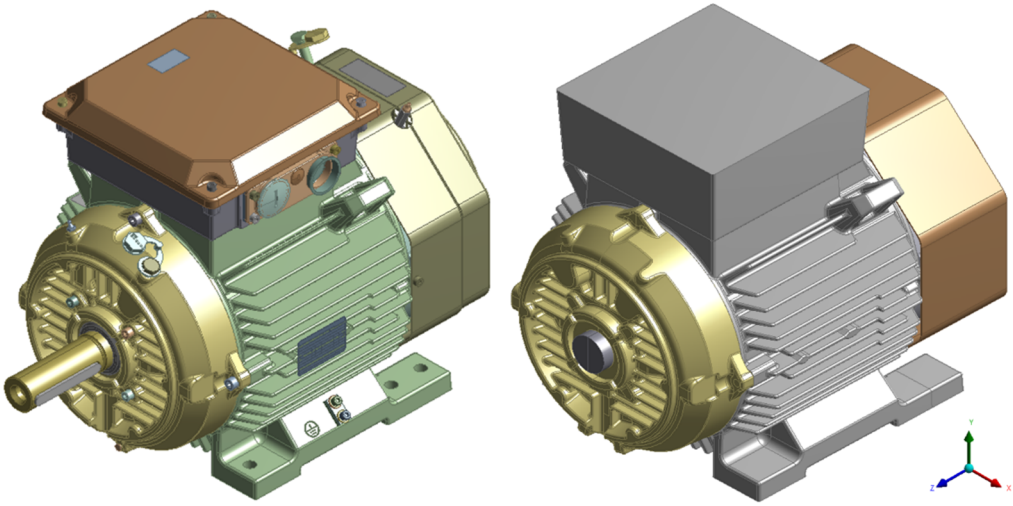


Figure 5.1: Geometrical simplifications, external housing

All the nuts and bolts were removed and their holes filled; the electrical connections coming from the terminal box were neglected.

The TEFC motor is cooled by blowing air over the finned frame with an external fan mounted on the rear shaft; Figure 5.2 and Figure 5.3 show a schematic representation of the external air cooling and the model of the radial fan employed on the motor under investigation; the rotor diameter is used to normalise the fan diameter.

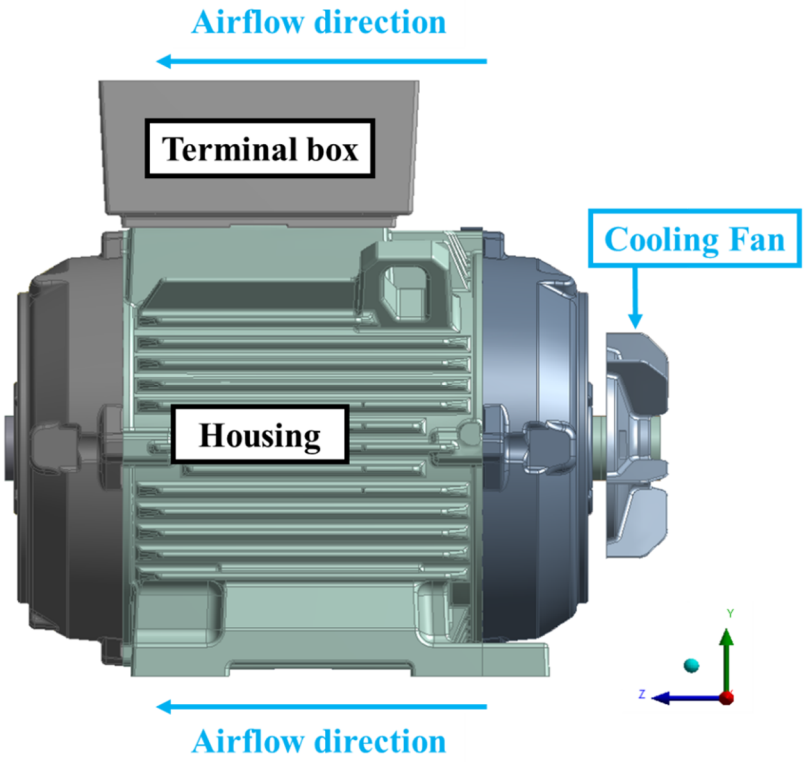


Figure 5.2: TEFC motor external air cooling (fan cover removed)

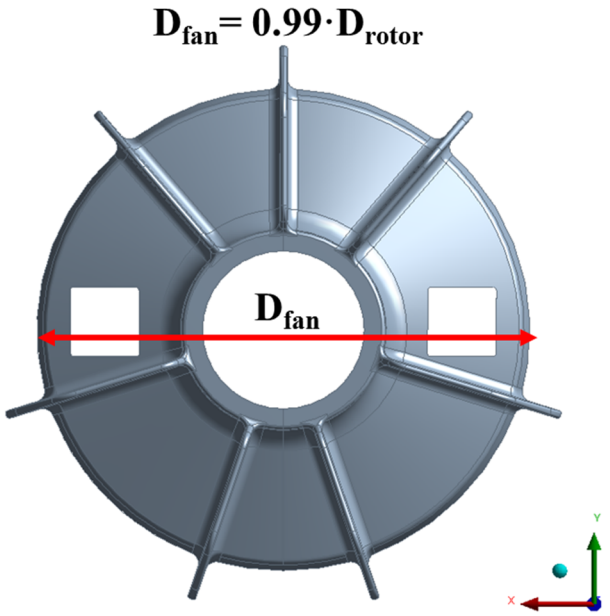


Figure 5.3: External radial cooling fan

As the heat removal is strongly dependent on the external cooling, an accurate modelling of the external fan and the forced airflow around the housing was essential in order to investigate the thermal performance of the selected TEFC machine. In order to reduce the computational cost associated with the fan modelling without excessively altering its original design, geometrical features of the back plate of the fan were neglected as their impact on windage losses and mass flow rate predictions were not significant. A comparison between the original and simplified geometry is reported in Figure 5.4; the internal surface of the back plate was smoothed using Ansys Design Modeller.

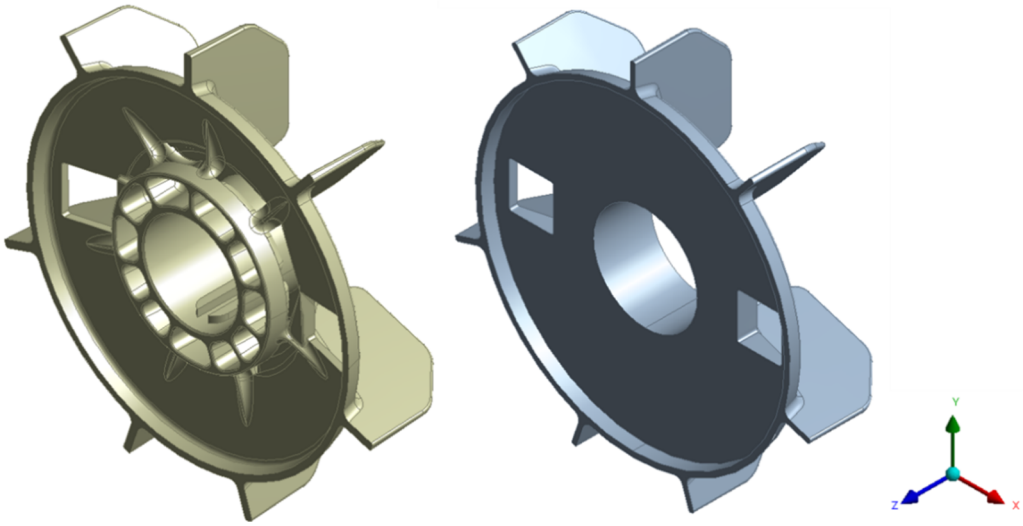


Figure 5.4: External radial fan, backplate simplification

In order to model an external domain with conditions similar to the real laboratory environment as possible the steel platforms, where the motor was located as reported in section 3.1, were created and included in the external housing domain as shown in Figure 5.5.

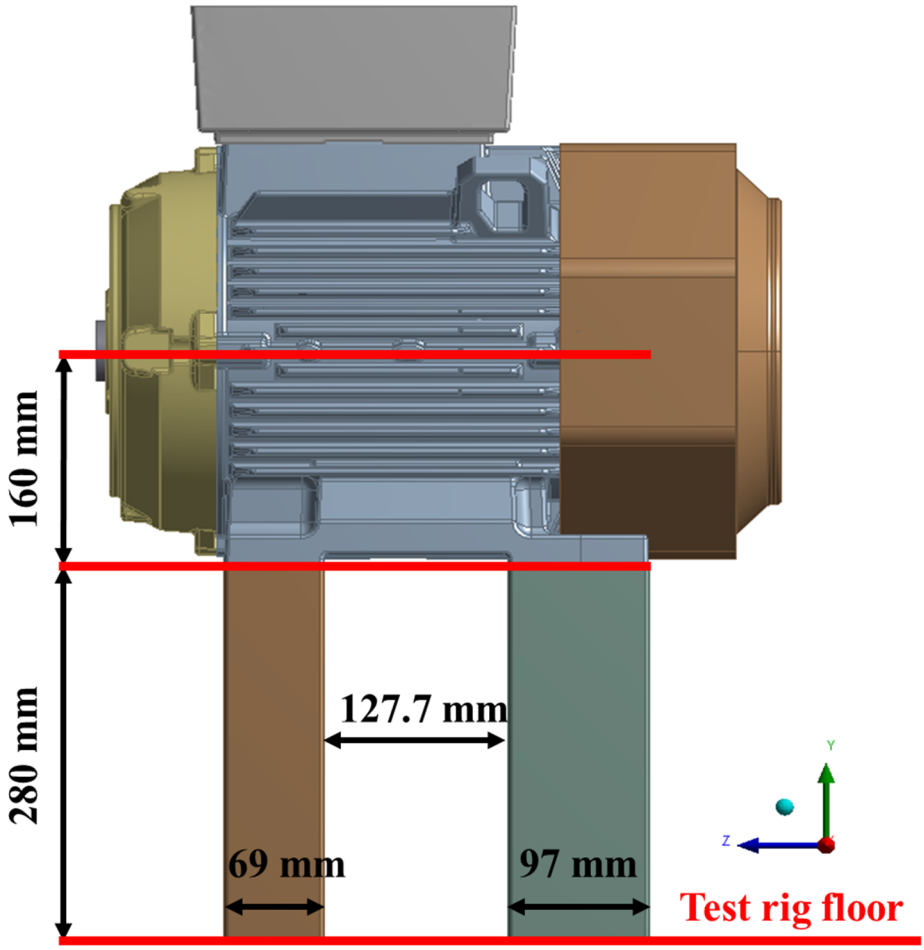


Figure 5.5: External solid domain, housing and platforms

The solid domain reported in Figure 5.5, which also includes the cooling fan shown in Figure 5.2, was used to model the external fluid domain. The machine geometry was used as the solid surface from which the external fluid domain grew; this is discussed and described in more details in following section 5.3.

5.3 Domain analysed

The development of a full 3D thermal model of the selected TEFC machine required an accurate investigation of the external forced airflow. A hemispherical fluid domain was created using Ansys Design Modeller in order to model the laboratory space around the machine as shown in Figure 5.6 and Figure 5.7; the external fluid domain walls had to be located sufficiently far away from the motor external housing walls to avoid interfering with the motor's air cooling from the fan. An initial external fluid domain (highlighted in green in Figure 5.6) was considered; however the domain walls were still too close to the TEFC motor walls and this did not allow the airflow to circulate freely in the external environment which could lead to unaccurate predictions of the mass flow rate at the fan inlet. Therefore, in order to avoid any kind of interference to the external airflow, a double sized external hemispherical fluid domain was modelled.

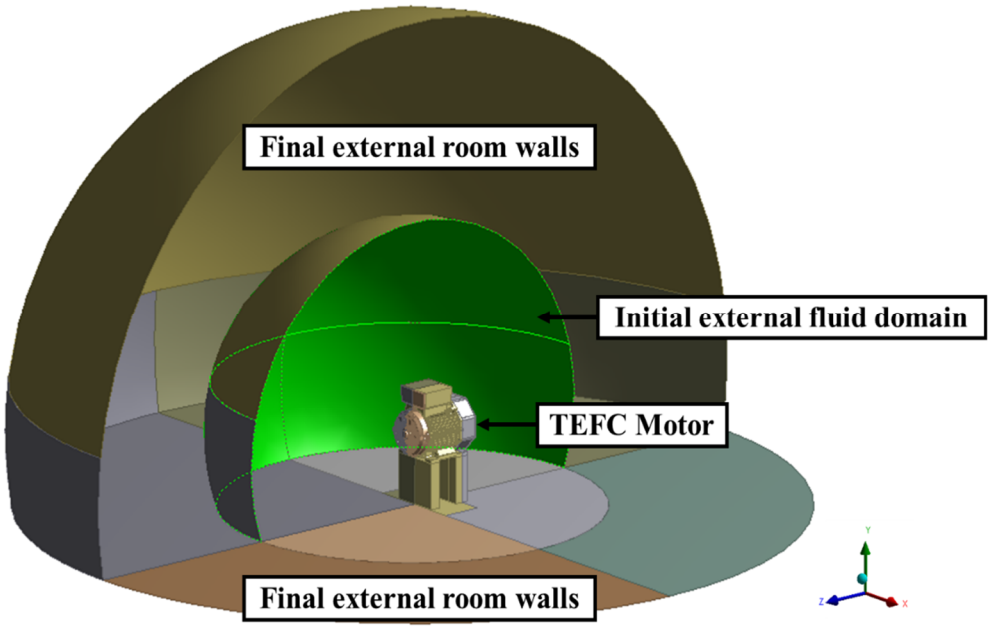


Figure 5.6: External hemispherical fluid domain

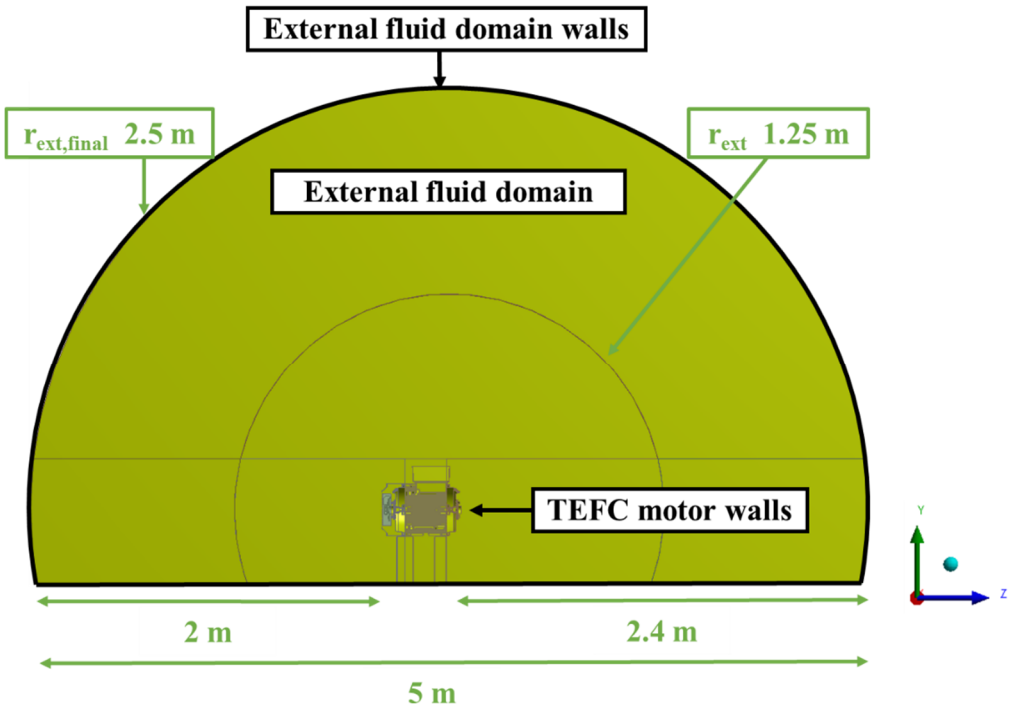


Figure 5.7: External hemispherical fluid domain dimensions

CFD was then utilised to investigate the external airflow fields present around the housing; the Multiple Reference Frame (MRF) approach was used in order to simulate the rotation of the external cooling fan around the z-axis at the rotational speed of 1500 rpm. The hemispherical fluid region shown in Figure 5.7 was split into 8 sub-regions or reference frames: one containing the rotating fan (Ext Fan) with the others set as stationary reference frames as depicted in Figure 5.8 and Figure 5.9, where the negative of the motor solid domain can be better visualised. The hemispherical domain consisted of 1 fluid regions around the fan (Ext Fan) and the finned frame (Ext Frame) respectively, 2 fluid regions on the Drive End (Ext DE 1 and Ext DE 2) and Non Drive End (Ext NDE 1 and Ext NDE 2) sides respectively and 2 top fluid regions above the machine's terminal box (Ext Top 1 and Ext Top 2).

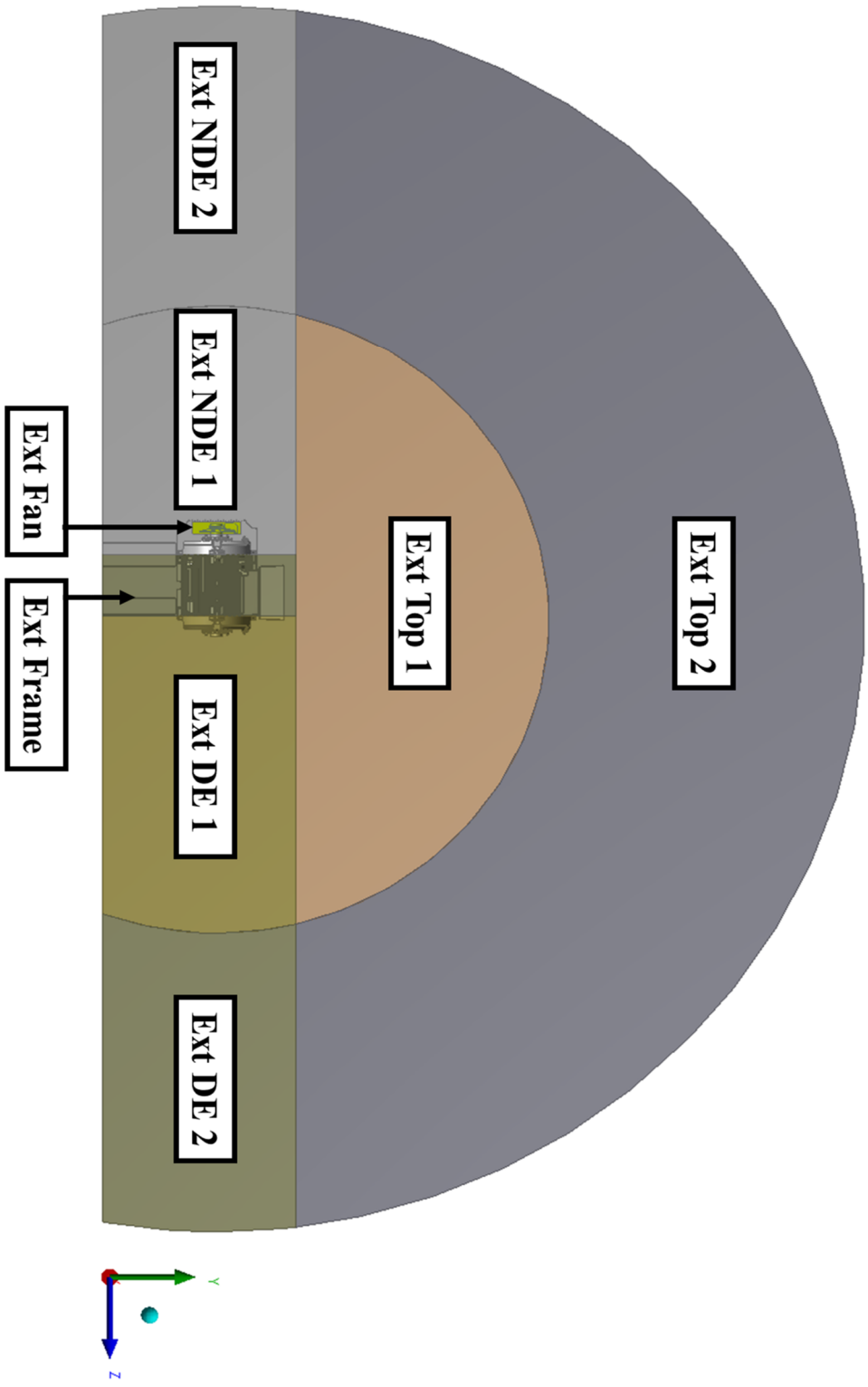


Figure 5.8: External fluid domain sub-regions – Ext Fan set as rotating frame

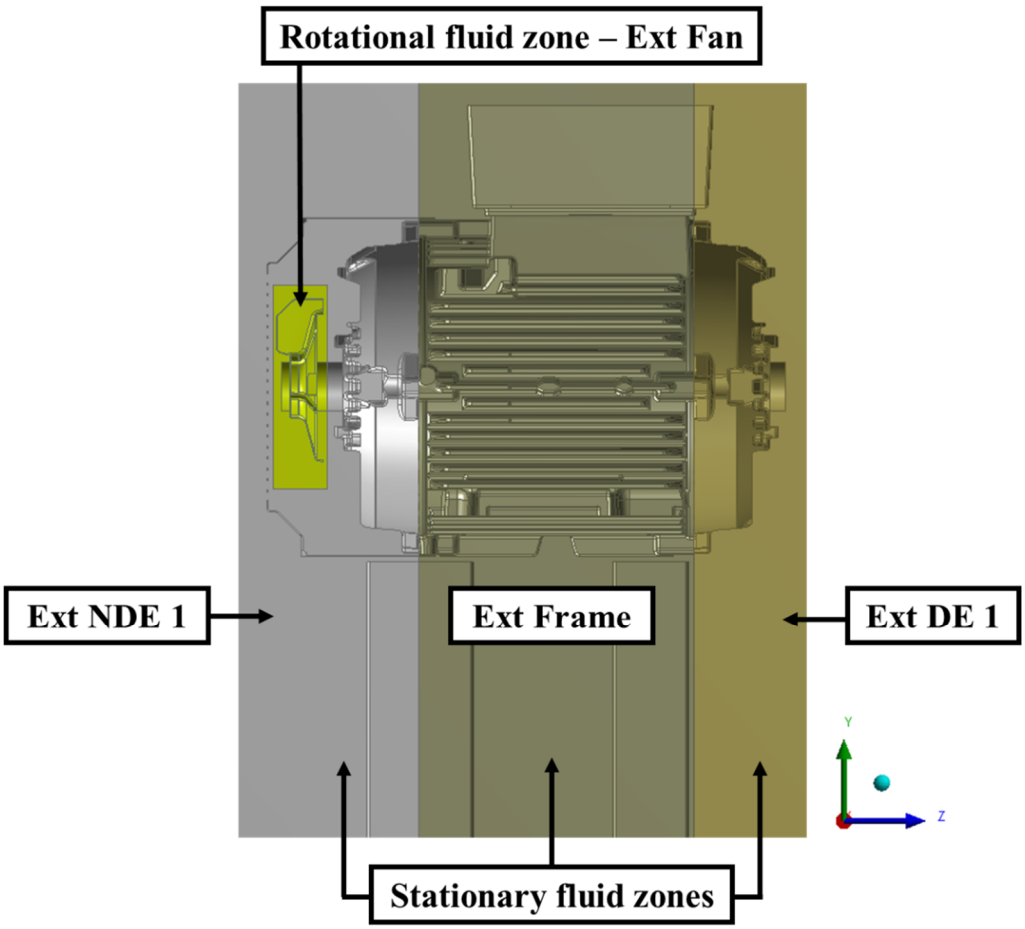


Figure 5.9: External fluid domain, MRF approach

In order to reduce the cell count and its associated computational cost and time, a 180° model of the hemispherical external domain was initially considered to model the external airflow distribution; this was possible due to the geometrical symmetry of the machine and cooling fan as shown in Figure 5.10.

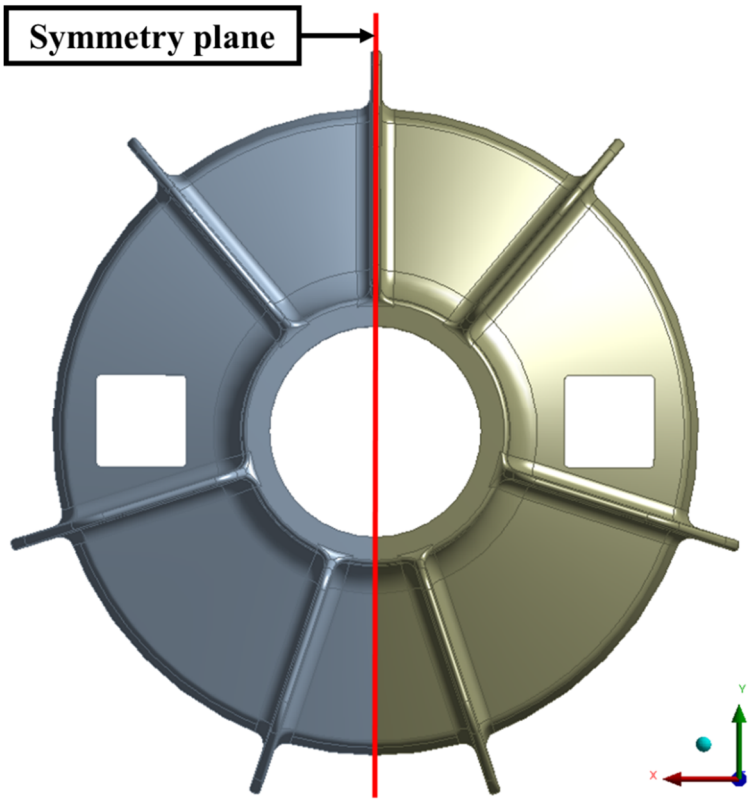


Figure 5.10: Fan symmetry

The validity of this assumption was then investigated by also modelling a full 360° geometry of the external domain: results of airflow velocity distribution and magnitude from both cases were then computed and compared as reported in section 5.3.1.

Tetrahedral elements were used to generate a suitable mesh for the external domain due to their capabilities to deal with complex surfaces and efficient growth into open spaces; local mesh refinements of 1.5 mm and 0.5 mm were adopted on the housing and fan blades walls respectively in order to capture the near-wall phenomena where higher velocity and pressure gradients were expected.

In order to let sub-regions communicate to each other, the walls at the interface should be manually paired if a non-conformal mesh is created between them: non-conformal interfaces require interpolation of data between different cell zones which increase the computational cost.

In this case, for a higher numerical accuracy, a conformal mesh was used due to its efficient passing of data across the interfaces thanks to the boundary nodes aligned at the same point on either side of the cell zone interfaces; when a conformal mesh was created the sub-regions were automatically paired with an interior interface.

The generated mesh is shown in Figure 5.11; it can be noted how the mesh was kept coarser in the regions far from the motor walls as no high velocity and pressure gradients were expected in those areas. On the other hand, local mesh refinements on the mid-air interfaces where performed in order to better capture the air flow velocity and distribution in proximing of the housing walls.

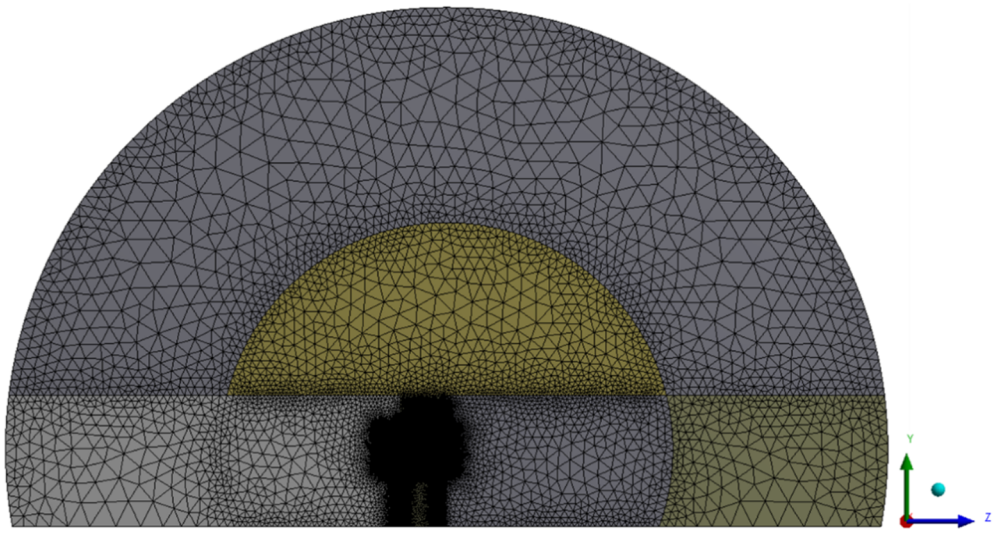


Figure 5.11: External fluid domain mesh

Table 5.1 below lists the cell count of the generated meshes per sub-region of the external fluid domain.

	Cell count	
Zone name	**180° model**	**360° model**
Ext Fan	2,410,408	5,483,735
Ext Frame	4,581,344	7,905,054
Ext DE 1	1,133,854	2,347,854
Ext DE 2	84,558	169,364
Ext NDE 1	1,509,053	3,134,795
Ext NDE 2	84,058	167,610
Ext Top 1	184,325	328,145
Ext Top 2	284,200	568,445
TOTAL	**10,271,800**	**20,105,002**

Table 5.1: External fluid domain cell count, refer to Figure 5.8 for naming of zones

As for the fluid flow investigation of the internal domain reported in section 4.3, the realizable k-ε turbulence model was implemented since it can generally provide better performance than the standard k – ε model [56]; standard residual plots of mass, velocities, turbulence quantities, monitors of local velocity and torque were used to assess convergence.

The PC running the simulations was a 3.70 GHz Intel Xeon Quad core CPU with 64GB RAM running the Windows 7 64-bit operating system; the numerical solution was computed in 1 day for the 180° external fluid domain case while 2 days were necessary for the 360° case.

5.3.1 180° and 360° external model - CFD results

A CFD investigation of the external fluid domain was carried out both for the 180° and 360° model. Results of airflow velocity and its distribution around the housing were computed and compared to identify the best modelling approach and to verify that the cooling fan was correctly being modelled. Numerical results of velocity are presented in a non-dimensional format: the tangential velocity of the cooling fan ($v_{original\ fan\ tip}$) was used to normalise the results of v^*_{ext} as in Equation 5.1.

$$v^*_{ext} = \frac{v}{v_{original\ fan\ tip}} \qquad \textbf{5.1}$$

The post-processing of results was carried out using Ansys CFD-Post; contour plots of velocity and results of mass flow rate were used to investigate and compare the airflow behaviour around the machine. Two main radial planes along the axial direction were created in order to plot the airflow velocity as shown in Figure 5.12; another plane was also created over the fan cover grid holes to compute the mass flow rate at the fan inlet.

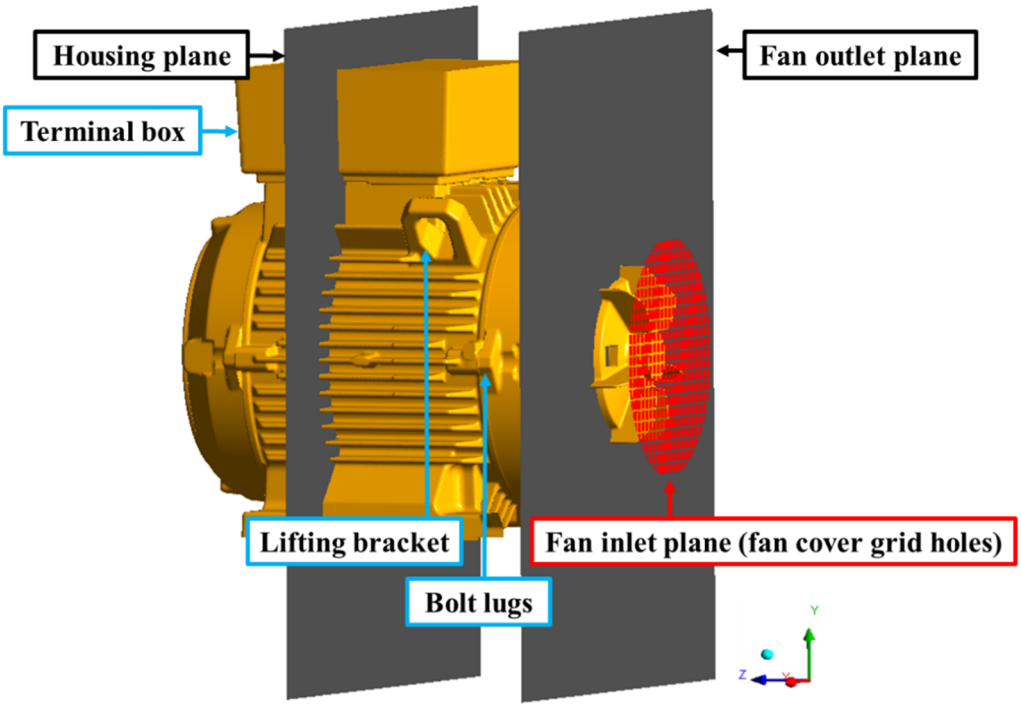


Figure 5.12: Radial planes along axial direction

The contour plot of velocity on the fan outlet plane was computed to verify if the cooling fan could be correctly modelled using the 180° model and therefore reduce the computational cost of the CFD model. Figure 5.13 and Figure 5.14 report the non-dimensional airflow velocity results plotted on the fan outlet plane for the 180° and 360° model respectively.

Considering the rotational speed of 1500 rpm and the fan diameter, both CFD models correctly predict the magnitude of the tangential velocity at the blade tips; however the 180° model shows a different airflow distribution at the fan outlet which is not matching each fan blade tips location (Figure 5.13) as it would be expected. This also affects the mass flow rate predictions computed at the fan inlet plane: the result from the 180° model is 60% lower than the one predicted from the 360° model.

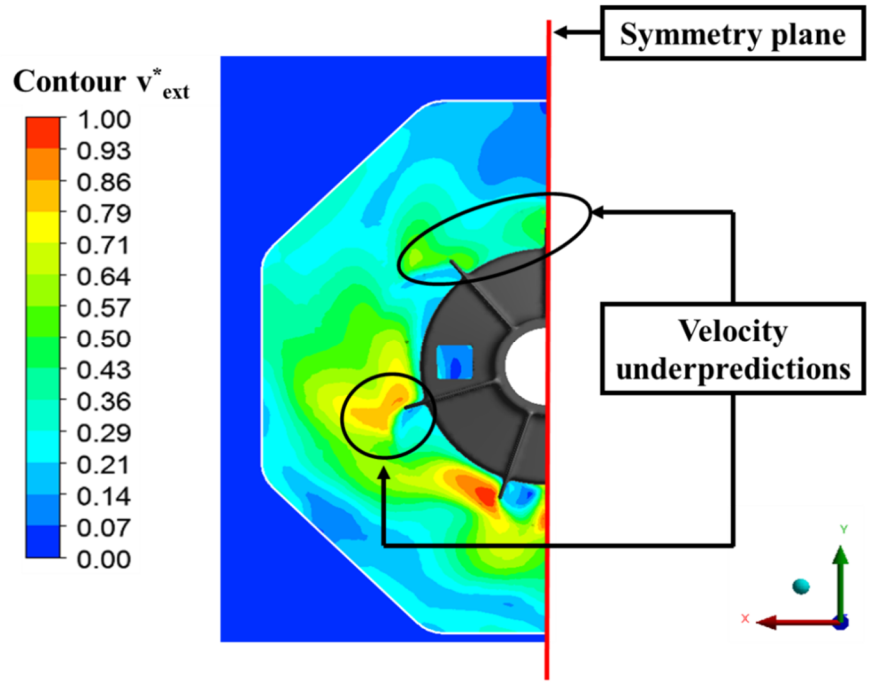


Figure 5.13: Fan outlet radial plane, non-dimensional velocity, 180° model

– v^*_{ext} = v/v$_{original\ fan\ tip}$

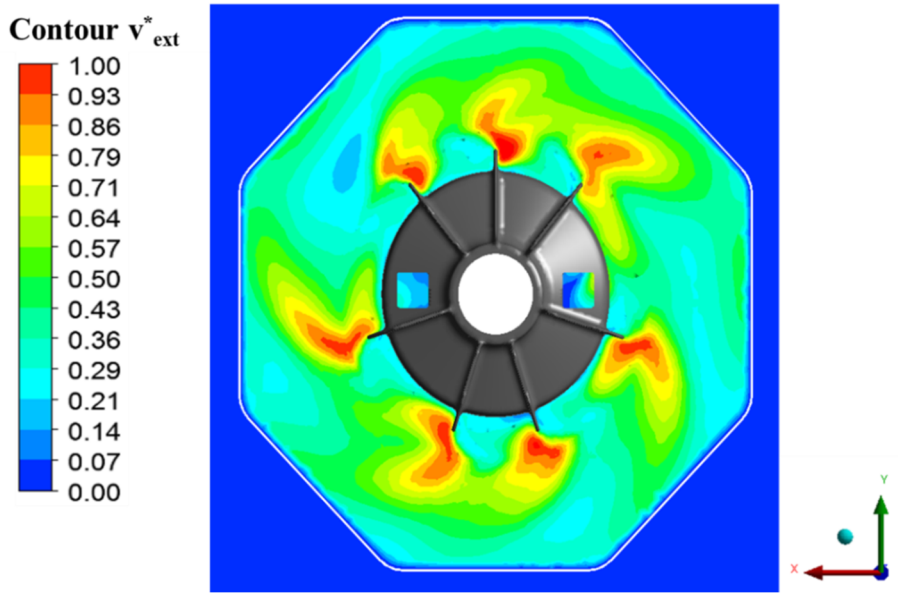


Figure 5.14: Fan outlet radial plane, non-dimensional velocity, 360° model

– v^*_{ext} = v/v$_{original\ fan\ tip}$

The different results between the two cases under investigation can be explained by the fact that a Symmetry Boundary Condition was employed in the 180° model to reduce the extent of the computational model. However, despite the physical symmetry of the domain, Ansys Fluent assumes a zero flux of all quantities across a symmetry boundary and therefore a zero normal velocity component at the symmetry plane [66].

Airflow velocity results from the 360° model (Figure 5.14) confirm that the external fluid domain, and therefore the full 3D thermal model of the selected TEFC machine, cannot be model using a 180° with symmetry boundary conditions; periodic boundary conditions cannot be employ as well due to the non-periodic geometry of the cooling fan.

The fan modelling approach of the 180° model has a significant impact on the airflow velocity distribution and magnitude around the external housing; this can be seen in Figure 5.15 and Figure 5.16 where the contour plots of non-dimensional velocity on the radial housing plane were computed for the 180° and 360° models respectively.

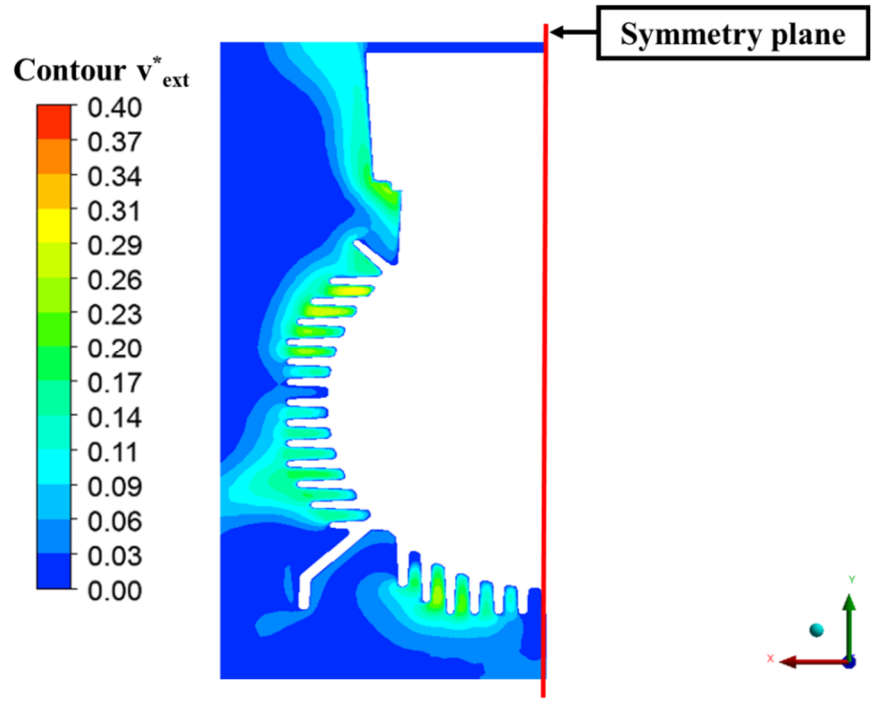


Figure 5.15: Housing radial plane, non-dimensional velocity, 180° model – $v^*_{ext} = v/v_{original\ fan\ tip}$

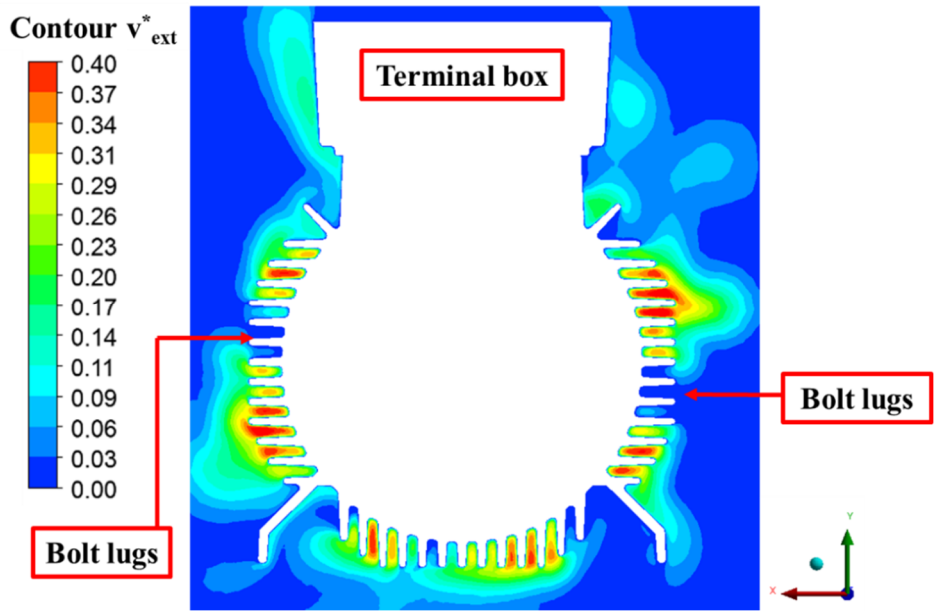


Figure 5.16: Housing radial plane, non-dimensional velocity, 360° model – $v^*_{ext} = v/v_{original\ fan\ tip}$

Results clearly show the importance of modelling the full geometry of the cooling fan as it significantly affects the external airflow and therefore the thermal predictions of the machine under investigation.

Figure 5.16 also shows how the CFD 360° model manages to predict and capture the typical uneven airflow distribution and behaviour of TEFC machines [4]; lower velocities are correctly predicted in the fins channels blocked by bolt lugs, lifting brackets and terminal box. The blockage effect to the external airflow can be better seen in Figure 5.17 below, where the airflow velocity streamlines around the housing are plotted.

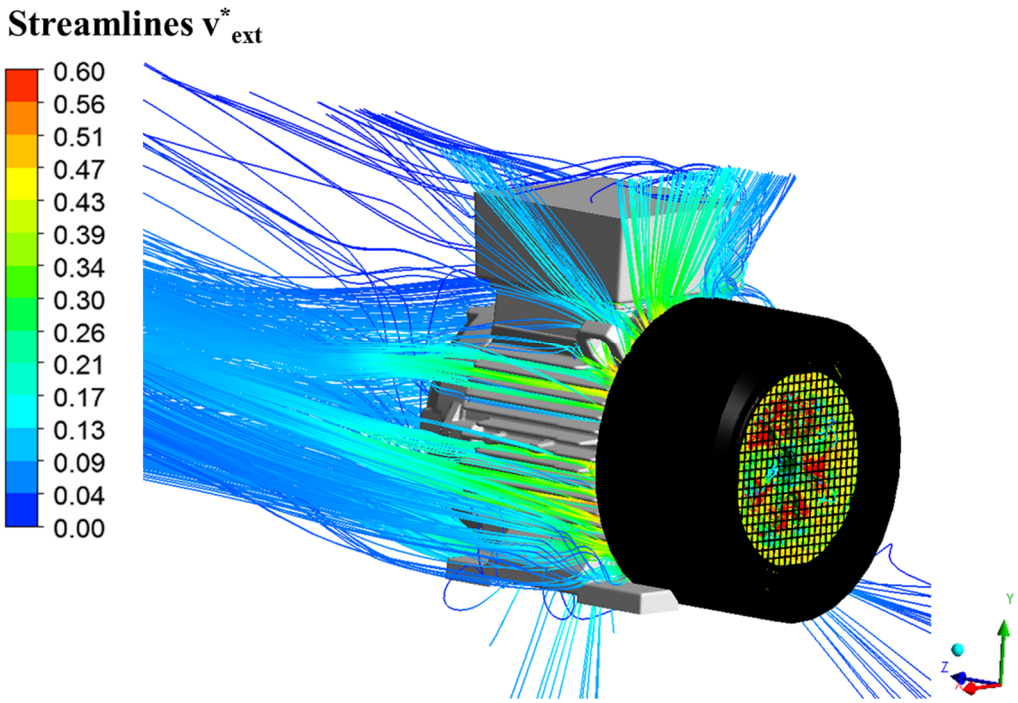


Figure 5.17: External airflow non-dimensional velocity streamlines – $v^*_{ext} = v/v_{original\ fan\ tip}$

Another deficiency of TEFC machines, which is well captured by the 360° model, is the air leakage from the open channels causing the local air velocity to be lower at the DE than at the NDE; this can be seen from the velocity results shown in Figure 5.14 (Fan outlet plane on NDE side of the machine) and Figure 5.16 (Housing plane on the DE side of the machine).

With the MRF approach used to model the fan rotation, only one steady-state solution is obtained for a fixed position of the fan relative to the stationary zones; the periodic fluctuations in the flow are not accounted for as it would happen with a SM transient approach. In order to verify if the MRF approach gave sensible results and to further investigate the impact on the airflow due to different angular fan positions, two other MRF cases of the fluid external domain were considered with the fan rotated of 90° (position "1") and 180° (position "2") respect to the original position considered in Figure 5.14 (position "0"). Figure 5.18 below schematically summaries the several fan angular positions investigated with the MRF approach; results of air velocity and mass flow rate were then computed and compared to assess the validity of the models developed.

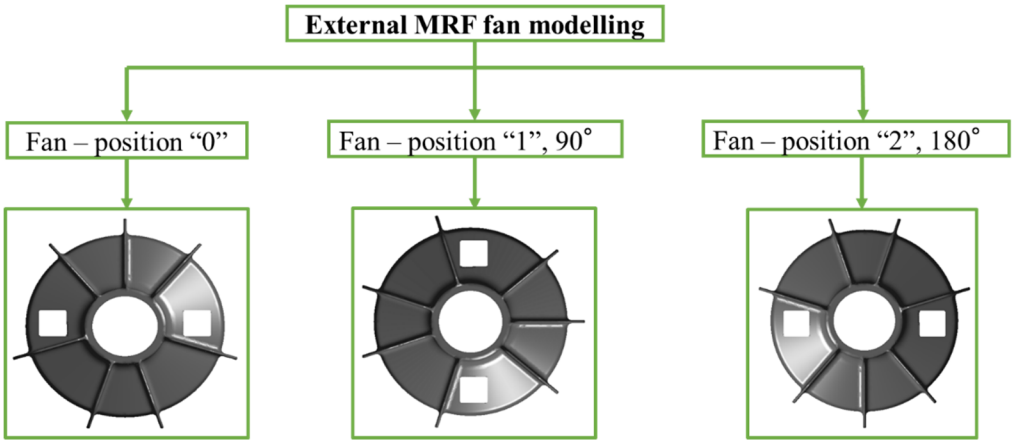


Figure 5.18: Fan angular position – MRF approach

Figure 5.19 and Figure 5.20 report the contours of non-dimensional airflow velocity results plotted on the fan outlet plane with the fan in position "1" and "2" respectively. In comparison with the results shown in Figure 5.14 (Fan – position 0) the airflow distribution changes accordingly with the position of the cooling fan; however this does not affect the velocity magnitude of the airflow. It was found that the different fan position does not significantly affect the airflow distribution and magnitude around the external housing; this can be seen in Figure 5.21 and Figure 5.22 where the contour plots of velocity on the radial housing plane were computed for the cases under investigation.

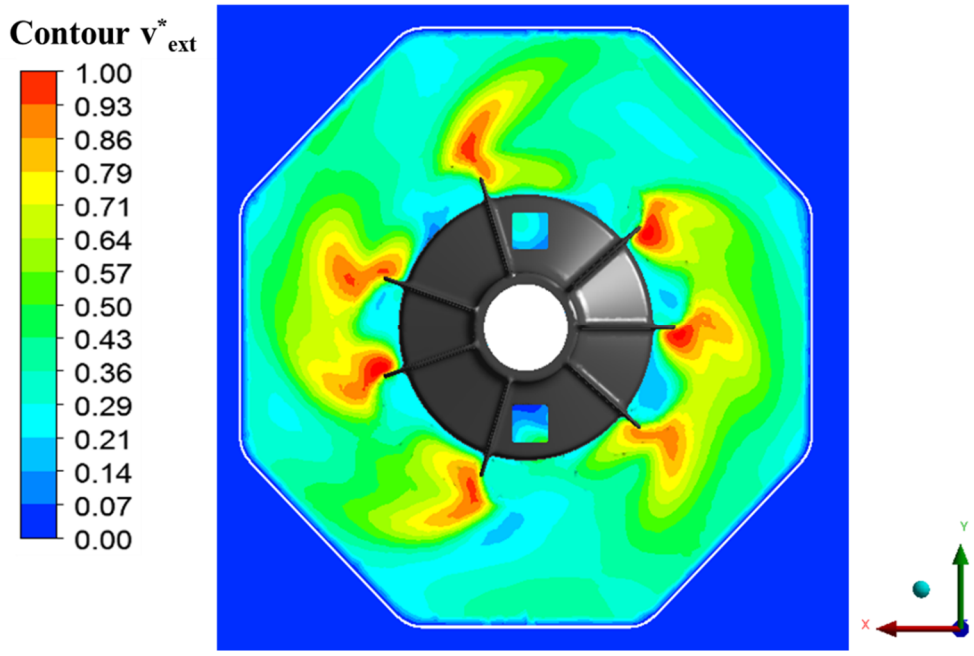


Figure 5.19: Fan outlet radial plane, non-dimensional velocity, Fan position "1" – $v^*_{ext} = v/v_{original\ fan\ tip}$

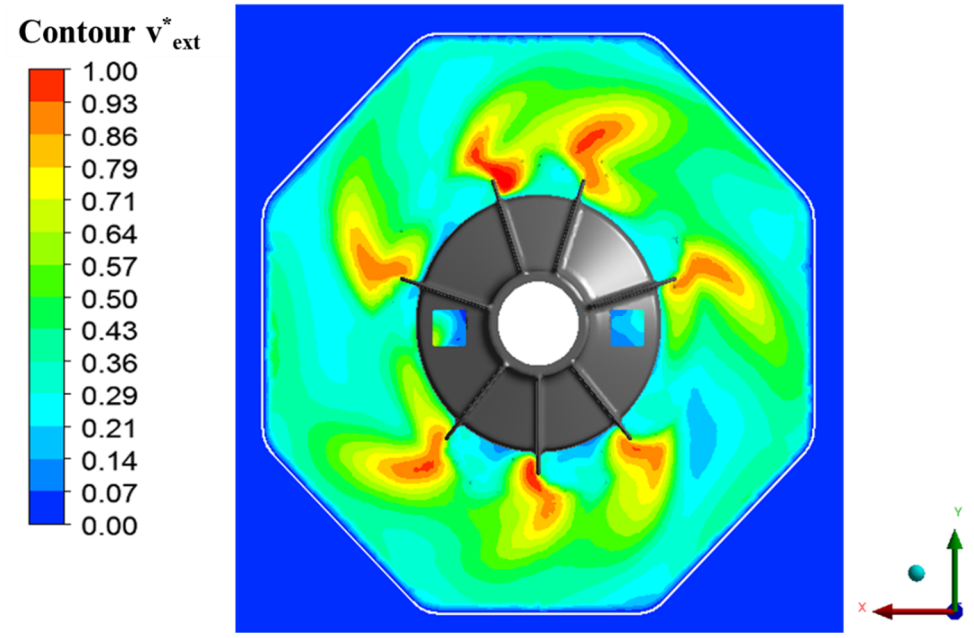


Figure 5.20: Fan outlet radial plane, non-dimensional velocity, Fan position "2" – $v^*_{ext} = v/v_{original\ fan\ tip}$

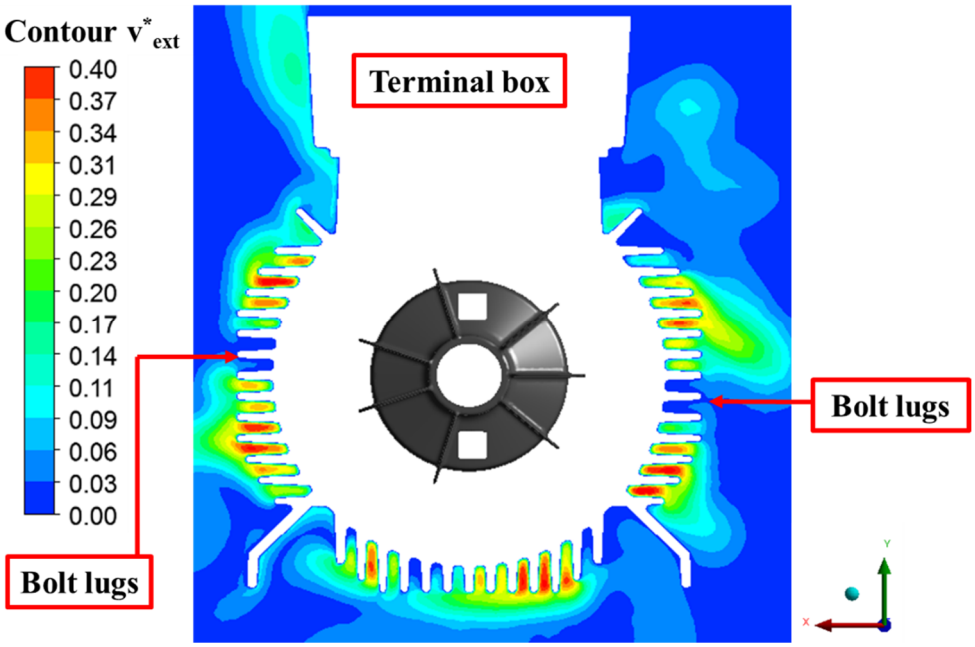


Figure 5.21: Housing radial plane, non-dimensional velocity, Fan position "1" – $v^*_{ext} = v/v_{original\ fan\ tip}$

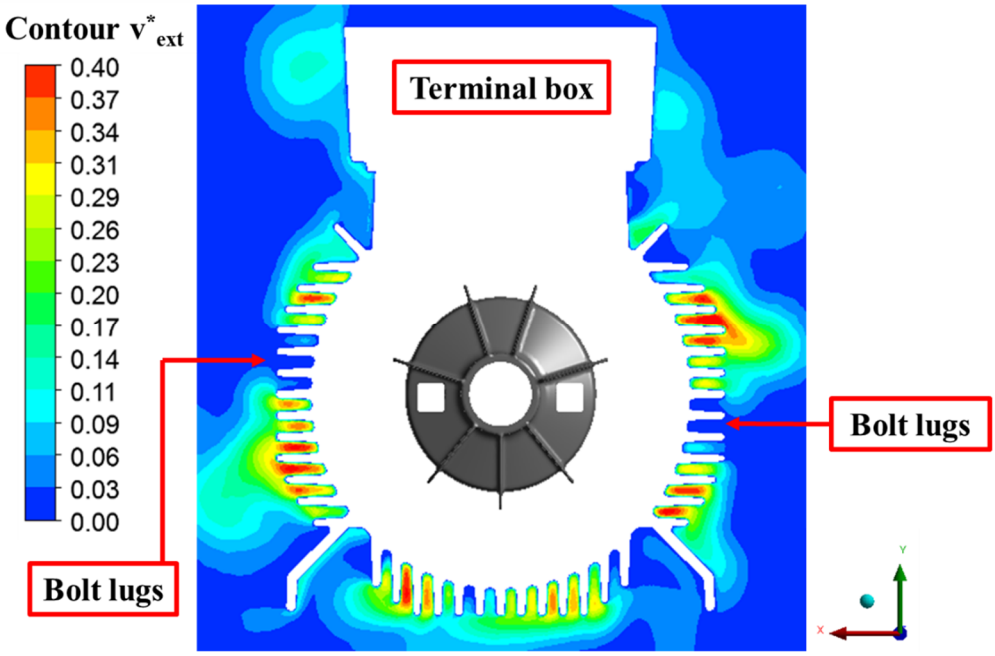


Figure 5.22: Housing radial plane, non-dimensional velocity, Fan position "2" – $v^*_{ext} = v/v_{original\ fan\ tip}$

The external mass flow rate was also numerically computed on the fan inlet plane (Figure 5.12) and results were compared as reported in Figure 5.23 below; the mass flow rate computed for the case with the fan in position "0" ($\dot{m}_{MRF,0}$) was used to normalise the results of $\dot{m}^*$ as in Equation 5.2.

$$\dot{m}^* = \frac{\dot{m}}{\dot{m}_{MRF,0}} \qquad \textbf{5.2}$$

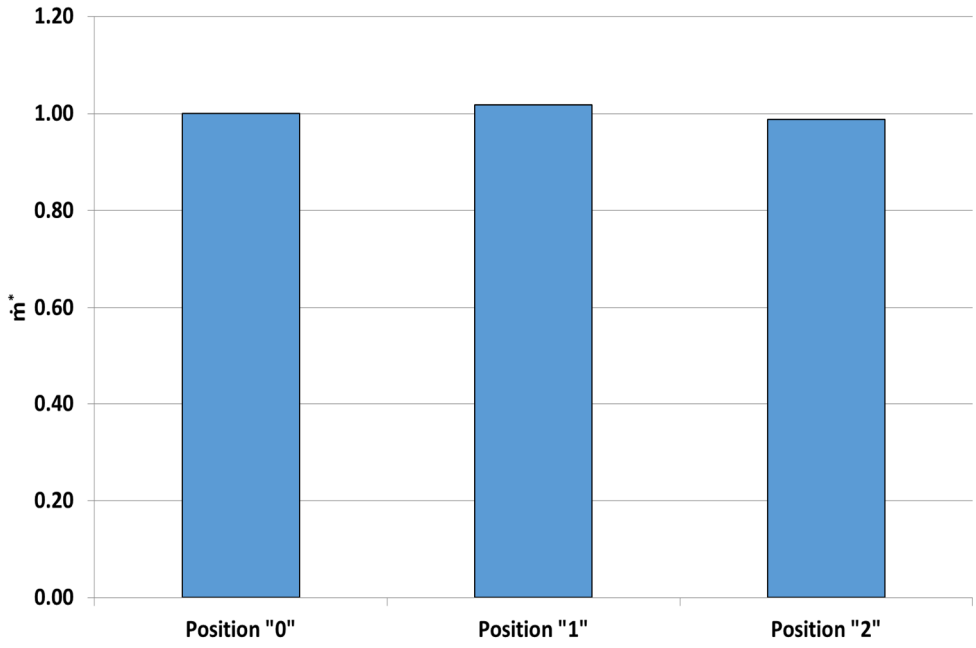


Figure 5.23: Mass flow rate comparison – Fan angular position

The computed results show how the airflow velocity distribution and magnitude were not significantly affected by the different fan position and therefore the MRF approach with the cooling fan in position "0" was used to model its rotation as presented and discussed in Chapter 6.

5.4 Optimisation and improvements

The external cooling system of TEFC machines is typically based on the forced convection with the external airflow driven by the fan mounted on the NDE side of the machine. In order to maximise the convective heat transfer coefficient, radial fins along the axial direction are usually included on the external housing in order to increase the contact surface with the airflow.

However not all the fin channels work at the same conditions as some of them are blocked by bolt lugs, lifting brackets and terminal box; another weakness of the TEFC cooling system is the air leakage from the fin open channels which causes the local air velocity to be lower at the DE than at the NDE side resulting in reductions of heat transfer rate. Both factors lead to an uneven airflow distribution as shown from results in previous section 5.3.1.

The optimisation process proposed in this work had two main targets:

- Reduction of the air leakage from the open fin channels.
- Increase of the external airflow velocity and the mass flow rate.

Both factors were aimed at improving airflow distribution around the external housing thus improving external cooling and therefore the thermal performance of the selected TEFC machine.

In order to reduce the air leakage from the fin open channels and physically provide a constraint to the airflow in the radial direction, a new fan cover geometry based on the original design was modelled as shown in Figure 5.24.

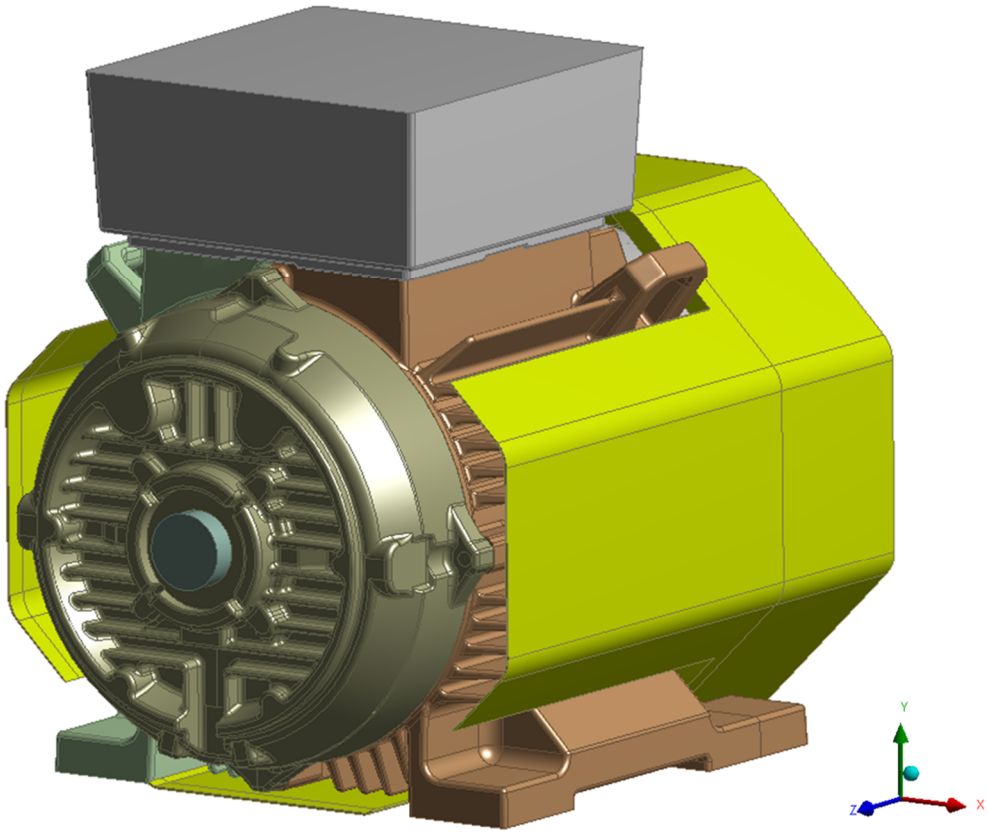


Figure 5.24: Proposed new Fan cover geometry

The new geometry of the fan cover was created by extruding the original design from the NDE to the DE side along the axial direction; this initial design approach was aimed to verify if a reduction of the air leakage from the fin channel could be achieved.

In addition, to increase the mass flow rate of the cooling air, an alternative fan geometry, based on the design of the 7-blades fan design supplied with the motor by the manufacturer, was considered; Figure 5.25 below shows a comparison between the two geometries.

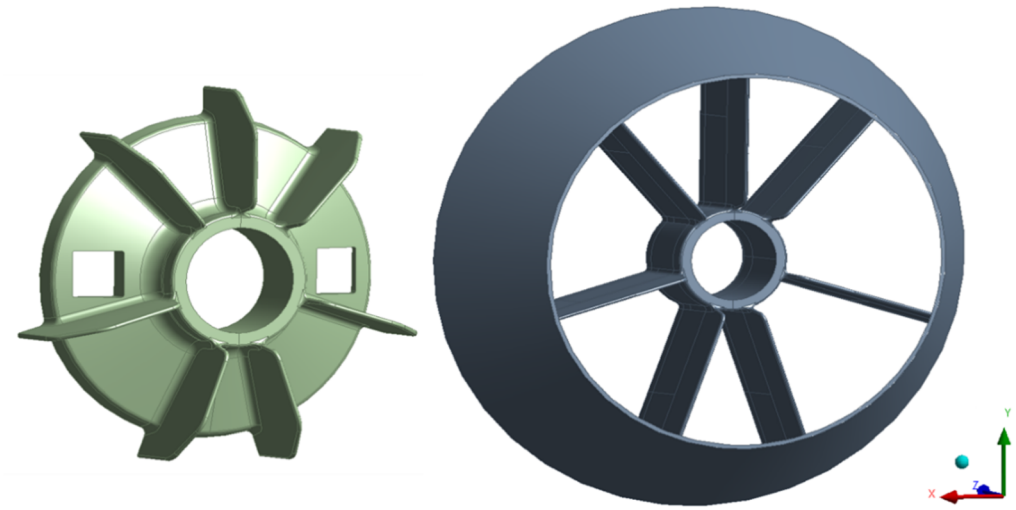


Figure 5.25: Fan – original (left) and proposed new design (right)

Within the provided fan cover, a larger fan could be accommodated; therefore, the diameter and the height of the fan blades could be increased by up to 72% and 10.4% respectively. Moreover, shrouded truncated blade tips were modelled in order to better direct the airflow around the external housing.

The original fan also had a large backplate which was removed in order to achieve greater airflow [69]; Table 5.2 below recaps the geometrical details of the proposed new fan.

	Original design	New design
Fan diameter $\mathbf{D_{fan}}$ [mm]	$0.99 \cdot D_{rotor}$	$1.72 \cdot D_{rotor}$

Table 5.2: New external cooling fan details

The impact of the proposed new cooling design, consisting of both the new fan cover and fan geometry reported in Figure 5.24 and Figure 5.25, was then investigated and results are reported in section 5.4.1 below.

5.4.1 CFD results

Similarly to section 5.3 and 5.3.1, a CFD fluid flow investigation of the 360° model of the external domain was carried out to verify if an improved airflow could be achieved without an excessive increase in the power requirement needed to drive the new fan.

Several cases (Figure 5.26) were considered in order to better relate and understand the improvements gained with each component of the proposed cooling design (new fan and fan cover); results of external airflow velocity and mass flow rate were used to investigate and compare the airflow behaviour around the TEFC machine housing for each case.

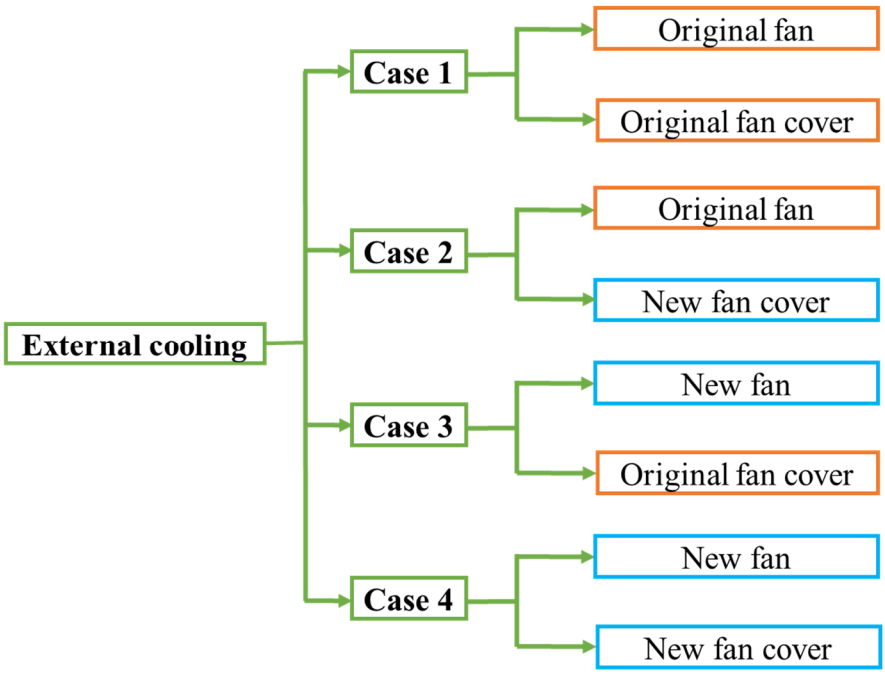


Figure 5.26: Proposed cooling design investigation

As depicted in Figure 5.27 and Figure 5.28 two lines (L_1 and L_2) were created along the axial direction in one of the housing fin channels at a different radial distance (inner line L_1 at x_1, outer line L_2 at x_2); the plotting of normalised external airflow velocity (v^*_{ext} as defined in Equation 5.1) for the several cases under investigation are reported in Figure 5.29 and Figure 5.30 for L_1 and L_2 respectively.

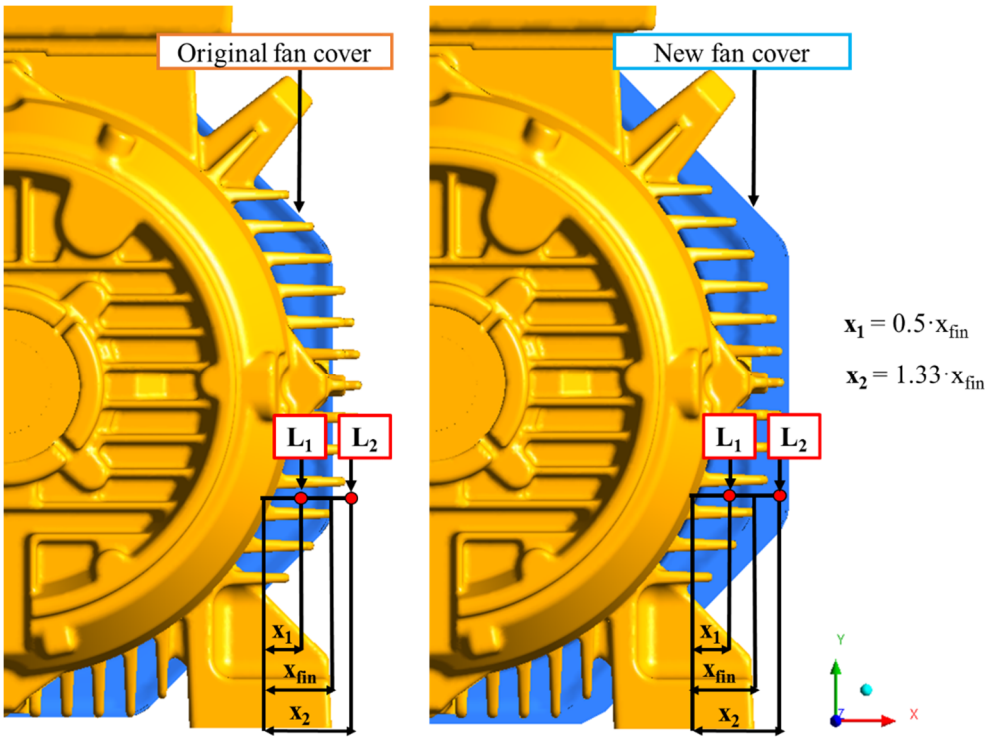


Figure 5.27: Fin channel, L_1 and L_2 x-radial location

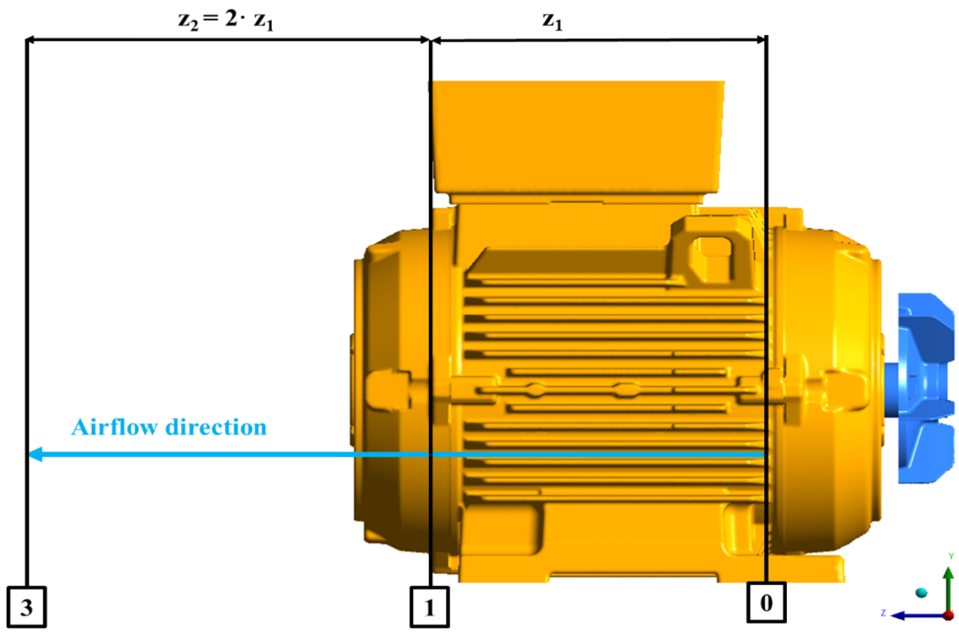


Figure 5.28: Fin channel, Airflow z-direction

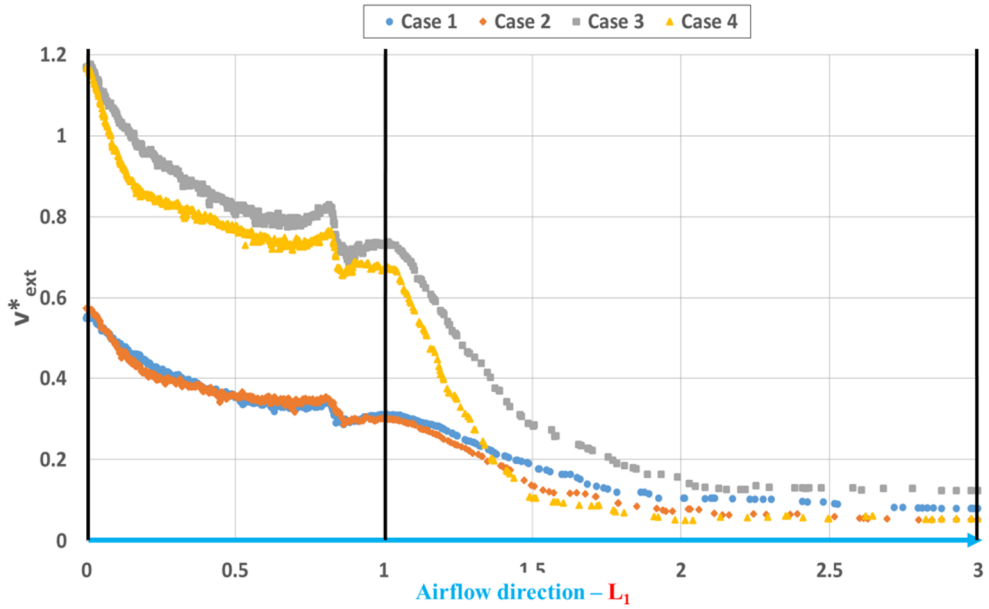


Figure 5.29: Fin channel, non-dimensional airflow velocity plot - L_1 – v^*_{ext} = v/v$_{original\ fan\ tip}$

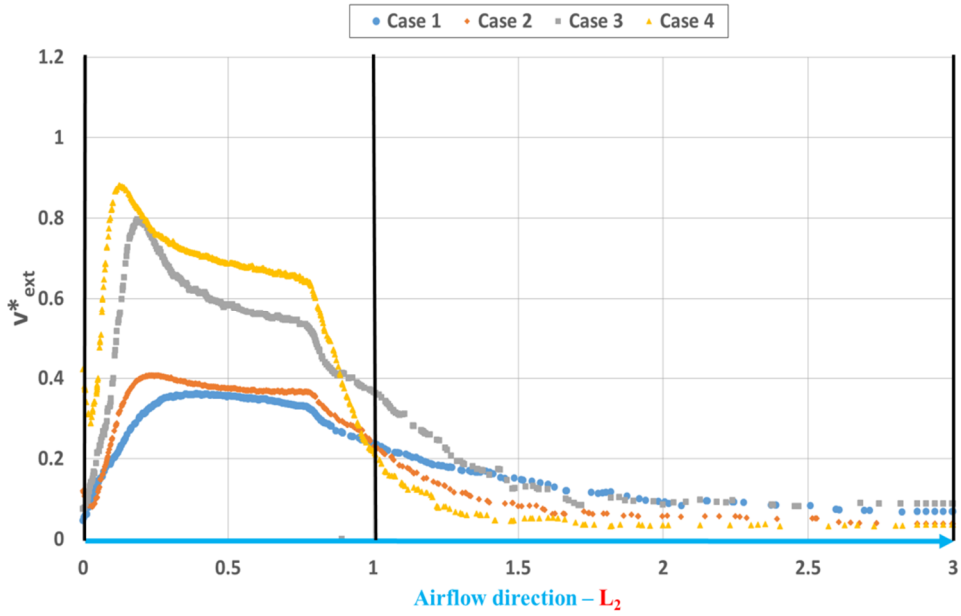


Figure 5.30: Fin channel, non-dimensional airflow velocity plot - L_2 – v^*_{ext} = v/v$_{original\ fan\ tip}$

Both results computed along L_1 (inner line in the fin channel) and L_2 (outer line in the fin channel) show how the air leakage from the open channel is causing the local air velocity to be lower at the DE than at the NDE. Inside the fin channel (L_1 - Figure 5.29) the airflow velocity is mostly and significantly affected by the new cooling fan (Case 3 and 4) whilst the implementation of the new fan cover does not lead to significant changes of airflow velocity and its distribution.

However, the impact of the proposed fan cover on the external airflow can be seen in Figure 5.30 where results of velocity are plotted along the outer line L_2; the comparison between Case 1 (original cooling design) and 2 (new fan cover only) already highlights the improvements on the airflow distribution due to the physical constraint provided by the new fan cover. The optimal condition for the external airflow is achieved by considering Case 4: the combination of the new fan and new fan cover allows to obtain higher velocities around the external housing and also a reduction of air leakage from the open fins channel.

The impact of the proposed cooling design on the airflow velocity and distribution around the housing can be better visualised in Figure 5.31 and Figure 5.32. Contour plots of non-dimensional velocity on the radial housing plane (as previously depicted in Figure 5.12) are reported for Case 1 (original cooling design) and 4 (New fan and new fan cover) respectively; as previously discussed, it can be seen how higher velocities and an improved airflow distribution can be achieved.

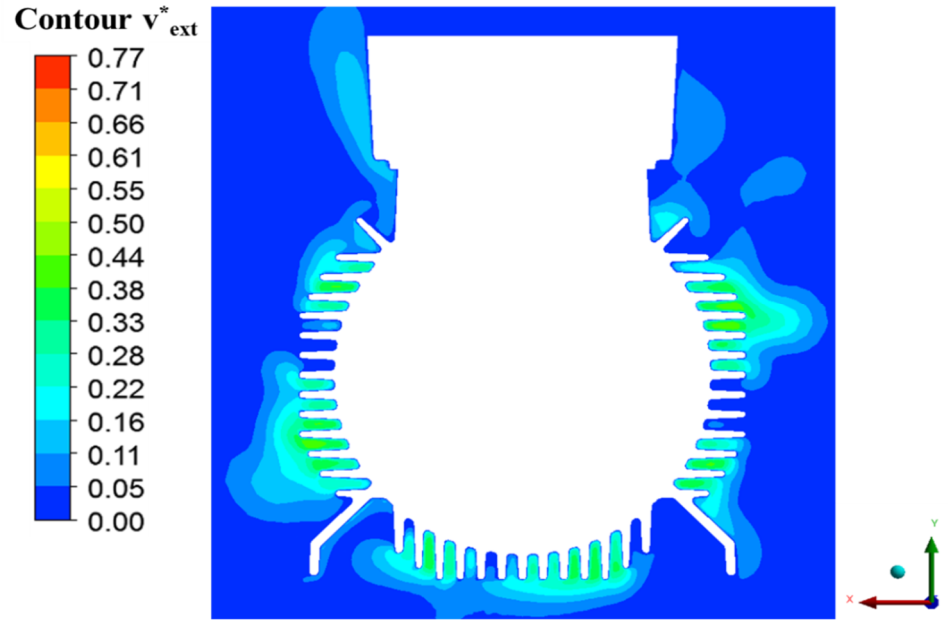


Figure 5.31: Housing radial plane, non-dimensional velocity, Case 1– v^*_{ext} = v/$v_{original\ fan\ tip}$

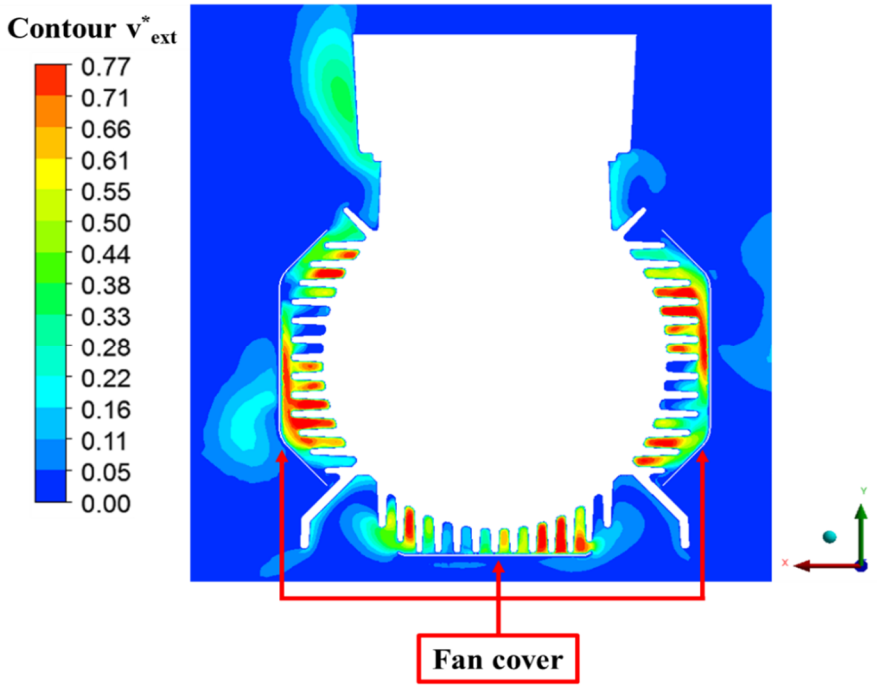


Figure 5.32: Housing radial plane, non-dimensional velocity, Case 4– v^*_{ext} = v/$v_{original\ fan\ tip}$

The mass flow rate was also computed at the fan inlet plane (as previously depicted in Figure 5.12) and results from all cases were compared as shown in Figure 5.33 below; with the proposed new cooling design (Case 4) an 84.3% increase of the mass flow rate can be achieved. As stated in section 5.3.1, the mass flow rate computed for the case with the original cooling design (Case 1) with the fan in position "0" was used to normalise the results of $\dot{m}^*$ (as in Equation 5.2).

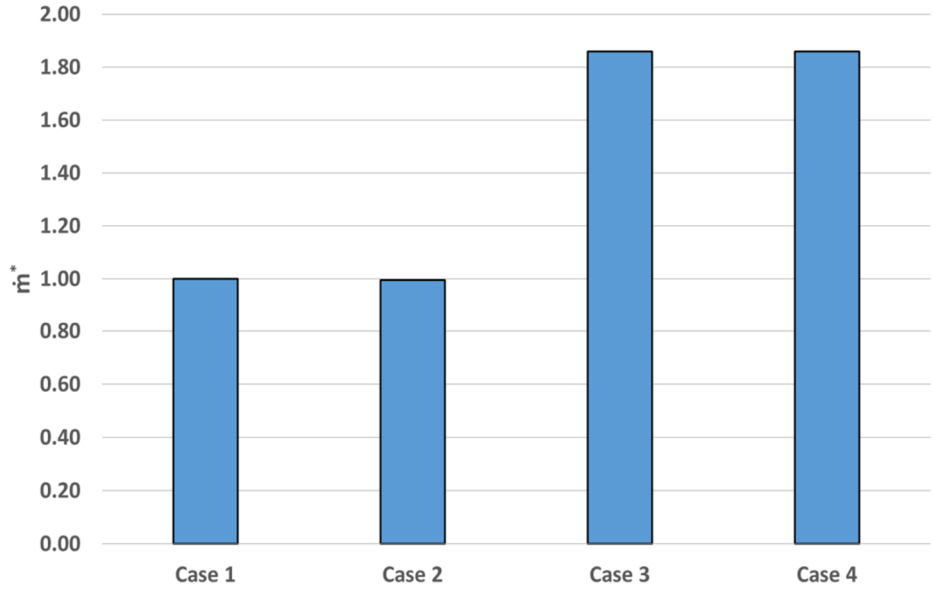


Figure 5.33: Non-dimensional mass flow rate comparison, Fan inlet plane, Case 1-2-3-4

It can be noted how the new fan (Case 3 and 4) is responsible for the increased mass flow rate and airflow velocity around the housing; as expected the case with the new fan cover only (Case 2) does not affect the mass flow rate as no design modifications were applied to the inlet. However the new fan cover manages to physically constrain the airflow coming from the fan into the fin channels all the way from the NDE to DE side of the machine (as can be seen in FigureFigure 5.30 and Figure 5.32) with consequent more uniform airflow distribution around the housing.

Results from Figure 5.29, Figure 5.30, Figure 5.32 and Figure 5.33 show how the proposed cooling design, as a combination of new fan and fan cover geometries, can potentially lead to sensible higher mass flow rate and to a reduction of the airflow leakage from the fins channels and to a more uniform airflow distribution around the machine.

The improved external cooling can also potentially have a strong impact on the thermal performance of the TEFC machine under investigation. A thermal analysis was therefore carried out in order to investigate how the improved external airflow can affect the predictions of the external heat transfer coefficients; the housing walls were set at a constant temperature of 50°C while the external walls of the fluid domain were set at 20°C which was used as reference temperature. The heat transfer coefficients were then computed (as in Equation 4.9) for different areas of the housing (Figure 5.34) and non-dimensional average results are presented in Figure 5.35 and Table 5.3, with percentage differences calculated as in Equation 5.4; the heat transfer coefficient calculated at the End Cap NDE surface ($h_{EndCap\ NDE,\ Case\ 1}$) from the original cooling design case was used to normalise the computed results as in Equation 5.3.

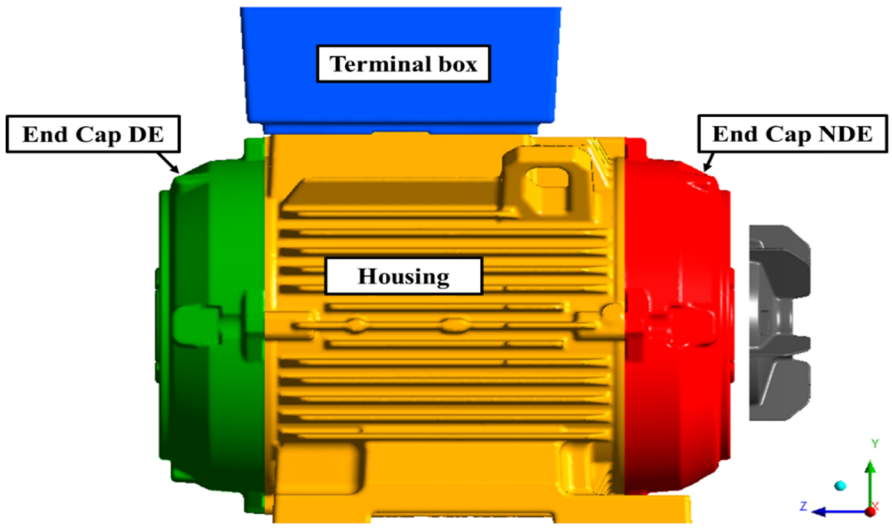


Figure 5.34: External heat transfer coefficient wall zones



Figure 5.35: Non-dimensional CFD heat transfer coefficients–Case 1-2-3-4

	Non-dimensional external heat transfer coefficient (h^*_{ext})			
	CFD - Case 1	CFD - Case 2	CFD - Case 3	CFD - Case 4
End Cap - DE	0.16	0.20 **(+20.5%)**	0.29 **(+57.5%)**	0.30 **(+61.4%)**
Terminal box	0.30	0.18 **(-51.3%)**	0.45 **(+40.8%)**	0.32 **(+8.5%)**
Housing	0.51	0.65 **(+24%)**	0.86 **(+51.3%)**	0.90 **(+55.7%)**
End Cap - NDE	1	1	1.5 **(+40.4%)**	1.5 **(+40.4%)**

Table 5.3: Non-dimensional CFD heat transfer coefficients – Case 1-2-3-4, percentage differences

$$h_{ext}^{*} = \frac{h_{ext}}{h_{End\ Cap\ NDE,Case\ 1}} \quad \textbf{5.3}$$

$$\%\ difference = \frac{|h_{ext,Case\ x} - h_{ext,Case\ 1}|}{\frac{1}{2} \cdot (h_{ext,Case\ x} + h_{ext,Case\ 1})} \cdot 100 \quad \textbf{5.4}$$

CFD results show how significant improvements of thermal predictions of the external heat transfer coefficient can be achieved with the proposed cooling design. It can be noted that the use of the extended fan cover (Case 2 and 4) leads to a reduction of the heat transfer coefficient on the terminal box surface. This can be explained by the fact that the new fan cover is forcing most of the cooling airflow over the housing surface with consequent rise of the local heat transfer coefficient; this is however beneficial since the main housing is a more critical area from the thermal point of view compared to the terminal box. As expected from previous fluid flow predictions, more significant thermal improvements are achieved with the use of the new fan (Case 3 and 4) which is responsible for the higher mass flow rate around the machine; however results of the heat transfer coefficient computed over the housing surfaces also highlight thermal improvements gained with the use of the extended fan cover (Case 2 and 4).

Numerical results show how the cooling arrangement of Case 4 (new fan and extended fan cover) can be considered the most promising cooling option: significant improvements, up to 60%, of the predictions of the external heat transfer coefficient can be achieved.

On the other hand, driving a bigger fan brings also a rise of the windage losses: this factor needs to be taken into account in the electrical machine designing process as it can affect the overall efficiency.

5.5 Summary

A CFD modelling of the external fluid domain was carried out; this analysis allowed the identification of the best modelling approach of the forced cooling airflow generated by the external fan mounted on the NDE side of the machine.

In order to reduce the computational cost of the CFD model, a 180° model with symmetry boundary conditions was initially considered; however, results show the requirement to use a full 360° case in order to correctly model the external fluid domain.

An alternative external cooling design, consisting of a new fan and an extended fan cover geometry, was considered and modelled in this work. Numerical results show how a sensible rise of the mass flow rate and an improved airflow distribution around the external housing can potentially be achieved. These factors have a significant impact on the predictions of the external heat transfer coefficients of the housing surfaces with an increase up to 50% compared to the original cooling design.

The strategy adopted within this work was based on the initial separate modelling of internal and external domains of the machine to gain a fuller understanding of the fluid flow and thermal behaviour of the most critical parts of the machine. The developed methodology presented in Chapters 4 and 5 was then combined to generate a full 360° conjugate thermal model of the selected TEFC machine to accurately predict and validate the thermal performance as shown in Chapter 6.

The impact of the proposed external cooling design on the overall thermal performances of the whole machine is presented and discussed in Chapter 7.

6 Validation of CFD conjugate model

6.1 Introduction

The modelling approaches presented and discussed in Chapter 4 and 5, for the internal and external fluid domain respectively, were combined and used to generate a 360º fluid model of the selected TEFC machine. Then, with the modelling addition of solid components and electrical/thermal losses distributed across the machine, a full conjugate heat transfer model was developed in order to investigate in detail the airflow and thermal behaviour of the TEFC machine.

This chapter presents a description of the 360º CFD conjugate model where all the fluid and solid zones of the machine are included in the meshing process and solver setup. The new end winding models developed and presented in section 4.3.1 (EWs model 1 and 2) were successfully discretised and implemented within the 360º CFD conjugate model.

The numerical results obtained from the CFD conjugate case using EWs model 1 were then validated experimentally to investigate the accuracy of the thermal model developed; the thermal validation testing was carried out at rated load condition (n = 1466 rpm, T = 71.6 Nm) as previously discussed in Chapter 3. A No-Load Test was also carried out for a speed range from 400 to 1500 rpm in order to validate the numerical predictions of the mechanical power losses: bearing friction and windage.

The flow chart reported below (Figure 6.1) schematically summarises the modelling process adopted in this work.

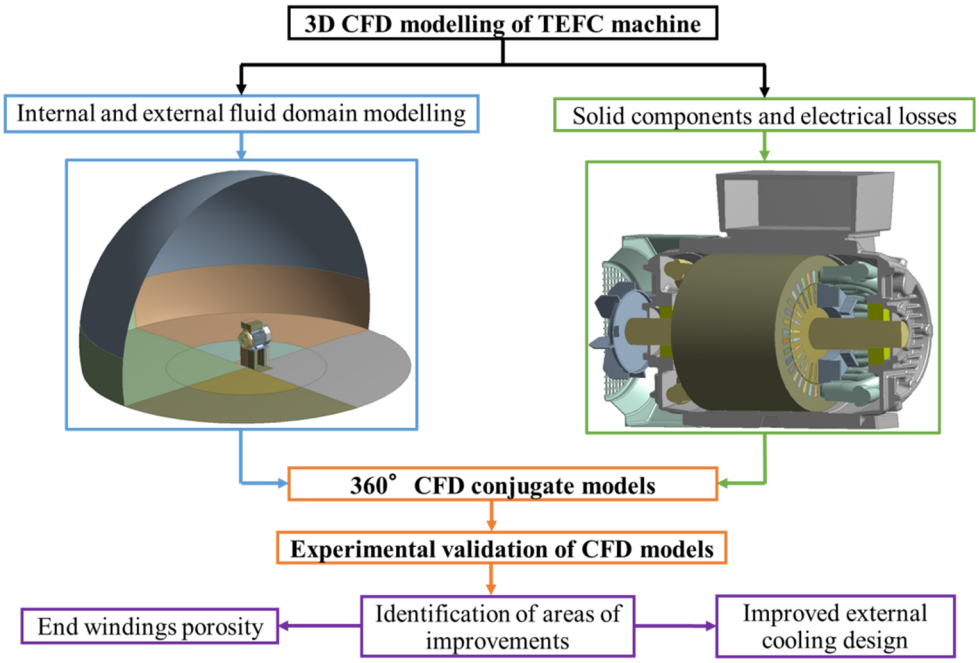


Figure 6.1: TEFC full thermal model, modelling approach

The development and experimental validation of the 360º CFD conjugate model is presented and discussed in this chapter. Once the CFD model was experimentally validated, further investigations of the impact of the potential geometry improvements discussed in section 4.4 and 5.4 were carried out; this is presented and discussed in Chapter 7.

6.2 Domain analysed

The 3D solid geometry of the TEFC machine components, including the simplified end windings geometry, was provided by the manufacturer as previously reported in section 4.3 and 5.2 (Figure 4.1 and Figure 5.1).

Several geometrical simplifications were considered as discussed in section 5.2. Features of the original design such as small grooves, chamfered corners and external bolts were removed being judged not relevant for simulation purposes; this had a direct impact on the mesh quality, mesh density and computational cost.

The more realistic end windings representations developed in this project (EWs model 1 and 2, Figure 4.10 and Figure 4.11), presented and described in section 4.3.1, were substituted into the simplified geometry initially provided as shown in Figure 6.2 below where the EWs model 1 is implemented.

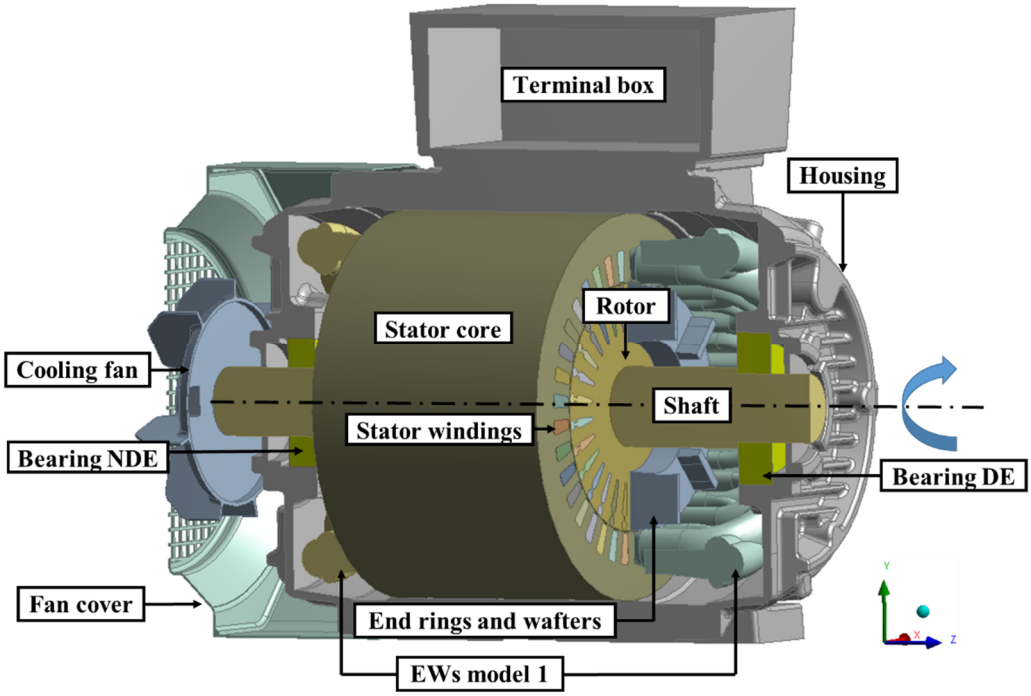


Figure 6.2: TEFC machine solid components – EWs model 1 implemented

The internal (airgap, end regions at DE an NDE) and external (laboratory environment) fluid domains, described in Chapter 4 and 5, were included with the solid components of the machine; bearings and stator windings were modelled as bulk solids and overall thermal properties were assigned as discussed later in section 6.2.2. The fluid domains were split into stationary and moving domain, in order to implement the rotation with the MRF approach as previously described in section 4.3.2 and 5.3. As shown in Figure 6.3 and Figure 6.4 below, the rotating fluid zones included the reference frames containing all rotating parts such as shaft, end rings, rotor and the external cooling fan.

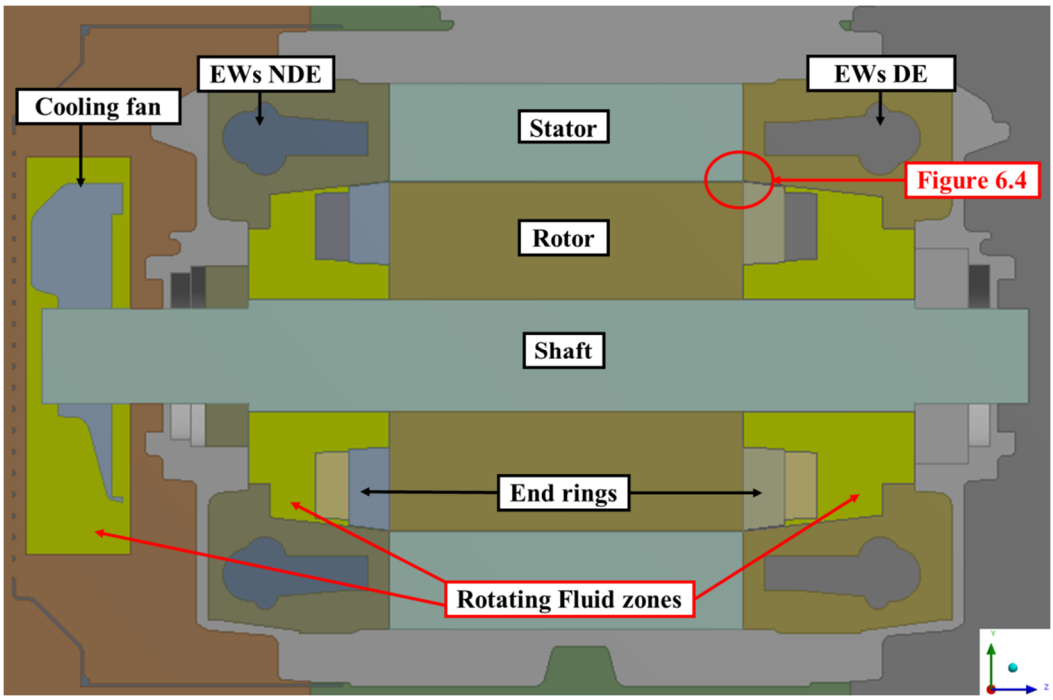


Figure 6.3: Fluid and solid domains, symmetry plane view

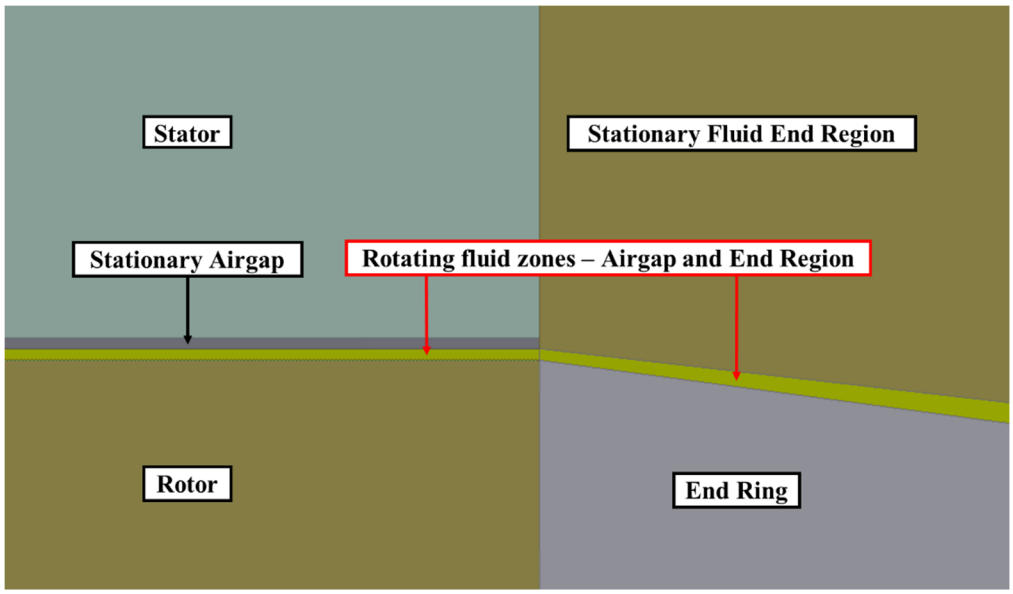


Figure 6.4: Rotating fluid zones – Airgap and End Region

Other bodies, such as stator and rotor lamination were split in more parts (Figure 6.5) to allow increased local meshing control and also to assign more realistic losses distribution to the solid components such as stator back iron and stator teeth; more details of the domain subdivision of stator and rotor lamination are provided in Table 6.1 below. More detailed information regarding the electrical losses distribution across the TEFC machine is provided in section 6.2.2.

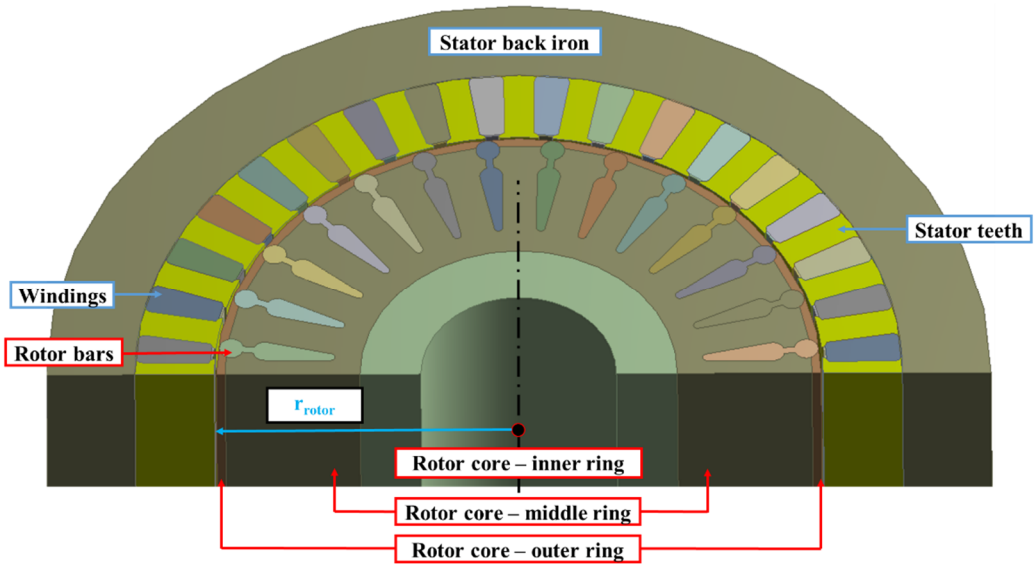


Figure 6.5: Rotor and Stator domain sub-division

Cell zone	Radius
Stator back iron	$1.56 \cdot r_{rotor}$
Stator teeth	$1.27 \cdot r_{rotor}$
Rotor core – outer ring	1
Rotor core – middle ring	$0.97 \cdot r_{rotor}$
Rotor core – inner ring	$0.52 \cdot r_{rotor}$

Table 6.1: Rotor and Stator domain sub-division

Following section 6.2.1 describes and presents more details of the several meshing techniques used to achieve an optimal mesh of the multi-body domain under investigation; section 6.2.2 instead discusses the boundary conditions and material properties assigned to develop a 360° CFD conjugate model of the selected TEFC machine.

6.2.1 Discretization process

The development and discretization of a full 360° model of an electrical machine, including both fluid flow and heat transfer analysis, required a significant modelling effort. Considering the complex structure of the domain under investigation, several meshing techniques available within Ansys Mesher were used simultaneously to achieve high quality and computationally efficient meshes.

The complexity of the multi-body geometries, their dimensions and cell zone type (solid or fluid regions) strongly affect both mesh density and element type which can vary within the domain. Hexahedral cells were adopted for simple geometry solid regions in order to achieve a high numerical accuracy and to reduce the number of elements. Complex fluid domains (such as the end regions) were discretised using tetrahedral elements due to their capability to fit complex and highly curved geometries.

The sweep meshing method and hexahedral cells were adopted for regular cross sections bodies such as airgap (section 4.3.3) stator core and windings, rotor core and rotor bars: 150 divisions along the axial direction were assigned. Conformal interfaces were created between the main components in the stator and in the rotor regions and an average cell size of 1.5 mm was adopted for a higher mesh quality. The result can be seen in Figure 6.6 below where an axial view of the generated mesh of stator and rotor is reported; the airgap domain is not included in order to better highlight the stator and rotor grid. The same meshing approach and cell size was used to discretise the shaft and the two bearings at the DE and NDE side respectively.

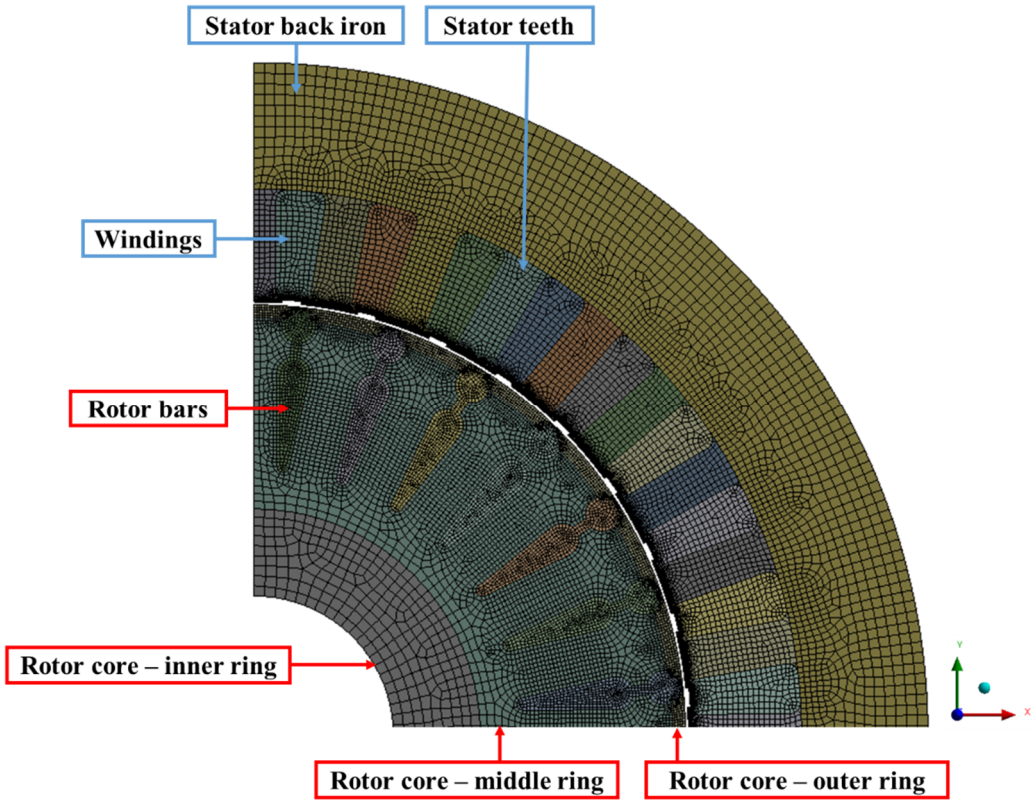


Figure 6.6: Stator and rotor mesh, axial view (airgap domain excluded)

Due to the complex geometry, the rest of the machine components were discretised using tetrahedral elements; non-conformal interfaces were generated to allow increased local meshing control. Despite the additional meshing complexity introduced using the new end windings geometries (EWs model 1 and 2), both models were successfully implemented and discretised as can be seen below in Figure 6.7 for EWs 1 case. Table 6.2 lists the cell count of the generated meshes of both EWs models.

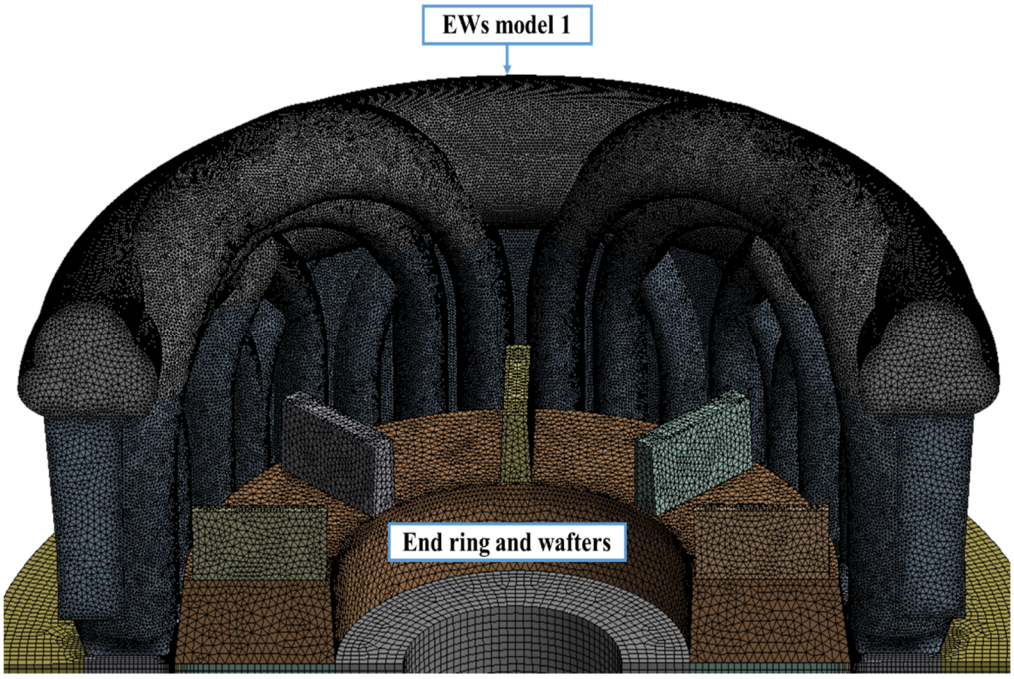


Figure 6.7: EWs model 1 mesh

Cell zone		Element number
EWs model 1	DE	8,456,005
	NDE	7,992,520
TOTAL		**16,448,525**
EWs model 2	DE	8,023,570
	NDE	7,565,148
TOTAL		**15,588,718**

Table 6.2: EWs model 1 and 2 – mesh cell count of EWs solid domain

The discretisation of the EWs model 1 and 2 provided a significant challenge: their complex geometry could be a source of high skewness cells at the solid-fluid interfaces between end windings and fluid end regions due to the high curved surfaces and sharp angles. Therefore local mesh refinements of 0.75 mm at the solid-fluid interface (Figure 6.8) were applied in order to achieve a high quality mesh and a suitable value of y^+; this allowed to better capture and model the near-wall phenomena and the heat transfer rate in this region.

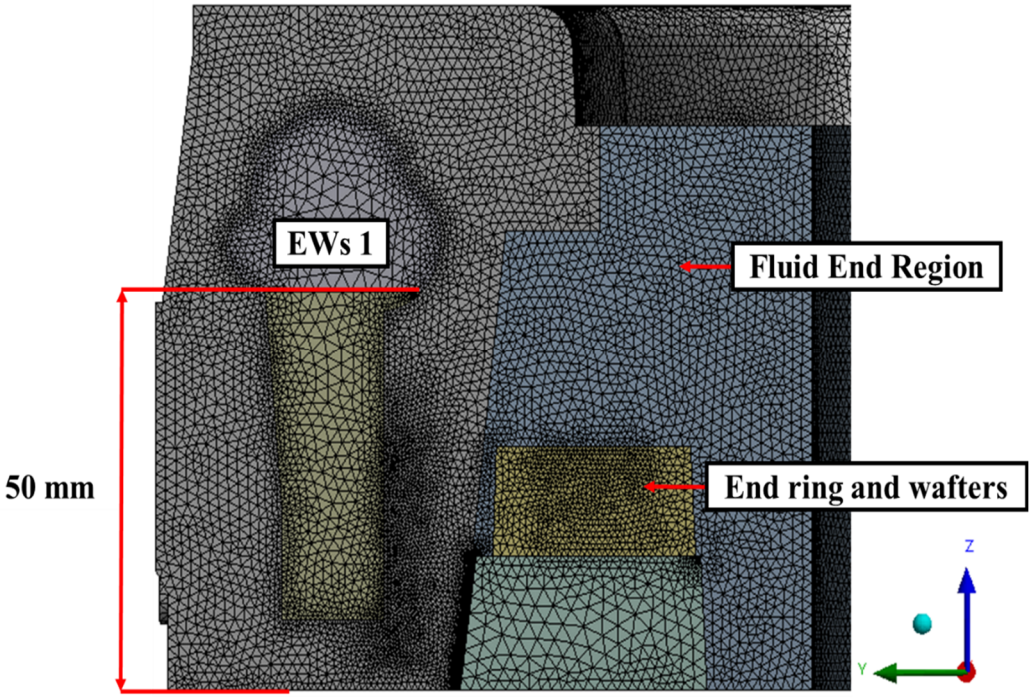


Figure 6.8: EWs model 1, solid-fluid interface refinement

As depicted in Figure 6.8, the new EWs geometry was axially sliced 50 mm above the stator slots. This geometry subdivision was performed in order to assign more realistic values of thermal conductivity along radial, axial and tangential directions; this aspect is discussed in more detail in the following section 6.2.2.

A specific mesh order was used to discretise the components of the domain in order to achieve a high quality grid; this was based on the user's experience and several attempts. Figure 6.9 below shows the final mesh for the 360° CFD model employing the EWs geometry 1; the grid counts about 108,057,081 and 110,150,313 for the model employing EWs geometry 1 and 2 respectively. More detailed information about the generated mesh for each cell zone is provided in Table 6.3.

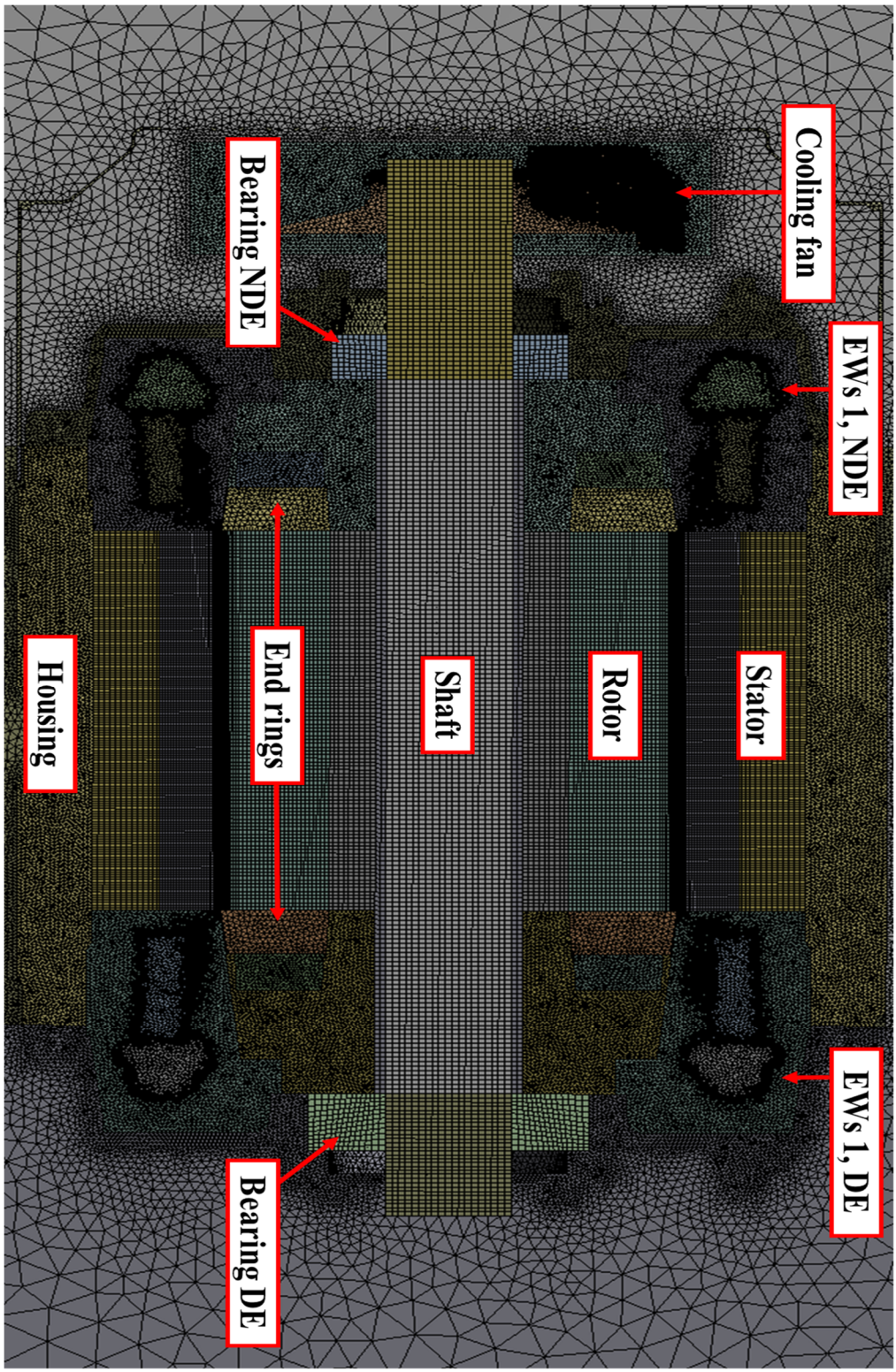


Figure 6.9: 360° CFD model, EWs model 1, symmetry plane view showing internal and external domain

Cell zone	Element number	Elements type
Rotor	2,055,600	Hexa
Rotor bars	1,254,500	Hexa
End Ring DE	375,567	Tetra
End Ring NDE	375,567	Tetra
Stator teeth	3,484,350	Hexa
Stator back iron	816,375	Hexa
Windings	1,480,800	Hexa
Shaft	117,444	Hexa
Bearing DE	14,476	Hexa
Bearing NDE	14,476	Hexa
Fan	1,914,456	Tetra
EWs 1 DE	8,456,005	Tetra
EWs 1 NDE	7,992,520	Tetra
AirGap	20,958,574	Hexa
End Region DE	13,271,997	Tetra
End Region NDE	12,849,081	Tetra
Housing	12,520,291	Tetra
External Fluid zone - total	20,105,002	Tetra
TOTAL	**108,057,081**	

Table 6.3: Mesh details of 360° CFD conjugate model – EWs model 1

The definition of the boundary conditions and the computational cost associated with the developed model is presented and discussed in section 6.2.2.

6.2.2 Boundary conditions and material properties

Once the geometry was defined and a suitable mesh generated, boundary conditions and material properties could be assigned to each machine component.

The definition of the boundary conditions was an essential and significant step in the setting up of the CFD model in the solver; these provided physical parameters and allowed the creation of interface boundary conditions within the multi-body domain and different cell zones for the heat transfer calculation. The interface boundary conditions required a manual merge operation using Fluent's mesh interface panel and in this work both coupled wall (solid-fluid zone interfaces) and interior boundaries (fluid-fluid or solid-solid zone interfaces) were created: a total of 75 interfaces were generated within the 360° conjugate models. A temperature boundary condition of 20°C was assigned to the external room walls (Section 5.3, Figure 5.7).

Thermal boundary conditions allowed the modelling of heat generation due to electromagnetic and mechanical losses occurring within the TEFC machine; these were implemented within the CFD model as energy source in the solid cell zones (W/m^3) with a uniform volumetric heat generation rate. The electrical losses were provided and experimentally validated by a team of electrical engineers and they were estimated by using Infolytica MagNet [70]; bearing friction losses at the rated speed and load were provided by the manufacturer. The chart below (Table 6.4) shows the estimated percentage distribution of the losses at rated load condition among the machine solid components.

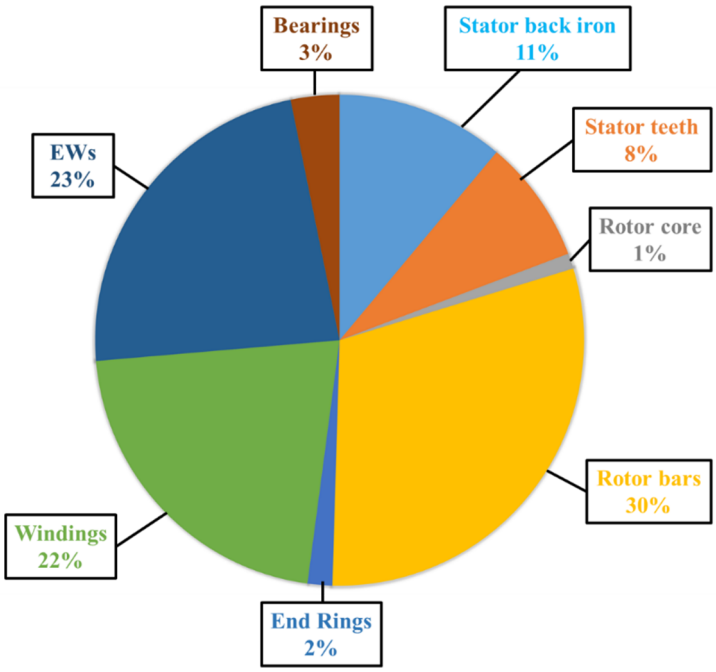


Table 6.4: TEFC machine losses distribution at 1,500 rpm

Once the interface and thermal boundary conditions were defined, material properties such as density, thermal conductivity and specific heat needed to be assigned to each machine component. The determination of thermal properties was a difficult task as they could be affected by several external factors such as manufacturing/assembly methods, operating conditions and incomplete material data [71]. The enclosed and external fluid was air which was assumed to be incompressible with thermal properties set from the internal database within Ansys Fluent as reported in Table 4.2 in section 4.3.2. Typical values, derived from machines of type and size comparable with the one under investigation, were used and implemented within the CFD model.

One of the most critical materials to thermally define and model in an electrical machine are the stator slot windings and end windings in the end region. These components are made of heterogeneous material consisting of conductors, electrical insulation, impregnation insulation and air; therefore thermal properties of the electrical windings can be highly dependent on the impregnation technique employed and manufacturing process. Overall values of thermal conductivity were analytically estimated [71] and assigned to windings and end windings. In the case under investigation, due to the non-isotropic nature of the windings thermal properties, the orthotropic function was used in order to implement different values of thermal conductivity along radial, axial and tangential directions of windings, EWs model 1 (Figure 6.10) and 2.

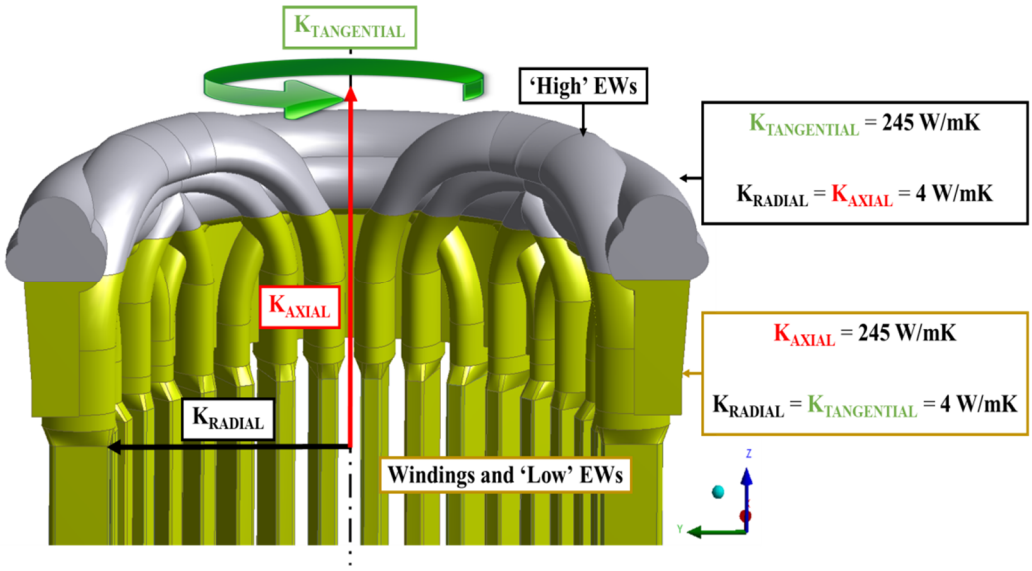


Figure 6.10: EWs sub-division for anisotropic thermal conductivity

The sub-division of the end winding geometry allowed the assignment of a more realistic thermal conductivity distribution for the machine conductors. For stator slots windings and 'low' end windings the highest value of thermal conductivity was assumed along the axial direction; for 'high' end windings the thermal conductivity along the tangential direction was assumed to be the

highest due to the alignment of the copper wires. Furthermore, in order to avoid divergent behaviour of the conjugate heat transfer solution due to the definition of an anisotropic thermal conductivity for windings and end windings, the following codes (recommended by Ansys technical support) were implemented into the Text User Interface (TUI) in Fluent [62]:

- (rpsetvar ‘temperature/explicit-relax? #t)
- (rpsetvar ‘temperature/secondary-gradient? #f)

The first code uses an explicit relaxation of temperature whilst the second disables the secondary gradient of temperature.

Table 6.5 below lists the materials and their properties used within the CFD conjugate model.

Component	Material	Density, ρ (kg/m^3)	Heat capacity, c_p (J/kg K)	Conductivity, k (W/mK)
EWs high	Copper and Insulation	5000	1300	4(axial), 4(radial), 245 (tangential)
EWs low	Copper and Insulation	5000	1300	245(axial), 4(radial), 4(tangential)
Windings	Copper and Insulation	5000	1300	245(axial), 4(radial), 4(tangential)
Rotor bars	Aluminium	2950	963	180
Rotor core	Iron	7800	450	25
Stator core	Iron	7800	450	25
Shaft	Steel	8030	502.48	16.27
Bearings	Steel	8030	502.48	16.27
Housing	Cast iron	7272	420	52
Fan	Polypropylene	1014	1260	0.25

Table 6.5: Employed materials

The developed 360° CFD conjugate model introduced a very high computational cost which could not be handled by the PC used for previous CFD analysis presented in Chapter 4 and 5. The full conjugate models presented in this Chapter and in Chapter 7 were therefore running on a high-spec computer facility during a visit by the author within ABB CRC located in Västerås (Sweden). The simulation time of the developed models was 5 days running on a 56 core CPU with 256GB RAM.

6.3 Experimental testing and validation

The objective of this work was to develop a full conjugate heat transfer model aimed to investigate in detail the airflow and thermal behaviour of the selected TEFC machine. As described in section 3.1, several experimental tests were carried out to provide validation of the 360° CFD conjugate model developed as described in section 6.2.

Experimental data and their comparison with numerical results are presented and discussed in the following sections. The end windings temperature rise (above ambient temperature measured at the fan inlet) experimentally measured on the DE side ($\Delta T_{exp,\ EWs\ DE}$) and the tangential velocity of the cooling fan ($v_{fan\ tip}$) were used to normalise the results of ΔT^* (Equation 6.1) and v^*_{ext} (Equation 5.1 – section 5.3.1) respectively; similarly, mechanical losses were normalised (P^*_m) by means of the measured data at the rated speed ($P_{m,exp,1500rpm}$) as shown in Equation 6.2.

$$\Delta T^* = \frac{\Delta T}{\Delta T_{exp,EWs\ DE}} \qquad \textbf{6.1}$$

$$P_m^* = \frac{P_m}{P_{m,exp,1500rpm}} \qquad \textbf{6.2}$$

6.3.1 Validation and results of thermal performance

Thermal performance of the TEFC motor was investigated by carrying out a load test where the induction motor was operating at rated full load condition (n = 1466 rpm, T = 71.6 Nm). The thermal steady-state condition was reached in approximately 4 hours and it was assumed to be achieved once the thermal measurements variation was within the tolerance range of the thermocouples employed in this work (±0.5 °C). Thermal measurements were then taken from the sensors placed in different areas of the machine (as described in detail in section 3.2) and used to validate the developed CFD model.

Accurate modelling of the temperature distribution is very important as it can provide an insight into the maximum operating temperature and the location of hot spots within the TEFC machine. In order to provide a general understanding of the temperature distributions within the machine, a mid-plane in the axial-z direction (Figure 6.11, x = 0 and y = 0) was created in the CFD model to plot contours of non-dimensional temperature rise through both fluid and solid domains as shown in Figure 6.12.

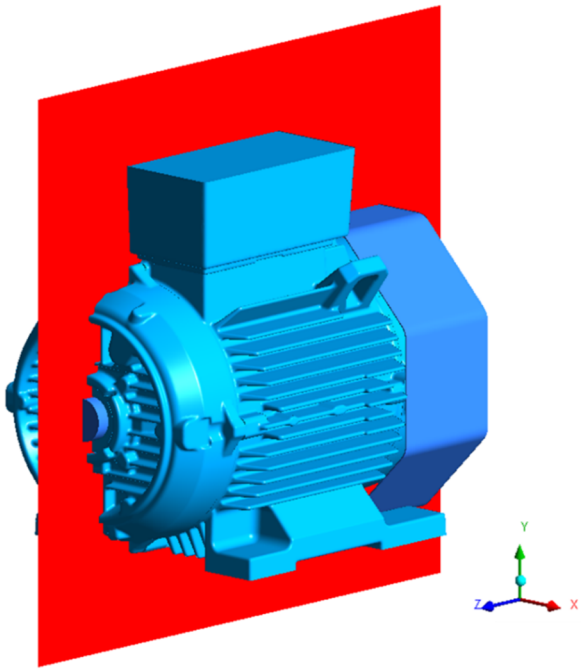


Figure 6.11: Axial mid-plane location (x = 0 and y=0)

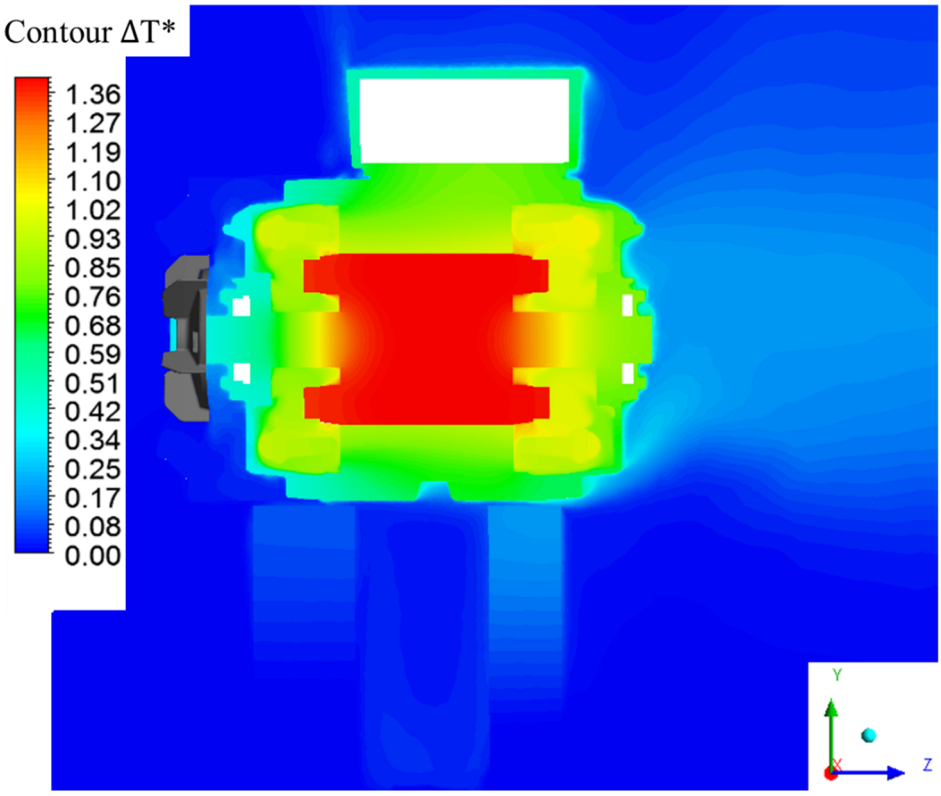


Figure 6.12: Non-dimensional TEFC machine temperature rise, axial mid-plane – $\Delta T^{*} = \Delta T / \Delta T_{exp,EWs\ DE}$

As can be seen from Figure 6.12 the rotor is clearly the hottest region and, as expected due to the cooling fan located at NDE side of the machine, the overall temperature profile of the whole domain is rising along the axial direction from NDE to DE. This can be better visualised in Figure 6.13 below where the contour of non-dimensional temperature rise along the axial direction of rotor and shaft is reported; conduction paths into the shaft from the rotor can also be seen.

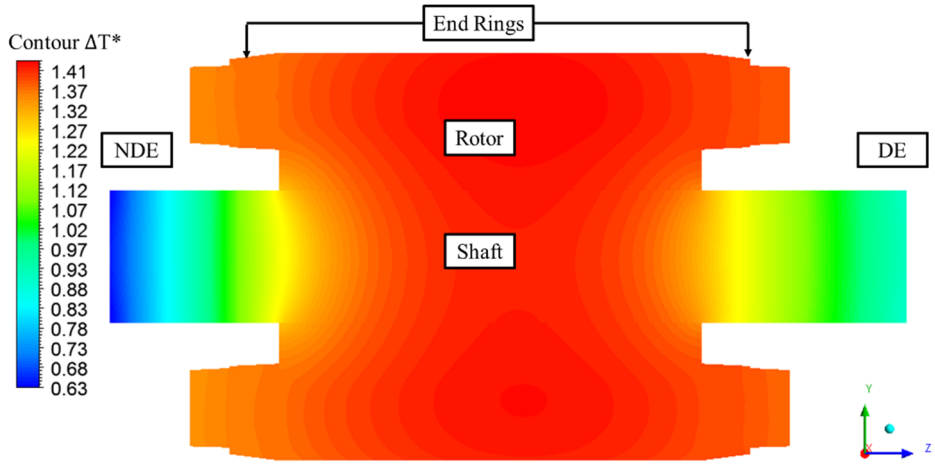


Figure 6.13: Non-dimensional rotor and shaft temperature rise, axial mid-plane – $\Delta T^* = \Delta T / \Delta T_{exp,EWs\ DE}$

As described in section 5.3.1, external housing blockages (bolt lugs, terminal box) had a significant impact on the external cooling airflow distribution around the machine and this was expected to affect thermal predictions since the two phenomena were linked. Figure 6.14 below shows contour of non-dimensional temperature rise of the stator and external air velocity (Equation 5.1)plotted on an axial plane in correspondence of the NDE side of the stator: it can be noted how the CFD model correctly predicts higher temperatures on the top part of the machine where the terminal box provides the most significant blockage to the external cooling airflow. The effect of temperature gradient between DE and NDE and terminal box blockage on the stator temperature distribution can be better seen in Figure 6.15 below, where a

contour of the axial and radial (DE and NDE side) view of the stator temperature rise is reported.

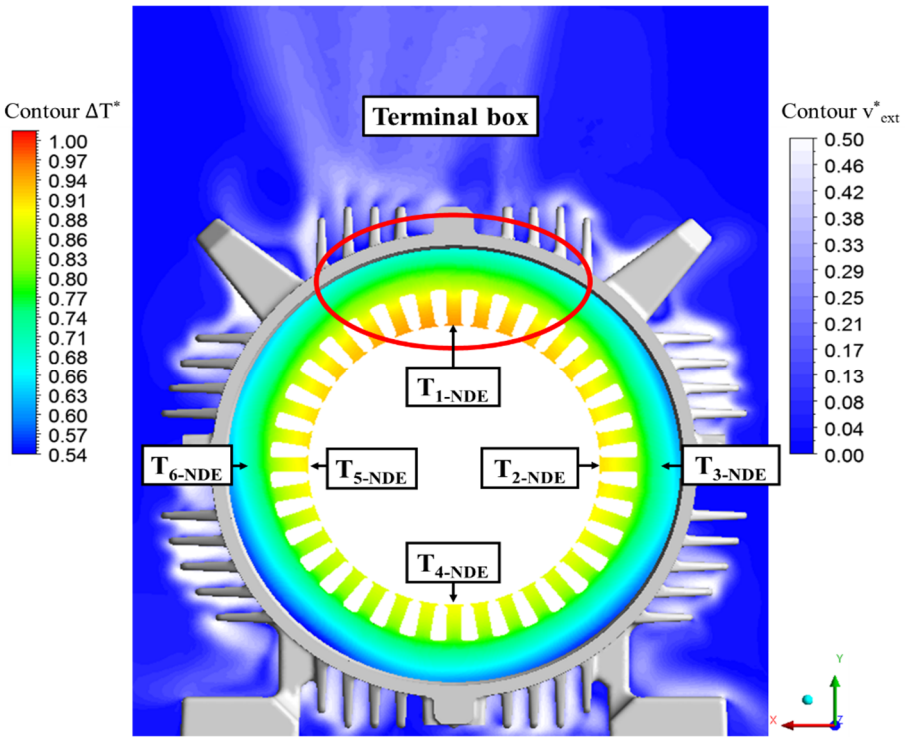


Figure 6.14: Non-dimensional velocity and stator temperature rise, NDE stator plane side

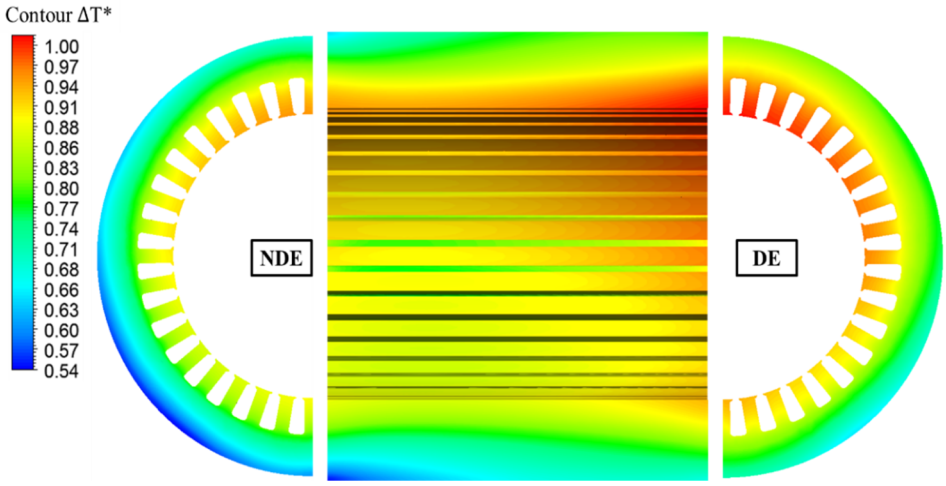


Figure 6.15: Non-dimensional stator temperature rise, axial gradient and DE-NDE side radial view – $\Delta T^{*} = \Delta T / \Delta T_{exp,EWs\ DE}$

As previously described in section 3.2.1, temperature measurements were taken from stator teeth and back iron on both NDE and DE side (Figure 3.6): a comparison between non-dimensional temperature rise results measured experimentally and those obtained numerically are shown in Figure 6.16 Figure 6.17 for DE and NDE stator side respectively. Table 6.6 below summarises in more detail the obtained results.

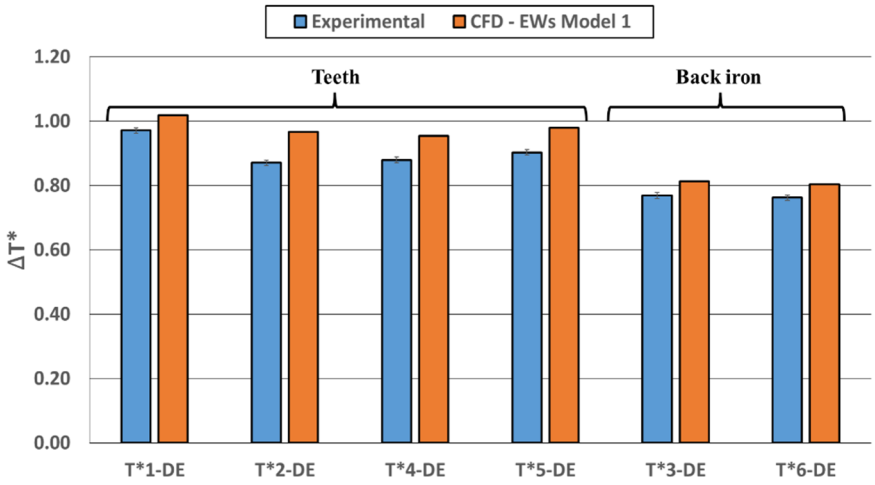


Figure 6.16: Stator teeth and back iron non-dimensional temperature rise, DE side

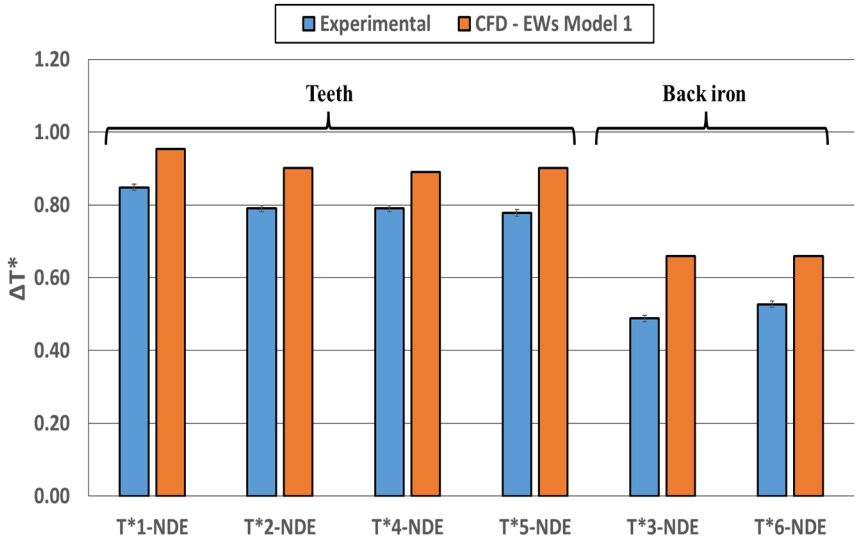


Figure 6.17: Stator teeth and back iron non-dimensional temperature rise, NDE side

			Non-dimensional Temperature rise (ΔT*)		
			Experimental	CFD	% difference with EXP
Stator DE	**Teeth**	$T^*_{1\text{-DE}}$	0.97	1.02	+4.70
		$T^*_{2\text{-DE}}$	0.87	0.97	+10.46
		$T^*_{4\text{-DE}}$	0.88	0.95	+8.13
		$T^*_{5\text{-DE}}$	0.90	0.98	+8.17
	Back iron	$T^*_{3\text{-DE}}$	0.77	0.81	+5.61
		$T^*_{6\text{-DE}}$	0.76	0.80	+5.27
Stator NDE	**Teeth**	$T^*_{1\text{-NDE}}$	0.85	0.95	+11.74
		$T^*_{2\text{-NDE}}$	0.79	0.90	+13.10
		$T^*_{4\text{-NDE}}$	0.79	0.89	+11.85
		$T^*_{5\text{-NDE}}$	0.78	0.90	+14.67
	Back iron	$T^*_{3\text{-NDE}}$	0.49	0.66	+29.89
		$T^*_{6\text{-NDE}}$	0.53	0.66	+22.39

Table 6.6: Stator teeth and back iron non-dimensional temperature rise, % difference with experimental data

$$\%\, difference = \frac{|\Delta T_{CFD} - \Delta T_{exp}|}{\frac{1}{2} \cdot (\Delta T_{CFD} + \Delta T_{exp})} \cdot 100 \qquad \textbf{6.3}$$

The percentange differences reported in Table 6.6 were calculated as in Equation 6.3. As can be seen, temperatures obtained numerically are consistently over predicting the experimental values: on the DE differences are within 10% while on the NDE are within 29.8%. However a good agreement is achieved and the trend is correctly captured by the CFD model. The CFD model also correctly captures the expected temperature distribution of the stator core: higher temperatures are computed on the stator teeth rather than the back iron due to higher losses and poorer external cooling effect. Furthermore, experimental results also confirm the impact of the external terminal box on the actual temperature distribution of the TEFC machine as predicted from the CFD model: this can be noted from Figure 6.16, Figure 6.17 and Table 6.6, where T^*_1 (temperature from the stator tooth on the top part of the machine,

just below the terminal box) is higher than the results from the other locations investigated in the stator region.

The experimentally measured and numerical results for the end winding and end region air show a similar trend as depicted in Figure 6.18 and Figure 6.19; Table 6.7 below summarises and shows the obtained results and the percentage difference between numerical and experimental data (calculated as in Equation 6.3). Higher temperatures are located on the DE side and overall on the top part of the machine; experimental data of $T^*_{EWs-DE_back}$ is not reported since the allocated thermocouple failed during the experimental test.

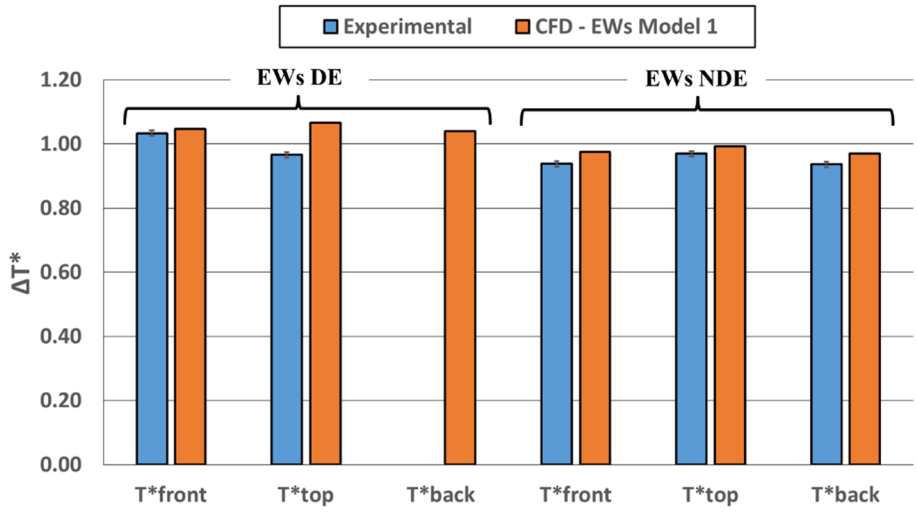


Figure 6.18: EWs non-dimensional temperature rise, DE and NDE side

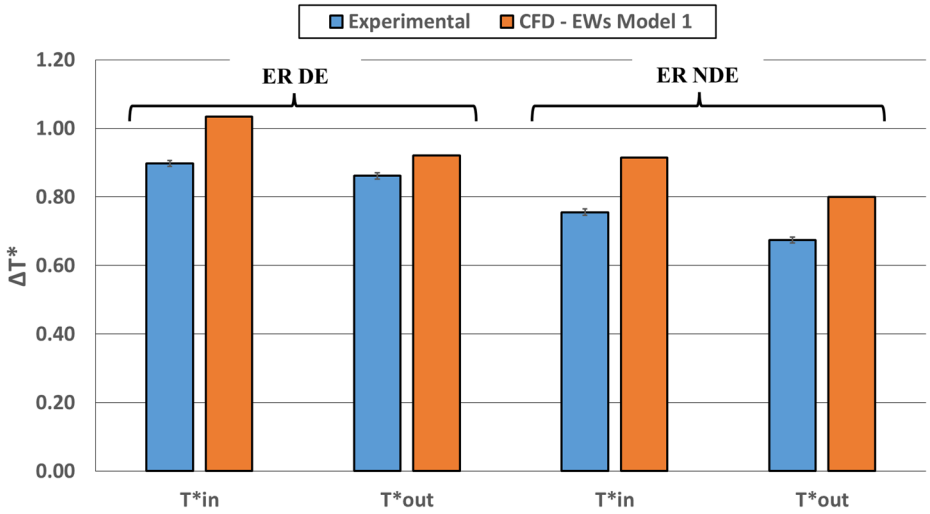


Figure 6.19: End region non-dimensional temperature rise, DE and NDE side

		Non-dimensional Temperature rise (ΔT*)		
		Experimental	CFD	% difference with EXP
EWs DE	$T^*_{EWs_front}$	1.03	1.05	+ 1.26
	$T^*_{EWs_top}$	0.97	1.07	+ 9.87
	$T^*_{EWs_back}$	0.25		
EWs NDE	$T^*_{EWs_front}$	0.94	0.98	+ 3.91
	$T^*_{EWs_top}$	0.97	0.99	+ 2.37
	$T^*_{EWs_back}$	0.94	0.97	+ 3.53
ER DE	$T^*_{ER_in}$	0.9	1.03	+14.16
	$T^*_{ER_out}$	0.86	0.92	+ 6.67
ER NDE	$T^*_{ER_in}$	0.76	0.91	+18.98
	$T^*_{ER_out}$	0.67	0.8	+17.07

Table 6.7: EWs and ER non-dimensional temperature rise, % difference with experimental data

As can be seen in Figure 6.18, Figure 6.19 and Table 6.7 the more realistic end windings representation (EWs model 1), the implemented thermal conductivity and electrical losses lead to accurate predictions of the complex fluid flow and

thermal phenomena occurring in the end regions; a good consistency between numerical and experimental results was found with maximum percentage difference of about 9.8% for the EWs on the DE side and about 15%-19% for the end region air temperature.

As described in section 3.2, temperature measurements of the external housing were also taken considering two different planes in the axial direction (Figure 3.9 – Section 3.2.1 and Figure 6.20) and three different angular locations per each plane (Figure 3.8 – Section 3.2.1).

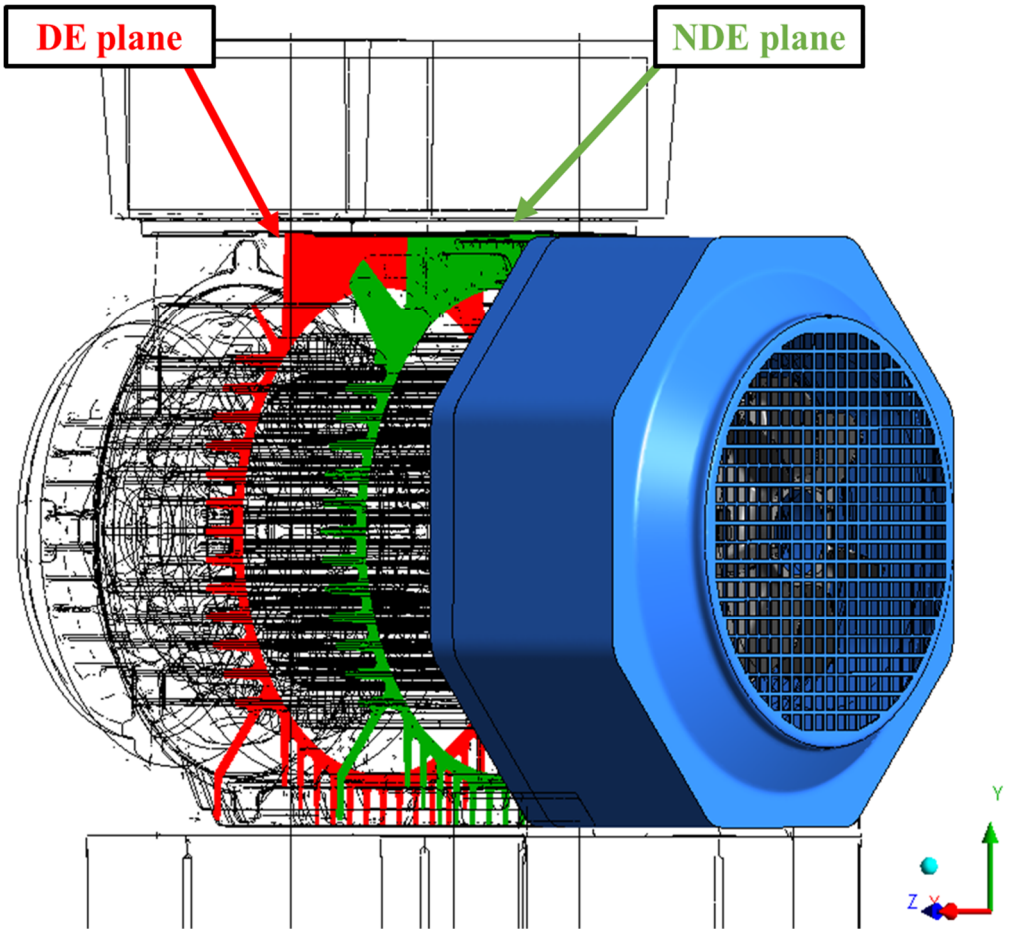


Figure 6.20: External housing planes, DE and NDE

In a TEFC machine the heat coming from the internal solid components, due to electrical losses in rotor and stator, is dissipated through the external housing

and therefore particular attention must be paid to the interface between the stator lamination and the frame. The CFD conjugate model was still over predicting experimental results but in this case major differences within 40% were found between numerical and experimental results of the housing. This discrepancy can be explained by the stator modelling approach used in this work: the stator was assumed to have a smooth external surface which was in perfect contact with the external housing.

In reality tiny airgaps exist due to surface roughness at the interface between the stator and the housing. In order to assess the impact of this on interface resistance regions of the stator-housing, interfaces were defined to experience increased thermal resistance; the contact surface between stator and external housing was reduced by 55% which led to an overall reduction of the heat transfer from stator to housing. A schematic representation and comparison between the Ideal Contact (I.C.) Stator and Interface Resistance (I.R.) Stator is presented in Figure 6.21; the location of stator-housing gaps is highlighted even though they are not fully shown due to confidentiality agreement.

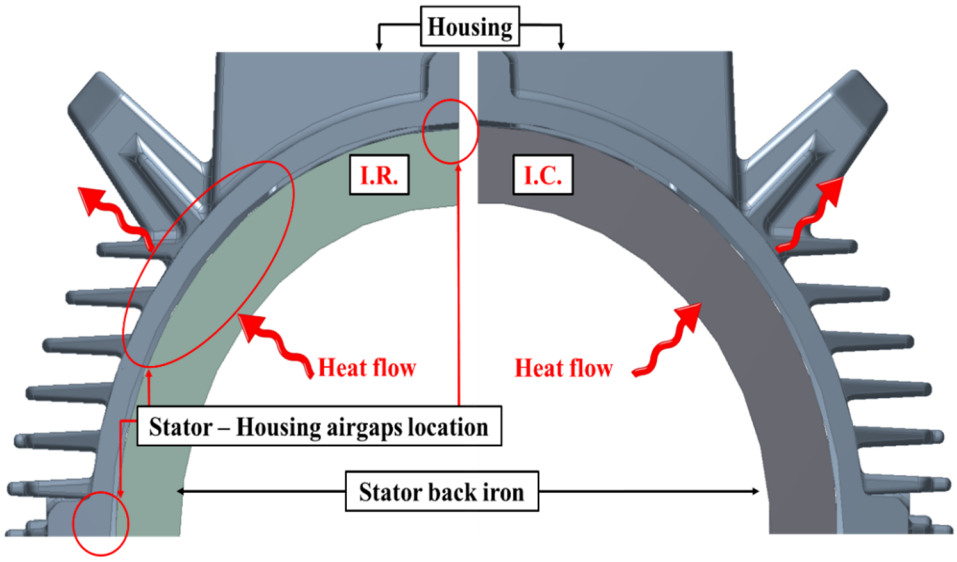


Figure 6.21: Stator-housing interface – Interface Resistance Stator (I.R. - left) and Ideal Contact Stator (I.C. - right)

In order to investigate the impact on the temperature distribution of the external housing, a CFD conjugate model using the I.R. stator geometry with airgaps (3 mm average thickness) as depicted in Figure 6.21 was considered. Figure 6.22 and Table 6.8 below shows a comparison between experimental and numerical results of the CFD models developed (employing I.C. and I.R. stator respectively) of the housing non-dimensional temperature rises on the DE plane. Percentage differences reported in Table 6.8 were calculated as in Equation 6.3.

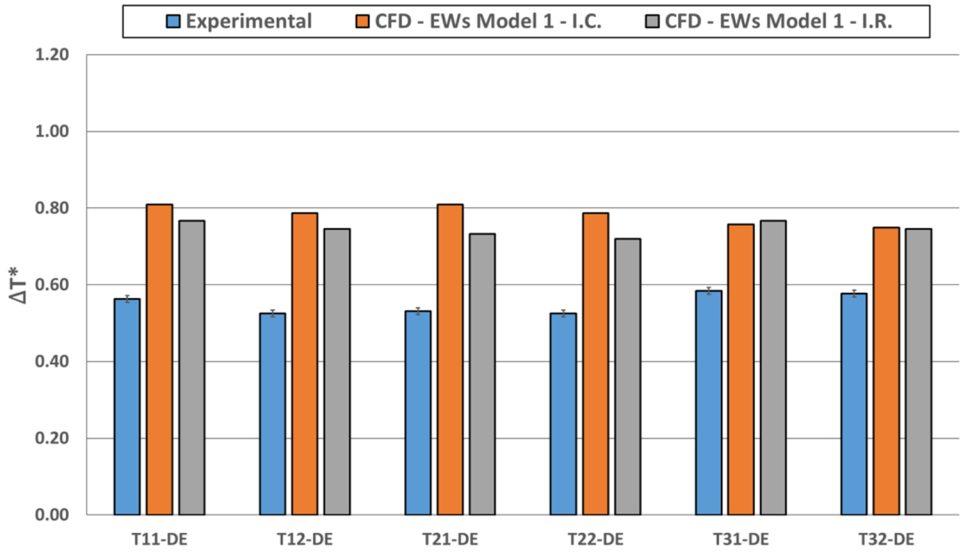


Figure 6.22: Housing non-dimensional temperature rises, DE plane

		Non-dimensional Temperature rise (ΔT*)		
		Experimental	CFD - I.C.	CFD - I.R.
Housing DE plane	$T^*_{11\text{-DE}}$	0.56	0.81 (**+35.8%**)	0.77 (**+30%**)
	$T^*_{12\text{-DE}}$	0.53	0.79 (**+39.78%**)	0.75 (**+34.5%**)
	$T^*_{21\text{-DE}}$	0.54	0.81 (**+41.4%**)	0.73 (**+31.4%**)
	$T^*_{22\text{-DE}}$	0.53	0.79 (**+39.9%**)	0.72 (**+31.2%**)
	$T^*_{31\text{-DE}}$	0.6	0.76 (**+25.9%**)	0.77 (**+21.8%**)
	$T^*_{32\text{-DE}}$	0.58	0.75 (**+25.9%**)	0.75 (**+23.05%**)

Table 6.8: Housing DE plane non-dimensional temperature rise, % difference with experimental data

As can be seen in Table 6.8, results show how the introduction and modelling of small airgaps (CFD – I.R. model) at the stator-housing interface can affect the thermal predictions of the TEFC machine leading to a reduction of the percentage differences with experimental results; a maximum decrease of about 10% was computed. In this case the reduction of the thermal contact between stator and housing leads to lower temperatures predicted for the external frame but also to an overall temperature rise of machine internal components. However, in comparison with experimental data, the predicted temperature rise of stator and end windings is not significant and differences are still in the same range as previously shown in Table 6.6 and Table 6.7.

Another factor which can explain the temperature differences between numerical and experimental results regards the external cooling fan. Due to technical issues during the project, it was found out that the provided CAD of the fan geometry used in the 360° CFD conjugate models and the real one of the TEFC machine used for experimental tests, had the same design but different size as shown in Figure 6.23. The smaller fan diameter leads to a reduction of the tangential fan velocity $v_{fan\ tip}$ (Equation 6.4) of about 37.6% at the rotational speed of 1500 rpm.

$$v_{fan\ tip} = \omega \cdot \frac{D_{fan}}{2} \qquad \textbf{6.4}$$

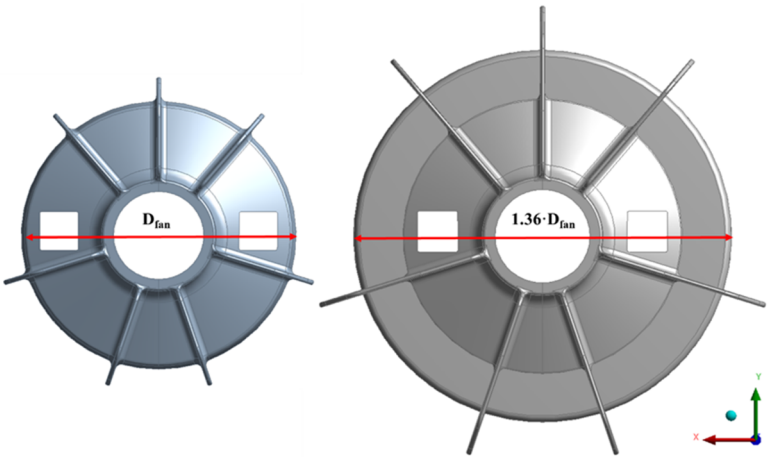


Figure 6.23: Fan geometry comparison, real sized fan on the right

The CFD modelling of a smaller fan would provide lower velocities of the cooling airflow around the external housing giving an overall reduction of the heat transfer rate (and therefore prediction of higher temperatures) compared to experimental measurements.

Although it was not possible to implement the geometry of the real fan within the 360° CFD conjugate model due to the unavailability of the high-spec computer facility in the final stage of this work, the smaller CAD geometry was edited according to real dimension (Figure 6.23); the real sized fan geometry was then implemented within the CFD external fluid domain presented in Chapter 5 which was used to investigate the impact on the external airflow and the heat transfer coefficient around the housing. The CFD model of the external fluid domain with the real sized fan had a cell count of 20,800,500 elements.

Results of external airflow velocity with the real sized fan were computed and compared with those calculated with the smaller fan presented in section 5.3.1. Figure 6.24 and Figure 6.25 reports the contour plots of non-dimensional velocity (Equation 5.1) on the radial housing plane (as defined in Figure 5.12 – Section 5.3.1) for the two cases under investigation; as expected results clearly show how higher external airflow velocities around the housing are achieved with the real sized fan due to the increased diameter.

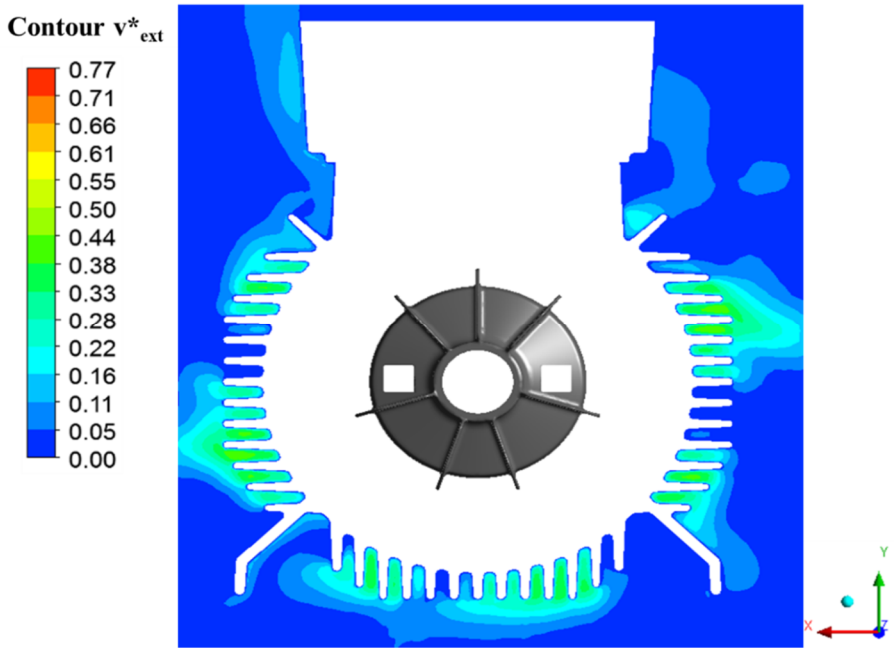


Figure 6.24: Housing radial plane, non-dimensional velocity, small fan – $v^*_{ext} = v/v_{original\ fan\ tip}$

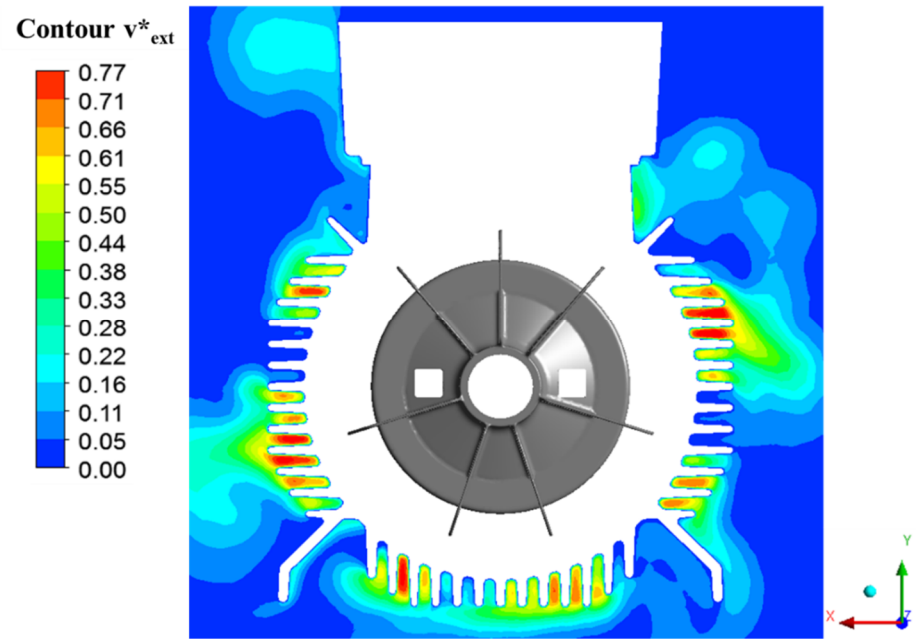


Figure 6.25: Housing radial plane, non-dimensional velocity, real sized fan– $v^*_{ext} = v/v_{original\ fan\ tip}$

Similarly to the analysis described in section 5.4.1, the heat transfer coefficient around the external housing (Figure 5.34) was computed in order to investigate how this was affected by the different external airflow; the housing walls were set at a constant temperature of 50°C while the external walls of the fluid domain were set at 20°C. The non-dimensional external heat transfer coefficients (h^*_{ext} as defined in Equation 5.3) were then calculated for both cases and results are presented in Table 6.9; as expected it can be seen how the real sized fan has a significant impact on the prediction of the heat transfer coefficients around the external housing with differences up to 57% (percentage differences calculated as in Equation 6.5).

	Non-dimensional external heat transfer coefficient (h^*_{ext})		
	CFD - small fan	CFD - real sized fan	% difference with CFD - small fan
End Cap - DE	0.16	0.29	+57.02
End Cap - NDE	1.00	1.25	+22.26
Housing	0.51	0.83	+47.46
Terminal box	0.30	0.41	+32.01

Table 6.9: non-dimensional CFD heat transfer coefficients – small and real sized fan percentage differences

$$\%\ difference = \frac{|h_{ext,CFD\ real\ fan} - h_{ext,CFD\ small\ fan}|}{\frac{1}{2}\cdot (h_{ext,CFD\ real\ fan} + h_{ext,CFD\ small\ fan})} \cdot 100 \qquad \textbf{6.5}$$

6.3.2 Validation and results of mechanical performance

Mechanical power losses such as bearing frictions and windage (fan and airgap) were also estimated and compared with experimental results. While the windage losses occurring in the airgap were computed as described in Chapter 4 (section 4.3.3), some modifications of the fan geometry (Figure 6.23) were necessary in order to accurately predict the associated windage losses.

As discussed in section 6.3.1, a CAD fan geometry smaller than the real one was used in the 360° CFD conjugate models due to technical issues during the project and the setting up of the experimental rig; the fan windage losses computed numerally with those models were therefore lower than experimental results due to the different size. The modelling of the real sized fan would provide higher windage losses due to the increased radius; the CFD 360° external fluid domain presented in Chapter 5 was used to compute the windage losses associated to the experimental real sized fan for a speed range from 400 to 1500 rpm.

Bearing frictions at the rated speed were provided by the manufacturer; by knowing the bearing models employed in the TEFC machine under investigation, the associated losses at lower speeds were analytically estimated using the model provided by the bearings manufacturer (SKF) [40].

As described in section 3.1 a No-Load Test was carried out for a speed range from 400 to 1500 rpm in order to validate the numerical predictions of the mechanical power losses: bearing frictions and windage. The TEFC machine terminals were left in an open circuit condition and the system was driven at different speeds by using the drive machine; the measured torque provided an estimation of the total mechanical power loss. Each operating point was run until no variations were identified in the torque readings. Torque measurements of each operating point were taken when variations in the torque readings were within the tolerance range of the torque meter used (0.1% of FSD - 0.1 Nm).

Figure 6.26 shows a comparison of the trend of the total non-dimensional mechanical power losses P^*_m (Equation 6.2) predicted with both fan models (Figure 6.23) and those experimentally measured; as can be seen a good agreement between the total estimated loss with the real sized fan model and the experimental measurements is achieved with a maximum difference of 9% (Equation 6.6). Due to the different size, the predictions given by the smaller CAD fan model are lower than experimental results with maximum difference of 20%.

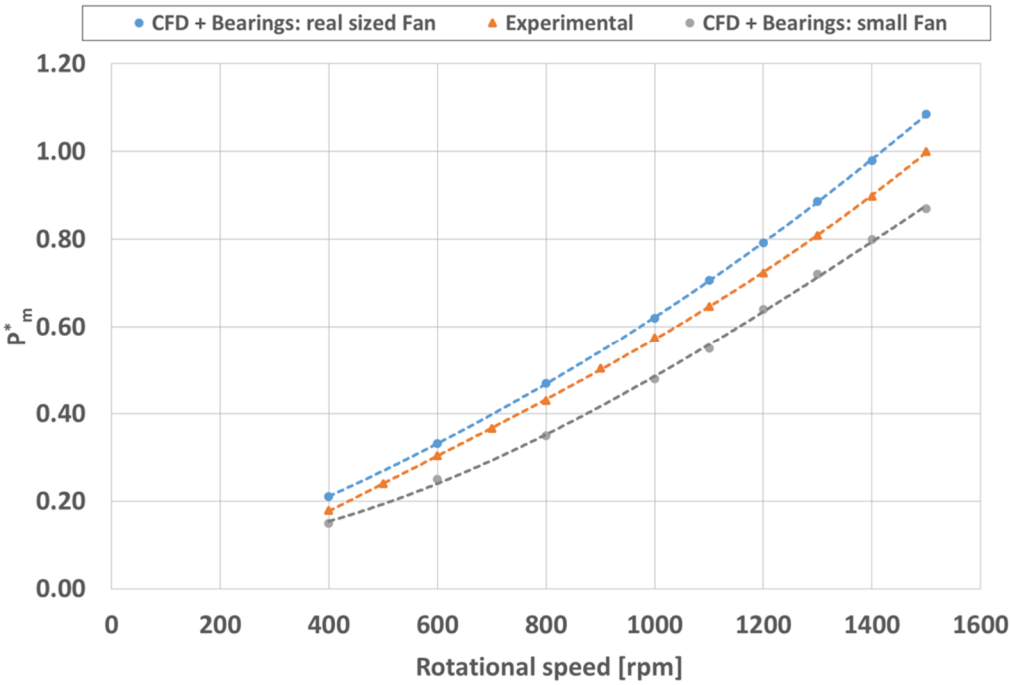


Figure 6.26: Mechanical power losses CFD (bearings + windage) and experimental trend

$$\%\, difference = \frac{|P_{m,experimental} - P_{m,CFD+Bearings}|}{\frac{1}{2} \cdot (P_{m,experimental} + P_{m,CFD+Bearings})} \cdot 100 \qquad \textbf{6.6}$$

6.4 Summary

A 360° CFD conjugate heat transfer model was developed and the airflow and thermal behaviour of the TEFC machine presented; the end windings models discussed in Chapter 4 were successfully implemented and used within the full conjugate model. The joint CFD conjugate analysis of internal and external domains provides a significant modelling challenge but, considering the structure of a TEFC machine, it is also an important tool in order to investigate the complex fluid flow and thermal phenomena occurring in both domains simultaneously.

Experimental tests were carried out and results were used to validate the model built. The developed CFD conjugate model is capable of predicting and capturing the complex internal and external fluid flow and thermal phenomena; a good agreement was found between experimental data and numerical predictions with the CFD model consistently over predicting experimental values with the trend correctly captured by the developed CFD model; higher difference were found on the thermal predictions of the external housing.

However there were two main factors which can justify those discrepancies. Numerical results showed the impact of tiny airgaps at the stator-housing interface on the overall thermal predictions of the machine; a more accurate modelling of the stator back iron outer surface, taking into account possible existing airgaps and surface roughness, would provide more accurate results of the thermal interface resistance and a better agreement with experimental results. In addition the cooling fan geometry, used in the 360° CFD conjugate model, had a radius smaller than the real one employed during experimental tests.

The CFD modelling of the real sized fan, due to computational limitations, was considered for a fluid flow and thermal investigation of the external fluid domain only; results show how the lower velocities predicted by the 360° CFD conjugate model (using the smaller fan) would explain the poorer cooling

effect and the overall temperatures over prediction compared to experimental results.

The impact of the real sized fan on the numerical estimation of the associate windage losses was also considered. This, in addition with bearing losses estimated analytically, provided a trend of the mechanical power losses which was in good agreement with experimental results with a maximum difference of 9%.

7 Machine optimisation and improvements

7.1 Introduction

Once the 360° CFD conjugate model was experimentally validated as presented and described in Chapter 6, further investigations of alternative cooling arrangements to improve the cooling capability and performance of the TEFC machine were carried out. The proposed configurations are summarised in Figure 7.1 below.

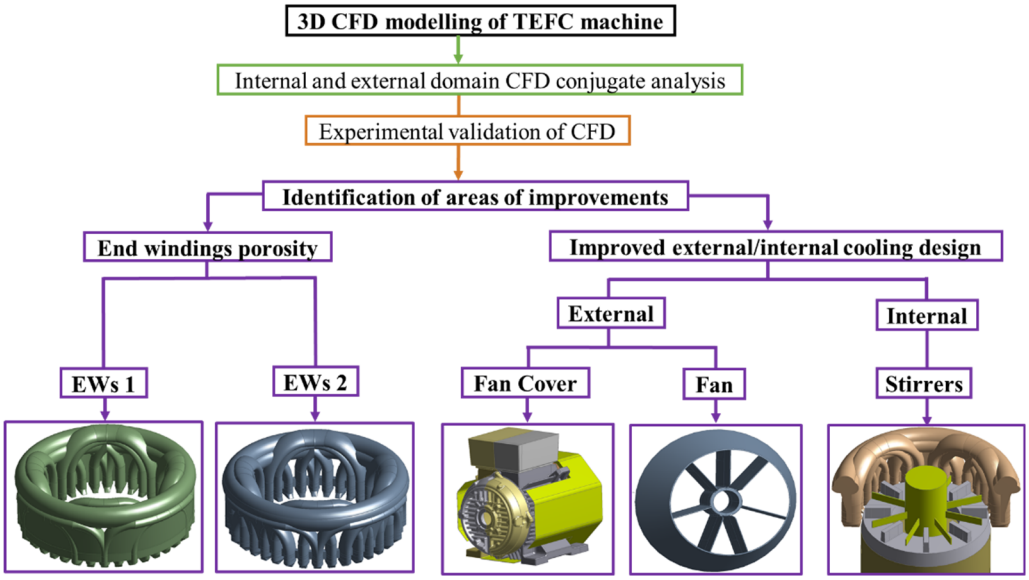


Figure 7.1: CFD modelling approach of alternative cooling configurations

The areas of improvements of the selected machine identified in this work were locally investigated in Chapters 4 (end region - end windings porosity and stirrers) and 5 (external domain - fan and fan cover) where potential benefits and drawbacks were discussed. The aim of the work presented in this chapter is to evaluate the impact of the proposed alternative cooling configurations on the overall thermal predictions and performance of the whole TEFC machine by means of the 360° CFD conjugate model described in Chapter 6; the same boundary conditions, material properties and electrical

losses described in section 6.2.2, were assumed for all configurations under investigation.

EWs model 1 and 2, presented and described in section 4.3.1 and 4.3.2.2, were both used to investigate the impact on the machine thermal predictions due to different levels of end windings porosity which led to a more uniform internal airflow distribution in the end regions: this is described in section 7.2.

Regarding the alternative internal cooling arrangement, two configurations of shaft mounted stirrers were investigated as described in section 4.4.1 (Stirrers model 1) and 4.4.2 (Stirrers model 2). Previous results from the local fluid flow and thermal investigation (internal domain only in Chapter 4 – Section 4.4) showed that Stirrers model 1 could lead to a rise of the heat transfer coefficient in the end region and therefore this was implemented within the 360° CFD conjugate model as described in section 7.3.

As described in section 5.4, the combination of a new fan and fan cover was considered and a fluid flow and thermal investigation of the external domain showed how a sensible rise of the mass flow rate of the air cooling and a more uniform distribution around the housing could be achieved; this led to significant improvements of the heat transfer coefficient. A CFD investigation with the developed full conjugate model, using the proposed fan and fan cover geometries, was carried out to evaluate the impact on the thermal performance of the TEFC machine: this is described in section 7.4 where experimental results from the proposed new fan are also presented.

For all the cases under investigation which are presented in the following sections, results of temperature rise ΔT^*, internal velocity v^*_{int} and mechanical power loss P^*_m were normalised as previously described in section 6.3 (ΔT^* - Equation 6.1, P^*_m - Equation 6.2) and 4.3.2 (v^*_{int} – Equation 4.2).

7.2 End Windings porosity: EWs model 1 and 2

As described in section 4.3.1, a new modelling approach for a more realistic end windings representation was considered in order to achieve more accurate and detailed predictions of the airflow distribution and of heat transfer rate from the end windings to the external housing of the TEFC machine. Previous CFD results from the local fluid flow and thermal investigation of the end region using the two new end windings geometries developed in this work (EWs model 1 and 2, section 4.3.2.2) show how a small change of porosity (from 3.7% to 15.2% for EWs model 1 and 2 respectively) can significantly affect the predictions of the complex thermal phenomena and the heat dissipation rate through the outer housing.

The impact of a more realistic end winding geometry on the overall thermal predictions of the whole TEFC machine was described in section 6.3.1 where EWs model 1 was implemented within the 360° CFD conjugate model; this geometry was judged to be the most physically realistic representation of the end windings. Results showed a good agreement between experimental and numerical predictions proving the accuracy and reliability of the CFD model developed. Following this, further investigations using both EWs model 1 and 2 allowed the impact of different levels of end windings porosity on the thermal performance of the TEFC machine to be assessed.

In the electrical machines the temperature of windings is a critical parameter as insulation lifetime is inversely related with rising temperature. The evaluation of the porosity impact of the two cases investigated was based therefore on the maximum and average winding temperatures seen. Figure 7.2 and Figure 7.3 show contours of non-dimensional temperature rise (ΔT^* as in Equation 6.1) of end windings and stator slots windings on the DE side as it was found out to be the hottest and therefore most critical part of the TEFC machine.

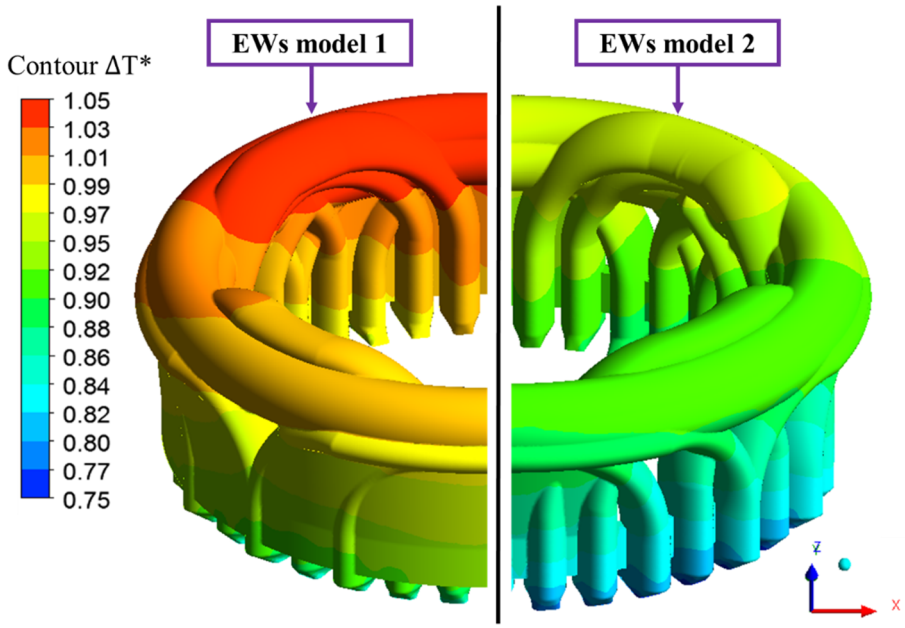


Figure 7.2: Non-dimensional EWs temperature rise, DE

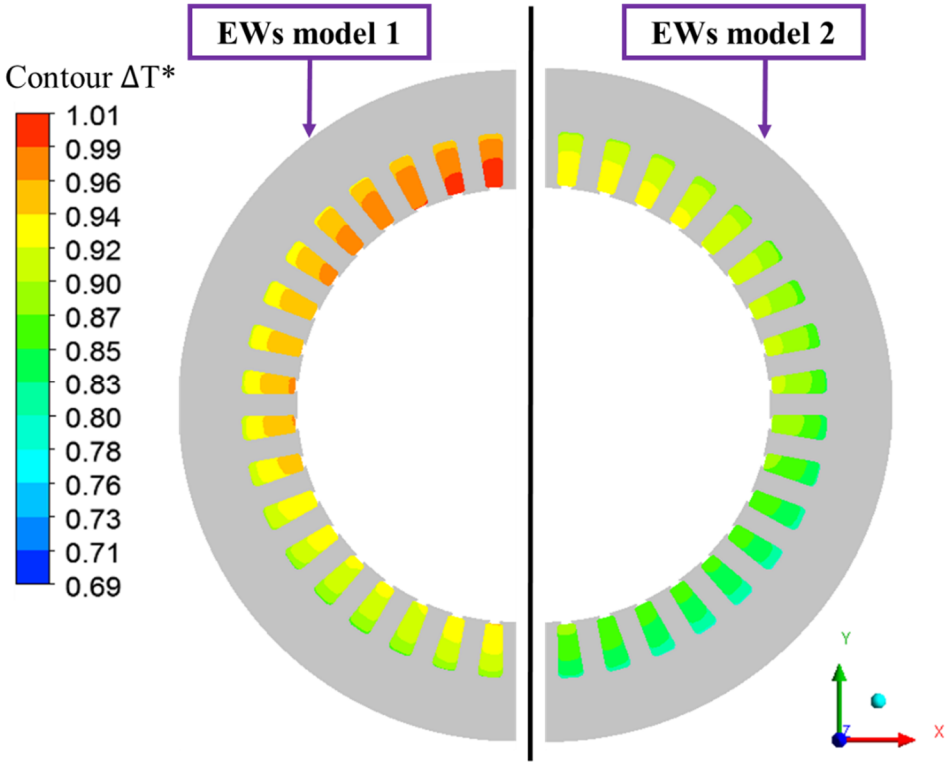


Figure 7.3: Non-dimensional windings temperature rise, DE

The joint conjugate analysis of internal and external domains of the selected TEFC machine allows the impact of the proposed internal cooling arrangement on the thermal performance to be assessed. Results computed from the comparison of both cases show how a higher level of porosity of the end windings geometry (EWs model 2 in this case) has impacts on the thermal predictions; the more uniform internal airflow distribution through the conductor cavities (as described in section 4.3.2.2), in conjunction with the external cooling typical of a TEFC machine, improves the heat dissipation rate through the external housing and an average reduction of the working temperature of about 7% is achieved. The same trend was found for the other machine components, such as rotor and stator core; an overview of the overall temperature drop of the machine can be seen in Figure 7.4 and Figure 7.5 where the maximum and average non-dimensional temperature rises are reported respectively. The normalised results presented in Figure 7.4 are reported in more detail in Table 7.1 where the percentage difference between the two cases under investigation, calculated as in Equation 7.1, is also presented.

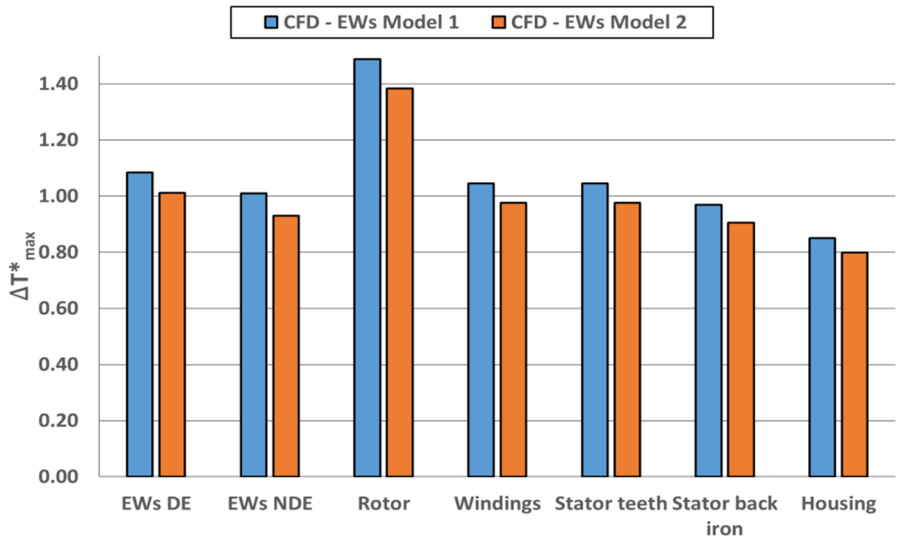


Figure 7.4: Machine components maximum non-dimensional temperature rise –EWs model 1 and 2

	Non-dimensional Max Temperature rise (ΔT^*_{max})		
	CFD - EWs 1	CFD - EWs 2	% difference with EWs 1 model
EWs DE	1.08	1.01	-6.82
EWs NDE	1.01	0.93	-8.15
Rotor	1.49	1.38	-7.34
Windings	1.04	0.98	-6.82
Stator teeth	1.05	0.98	-6.78
Stator back iron	0.97	0.90	-6.81
Housing	0.85	0.80	-6.17

Table 7.1: Machine components maximum non-dimensional temperature rise –EWs model 1 and 2, % difference

$$\%\ difference = \frac{|\Delta T_{CFD,EWs\,2} - \Delta T_{CFD,EWs\,1}|}{\frac{1}{2}\cdot(\Delta T_{CFD,EWs\,2} + \Delta T_{CFD,EWs\,1})} \cdot 100 \qquad \textbf{7.1}$$

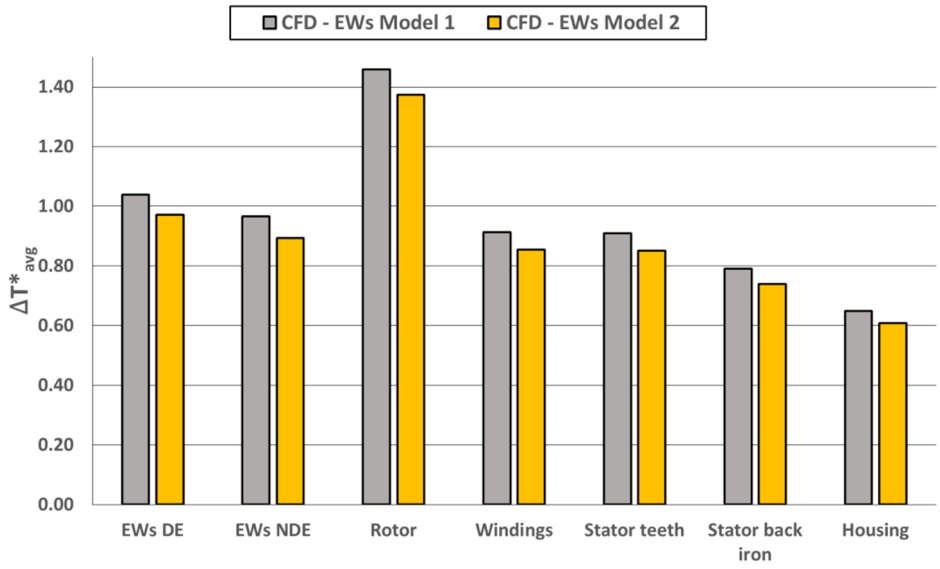


Figure 7.5: Machine components average non-dimensional temperature rise –EWs model 1 and 2

A more controlled and accurate winding process, capable of maximising the level of openness, as assumed for EWs 2, through the bundle of conductors in the end regions, can be considered a promising cooling option for a TEFC machine. Significant temperature drops can be achieved without altering the original machine geometry/design and without introducing additional mechanical losses; moreover, lower working temperatures would also lead to improvements in terms of increasing insulation lifetime and reducing copper losses which are strongly dependent upon the temperature.

7.3 Improved internal cooling design

As described in section 4.4.1, in accordance with literature on similar works in this area, the introduction of shaft mounted stirrers in the end region can have a beneficial effect on thermal performance. However, the local investigation presented in section 4.4 and in previous works by Micallef et al. [54], were not considering the machine as a whole and therefore the impact of the external cooling of the TEFC machine on the computed results was not considered.

In the present work, the stirrers configuration (Stirrers model 1, section 4.4.1) which provided better local results in terms of heat transfer coefficient computed on the end windings and external frame surfaces was investigated and compared with the original machine design case. The new geometry was implemented within the 360° CFD conjugate model described in section 6.2 (EWs model 1 implemented) in both end regions of the TEFC machine (DE and NDE).

Results of temperature and velocity were computed in order to assess the effectiveness of the proposed cooling design. Similarly to the results presented in section 4.4.1, the internal airflow is significantly affected by the stirrers with overall higher velocity achieved in the end region compared to the original design case. As expected the internal airflow distribution and magnitude is not influenced by the external cooling due to the structure of the TEFC machine whose enclosure does not allow the external air to circulate internally. Figure 7.6 shows a comparison of contours of non-dimensional velocity of the primary swirling flow in the end region between the original and proposed cooling design.

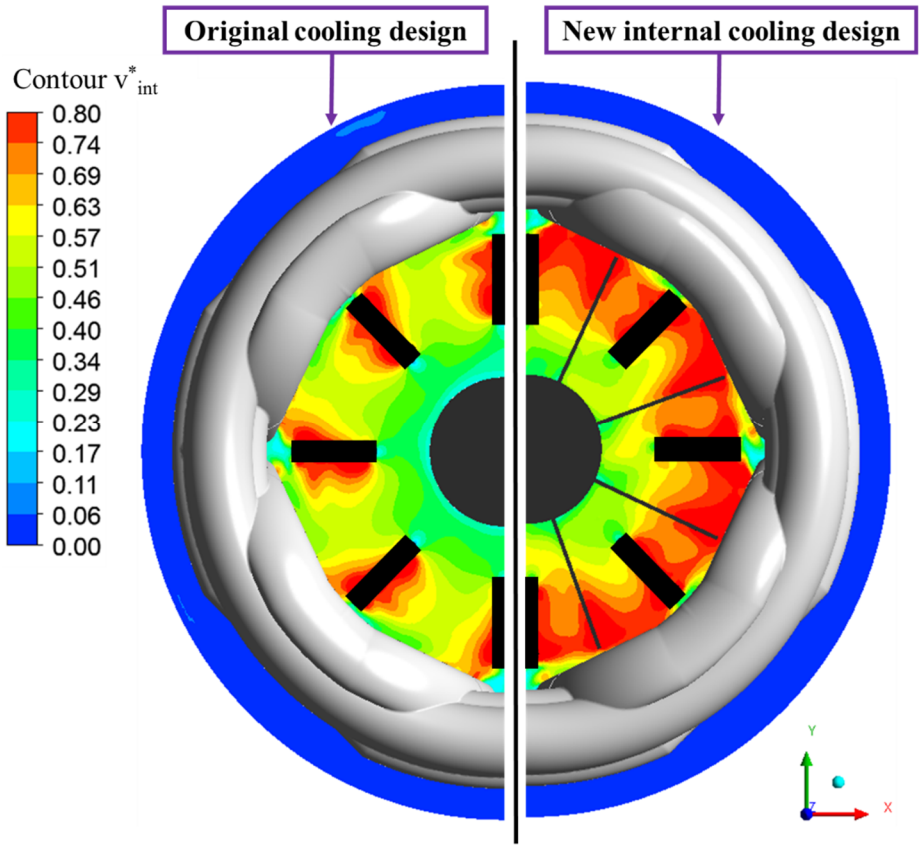


Figure 7.6: Non-dimensional end region airflow velocity magnitude

However, as can be seen from Figure 7.7, the impact of the stirrers on the temperature of the end windings is only marginal. The same trend was found also for the other machine components; in addition an increase of the overall windage losses by up to 10% was computed. In the TEFC machine under investigation the dominant cooling effect is therefore due to the external airflow; small geometrical internal changes do not significantly affect the heat flow dissipation rate.

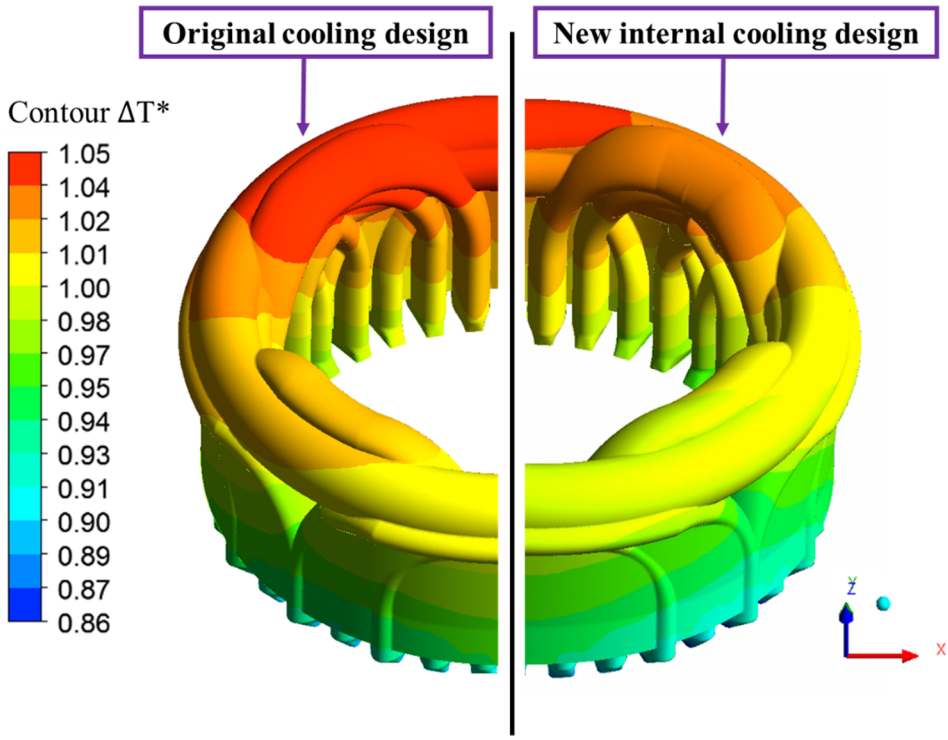


Figure 7.7: Non-dimensional EWs temperature rise, DE

Results clearly show that the introduction of stirrers in the end regions does not lead to significant improvements of the machine thermal performance; moreover, as expected there is a drawback due to additional windage losses which are introduced by the proposed internal cooling design.

However it is the opinion of the author that a combination of shaft mounted stirrers with a direct control of the end winding porosity (as discussed in section 7.2) could be considered to reduce the internal convective thermal resistance between end winding and frame and therefore increase the overall heat transfer coefficient in the end region (as discussed in section 4.4.1). The proposed design modification would lead to higher internal airflow velocities while a controlled winding process would provide a more uniform airflow distribution in the end region of the TEFC machine with consequent rise of the heat dissipation rate through the external housing.

7.4 Improved external cooling design

As discussed in section 5.4, an alternative external cooling arrangement was considered in this work to improve the TEFC machine performance: the proposed design consisted of a new fan and fan cover both aimed to create an enhanced and more uniform airflow distribution around the external housing. The CFD study of the external fluid domain presented in section 5.4.1 shows how the proposed cooling design can provide a significant rise of the cooling mass flow rate and a reduction of the airflow leakage from the fins channels; both these factors led to sensible improvements of the external heat transfer coefficient predictions by up to 50%.

The new fan and fan cover geometries were therefore implemented within the 360° CFD conjugate model presented in section 6.2 which was used to numerically assess the effectiveness of the proposed cooling design and its impact on the thermal predictions of the TEFC machine at rated load condition.

The maximum windings temperatures were computed and results were compared with those from the original cooling design case; this is shown in Figure 7.8 and Figure 7.9 below where contours of non-dimensional temperature rises of end windings and stator slots windings on the DE side are reported. It can be noted how the new external cooling design significantly affects the thermal predictions of the TEFC machine; due to the increased mass flow rate and more uniform airflow distribution around the external housing a considerable windings temperature rise reduction of about 30% can be achieved.

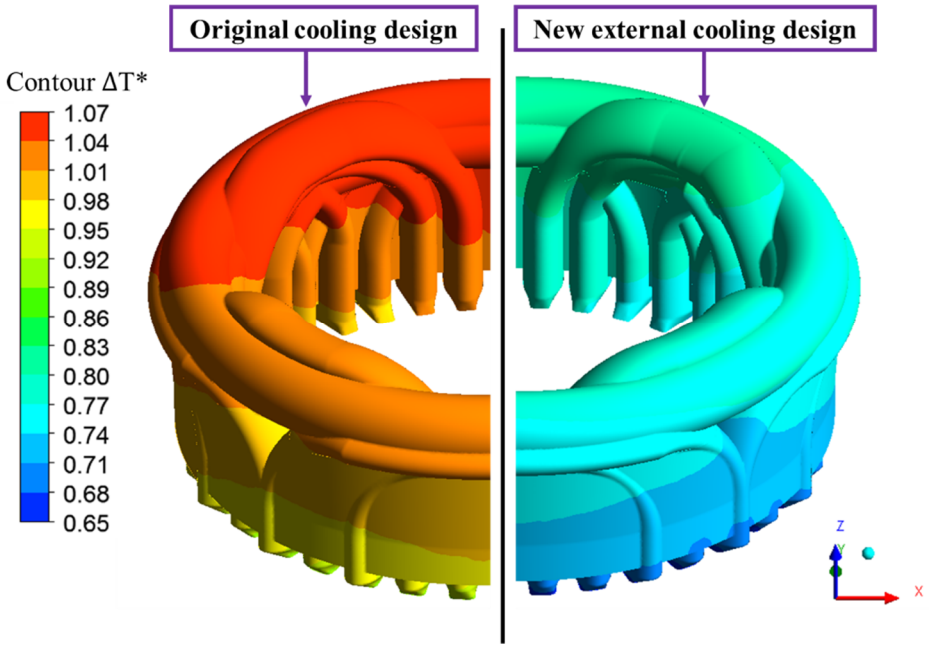


Figure 7.8: non-dimensional EWs temperature rise, DE

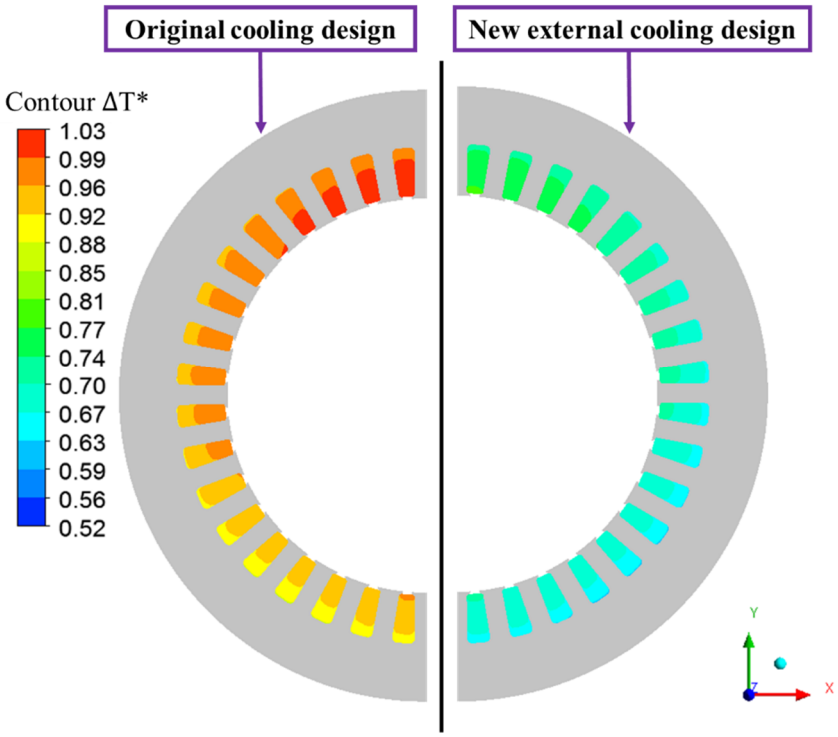


Figure 7.9: non-dimensional stator temperature rise, DE

The new external cooling arrangement has a significant impact on the thermal CFD predictions of the other machine components as well; an overview of the overall temperature drop of the machine can be seen in Figure 7.10 and Figure 7.11 below where the maximum and average non-dimensional temperature rises are reported respectively. The normalised results presented in Figure 7.10 are reported in more detail in Table 7.2 where the percentage differences between the two CFD cases under investigation, calculated as in Equation 7.2, are presented; an average temperature rise reduction of about 30% is achieved.

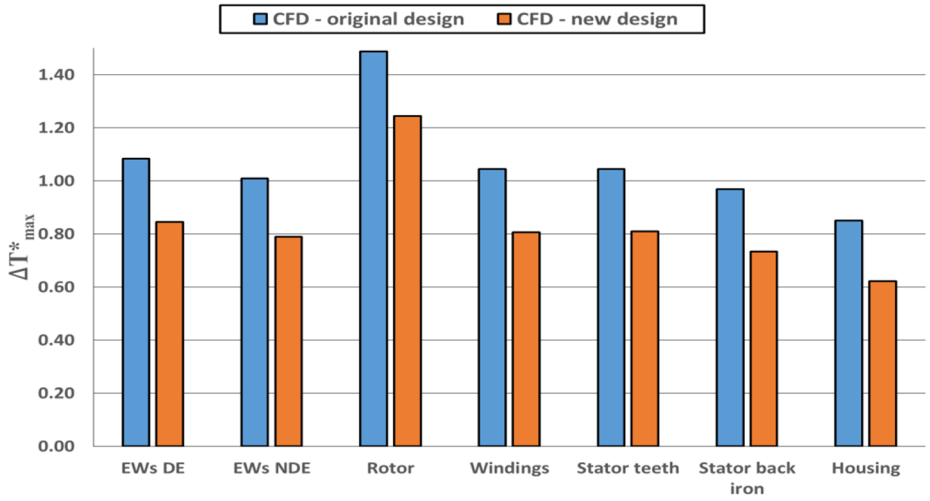


Figure 7.10: Machine components maximum non-dimensional temperature rise – original and proposed external cooling design

	Non-dimensional max Temperature rise (ΔT^*_{max})		
	CFD - Original design	CFD - New design	% difference with EWs 1 model
EWs DE	1.08	0.84	-26.85
EWs NDE	1.01	0.79	-26.71
Rotor	1.49	1.24	-18.95
Windings	1.04	0.81	-27.23
Stator teeth	1.05	0.81	-27.07
Stator back iron	0.97	0.73	-29.36
Housing	0.85	0.62	-33.03

Table 7.2: Machine components maximum non-dimensional temperature rise – original and proposed external cooling design

$$\% \, difference = \frac{|\Delta T_{CFD,new\ design} - \Delta T_{CFD,original\ design}|}{\frac{1}{2} \cdot (\Delta T_{CFD,new\ design} + \Delta T_{CFD,original\ design})} \cdot 100 \quad \textbf{7.2}$$

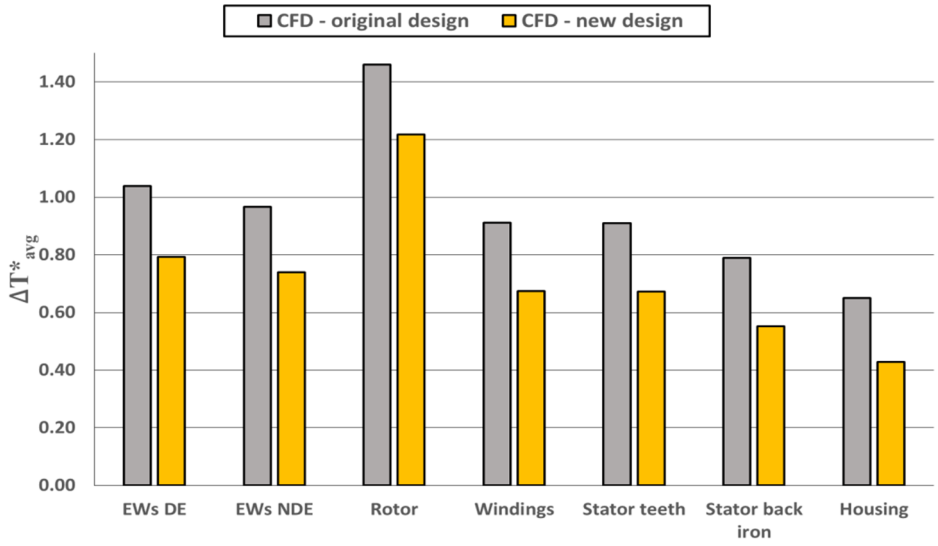


Figure 7.11: Machine components average non-dimensional temperature rise – original and proposed external cooling design

The impact of the proposed external cooling design on the overall machine efficiency was considered; the achieved temperature drop could lead to a reduction of approximately 25.7 W of the machine copper losses.

On the other hand, the use of a bigger fan introduces an additional 20 W of windage losses at 1500 rpm which almost negates any improvements of the overall machine efficiency. The mechanical power losses associated with the proposed external cooling arrangement were numerically estimated as described in section 6.3.2 for a speed range from 400 to 1500 rpm. Figure 7.12 below reports the trend of mechanical power losses of the two cases under investigation and their rise due to the proposed fan design.

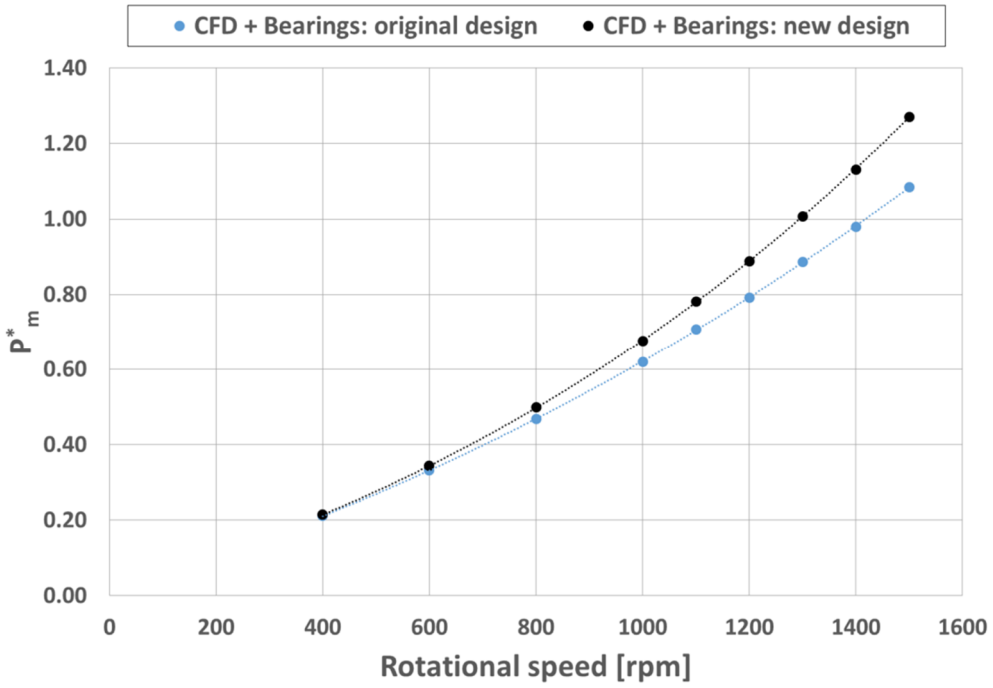


Figure 7.12: Non-dimensional mechanical power losses – original and new design

Although the proposed cooling arrangement only marginally affects the performance, it is worth highlighting that the significant reduction achieved in the operating temperature can have an important impact on the lifetime of the materials and insulation without any drastic changes of the machine design and its efficiency.

CFD results show that the proposed external cooling design can be considered the most promising option in terms of reduction of the machine working temperature simply using a different fan and fan cover design model; for this reason, the new arrangement was also experimentally tested and results investigated.

The experimental investigations utilised a 3D printed version of the new fan described in section 5.4 which was manufactured in ABS material; a suitable CAD model, taking into account the keyway feature to fit on the machine shaft, was created by the author. Figure 7.13 below shows a comparison between the original and the proposed fan design; in Figure 7.14 the latter is shown successfully mounted on the NDE side of the TEFC machine shaft.

The extended fan cover required further mechanical design investigation and therefore it was not included in the experimental investigation; however this will be object of future works.



Figure 7.13: Original (left) and proposed new fan (right) design

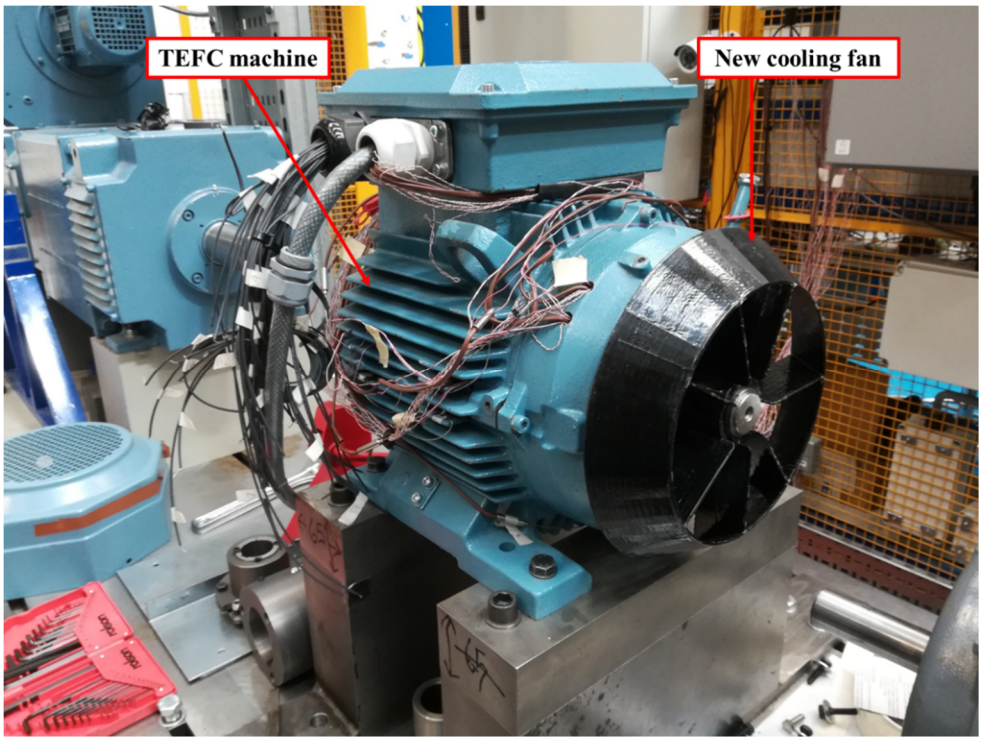


Figure 7.14: 3D printed new fan mounted on the TEFC machine, tests included the original fan cover design

As described in section 6.3, a load test at rated full load condition (n = 1466 rpm, T = 71.6 Nm) was conducted to investigate the impact of the new fan on the thermal performance of the TEFC machine; temperature measurements were taken as described in previous sections and results were compared with experimental data from the original cooling design case.

A comparison of the stator teeth and back iron non-dimensional temperature rises on DE and NDE side of the machine is reported in Figure 7.15 and Figure 7.16 below respectively; more details of the normalised temperature rise results and percentage differences between the two cooling designs, calculated as in Equation 7.3, are presented in Table 7.3.

Similarly, results of non-dimensional temperature rises of the end windings and end region air are reported in Figure 7.17, Figure 7.18 and Table 7.4.

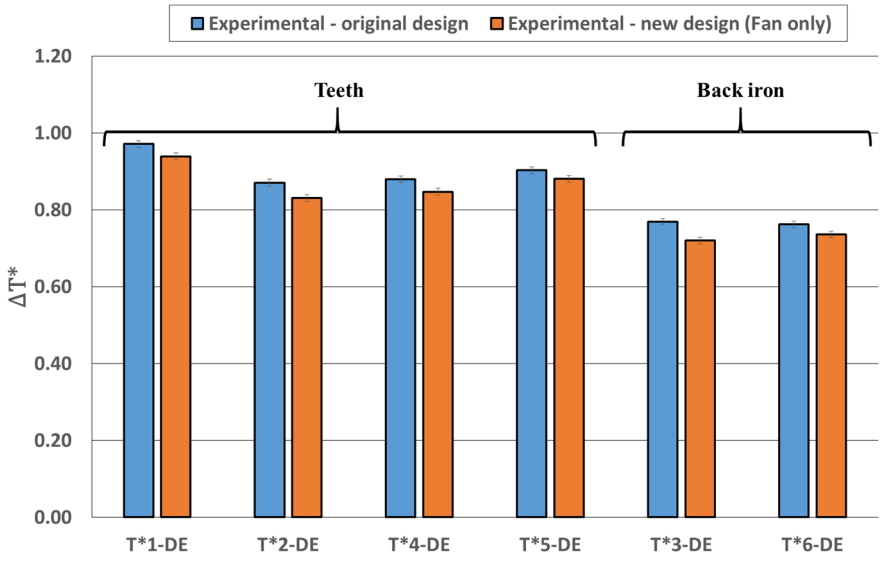


Figure 7.15: Stator teeth and back iron non-dimensional temperature rise, DE side

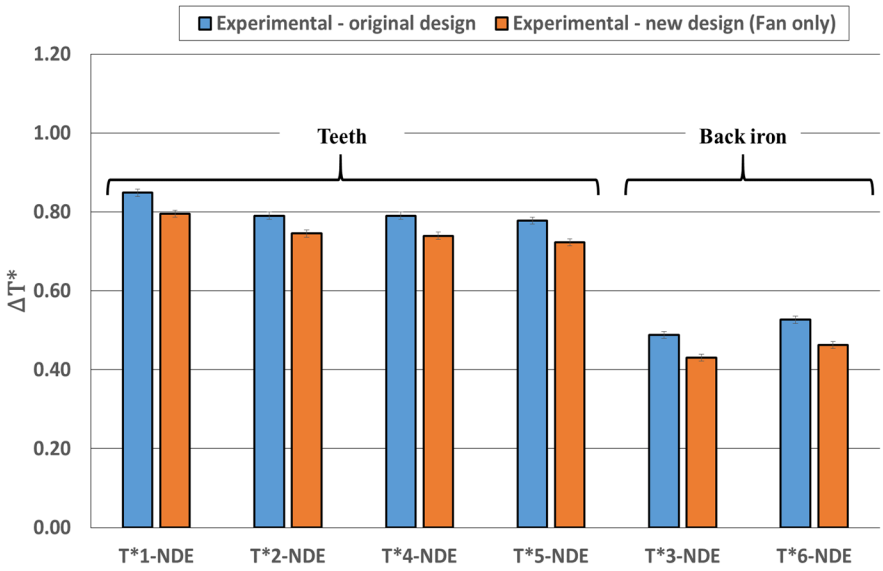


Figure 7.16: Stator teeth and back iron non-dimensional temperature rise, NDE side

			Non-dimensional Temperature rise (ΔT*)		
			Original design	New design (Fan only)	% difference with original design
Stator DE	Teeth	$T^*_{1\text{-DE}}$	0.97	0.94	-3.35
		$T^*_{2\text{-DE}}$	0.87	0.83	-4.74
		$T^*_{4\text{-DE}}$	0.88	0.85	-3.79
		$T^*_{5\text{-DE}}$	0.90	0.88	-2.51
	Back iron	$T^*_{3\text{-DE}}$	0.77	0.72	-6.59
		$T^*_{6\text{-DE}}$	0.76	0.74	-3.47
Stator NDE	Teeth	$T^*_{1\text{-NDE}}$	0.85	0.80	-6.41
		$T^*_{2\text{-NDE}}$	0.79	0.75	-5.89
		$T^*_{4\text{-NDE}}$	0.79	0.74	-6.63
		$T^*_{5\text{-NDE}}$	0.78	0.72	-7.31
	Back iron	$T^*_{3\text{-NDE}}$	0.49	0.43	-12.54
		$T^*_{6\text{-NDE}}$	0.53	0.46	-12.93

Table 7.3: Stator non-dimensional experimental temperature rise, original and new cooling design % difference

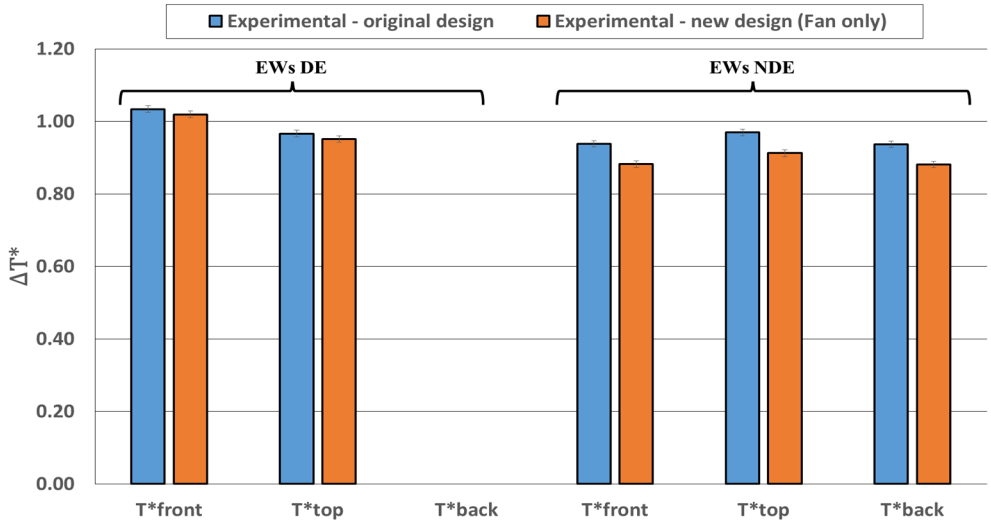


Figure 7.17: EWs experimental non-dimensional temperature rise, original and new cooling design

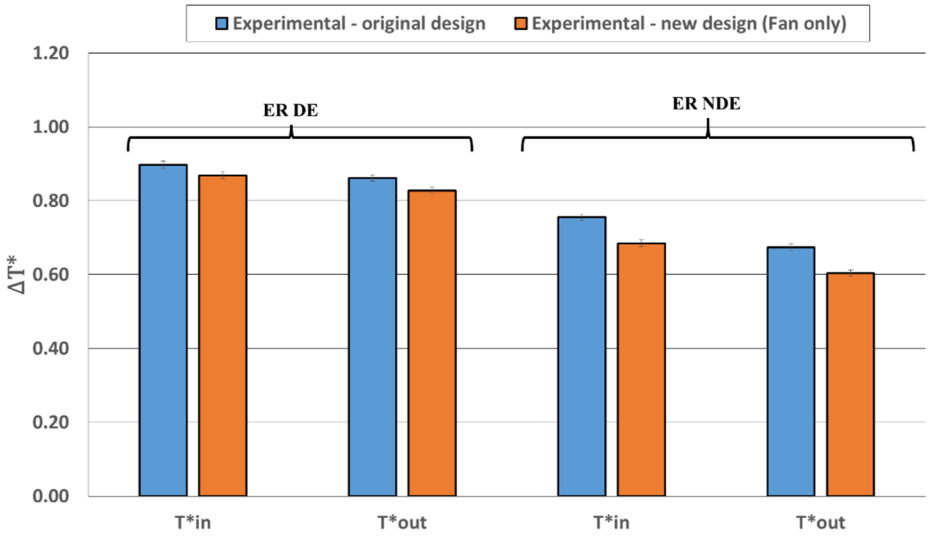


Figure 7.18: End region experimental non-dimensional temperature rise, original and new cooling design

		Non-dimensional Temperature rise (ΔT*)		
		Original design	New design (Fan only)	% difference with original design
EWs DE	$T^*_{EWs_front}$	1.03	1.02	-1.42
	$T^*_{EWs_top}$	0.97	0.95	-1.50
	$T^*_{EWs_back}$			
EWs NDE	$T^*_{EWs_front}$	0.94	0.88	-6.15
	$T^*_{EWs_top}$	0.97	0.91	-6.04
	$T^*_{EWs_back}$	0.94	0.88	-6.10
ER DE	$T^*_{ER_in}$	0.9	0.87	-3.29
	$T^*_{ER_out}$	0.86	0.83	-4.02
ER NDE	$T^*_{ER_in}$	0.76	0.68	-9.81
	$T^*_{ER_out}$	0.67	0.6	-11.07

Table 7.4: EWs and ER experimental non-dimensional temperature rise, original and new cooling design % difference

$$\%\, difference = \frac{|\Delta T_{exp,new\ design} - \Delta T_{exp,original\ design}|}{\frac{1}{2} \cdot (\Delta T_{exp,new\ design} + \Delta T_{exp,original\ design})} \cdot 100 \qquad \textbf{7.3}$$

The proposed cooling design improvement consisting of the fan only led to an overall temperature reduction of about 13%; in comparison with CFD predictions (Table 7.2), the achieved temperature reduction is lower than expected (30% predicted against 13% measured).

However, there are two main reasons which can be addressed which can justify the differences between experimental results and CFD predictions:

- The extended fan cover, which was implemented with the new fan in the 360° CFD conjugate model, was not used during the experimental test. The thermal impact of the improved airflow distribution around the housing and the reduced air leakage from the fin channels (as described in section 5.4.1) was therefore not taken into account.
- As described in section 6.3.1, in the 360° CFD conjugate model with the original cooling design the fan geometry used was smaller than the real one provided for the experimental tests (Figure 6.23). Therefore the improvements seen from the CFD models, as reported in Figure 7.10 and Table 7.2, were expected to have a minor impact on the experimental thermal performance of the TEFC machine.

As described in section 6.3.2, a No-Load Test was carried out for a speed range from 400 to 1500 rpm in order to investigate the mechanical power losses associated with the proposed cooling arrangement. The CFD 360° external fluid domain presented in Chapter 5 was used to compute the windage losses associated with the new fan design for the speed range under investigation.

Figure 7.19 below shows a comparison of the trend of the total non-dimensional mechanical power losses P^*_m (Equation 6.2) predicted numerically and those experimentally measured; as can be seen a good agreement was achieved.

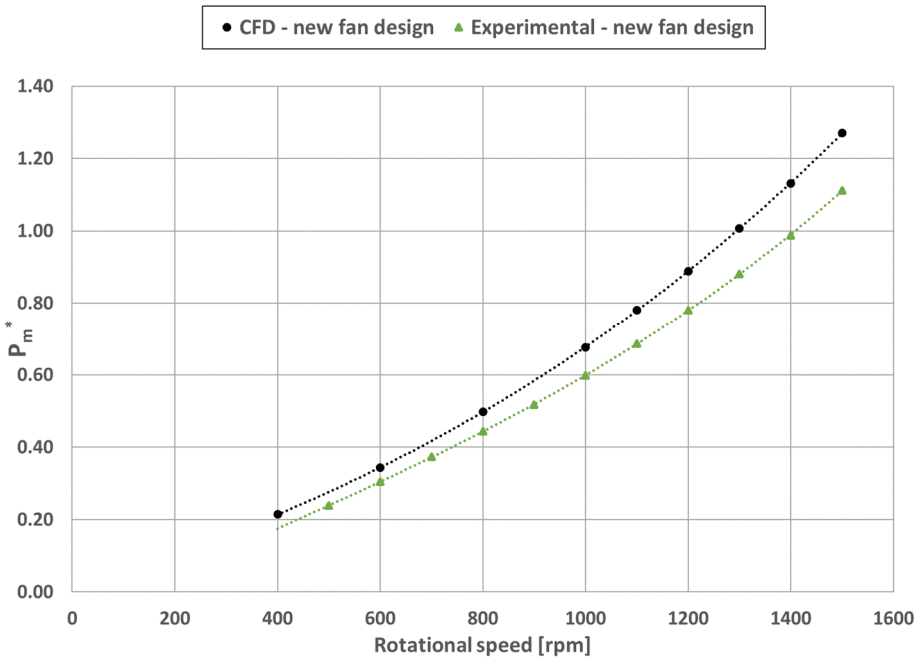


Figure 7.19: Non-dimensional mechanical power losses CFD (bearings + windage) and experimental trends

7.5 Summary

The 360° CFD conjugate model of the whole TEFC machine, validated in Chapter 6, was used to numerically assess the effectiveness of the proposed alternative cooling arrangements on the cooling capability and the overall performance of the selected machine.

The use of a more porous end windings configuration provided a more uniform internal airflow distribution in the end regions and improved the thermal performance of the machine. Numerical results showed how a small change of porosity of the end windings geometry of about 11% can affect and reduce the overall machine working temperature at rated full load condition: a temperature reduction of about 7% can be achieved. The introduction of a more accurate control of the machine winding process, in order to maximise the level of porosity through the bundle of conductors in the end regions, improves the performance of the TEFC machine under investigation. Sensible cooling improvements can be achieved without altering the original design of the machine and without the addition of further losses which could negatively affect the overall machine efficiency.

Several other changes of the existing original machine cooling design were also considered. Although the internal alternative cooling arrangement consisting of shaft mounted stirrers only had a negligible effect on the machine thermal performance, the proposed external design showed considerable positive impact on thermal predictions of the TEFC machine.

The numerical analysis of the machine performance with the proposed external cooling design showed that a significant overall reduction of the working temperature of about 30% can be achieved, with consequent benefits of the machine materials lifetime. Experimental tests were carried out to investigate the impact of the fan only (fan cover required further mechanical analyses) on the thermal performance of the TEFC machine; thermal measurement showed that an overall temperature reduction of about 13% was achieved.

8 Conclusions and Recommendations

TEFC machines are the most commonly used in ordinary industrial enviroments due to their robustness and capability to work in dirty, moist or mildly corrosive operating conditions. The design of this type of machine has been unchanged for decades, being a low cost high volume design where the benefits around improvement have been regarded as marginal. However, with the increasing emphasis on efficiency and sustainability there is now a growing awareness within industry of the need to address the thermal management of this machine type; this is a crucial step since any rise in temperature can significantly reduce the overall machine efficiency.

The work described in this thesis develops a full thermal CFD 3D model of a typical low voltage TEFC induction motor and look at detailed airflow and heat transfer modelling of such a machine in order to identify the most promising areas of improvement. The main steps of this work can be summarised as follows:

1. Investigation of the nature of the complex flow field in the end region.
2. Development of a new modelling approach for a more realistic end windings representation to achieve more accurate thermal predictions.
3. Performance of a joint internal and external fluid flow and heat transfer conjugate analysis of the whole selected TEFC machine.
4. Experimental validation of the CFD thermal models developed.
5. Use of the validated model to develop a full understanding of the thermal behaviour of the TEFC machine and to identify opportunities to improve performance.
6. Investigation of alternative cooling arrangements and their impact on the TEFC machine performance.

8.1 CFD thermal modelling conclusions

CFD allows the modelling and simulation of very complex geometries and fluid flows, with a high degree of detail and flexibility, allowing accurate predictions of temperature distribution within the electrical machine to be achieved.

Despite the geometrical symmetry of the TEFC machine under investigation, a full 360° CFD model was necessary to correctly model the external airflow and to have sensible predictions of the thermal performance of the machine. In the present work it was observed that periodic boundary conditions could not be employed due to non-periodic geometry of the cooling fan. CFD results also showed that a 180° model with symmetry boundary conditions could not be used due to under predictions of external airflow velocity and mass flow rate of about 60% compared to the 360° model; this was due to the fact that Ansys Fluent assumed a zero normal velocity component at the symmetry plane.

Due to the structure of the machine under investigation (totally enclosed), the development of a full 3D thermal model required the joint simultaneous analysis of internal and external fluid and solid domains.

The CFD conjugate model developed was then experimentally validated; tests at rated full load condition were performed and measured results were compared with numerical predictions with maximum percentage differences of about 30% achieved. No-Load tests were also carried out which allowed to validate the numerical predictions of mechanical losses.

A new methodology based on the modelling of more realistic end windings representation, which potentially can be applied to different kinds of machines, was developed in this work. This novel approach provides an improved and accurate prediction of complex fluid flow and heat transfer phenomena compared to a simplified representation commonly used. This aspect is confirmed and validated by experimental thermal results measured in the

machine end regions; a good agreement with numerical predictions is achieved with maximum differences of about 9.8%.

As one of the objectives of this work, most promising areas of improvements were identified and the impact of alternative cooling designs on the overall machine efficiency were investigated with the numerical model developed and experimentally validated as stated above.

This part of the study highlights important features worth considering when designing end regions of TEFC induction motors; a more accurate and detailed control of the porosity of the end windings geometry can lead to sensible cooling improvements without altering the original design of the whole machine. This was confirmed by numerical predictions of the CFD conjugate model developed; two different level of end windings porosity (3.7% and 15.2% for EWs model 1 and 2 respectively) were considered and their impact on the overall machine thermal performance was investigated. CFD results showed how the small change of porosity considered led to an overall machine temperature reduction of about 7% (EWs model 2).

An alternative external cooling design consisting of a new fan and fan cover was considered and the impact on the overall machine efficiency was considered; a significant temperature reduction of about 30% was achieved. The achieved temperature drop could lead to a reduction of copper winding losses of about 25.7 W but also to a 20 W increase of the windage losses. However the achieved temperature drop of critical components, such as windings, which lead to significant improvements in terms of materials lifetime can thus be achieved without any net reduction in efficiency.

Experimental tests were carried out to investigate the impact of the proposed fan design only (fan cover required further mechanical analyses) on the thermal performance of the TEFC machine; thermal measurement showed that an overall temperature reduction of about 13% was achieved.

Geometrical modifications of the internal original cooling design, consisting of shaft mounted stirrers, were considered too. Numerical results showed that their impact on the machine thermal performance was only marginal against a rise of the overall windage losses by up to 10%. Results showed that more significant thermal improvements can be achieved combining the stirrers configuration with other cooling optimisations as previously discussed.

8.2 Novelty in this Thesis

- Development of a more realistic and detailed end windings geometric representation in order to more accurately capture complex fluid flow and thermal phenomena occurring the end region.
- CFD investigation of different levels of end windings porosity and their impact on local fluid flow and thermal predictions in the end region.
- Creation of CFD methodology for conjugate heat transfer analysis of full 3D TEFC machine including internal/external fluid and solid domains for accurate understanding and prediction of machine thermal behaviour.
- Experimental validation of developed CFD methodology.
- Use of 360° CFD conjugate model developed to assess alternative cooling designs.

8.3 Future works

- Experimental investigation of a more accurate and controlled winding process to improve the internal airflow distribution in the end regions aimed to reduce the thermal resistance between EWs and the external frame.
- Experimental investigation of the proposed external cooling design (fan and fan cover) and its impact on the external airflow cooling.
- Use of infrared fibre-optic sensors for measuring temperature of rotor core.
- Further CFD and experimental investigation of stator-housing airgaps: a round stator geometry or thermal silicone to fill the void spaces could be both considered to reduce the overall thermal resistance.

References

1. Brown, T., Gambhir, A., Florin, N., Fennel, P., *Reducing CO2 emissions from heavy industry: a review of technologies and considerations for policy makers*. Grantham Institute for Climate Change 2012.
2. *ABB Group, Motor guide - Low voltage motors*.
3. Pyrhonen, J., Jokinen, T., Hrabovcová, V., *Design of Rotating Electrical Machines*. 2014, Chichester, West Sussex, United Kingdom: Wiley.
4. Staton, D. A., Boglietti, A., Cavagnino, A., *Solving the More Difficult Aspects of Electric Motor Thermal Analysis in Small and Medium Size Industrial Induction Motors.* IEEE Transactions on Energy Conversion, 15 August 2005. 20(3): p. 620-628.
5. Yazicioğlu, B., Yüncü, H., *A Correlation for optimum fin spacing of vertically-based rectangular fin arrays subjected to natural convection heat transfer*. Vol. 29. 2009. 99-105.
6. Valenzuela, M.A., Tapia, J.A., *Heat Transfer and Thermal Design of Finned Frames for TEFC Variable Speed Motors*. in *IECON 2006 - 32nd Annual Conference on IEEE Industrial Electronics*. 2006.
7. Micallef, C., *End Winding Cooling in Electrical Machines*, in *Department of Mechanical, Materials and Manufacturing Engineering*. 2006, University of Nottingham: Nottingham.
8. DeWaard, S.J., *Cutaway view of TEFC induction motor*. 2011: Rotterdam Ahoy Eurosport.
9. Ltd, M.D. *www.motor-design.com/motorcad.php*. 1990.
10. Bejan, A., *Heat transfer*, ed. Wiley. 1993.
11. Boglietti, A., Cavagnino, A., Staton, D., *Determination of Critical Parameters in Electrical Machine Thermal Models.* IEEE Transactions on Industry Applications, 2008. 44(4): p. 1150-1159.
12. Staton, D. A., Pickering, S.J., Lampard, D., *Recent Advancement in the Thermal Design of Electric Motors*, in *SMMA "Emerging Technologies for Electric Motion Industry"*. 2001: Durham, North Carolina, USA.
13. Staton, D.A., Cavagnino, A., *Convection Heat Transfer and Flow Calculations Suitable for Analytical Modelling of Electric Machines*. in *IECON 2006 - 32nd Annual Conference on IEEE Industrial Electronics*. 2006.
14. Boglietti, A., Cavagnino, A., Stator, D.A., Popescu, M., Cossar, C., McGilp, M.I., *End Space Heat Transfer Coefficient Determination for Different Induction Motor Enclosure Types*. in *2008 IEEE Industry Applications Society Annual Meeting*. 2008.
15. Micallef, C., Pickering, S.J., Simmons, K.A., Bradley, K.J., *Improved Cooling in the End Region of a Strip-Wound Totally Enclosed Fan-Cooled Induction Electric Machine.* IEEE Transactions on Industrial Electronics, 2008. 55(10): p. 3517-3524.
16. Mejuto, C., Mueller, M., Staton, D.A., Mebarki, S., Al-Khayat, N., *Thermal Modelling of TEFC Alternators*. in *IECON 2006 - 32nd Annual Conference on IEEE Industrial Electronics*. 2006.

17. Farsane, K., Desevaux, P., Panday, P.K., *Experimental study of the cooling of a closed type electric motor.* Applied Thermal Engineering, 2000. 20(14): p. 1321-1334.
18. Hay, N., Lampard, D., Pickering, S.J., Roylance, T.F., *Air flow and heat transfer over the ribbed surface of an externally cooled electric motor.* Proceedings of the ASME-JSME Thermal Engineering Joint Conference, Vol. 1: p. pp 321-326.
19. Tóth, K., *Examination of heat transfer conditions of finned motor case for shell-heated motors,* Periodica Polytechnica Electrical Engineering (Archives); Vol 24 No 3-4 (1980), 1980.
20. Childs, P.R.N., Long, C.A., *A Review of Forced Convective Heat Transfer in Stationary and Rotating Annuli.* Proceedings of the Institution of Mechanical Engineers, Part C: Journal of Mechanical Engineering Science, 1996. 210(2): p. 123-134.
21. Howey, D.A., Childs, P.R.N., Holmes, A.S., *Air-Gap Convection in Rotating Electrical Machines.* IEEE Transactions on Industrial Electronics, 2012. 59(3): p. 1367-1375.
22. Kuosa, M., Sallinen, P., Larjola, J., *Numerical and experimental modelling of gas flow and heat transfer in the air gap of an electric machine.* Journal of Thermal Science, 2004. 13(3): p. 264.
23. Saari, J., *Thermal modelling of high-speed induction machines*. 1995. 2-82.
24. Jakoby, R., Kim, S., Wittig, S., *Correlations of the Convection Heat Transfer in Annular Channels With Rotating Inner Cylinder.* Journal of Engineering for Gas Turbines and Power, 1999. 121(4): p. 670-677.
25. Micallef, C., Pickering, S.J., Simmons, K.A., Bradley, K.J., *Windage loss and Heat transfer in high speed, small rotaing concentric cylinders*, in *UK Heat Transfer Conference*. 2005: Manchester.
26. Taylor, G.I., *Stability of a viscous liquid contained between two rotating cylinders.* Philosophical Transactions of the Royal Society of London. Series A, Containing Papers of a Mathematical or Physical Character, 1923. 223(605-615): p. 289.
27. Becker, K.M., Kaye, J., *Measurements of Diabatic Flow in an Annulus With an Inner Rotating Cylinder.* Journal of Heat Transfer, 1962. 84(2): p. 97-104.
28. Jr, C.G., *Heat transfer characteristics of the rotational and axial flow between concentric cylinders.* Transactions of the ASME, 1958. 80: p. 79-90.
29. Fénot, M., Dorignac, E., Giret, A., Lalizel, G., *Convective heat transfer in the entry region of an annular channel with slotted rotating inner cylinder.* Applied Thermal Engineering, 2013. 54(1): p. 345-358.
30. Trigeol, J.F., Bertin, Y., Lagonotte, P. *Thermal modeling of an induction machine through the association of two numerical approaches.* IEEE Transactions on Energy Conversion, 2006. 21(2): p. 314-323.
31. Becker, K.M., Kaye, J., *The Influence of a Radial Temperature Gradient on the Instability of Fluid Flow in an Annulus With an Inner Rotating Cylinder.* Journal of Heat Transfer, 1962. 84(2): p. 106-110.
32. Haumer, A., Kral, C., Kapeller, H., Bäuml, T., *The AdvancedMachines Library: Loss Models for Electric Machines*. 2009.

33. Zivotic-Kukolj, V., Soong, W.L., Ertugrul, N., *Iron Loss Reduction in an Interior PM Automotive Alternator.* IEEE Transactions on Industry Applications, 2006. 42(6): p. 1478-1486.
34. Fiorillo, F., Rietto A.M., *Rotational and alternating energy loss vs. magnetizing frequency in SiFe laminations.* Journal of Magnetism and Magnetic Materials, 1990. 83(1): p. 402-404.
35. Krings, A., *Iron Losses in Electrical Machines - Influence of Material Properties, Manufacturing Processes and Inverter Operation*. 2014, KTH School of Electrical Engineering: Sweden.
36. Mi, C.C., Slemon, G.R., Bonert, R., *Minimization of iron losses of permanent magnet synchronous machines.* Energy Conversion, IEEE Transactions on, 2005. 20(1): p. 121-127.
37. Paulides, J.J.H., Jewell, G.W., Howe, D., *An evaluation of alternative stator lamination materials for a high-speed, 1.5 MW, permanent magnet generator.* Magnetics, IEEE Transactions on, 2004. 40(4): p. 2041-2043.
38. Saari, J., *Thermal Analysis of High-Speed Induction Machines*. 1998, Acta Polytechnica Scandinavica, Helsinki University of Technology.
39. Bilgen, E., Boulos, R. *Functional Dependence of Torque Coefficient of Coaxial Cylinders on Gap Width and Reynolds Numbers.* Journal of Fluids Engineering, 1973. 95(1): p. 122-126.
40. SKF, *Rolling bearings and seals in electric motors and generators*. 2013.
41. Boglietti, A., Cavagnino, A., Staton, D.A., Shanel, M., Mueller, M., Mejuto, C., *Evolution and Modern Approaches for Thermal Analysis of Electrical Machines.* IEEE Transactions on Industrial Electronics, 2009. 56(3): p. 871-882.
42. La Rocca, A., Pickering, S.J., Eastwick, C.N., Gerada, C., *Enhanced cooling for an electric starter-generator for aerospace application*. in *7th IET International Conference on Power Electronics, Machines and Drives (PEMD 2014)*. 2014.
43. Mellor, P.H., Roberts, D., Turner, D.R., *Lumped parameter thermal model for electrical machines of TEFC design.* IEE Proceedings B - Electric Power Applications, 1991. 138(5): p. 205-218.
44. Boglietti, A., Cavagnino, A., Staton, D.A., *TEFC induction motors thermal models: a parameter sensitivity analysis.* IEEE Transactions on Industry Applications, 2005. 41(3): p. 756-763.
45. Mejuto, C., Mueller, M., Shanel, M., Mebarki, A., Staton, D.A., *Thermal modelling investigation of heat paths due to iron losses in synchronous machines*. in *2008 4th IET Conference on Power Electronics, Machines and Drives*. 2008.
46. Gilson, G.M., Raminosoa, T., Pickering, S.J., Gerada, C., Hann, D.B., *A combined electromagnetic and thermal optimisation of an aerospace electric motor*. in *Electrical Machines (ICEM), 2010 XIX International Conference on*. 2010.
47. Wenying, J., Jahns, T.M., *Coupled electromagnetic/thermal machine design optimization based on finite element analysis with application of artificial neural network*. in *Energy Conversion Congress and Exposition (ECCE), 2014 IEEE*. 2014.

48. Rajagopal, M.S., Aswatha Narayana, P.A., Quadir, G.A., Seetharamu, K.N., *Numerical and Experimental Heat Transfer Studies on Totally Enclosed Fan Ventilated Machines.* Electric Power Components and Systems, 2002. 30(8): p. 791-806.
49. Mugglestone, J., Pickering, S.J., Lampard, D., *Effect of geometric changes on the flow and heat transfer in the end region of a TEFC induction motor*. in *1999. Ninth International Conference on Electrical Machines and Drives (Conf. Publ. No. 468)*. 1999.
50. Micallef, C., Pickering, S.J., Simmons, K.A., Bradley, K.J., *Improvements in Air Flow in the End Region of a Large Totally Enclosed Fan Cooled Induction Motor*. in *IEEE International Conference on Electric Machines and Drives, 2005.* 2005.
51. Hettegger, M., Reinbacher-Köstinger, A., Bíró, O., *Characterizing the convective wall heat transfer on convoluted shapes in the end-region of an induction machine*. in *2012 XXth International Conference on Electrical Machines*. 2012.
52. Mugglestone, J., Lampard, D., Pickering, S.J., *Effects of end winding porosity upon the flow field and ventilation losses in the end region of TEFC induction motors*. in *1997 Eighth International Conference on Electrical Machines and Drives (Conf. Publ. No. 444)*. 1997.
53. Basso, G.L., Chong, Y.C., Goss, J., Staton, D.A., *Improved thermal model for predicting end-windings heat transfer*. in *2017 IEEE Energy Conversion Congress and Exposition (ECCE)*. 2017.
54. Saliba, A., Micallef, C., *Investigating the cooling performance of the end region of a small Totally Enclosed Fan Cooled (tefc) induction motor*. in *5th IET International Conference on Power Electronics, Machines and Drives (PEMD 2010)*. 2010.
55. Connor, P.H., Pickering, S.J., Gerada, C., Eastwick, C.N., Micallef, C., *CFD modelling of an entire synchronous generator for improved thermal management*. in *6th IET International Conference on Power Electronics, Machines and Drives (PEMD 2012)*. 2012.
56. Xu, Z., La Rocca, A., Pickering, S.J., Eastwick, C.N., Gerada, C., Bozhko, S., *Mechanical and thermal design of an aeroengine starter/generator*. in *2015 IEEE International Electric Machines & Drives Conference (IEMDC)*. 2015.
57. Jungreuthmayer, C., Bäuml, T., Winter, O., Ganchev, M., Kapeller, H., Haumer, A., Kral, C., *A Detailed Heat and Fluid Flow Analysis of an Internal Permanent Magnet Synchronous Machine by Means of Computational Fluid Dynamics.* IEEE Transactions on Industrial Electronics, 2012. 59(12): p. 4568-4578.
58. Kral, C., Haumer, A., Haigis, M., Lang, H., Kapeller, H., *Comparison of a CFD Analysis and a Thermal Equivalent Circuit Model of a TEFC Induction Machine With Measurements.* IEEE Transactions on Energy Conversion, 2009. 24(4): p. 809-818.
59. La Rocca, S., Pickering, S. J., Eastwick, C.N., Gerada, C., Connor, P.H., Rönnberg, K., *Challenges in modelling totally enclosed fan-cooled electrical machines*, in *International Heat Transfer Symposium and Heat Powered Cycles Conference*. 2016: Nottingham.

60. Moon, S.H., Jung, Y.H., Kim, K.W, *Numerical investigation on thermal-flow characteristics of a totally enclosed fan cooled induction motor*. in *2016 XXII International Conference on Electrical Machines (ICEM)*. 2016.
61. Chen, Y., Chen, B., Chen, C., *CFD Thermal Analysis and Optimization of Motor Cooling Fin Design.* Heat transfer: Volume 3, 2005.
62. Connor, P.H., *Computational Fluid Dynamics Modelling of a Synchronous Electric Generator*, in *Department of Mechanical, Materials and Manufacturing Engineering*. 2013, University of Nottingham: Nottingham.
63. La Rocca, A., *Thermal analysis of a high speed electrical machine*, in *Department of Mechanical, Materials and Manufacturing Engineering*. 2016, University of Nottingham: Nottingham.
64. Versteeg, H.K., Malalasekera, W., *An introduction to Computational Fluid Dynamics: The Finite Volume Method*. second edition ed. 2007: Prentice Hall.
65. Shanel, M., *Investigation of Rotor Cooling in Salient Pole Electrical Machines*, in *Department of Mechanical, Materials and Manufacturing Engineering*. 2002, University of Nottingham: Nottingham.
66. *Ansys Mesher and Fluent 17.2, User manual*.
67. Oslejsek, O., *The cooling of end winding of small enclosed electric machines.* Elektrotech, 1972. 61: p. 548-556.
68. Mugglestone, J., Pickering, S.J., Lampard D., *Prediction of the heat transfer from the end winding of a TEFC strip-wound induction motor*. in *Electric Machines and Drives, 1999. International Conference IEMD '99*. 1999.
69. Pickering, S.J., Thovex, F., Wheeler, P., Bradley, K., *Thermal Design of an Integrated Motor Drive*. in *IECON 2006 - 32nd Annual Conference on IEEE Industrial Electronics*. 2006.
70. *Infolytica MagNet 7.8, User manual*.
71. Simpson, N., Mellor, P.H., Wrobel, R., *Estimation of equivalent thermal parameters of electrical windings*. in *2012 XXth International Conference on Electrical Machines*. 2012.

Appendices

A. Dimensionless numbers

Equations below report the dimensionless numbers discussed in Chapter 2.

- Reynolds number:

$$Re = \frac{\rho v L}{\mu} \quad \text{A.1}$$

Where ρ is the fluid density [kg/m^3], v is the fluid velocity [m/s], L is the surface length [m] and μ the fluid dynamic viscosity [kg/sm]

- Grashof number:

$$Gr = \frac{\beta\ g\ \Delta T\ \rho^2\ L^3}{\mu^2} \quad \text{A.2}$$

Where β is the coefficient of cubical expansion of the fluid [K^{-1}], g the gravitational acceleration [m/s^2] and ΔT the temperature gradient [°C].

- Nusselt number:

$$Nu = \frac{hL}{k} \quad \text{A.3}$$

Where k is the fluid thermal conductivity [W/mK], h [W/m^{2}K] is the convective heat transfer coefficient and L is the characteristic length [m].

In the case of natural and forced convection, the following correlations, as combination of dimensionless numbers, can be employed.

Natural convection $$Nu = a\ (Gr\ Pr)^b$$ A.4

Forced convection $$Nu = a\ (Re)^b\ (Pr)^c$$ A.5

Where *a*, *b*, *c* are constants depending from the correlation used.

- Prandtl number:

$$Pr = \frac{c_p\ \mu}{k}$$ A.6

where c_p is the fluid specific heat capacity [kJ/kgK].

B. Theory behind CFD

This section provides a brief description of the theory associated with CFD regarding the governing equations of fluid flow and heat transfer.

The governing equations of fluid flow are known as the Navier-Stokes equations and of coupled non-linear second order partial differential equations. There are three distinct momentum equations along all three dimensional directions which are solved with the continuity and energy equation [64]: these are reported below.

x-momentum $$\rho \frac{Du}{Dt} = -\frac{\partial \rho}{\partial x} + div(\mu\ grad\ u) + S_{Mx} \quad \textbf{B.1}$$

y-momentum $$\rho \frac{Dv}{Dt} = -\frac{\partial \rho}{\partial y} + div(\mu\ grad\ v) + S_{My} \quad \textbf{B.2}$$

z-momentum $$\rho \frac{Dw}{Dt} = -\frac{\partial \rho}{\partial z} + div(\mu\ grad\ w) + S_{Mz} \quad \textbf{B.3}$$

continuity $$\frac{\partial \rho}{\partial t} + div(\rho u) = 0 \quad \textbf{B.4}$$

energy $$\rho \frac{Di}{Dt} = -\rho\ div\ u + div(k\ gradT) + \Phi + S_i \quad \textbf{B.5}$$

By using the variable Φ the Navier-Stokes equations can be represented by the transport equation as in Equation B.6:

$$\frac{\partial}{\partial t}\left(\int_V \rho\phi dV\right) + \int_A \vec{n}(\rho\phi\vec{u})dA = \int_A \vec{n}(\Gamma grad\phi)dA + \int_V S_\phi dV \qquad \textbf{B.6}$$

Rate of increase of Φ	+	Net rate of decrease of Φ due to convection across the boundaries	=	Rate of increase of Φ due to diffusion across the boundaries	+	Net rate of creation of Φ due to sources

Replacing the property Φ by for velocities along x, y and z-directions, the momentum equations are formed; if the internal energy *i* is used instead the energy equation is formed [64].

B.1 Turbulence Modelling

In case of turbulent flow the Direct Numerical Solution (DNS) approach can be used to solve the Navier-Stokes equations; as requirement of this method, the cells size has to be smaller than the Kolmogorov length scale [64] and therefore extremely fine meshes are required. The computational cost of this approach is not manageable with ordinary PCs and for this reason several turbulence models based on time averaged velocities were developed.

Equation B.7 below shows the velocity components considered: an average ($\bar{u}_i$) and a fluctuating (u'_i) term.

$$u_i = \overline{u_i} + u_i' \qquad \textbf{B.7}$$

By substituting this velocity into the Navier-Stoke equations a new set of equations known as Reynolds Averaged Navier-Stokes (RANS) are obtained. Six additional terms are introduced (Reynolds Stresses) leaving open equations which are closed by using the turbulence models.

One of the most widely used models, robust and suitable for most of engineering problems is the two-equation Standard k-ε, an Eddy Viscosity Model (EVM) based on the Boussinesq approximation; this approximation treats density as a constant value in all solved equations, except for the buoyancy term in the momentum equation. k and ε are the turbulent kinetic energy and the dissipation rate respectively, defined as in Equation B.8 and Equation B.9.

$$k = \frac{1}{2}(u'^2 + v'^2 + w'^2) \quad \textbf{B.8}$$

$$\varepsilon = \frac{dk}{dt} \quad \textbf{B.9}$$

Other variants of the two-equation k-ε models are available:

- RNG k-ε, suitable for complex shear flows involving rapid strain, moderate swirl, vortices, and locally transitional flows; it can cause convergence issues and unstable solutions.
- Realizable k-ε, can provide superior performance compared with the Standard k-ε model for flows involving rotation.

Other turbulence models are also available and their use is strongly dependent from the problem analysed and the flow nature expected. For problems involving external flows where viscous forces are significant the Shear Stress Transport (SST) k-ω can be more appropriate. This is a Reynolds Stress Model (RSM).

The RSM models, generally do not assume the turbulence to be isotropic as in the EVM models. They use six different transport equations to model each of the six distinct Reynolds stresses; this aspect leads to higher computational costs which outweigh their benefits [7].

Due to its stability and suitability for modelling electrical machines [65] the Realizable k-ε turbulence model was used in this work.

B.2 Wall Treatment

An accurate modelling of the complex turbulent phenomena occurring in proximity of walls is important for successful predictions of frictional drag, and thermal boundary layer. Vorticity effects in the near-walls regions can increase the turbulent momentum and thermal boundary layers where significant gradients occur.

Figure 0.1 below reports the dimensionless velocity $U/U\tau$, where $U\tau$ is the friction velocity, against the dimensionless wall distance y^+; the obtained profile is very common to many flows in the proximity of the walls. Depending on the order of the viscous effects, in the boundary layer three regions can be identified; the viscous sublayer where the viscous effects are dominant, a buffer layer where both contributes are comparable, and the fully turbulent region where turbulence plays a major role.

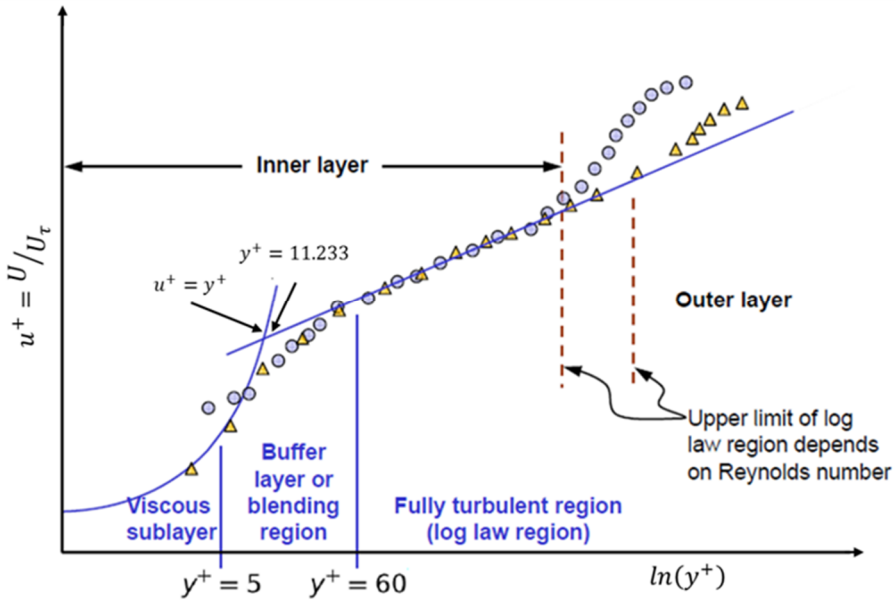


Figure 0.1: Near-Wall Regions [66]

$U\tau$ and y^+ are defined in Equation B.10 and Equation B.11 below: τ_{wall} is the shear stress, ρ the fluid density, y the wall distance and v the fluid kinematic viscosity.

$$U_\tau = \sqrt{\frac{\tau_{wall}}{\rho}} \quad \textbf{B.10}$$

$$y^+ = \frac{yU_\tau}{\nu} \quad \textbf{B.11}$$

Figure 0.2 below reports the two wall modelling strategies commonly available in CFD: the Wall Function Approach and the Near-Wall Model Approach. The latter is capable of resolving the viscous sublayer but requires a y^+ value of about 1, implying a very fine mesh in proximity of walls and therefore a sensible increase of cell count; the Wall Function instead does not resolve the viscous sublayer and requires significantly lighter meshes the y^+ needed being between 30 and 300.

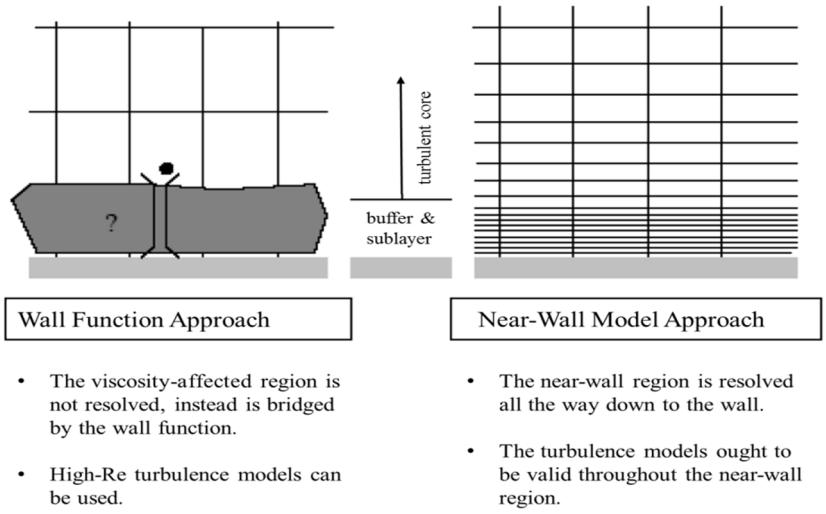


Figure 0.2: Wall Modelling Approaches [66]

In this work, the Enhanced Wall Treatment function available in Ansys Fluent is used; this allows to switch between near wall resolving and wall function modelling dependent on the commonly used y^+ value. This is used to interpret which flow regime is being experienced by the first cell in the mesh.

C. CFD General Algorithm

The CFD codes available for numerical analyses have all similar approach and algorithms which is schematically depicted in Figure 0.3 below. The definition of the problem is an extremely important step; quantities looked for, degree of accuracy required and domain needed should be clearly known before using any software.

The main steps of CFD software are as follows:

- Pre-processor: creation of the geometry representative of the regions in examination, fluid, solid or both; this will be the domain of the CFD study. The domain is then discretised using a suitable mesh (or grid).
- Solver: set up of thermal properties of the domain and specification of boundary conditions. The discretised conservation equations are solved iteratively for each element until convergence.
- Post-processor: numerical results obtained are processed and their accuracy analysed.

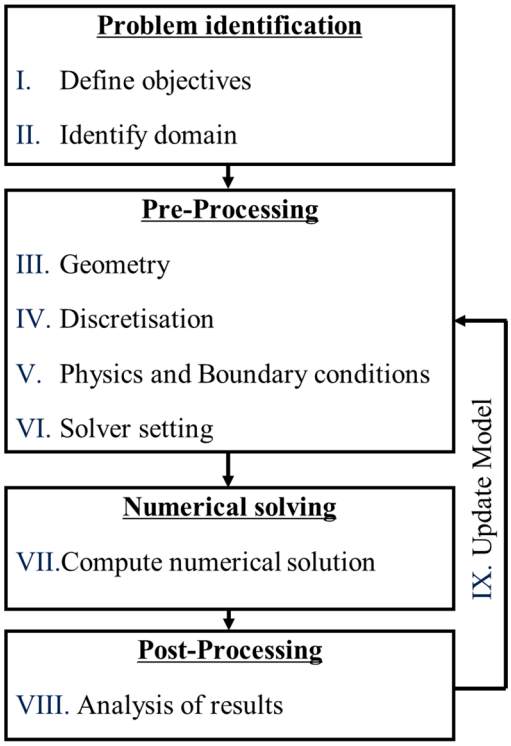


Figure 0.3: CFD process

C.1 Domain Identification

The identification of the domain is generally strictly linked to the objectives of the analysis; however the choice can also be based on the user's experience. Dependently from the kind of analysis required, only fluid domain or both fluid and solids domains (conjugate heat transfer analyses) can be modelled. In the case axisymmetric domains, as in the case of electrical machines, it can be chosen whether modelling the full 3D domain [62], a limited sector as done in [7, 21] or, if geometries are particularly simple, a 2D section only.

C.2 Geometry of Domain

The geometry created for CFD analysis needs to be capable of capturing the most crucial fluid flow and heat transfer phenomena; however, simplifications of the original domain are often required when they have a negligible impact on the heat or fluid flow.

C.3 Domain Discretisation

The discretisation process consists of sub-dividing the whole fluid or solid domain into a large number of small volumes or cells; the properties of each cell are then computed with respect to each other to solve the flow and thermal physics required. In the case of 3D models, CFD codes usually employ tetrahedral (tetra), hexahedral (hexa), prismoidal (prism) or pyramidal volumes shown in Figure 0.4. In this work tetrahedral and hexahedral elements are mostly used.

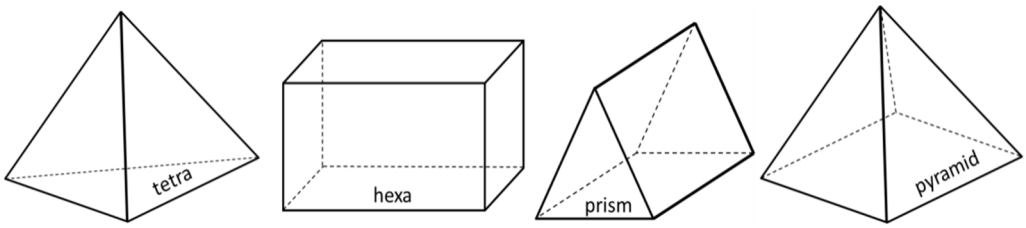


Figure 0.4: Typical mesh elements

The user's experience also plays an important role on the generation of a good mesh. In the case of multi-body domains the selection of the cell type is strongly linked to the complexity of the geometries, dimensions and zone type (fluid or solid regions).

For solid regions having simple geometries hexa elements are commonly used as this tends to reduce the mesh count and hence the computational cost. Complex fluid domains, such as in the end region of electrical machines, are usually discretised using tetra elements as it was done in this work.

Generally speaking, hexa elements lead to quicker solution convergence and, in case of mesh adaption, cell quality remains unchanged; using tetra elements instead angles might deteriorate leading to high skewed cells which can be source of numerical inaccuracies. The skewness (Equation C.1) is one of the main parameter which is usually used to check the quality of the generated mesh. The optimal cell size refers to an equilateral cell; skewness above 0.97 is considered unacceptable.

All meshes generated in this work have a maximum skewness of 0.95 which is considered acceptable [66]. This parameter generally provides an indication about the quality of the mesh generated.

$$Skewness = \frac{optimal\ cell\ size - cell\ size}{optimal\ cell\ size} \quad \textbf{C.1}$$

Another important parameter used to judge the quality of the mesh is the aspect ratio: this is defined as the ratio between the long and the short edges of the element and generally this value should not exceed 100.

The mesh count can strongly affect the computational cost and running time of the simulation. The number of grid cells depends on how detailed the information about the flow is required and by the accuracy of the solution. The size of the cell should be small enough to capture the local flow behavior adequately and to ensure that the changes in properties from cell to cell are not too large. Since a too coarse or too fine meshes can lead to low quality of solution, it is recommended to start computing the case using a coarse mesh, then gradually refining the mesh until the same solution is obtained; this process is called Mesh Independency Analysis. Finer meshes are then only recommended for limited regions where higher gradients are expected, this aims to resolve the most relevant flow details.

C.4 Solver Settings

Once the geometries and domains are defined and the turbulence model is selected, it is necessary to specify in which order the Reynolds Averaged Navier-Stokes (RANS) equations are solved and the degree of accuracy the field variables should be interpolated within each cell/element. Two solvers options are available in Fluent:

- Pressure Based: mass and momentum equations are solved at the same time, followed by the energy equation and the turbulence equations.
- Density Based: mass, momentum and energy at the same time followed by the turbulence equations last.

Density Based solver is usually recommended for high speed compressible flows involving combustion or hypersonic flows. The Pressure Based solver provides good performance for a wide range of compressible flows and also requires lower memory; for these reasons the Pressure Based solver is adopted in this work.

During the computation variables are stored at the centre of the grid cell, φ, these must be interpolated to the faces of the control volumes, φ_f (Figure 0.5).

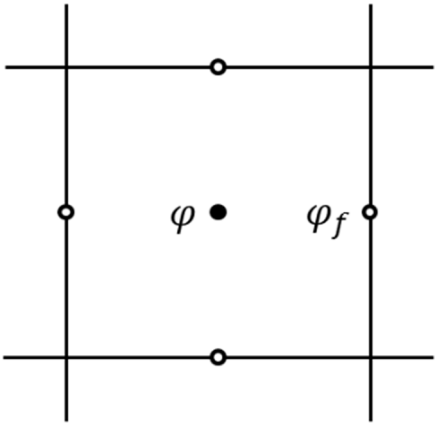


Figure 0.5: Control volume

Four interpolation schemes are available in Fluent [66]:

- *First-Order Upwind* – this is a 1st order accuracy scheme and therefore it is the easiest to converge; the face values is set equal to the cell-centre value of φ in the upstream cell.
- *Power Law* – This scheme interpolates the face value of a variable, using the exact solution to a one-dimensional convection-diffusion equation. It is recommended for flows with very low Reynolds number.

- *Second-Order Upwind* – this is a 2nd order accuracy scheme and it is more accurate compared to the previous schemes described. In this case φ_f depends on cell-centred values, its gradient $\nabla\varphi$ and the vector $\vec{r}$ directed from the cell centroid toward the face centroid upstream cell gradient (Equation C.2). This scheme is suitable when mostly tetrahedral elements are used; for this reason it was employed in this work.

$$\varphi_f = \varphi + \nabla\varphi\,\vec{r} \qquad \textbf{C.2}$$

- *Quadratic Upwind Interpolation* (QUICK) – this is a 3rd order accuracy scheme and therefore it is more accurate of the schemes described above; however it can only be used with hexa dominant meshes.

When the Pressure Based solver is selected as in this work, numerical algorithms for the pressure-velocity coupling must be implemented; these derive an equation for pressure by using a combination of continuity and momentum equations. Within Fluent the most robust and suitable for steady-state simulation is the Semi-Implicit Method for Pressure-Linked Equations algorithm, known as SIMPLE.

C.5 Convergence

The number of iterations to a converged solution is linked to the domain extensions, mesh count and physics involved.

The following conditions are considered to assess the convergence of the solution:

- The solution is steady and it does not change with subsequent iterations.
- Overall momentum, mass and energy are balanced.
- All equations are obeyed in all control volumes to a specified tolerance.

In Fluent the solution accuracy and whether the solution has convergence issues or not can be judged from the plotting of residuals; these consist of the difference between the previous and current result of an equation and they can be plotted for all equations considered. Additional monitors can be also created and plotted for quantities which can be particularly important for the type of problem considered. In the case of electrical machines a parameter to be monitored is the moment given by the viscous force generated on the rotor surface due to the rotation; this is particularly important for achieving an accurate prediction of the windage generated.

General Fluent guidelines suggest that good convergence can be assumed when continuity and momentum equations converge with an order of 10^{-3} and 10^{-7} for the energy equation. For particularly complex domains 10^{-3} might not be achieved but if residuals no longer change an order of 10^{-2} can still be considered converged.

C.6 Post-Processing

Post-Processing groups all operations aimed to analyse the numerical data computed. A converged solution does not necessarily mean reliable results; it is essential that the user checks the obtained data to assess their consistency. Once that is done, the solution can be post-processed and data of interest can be plotted using graphs, contours, streamlines or vectors.